Development of a novel system to measure and calculate tooth movements for studying the properties of the periodontal ligament

Ph.D. thesis

By

He Liu

October 2006

School of Engineering

Cardiff University

Acknowledgements

I would like to express my gratefully thanks to my supervisor, Dr Sam Evans, for his guidance, advice and enthusiastically help throughout my studies. I would also like to express my gratefully thanks to Dr Cathy Holt, for her earnestly, enthusiastically, valuable help and suggestions in my studies. I would also like to express my thanks to all the colleagues in this project, especially to: Professor John Middleton from the Dental School, for his help in dental study; Dr Jeremy Knox from the Dental School, for his help in clinical experiments. I wish to thank: The Engineering and Physical Sciences Research Council, UK, for their financial support. I would also like to thanks: my friends in the Institute of Medical Engineering and Medical Physics, and in the Manufacturing Engineering Centre, and members of mechanical workshop, in the School of Engineering, Cardiff University, for their help.

Finally, I would like to express my deepest gratitude to my mother, father and my family for their continuous support and encouragement.

Abstract

Motion analysis techniques have been widely used in biomechanics for measuring large-scale motions such as gait, posture etc, but have not yet been significantly explored for measuring smaller movements such as tooth movement under load. In principle, very accurate measurements could be possible and this could provide a valuable tool in many engineering applications. The aim of this study was to develop a novel system to measure and calculate tooth movements with 6DOF in 3D space for studying the properties of the periodontal ligament.

The Qualisys ProReflex-MCU120 motion capture system has been developed to measure micro-movements. The calibration frame was designed and made for the system calibration. The system accuracy was ±1.17%, ±1.67% and ±1.31% for diamond markers; ±1.81%, ±2.37% and ±1.39% for spherical markers in x, y and z directions in the range of 20 - 200μm. These results demonstrated that the system is accurate enough to measure small-scale movements.

To measure tooth movement, two retroreflective marker clusters, two pointers and one plane for the pointer calibration were created. The two marker clusters were fixed on the measured tooth and the reference tooth for measurements. The pointer was used to identify the three landmarks for identifying anatomical coordinate system of tooth. Data analysis software was developed and evaluated for calculating tooth movement in 6DOF. In the data analysis software, the three coordinate systems method was used with transformation matrices to give 6DOF results. The evaluation results of a complete system were ±3.2%, ±2.8% and ±2.4% for rotations; ±5.3%, ±7.7% and ±4.7% for translations in x, y and z directions in the term of accuracy. For producing tooth measurements, loading devices and loading control system were designed and tested.

The experiments were carried out on human volunteers in clinical setting. Loads of 0.196N, 0.294N and 0.49N were separately applied to the measured tooth in the buccal direction and the intrusive direction for 10s and 30s, respectively. The experimental results demonstrated that, with the buccal loading, the tooth translations were 32μm for load of 0.294N, and 41μm for load of 0.49N in the y direction of the anatomical coordinate system, tooth rotations were 0.09° and 0.07° for load of 0.294N, and 0.1° and 0.06° for load of 0.49N in the x and z directions; with the intrusive loading, tooth movements were 37μm, 15μm and 54μm for load of 0.196N, and 140μm, 51μm and 25μm for load of 0.49N in the x, y and z directions, tooth rotations were 0.04°, 0.07° and 0.2° for load of 0.196N, and 0.26°, 0.195° and 0.35° for load of 0.49N about the x, y and z directions.

Overall, a novel system of measuring and calculating tooth movement has been developed. It could be useful in applications in many other engineering fields.

Contents

Chapter 4 Methods of data acquisition, processing and software evaluation

Chapter 1 Introduction

Optical motion analysis techniques have been widely used in biomechanics for measuring large scale motions such as gait, posture, and movement of the human body (Capello et al., 1997; Cappozzo et al., 1996; Hunt et al., 2001; Green et al., 1994; Hirokawa et al., 2001; Holt et al., 2000; Jones et al., 2001a). Haggmann-Henrikson et al. (1998) used the Qualisys Mac Reflex three-dimensional motion capture systems to measure chewing movements. However these techniques have not yet been significantly explored for measuring smaller movements, such as tooth movement under load.

The aim of this study is to measure and calculate tooth movement with 6 degrees of freedom (6DOF) in 3 dimensional spaces for establishing an accurate finite element model of the periodontal ligament (PDL) to allow determination of the quantitative dynamic response of tooth mobility. There are many different precision measurement instruments which can measure small displacements, such as laser displacement sensors (LDS), coordinate measurement machines (CMM), atomic force microscopes (AFM) etc. But most of them cannot meet the requirements of measuring tooth movement in 3D space because of the restrictions of their structures or measurement methods. Thus to investigate a high precision 3D measurement system is valuable for measuring tooth movement accurately, as a step towards studying the mechanical properties of the PDL and establishing a constitutive finite element model of the PDL; and such a system might have many other useful applications.

The PDL is a soft tissue which connects between the root of a tooth and the surrounding alveolar bone. It consists of blood vessels and collagen fibres which are embedded into the alveolar bone to form a solid part. The biological structure of the PDL is very complicated. To understand PDL mechanical properties and model the PDL accurately is a key to assess the relative merits of different treatment options, materials and systems, and would assist in planning treatment in particular cases. In clinical treatment, even small reductions in treatment time and improvements in success rates could produce large savings for the National Health Service (NHS) as well as improvement of the patients' quality of life, because the NHS pays £2,000 or more to save one child teeth and the orthodontic period takes about a year at the moment (The report from British Orthodontic Society, 2001).

The study of the PDL mechanical properties dates back at least a century. Indeed, even as early as 1904, dental scientists, such as Wallace (1904) and Trauner (1912) were investigating the mechanical properties of the PDL. Previous studies used animals, ranging from rats and monkeys to rabbit and pigs (Webb et al., 1994; Fullmer 1959; Diamant et at., 1972; Dorow et al., 2002a). Clearly, the results obtained do not always relate to the situation in humans and the results only were given in one dimension. Jones et al. (1998) used a LAS5010 laser displacement sensor to measure tooth movement to investigate the behaviour of the PDL. Unfortunately, the mechanical properties of the human PDL, which include viscoelastic, porohyperelastic and anisotropic behaviour, are still not well understood due to the fact that specimens of the PDL are very small and dehydrate rapidly, making mechanical testing difficult.

There is considerable evidence to show that the deformation of the PDL has a key influence on orthodontic tooth movement (Moxham and Berkovitz 1979; Parfitt 1960; Picton 1962; Wills et al., 1978). Thus measuring and calculating tooth movement of 6DOF under load, deforming the PDL, provide a practical approach to understanding the mechanical properties of the PDL.

The tooth movement caused by orthodontic forces in a short period is very small. The results of Hickman (1997) showed that the maximum tooth displacement under 0.5N lingual load is approximately range of 12 - 132μm. To measure such small movements accurately, a high precision measurement system is crucial. In principle, the Qualisys motion capture system, including Qualisys track manager (QTM) and motion camera units (MCUs), could be used to achieve very small scale measurements in 3D space because the system resolution is 1/60,000 of the diagonal field of view according to the manufacture's technical literature (QTM manual, 2004). This means that the system resolution could be less than 1µm if the field of view is small enough. In fact, the system accuracy, repeatability, noise, actual resolution and optimal angle of the camera placements have not been previously explored in a small field of view. Measurements of 6DOF human tooth movements also have not been developed.

In this study, there were two systems that needed to be developed: (1) the QTM system for measuring tooth movement in 3D space; (2) the biomechanical measurement system for giving tooth movement in 6DOF. This system included the QTM system and the software of data processing. With the development of a novel system to measure and calculate tooth movement in 6DOF, much work must be done. The following presents the objectives of this study:

- To develop a novel system to measure and calculate tooth movement in 6DOF, including:
    1. Calibration methods for the optical motion analysis system;
    2. Method of calculation of the field of view;
    3. Method of detection of random noise;
    4. Method of evaluation system resolution, accuracy and repeatability;
    5. Evaluation of the effects of camera convergence angle on accuracy and repeatability;
    6. Results analysis and discussion;
- To establish a method of measuring tooth movement;
- To develop software to calculate tooth movements with 6DOF based on the method for knee measurement developed by Holt et al. (2000);
- Evaluation of the biomechanical measurement system;
- To design, compare and evaluate methods of loading the tooth;

- To design and test the control system for the loading device;
- To design the method of clinical experiments and perform experiments in a clinical setting;
- Analysis and discussion of the experimental results.

The novel system to measure and calculate tooth movements in human living teeth with 6DOF in 3D using motion analysis techniques has been successfully developed and applied in measuring tooth movement in a clinical setting. The results show that the system could be applied not just to biomechanics research but also potentially applied to many other engineering fields.

The fulfilment of the above objectives was concerned with several different investigations. In order to present all work clearly, the thesis is separated into nine chapters, each with its own introduction, methods, results, and discussion.

This thesis is written for the reader with a background in motion analysis techniques, metrologies, 3D data processing, general engineering and basic dental knowledge. The author recognises that some technical terms in particular may be unfamiliar, so a glossary is provided in Appendix A.

Chapter 2 Literature review

2.1 Introduction

To develop a novel system of measuring and calculating tooth movement in 6DOF, it is essential to survey and understand previous study methods, the diversity of approaches, and advantages and disadvantages in the application of measuring tooth movement. A considerable amount of literature was surveyed because of the multidisciplinary nature of the project. In this chapter, the following topics will be presented and discussed:

- The structural organization of teeth and the PDL, which affects tooth movement;
- The biomechanical properties of the PDL, described in historical research;
- How do the teeth move under load?
- What loading methods were used in measuring tooth movement?
- Why do we measure tooth movement?
- What methods have been used to measure small-scale movements, to process the captured data and produce the results of tooth movement with 6 degrees of freedom (6DOF)?
- What are the motion capture system and their applications?

2.2 Tooth movements

2.2.1 The teeth and the structural organization of the PDL

There are two types of teeth: primary teeth and permanent teeth. There are twenty primary teeth and they last about six or seven years. These are followed by 32 permanent teeth which will last a lifetime if they are correctly cared for. The tooth and the PDL are the objects of research in this study and experiments were carried out using permanent teeth in this study. Therefore it is necessary to understand them in general terms, particular structure and specific features. Figure 2.1 shows 32 permanent teeth with the names (Dental education site 1997).

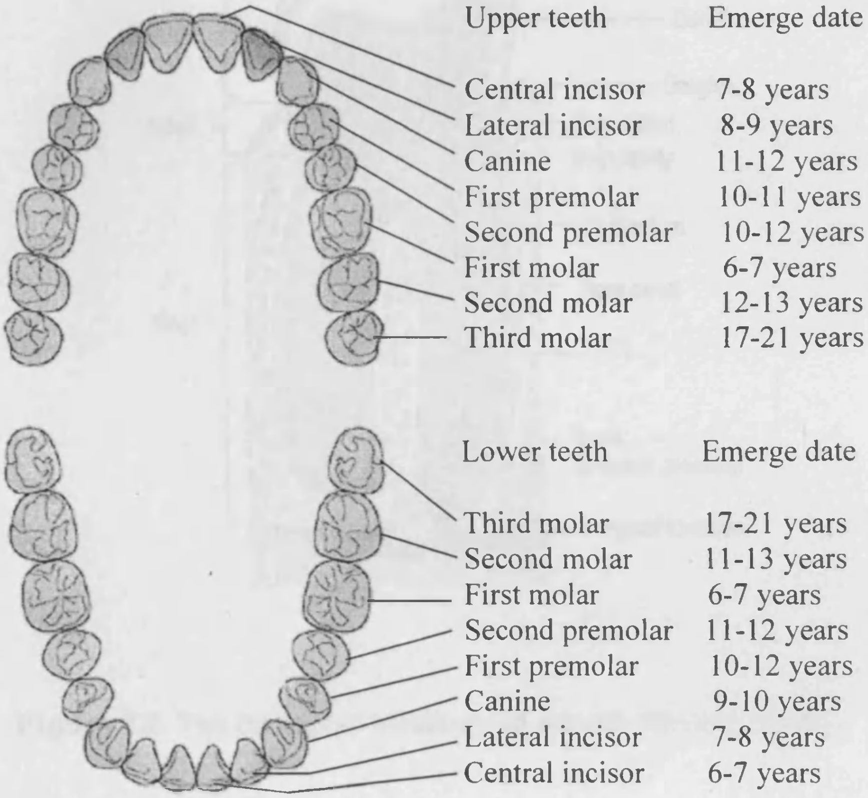

Figure 2.1 Permanent teeth and their names (Dental education site 1997)

A tooth consists of three parts: the crown, the neck, and the root. The crown is the part which can be seen above the gums (gingiva), the neck is at the gum line, and the root is hidden under the gum. In fact, teeth have a very complex biological structure, as shown in Figure 2.2 (Grubb, 1999). The outermost layer is the enamel, the bulk of the tooth is dentin, and there is a coating of cementum on the outer surface beneath the gum. In the centre, there is the 'pulp' which consists of connective tissue, blood vessels and nerves. The blood vessels nourish the tooth and the nerves transmit sensations of pain to the brain.

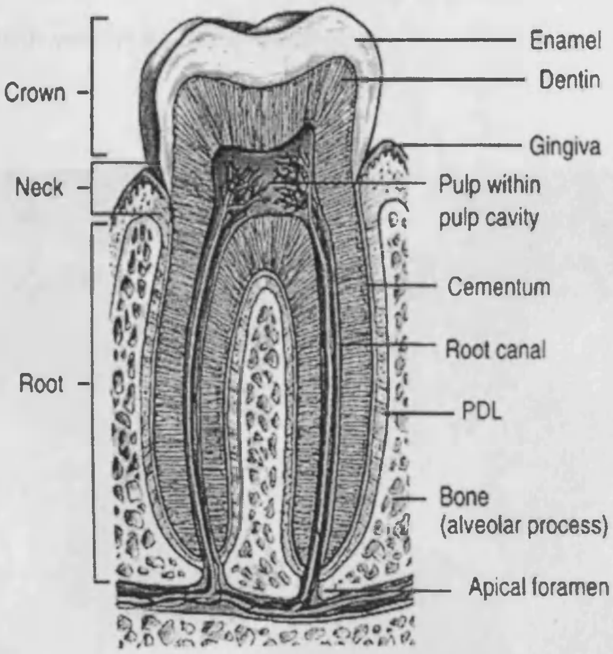

Figure 2.2 The biological structure of a tooth (Grubb, 1999).

The crown of each tooth has a coating of enamel. Enamel lies over the dentin in the crown of the tooth. It forms the outermost covering of the crown. It enables the tooth to withstand the pressure placed on it during biting and chewing. Enamel consists of mineral salts and a small amount of water. Enamel is white but transparent. The major component of the inside of the tooth is dentin. Dentin is harder than bone. It consists mainly of mineral salts and water but also has some living cells. Dentin has a highly organized structure with an array of parallel pores, as shown in Figure 2.3 (Grubb, 1999). Below the gum, cementum overlies the dentin in the root of the tooth. In most cases, the cementum and the enamel meet where the root ends and the crown begins. The cementum is more like bone in structure. Cementum is as hard as bone and consists mainly of mineral salts and water. Its purpose is to act as the anchorage of the periodontal ligament - a bunch of collagen fibres that hold the tooth in place and act as shock absorber between tooth and jawbone. The PDL contains elastic fibres to allow some movement of the tooth within its bony socket.

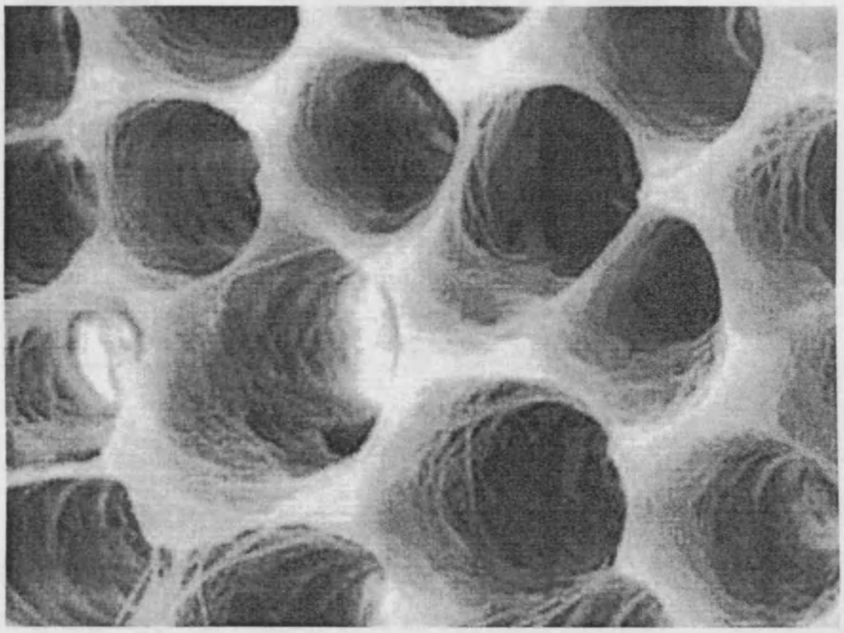

Figure 2.3 The structure of dentin with an array of parallel pores (Grubb, 1999).

Figure 2.4 shows the biological structure of the PDL (Sloan, 1978). The PDL is a soft tissue connected between the root of the tooth and alveolar bone. In humans, the width of the PDL ranges from 150μm to 200μm (Coolidge, 1937). Occlusal loading affects the width of the PDL. If occlusal forces are within physiological limits, increased occlusal loading leads to an increase in width through a thickening of the fibre bundles and an increase in diameter and number of Sharpey's fibres (Kronfeld, 1931). Forces that exceed this limit cause lesions that are characteristic of trauma from occlusion. When occlusal loading is diminished or absent, the width of the PDL decreases.

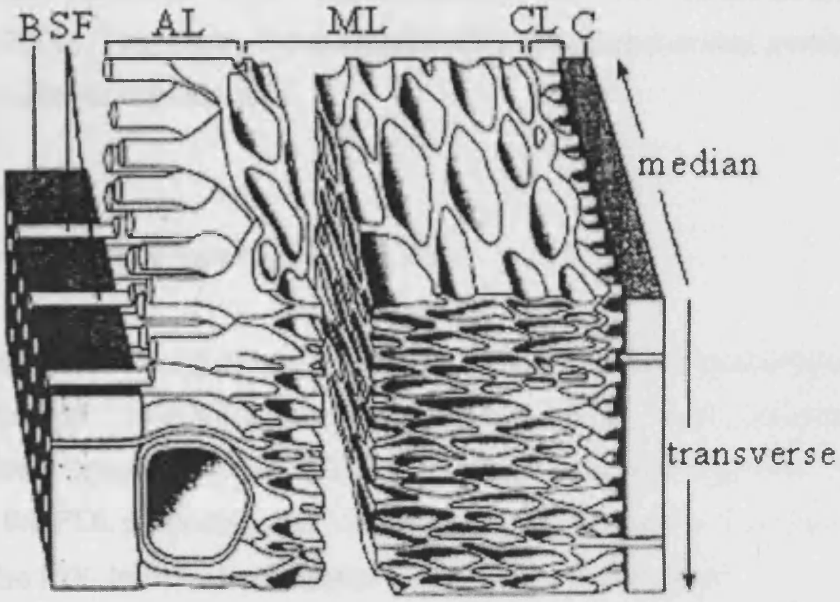

Figure 2.4 The biological structure of the PDL. Sharpey fibres (SF) grow into the alveolar bone (B), a continuation of the round fibre bundles of the alveolar layer (AL). A similar arrangement exists on the opposite side, the cemental layer (CL) where the PDL is attached to the cement (C) of the tooth. The middle layer (ML) shows longitudinal lamination (Sloan, 1978).

The fibres are reduced in number and density, and they eventually become oriented parallel to the root surface (Anneroth, and Ericsson, 1967). The PDL consists of collagen fibres which are embedded into the root cementum and the alveolar bone, together with the blood vessels to form a substantial part. The PDL has a sensitive proprioceptive mechanism which can detect minute changes in forces applied to the teeth (Palmer 1999). Forces applied to the teeth are dissipated through compression and redistribution of the fluid elements as well as through the fibre system. Forces transmitted through the PDL can result in remodelling and tooth movement, as seen in orthodontics, and an increase in tooth mobility. The deformation of the PDL has a key influence on orthodontic tooth movement (Middleton et al., 1990; Wilson et al., 1994; Jones et al., 1998; Knox et al., 2000). Therefore, the understanding of biomechanical properties of the PDL is crucial for orthodontics.

2.2.2 Biomechanical properties of the PDL

The PDL is a complex living material, thus it is difficult to obtain specimens due to rapid dehydration. Scientists and researchers have been studying the biomechanical properties of the PDL using various approaches over the last century. For the PDL properties, the following specific features are of interest:

- Can the PDL transfer both tensile and compressive stress?
- Is the PDL essentially an anisotropic feature?
- Does the PDL experience large deformations under load?
- Does the PDL display time-dependent response to loads?
- How sensitive is the PDL to loading rate and recent strain history?
- Are there differences between in vivo and in vitro tests?
- Can the PDL be modelled using linear elasticity, small deformation theory (Middleton et al., 1990)?
- How does fluid flow within the PDL?

The term 'PDL' has long been used to identify the soft tissue surrounding the root of tooth (Wallace 1904). The properties of the PDL were first studied by Pfaffmann in 1939. However, by then histologists had described a variety of nerve endings within the PDL (Lashley, 1916; Stewart, 1927; Lewinsky and Stewart, 1936; van der Sprenkel, 1936; Brashear, 1936; Bradlaw, 1939).

Parfitt (1960) started his experiments on human maxillary incisors. An intrusive load, that is, one which loads the tooth vertically upwards along the axis of the tooth length, was applied manually as an increasing force at various rates until the desired peak force was obtained. Parfitt reported that, if the intrusive force was increased gradually and evenly, the displacement of the tooth showed an initial rapidly rising phase with loads up to about 1N. He calculated that the mean displacement for a thrust of 1N was approximately 20µm, while an increase from 1N to 10N produced an additional movement of only 8µm, and less displacement of the tooth was produced if the load was applied rapidly. When an intrusive load was removed, the tooth recovered its original position in two phases. The first recovery phase showed a rapid return towards its original position in an almost linear manner with time. The second phase involved a slower recovery, there being an apparent logarithmic relationship between movement and time.

Picton (1962, 1963) developed extensively the work of Parfitt. In 1962-1963, he published the results of studies on tooth mobility in human maxillary incisors, mandibular first premolars and maxillary first molars during biting. His apparatus consisted of two movement transducers incorporating resistance-wire strain gauges soldered to the wings of a rubber dam clamp, which was placed on the test tooth. Metal pointers from the transducers rested on the teeth immediately adjacent to the test tooth to provide reference points. A biting force of up to 20N was applied to the test tooth via a dynamometer anchored to teeth in the opposing jaw. Three thrusts were made to each tooth studied, the time interval between thrusts being 30 seconds to 1 minute. He claimed that tilting of the teeth during the biting thrusts could be accounted for. However, he emphasized that, since the adjacent reference teeth were also probably displaced by the thrusts, the values obtained for tooth mobility were not to be regarded as absolute. Although considerable variation was sometimes found between consecutive thrusts, the pattern and amount of intrusive tooth movements were similar to those obtained by Parfitt (1960). Thus, the load-tooth mobility curves revealed an initial phase of relatively free movement followed by a second phase of less movement. However, the changeover between the two phases appeared to be rather variable, and tended to occur at the higher load of approximately 4N. Later experiments by Picton (1964) generally confirmed his early study.

Wills et al (1978) suggest that different loading rates do have a significant effect on tooth mobility. They reported that the rapid application of loads rising to 4N caused less tooth displacement than with loads applied more gradually. Their experiments described the relationship between intrusive force and tooth mobility was 'non-Hooke's law' and they proposed possibility that the periodontium might have viscoelastic properties. They did experiments on monkeys and provided records of the pattern of displacement and recovery of the monkey incisor with an intrusive load applied as a ramp function, and likened the response to the force-displacement relationship of a Voigt element. They also listed five other characteristics of the stressed PDL, which they claimed identified this tissue as viscoelastic: (1) Loads sustained for many seconds or minutes cause creep; (2) There is an inverse relationship between the rate of loading and the displacement; (3) The higher the rate of loading, the less is the distinction between the early and late phases of displacement; (4) If loading is repeated at intervals of less than 1.5 minutes, the recovery becomes progressively more incomplete; (5) The rate of recovery is directly related to the loading rate and indirectly related to the duration of the load.

Moxham and Berkovitz (1979) tested the rabbit mandibular incisor. An extrusive load, i.e., a load that acts to pull the tooth out along the long axis of the tooth, was suddenly applied on the rabbit incisor and maintained for 5 minutes and then suddenly removed. It was found that the tooth movement in 5 minutes had two phases during extrusive loading. During the first phase, there is a rapid, instantaneous extrusion of the tooth. The second phase involves a more gradual extrusion. The results showed that, both first and second phases of the extrusive and recovery cycles are force dependent, and indicated that the responses do not have Hooke-type characteristics. The results may also support the view that the periodontal tissues behave viscoelastically.

Coelho and Moxham (1989) studied the intrusive mobility of the guinea pig incisor. Experiments were performed on the right mandibular incisors of 16 male guinea pigs (average weight 500g) under anaesthesia. A variable capacitance displacement transducer was used to monitor tooth position continuously. It was found that the pattern of mobility was consistent with the view that the periodontal tissues are viscoelastic. Coelho and Moxham claimed that, if the loads were held on the teeth for short durations, they are equal to mastication in humans, and then more nearly elastic responses are produced. This latter finding has been confirmed on the teeth of monkeys by Picton (1989).

Inoue (1989) investigated changes in the biomechanical properties of the periodontal tissue during canine retraction, in terms of tooth mobility. The upper canines on both sides of ten orthodontic patients were moved in the distal direction for about four weeks with an initial force of 1.96N. The amount of tooth movement and the magnitude of tooth mobility were measured every 3 or 4 days during retraction. The tooth movement curve was divided into three phases: an initial phase, a lag phase and a post-lag phase. Research indicated that the biomechanical properties of the periodontal tissue change in response to each phase of tooth movement.

Middleton et al. (1990) used a three dimensional finite element model to investigate the biomechanical response of an upper canine tooth. The computer model was developed from ceramic replicas and x-rays, and consisted of cancellous and cortical bone, the periodontal ligament, dentine and pulp chamber. A horizontal force was applied at the tip of the crown and at the cervical margin. A rotation force was applied at the cervical margin of the tooth crown. The resulting displacements and stress field for each load case were presented with particular emphasis being placed on the response of the periodontal ligament. The investigation showed that quantitative information on initial tooth movement can be accurately predicted and used to evaluate the response of orthodontic treatment.

McGuinness et al. (1991) used a three dimensional finite element model, developed by Middleton et al. (1990), of a human maxillary canine tooth to predict the maximum principal stresses in the PDL when various orthodontic forces were applied. It was found that a 1N tipping force produced stresses at the cervical margin of the PDL as high as 0.196N/mm^2 and apical stresses up to -0.034N/mm^2. In 1992, they published new results from the continuing research. The maximum stress induced at the cervical margin of the PDL was 0.072N/mm^2 and maximum stress induced at the apical foramen was 0.0038N/mm^2. The results suggest that even with 'perfect' mechanics it would be difficult to obtain canine movement by pure translation.

Wilson et al. (1994) studied the stress in the PDL during vertical tooth movement based on the research of Middleton et al. (1990) and McGuinness et al. (1991, 1992). The vertical intrusive movement of teeth was considered difficult and the most routine clinical vertical movement of teeth was confined to extrusion. In studying the FE model, the PDL behaviour was assumed to be linearly-elastic. When intrusive and extrusive forces of 1N were applied to the surface of the crown of a tooth model, the maximum cervical margin stress in the PDL was 0.0046N/mm^2 and the apical maximum stress was 0.0021N/mm^2. They consider that the periodontal stress distribution was highly complex within the 3D FE model.

Qian et al. (1999) created a three-dimensional finite element model to analyse the influence of the PDL fibres on the orthodontic tooth movement. Their model used the following materials: dentin, the PDL fibre, the PDL non-fibrous matrix, and the cortical and cancellous bones of the mandible. Because the Young's modulus and Poisson's ratio of the PDL fibre are not very clear, the model is not very reliable.

Soncini and Pietrabissa (1999) established a mathematical model of tooth movement based on the PDL characteristics with two elastic constants – instantaneous behaviour $K'_{PDL,}$ long term behaviour K''_{PDL} , and a viscous parameter η_{PDL}; the bone characteristic with an elastic component K_{AB} and a viscous parameter η_{AB}. The aim was to form standard geometrical references and parameters to support the orthodontist in designing orthodontic treatment. The model has been evaluated by comparison with those of published experimental works. The comparison curves were quite close and demonstrated that the PDL has elastic and viscous characteristics.

Bourauel et al. (2000) developed a numerical model based on bone remodelling theories to simulate orthodontic tooth movements. The root of a canine was modelled in an idealized way in the form of an elliptical paraboloid and was processed with a finite element program. The finite element model was loaded with several different force systems. The mechanical loads firstly in the periodontal ligament and secondly in the alveolar bone were taken to simulate the tooth movements, such as mesial tipping around the centre of resistance, rotation around the long axis of the tooth, uncontrolled tipping around the root tip, canine retraction, extrusion and intrusion. Comparison with clinical experience was performed by calculating the orthodontic tooth movements based on the assumption of a fixed position of the centre of resistance.

Pini et al. (2000) evaluated the stress-strain behaviour of fresh frozen bovine PDL in both tension and compression by using uniaxial tests. A uniaxial testing machine was built under a microscope to apply displacements with a computer driven stepper motor and forces in the 100N range were measured. The microstructure of the bovine PDL was examined by using a scanning electron microscope. The PDL strain was recorded by video analysis and a linear variable differential transformer (LVDT). A typical stress-strain curve of the bovine PDL demonstrated that, for relatively large increments in strain, there occurs little change in stress. Upon compressive loading, the curve displayed a rapid decrement in stress for small changes in strain and the compressive stress appears to rise at a faster rate than for tensile loading.

Natali et al. (2000) performed a FE numerical analysis of the short time response of the PDL. The formulation was based on the consideration of different isotropic hyperelastic constitutive models (Marsden and Hughes 1982). A three dimensional model of an incisor with surrounding periodontal ligament was loaded by a vertical intrusive force. The results demonstrated that viscous behaviour can be considered to describe the properties of the PDL.

Knets et al. (2001) analysed the stress in the human mandible during simulated tooth clenching using a 3D finite element model. The complete solution was performed and the results were compared with clinical observations and experimental data from mechanical test on samples. The model is useful for analysing the properties of the jaw bone and a step towards the analysis of tooth movement.

Krstin et al. (2002a, b) investigated the material behaviour of human periodontal ligament using specimens of human mandible. From their experiments it was concluded that the material behaviour of the PDL under load is very complex and that it depends on many factors. The main factors that influenced the results were the consequence of the preparation process and experimental set-up. During the preparation and the cutting of the specimens, the tissue was damaged and some surface structures were mechanically destroyed or burned. A second factor that influenced the behaviour in a significant way was drying out and the moisture of the specimens. A third important factor that needs to be considered is the experimental set-up and clamping of the specimens. The material behaviour of the PDL was investigated and the main characteristics of viscoelastic behaviour shown. Stress-strain curves in loading up to a fixed strain and unloading were recorded and demonstrated hysteresis. The PDL was shown for the tissue with complex material behaviour and time dependent material properties. It is characterized by a non-linearity and time dependency and additionally depends on the previous loading history.

In 2002a,b,c, 2003a,b,c and 2004, Dorow et al. and Natali et al. developed a viscoelastic constitutive model for the PDL capable of accounting for large strain, anisotropy, and inelastic time-dependent effects. They believed that the PDL exhibits anisotropy and inelastic time-dependent effects. The anisotropy characteristics of the PDL are determined by the distribution of collagen fibres, and time-dependent viscous phenomena are due to microstructural modifications during loading, such as fluid fluxes moving through the solid and the internal rearrangement of fibres and constitutive adaptation. The experimental tests were carried out on specimens from adult pigs to obtain stress-relaxation and cyclic stress-strain curves. The comparison of experimental and numerical results revealed good correspondence and confirmed the capability of the formulation assumed to properly predict the viscoelastic behaviour of the PDL.

Kawarizadeh et al. (2004) investigated whether stress or strain within the PDL, or rather in bone, plays a role in initiating biological responses in orthodontic tooth movement. The upper first molars of 11 rats were moved with a closed nickel titanium alloy coil spring for 3 to 12 days and three rats served as controls. The molars and incisors were notched on the mesial and distal surfaces to ensure maximum retention of the spring. The appliance was activated immediately upon intrusion with an initial tensile force of 0.5N. The movement of the roots of the teeth was scanned using a camera mounted on a light microscope and viewed with image software on a personal computer. Based on histological sections, finite element models were developed and the results from the FE models were compared with experiment results. The results indicated a direct correlation of the calculated stress/strain values in the PDL with the distribution of osteoclasts in the alveolar bone. These seem to be the mechanical factor of tissue reaction to orthodontic force application.

Ziegler et al. (2005) examined the elastic properties of the PDL in eight multi-rooted teeth of six pigs using a combined experimental and numerical study. The initial tooth movement surrounded by the periodontium under the maximum load of 6N was measured in three–dimensional space by optoelectronic planar sensors (Hinterkausen et al., 1998). The intrusion load was applied gradually on the tooth via a force and torque sensor. A waiting period of 40 seconds was kept between each load step and the measurement was taken over about 1.5-2 hours. 3D finite element models were constructed based on transverse sections of resin embedded teeth and the same force system in the experiments was used in the numerical simulation. The results showed that the PDL exhibited the non-linear force/ displacement behaviour which could be described in a bilinear manner.

The PDL mechanical properties are highly complex and are still being investigated. Until now, most investigators prefer the viscoelastic theory to describe the biomechanical property of the PDL, because the viscoelastic viewpoints can explain the present experimental data concerning the force-displacement characteristics of teeth. But there is a lack of papers in the literature, and at present, none of the questions at the beginning of this section can be answered.

2.2.3 Relationship between tooth movements and force

Conventionally, there are two types of force that make teeth move: masticating forces and orthodontic forces. In studying tooth movement, forces are divided into intrusion; extrusion (eruption); buccal loading, i.e., a load that acts to push the tooth in horizontal direction, and lingual loading, i.e., a load that acts to pull the tooth in horizontal direction; and twisting, i.e. a couple of force that acts to rotate the tooth about the long axis of the tooth.

The teeth are surrounded by gum tissue (also called gingiva) at the neck area. Under the gum tissue, the PDL encases the root of the tooth and lies between the root of the tooth and the alveolar bone. When the force is applied to teeth, the PDL is stretched on one side and is compressed on the other. The bone then grows in to support the tooth in its new position.

Teeth are socketed in the bone of the maxilla for the upper teeth and the mandible for the lower teeth. The PDL is a sort of messenger which relates between the root of the tooth and the alveolar bony socket. Pressure between the PDL and alveolar bone causes the bone to create osteoclasts, and break down the bone to restore the normal spacing between the teeth and bone. The corresponding tension on the PDL and the alveolar bone behind the movement causes the bone to create osteoblasts which effectively build new bone to restore the normal spacing between the root of the tooth and the alveolar bone. The initial osteoclast process takes approximately 72 hours to get fully going; the osteoblast process takes approximately 90 days. The stabilizing result takes about 10 months (Rice, 2006).

If a force applied on the tooth is of a short duration, the force will create a stress-strain field in the root of the tooth and cause a deformation of the PDL. The deformation of the PDL results in the tooth movement in the early phase. If the force is removed, the stress-strain field will be gradually reduced to zero. The deformation of the PDL will attempt to go back to its original position. The movement of the tooth has different types according to the force orientation applied to the tooth. Normally there are the following types:

Rotation movement (Orthodontics, 1999) – the forces applied on the tooth are a couple and the positions of forces have a distance from the centre of resistance

(CR). Rotation movements of the tooth are occurred around the centre resistance. Rotation movements are shown in Figure 2.5.

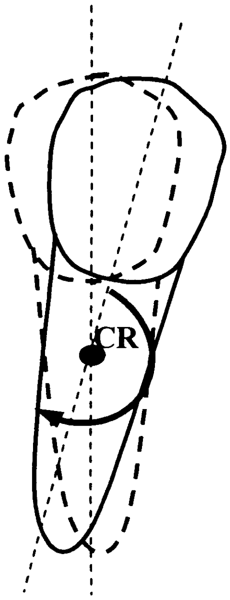

Figure 2.5 The tooth rotation movements.

Translation movement (Orthodontics, 1999) – it is bodily movement of the tooth when the force directly applied to the tooth. Translation movements are divided to intrusion and extrusion. Intrusion is the tooth translation into the bone when the force applied on the tooth; extrusion is the tooth translation out of the bone; as shown in Figure 2.6 (a), (b).

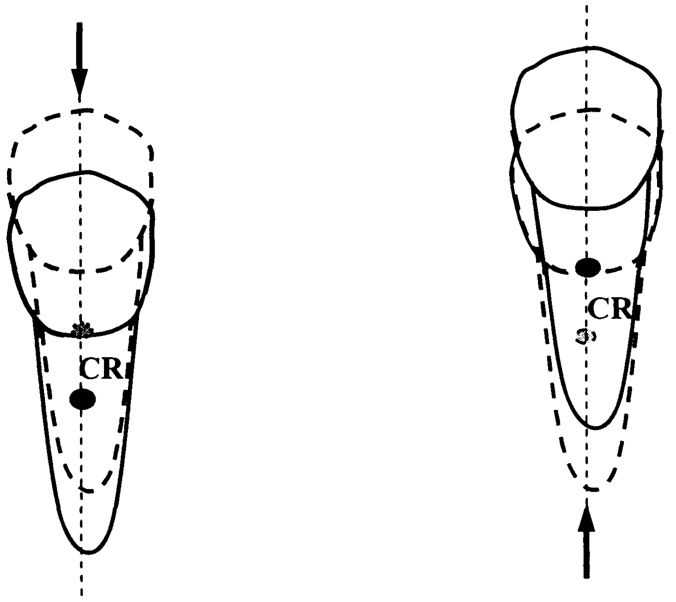

(a) Intrusion **(b)** Extrusion

Figure 2.6 The tooth translation movements.

Tipping movement (Orthodontics, 1999) – this is the motion created by a single force acting at a distance from the centre of resistance (CR) of the tooth. It includes two components: rotation and translation. Tipping movements are shown in Figure 2.7.

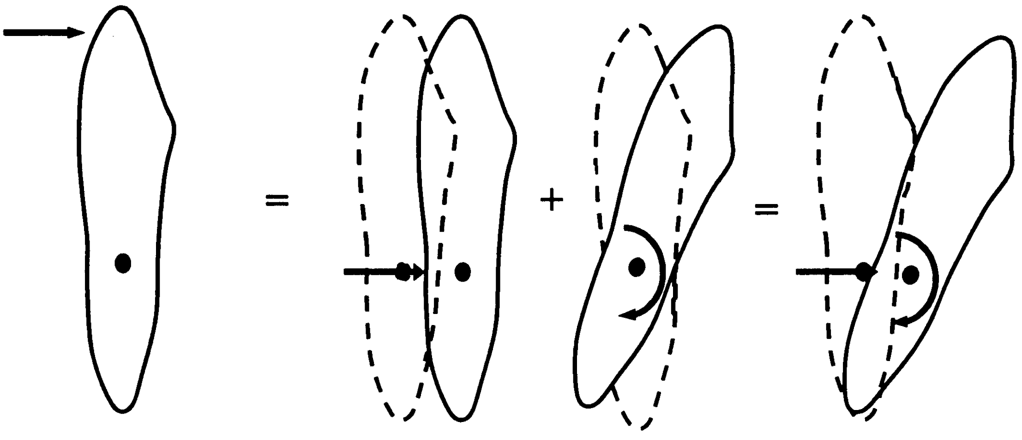

(a) Translation **(b)** Rotation

Figure 2.7 The tooth tipping movements

In tooth movement, the PDL plays an important role. Its mechanical properties will affect the amplitude of tooth movement when the forces apply to the tooth.

Ross et al. (1976) and Burstone et al. (1978) established tooth displacement under load in a lingual direction. They found that tooth movement under load was non-linear and time dependent. If the direction of load applied to the tooth was in the horizontal direction, the relationship between force and tooth displacement is shown in Figure 2.8.

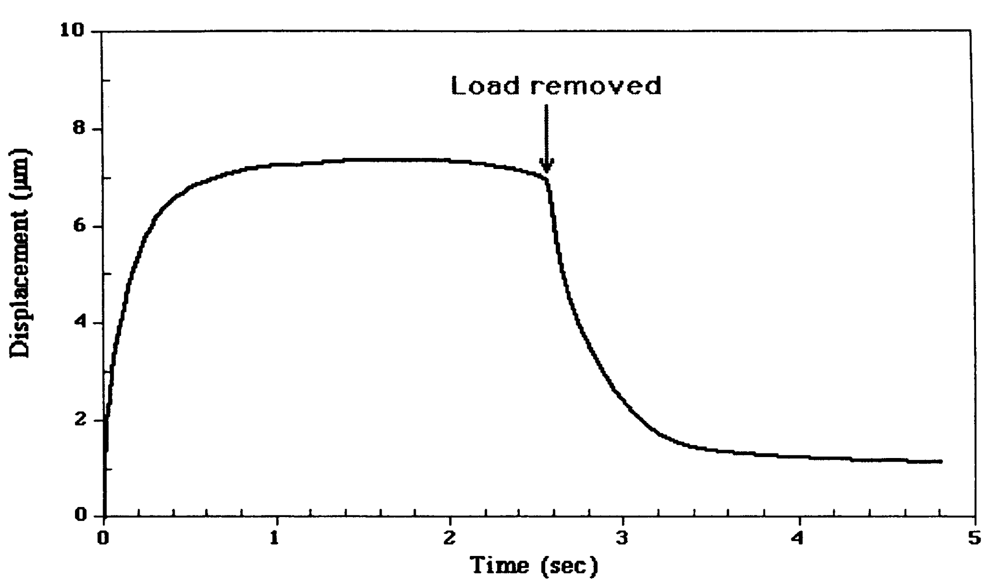

Figure 2.8 Horizontal displacement of a human maxillary central incisor after sudden application and removal of a 0.05 N horizontal force. (Berkovitz *et al*, 1995).

The graph shows that initially the resistance of the tooth was minimal, but the resistance gradually increased with loading time. They reported that the resistance of the PDL to horizontal loading cannot be explained in terms of a simple linear mechanical model.

2.3 Methods of loading on the tooth

In orthodontic treatment, forces are applied to teeth by brackets and a stainless steel wire. Stable orthodontic results can be seen after long treatment duration.

To study tooth movement over a short duration, Volp et al. (1999) designed an air pressure loading device to be used in a clinical study. The device consisted of an aluminium cylinder, a target pin, a nylon cone and a stainless steel probe (Figure

2.9). The air pressure was applied through small-bore tubing into the chamber of an aluminium cylinder. The pressure bears onto the surface of a nylon piston lying within the cylinder. The piston, responding to the pressure, drives forward a sleeved, stainless-steel-ball-ended probe against the selected point of application on the tooth. This method has been used in clinical experiments. The method required fixing the patient's head to guarantee the loading probe touched on the correct position on the tooth.

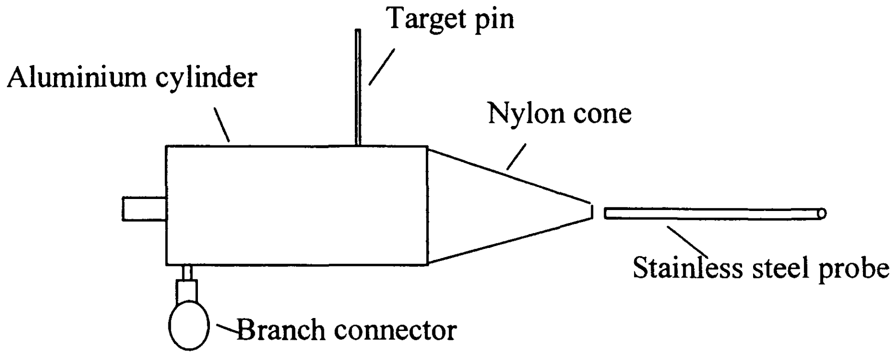

Figure 2.9 Air pressure loading method.

Friedrich et al. (1999) used a specially designed elastic archwire fixed on the patient's head and connected the elastic archwire with a bracket on the tooth to create load. The loading system is shown in Figure 2.10. The device consisted of a slot section, a base section, a rigid frame and an elastic archwire. A slot section was connected with the elastic archwire before use. At the start of the operation, the slot section was connected with the base section. A small space between the base and slot sections ensured that the force acted on the tooth. The force generated by the elastic archwire was transmitted to the tooth by the bracket (base).

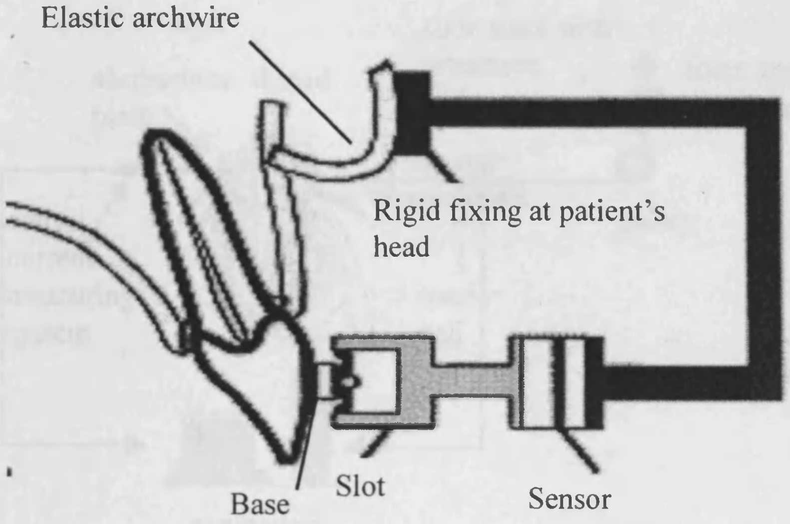

Figure 2.10 Elastic archwire loading with a slot and a bracket (Friedrich et al 1999).

Dorow et al (2002b) designed a spring loading system with load cell to load teeth "in vivo" (Figure 2.11). The system includes a loading spring, a retraction spring, a load cell and a thread. A linearly increasing force could be applied to the tooth crown via the thread, the pulley and the spring that ensured a gradual force increase. The force acting directly on the tooth crown was measured by a load cell that moved on a slide track in order to prevent concussions. Two springs were fixed to the slide track. These springs ensured that the load cell returned to its original position after force relief.

Ren et al. (2003) used the spring loading method to load 0.1N onto the rat's teeth to investigate why orthodontic procedures seem to consume more time in adults than in juveniles. The loading method is shown in Figure 2.12. This method is not suitable for direct use on a human tooth loading because it is difficult to put the loading spring into a human mouth.

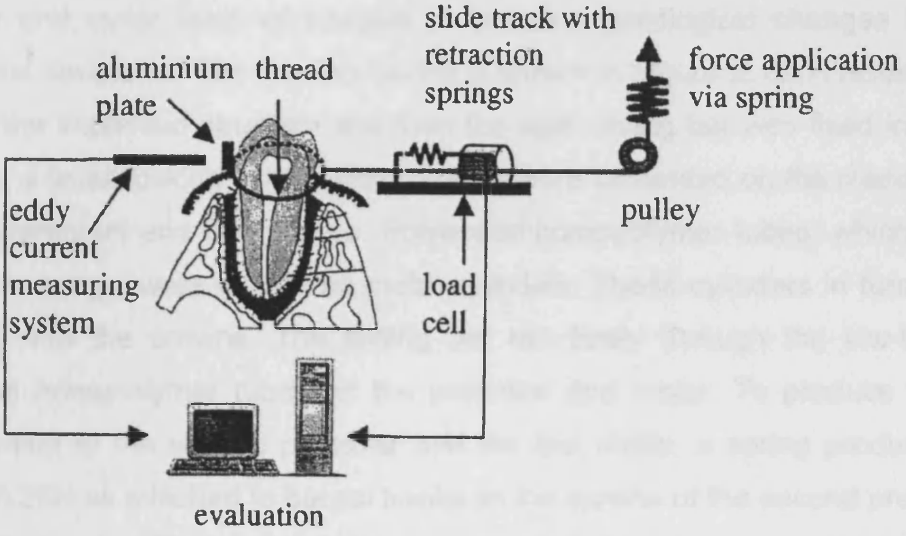

Figure 2.11 Spring loading system with experimental setup (Dorow et al. 2002b).

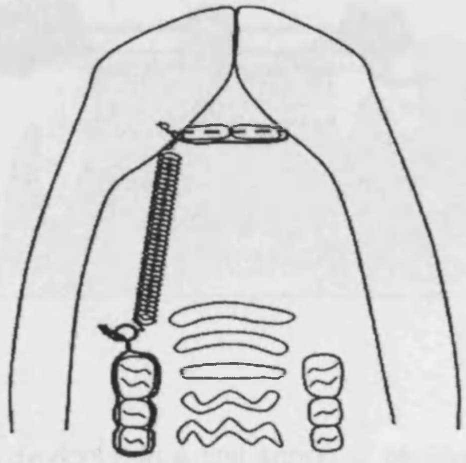

Figure 2.12 Spring loading onto the rat's teeth. Two incisors are pinned together by a ligature wire going through the snout. Three molars are circled by a ligature wire and bonded together by a light-cure material. A force of 0.1N is applied by a super-elastic spring (Ren et al. 2003).

Von Böhl et al. (2004) designed another loading device which they used on premolar and molar teeth of beagles to evaluate histological changes in the periodontal structures. The loading device is shown in Figure 2.13. A holder was fixed on the implanted structure and then the rigid sliding bar was fixed into the holder by a small locking screw. Alloy crowns were cemented on the mandibular second premolars and first molars. Polyacetal homopolymer tubes, which were used as bearings, were glued into metal cylinders. These cylinders in turn were soldered onto the crowns. The sliding bar ran freely through the low-friction polyacetal homopolymer tubes on the premolar and molar. To produce bodily displacement of the second premolar and the first molar, a spring producing a force of 0.25N as attached to buccal hooks on the crowns of the second premolar and the first molar. These springs exert a constant, continuous, mutual force on both teeth over a wide range of activation.

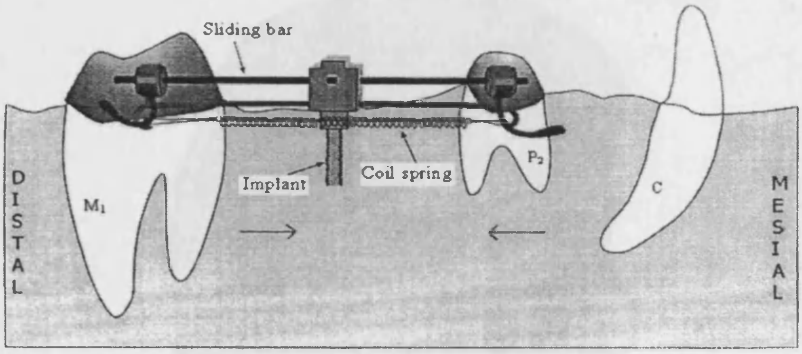

Figure 2.13 Loading device with a coil spring of reciprocal force of 0.25 or 3N to make the bodily displacement of the premolar and molar of beagle dog in the direction of the arrows (Von Böhl et al. 2004).

Roberts-Harry and Sandy (2004) reviewed headgear loading methods. Headgear is not a recent invention, as headgear has been used as early as 1861. The structure of the headgear is shown in Figure 2.14. The force from the headgear is usually applied to the teeth via a face-bow. The direction of the force applied to the teeth can be varied depending on the type of headgear that is fitted. Headgear can be applied to both the maxillary and mandibular dentition. The main problem with headgear is safety because the headgear connects to the prongs at the end of the face-bow that fits into the headgear tubes on the intra-oral appliance. So headgear may be dangerous and could cause injury to the face or elsewhere.

Except for the method of headgear loading, until now, there is no report of multi-directional force applied to a human tooth by an integrated mechanical device in the literature.

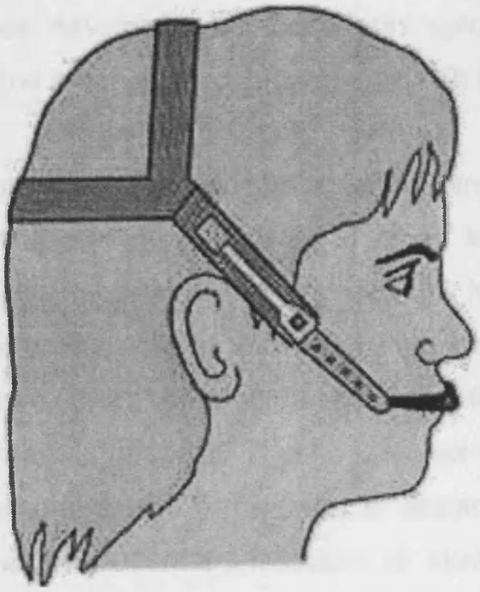

Figure 2.14 Headgear loading on human teeth (Roberts-Harry, and Sandy 2004).

2.4 Methods of measuring tooth movements

There are pieces of equipment that can perform accurate and small scale measurement in 3D space, such as the atomic force microscope (AFM) and the coordinate measurement machine (CMM) etc. AFM is mainly adapted to measure the various sizes and shapes of a surface by using a probe mounted at the end of a cantilever and moving the probe over the surface of a sample in a raster scan. The structure of the AFM is very complex which limits its use in measuring tooth movement. The CMM uses a fixed multiple-stylus probing system with software to measure and calculate the sizes of different work-pieces. Normally it is used for measuring the static size of objects due to the restriction of mechanical structure. To measure tooth movement, in the early stage, researchers used a dial indicator (Muhlemann 1951), movement transducers (Picton 1962, 1963) or complex holographic techniques (Pryputniewicz 1978) to measure the tooth movement in 2D or 3D space. In recently two decades, most of the recording devices developed are based on optoelectronic techniques (Middleton et al. 1996) and magnetic (Yoshida et al. 2000) techniques.

Muhlemann (1951) employed a dial indicator attached intra-orally to record tooth displacement and a hand-held dynamometer to apply loads. He published a series of papers describing mobility of monkey teeth. A load of 1N produced a displacement of approximately 150μm and a 5N load produced only a further 50μm displacement. Parfitt (1960) reported that tractional forces of approximately 0.15N and 0.3 N caused a human maxillary central incisor to extrude by 6μm and 8μm respectively. Picton (1962, 1963) used similar apparatus with Parfitt which were strain gauges and movement transducers to study tooth movement in human maxillary incisor, and obtained similar results to Parfitt. However Picton emphasized that since the adjacent reference teeth were also probably displaced by the load, the values obtained for tooth displacement were not to be regarded as absolute. Heners (1974) claimed that human maxillary central incisors extruded by about 20μm with 5N loads.

Pryputniewicz (1978) claimed that previous work was unreliable because the experiments used techniques that were relatively inaccurate, and could not measure three-dimensional displacements. He employed complex holography techniques to study the tooth mobility in 3D space. His experiments show that the largest motion was in the lingual-labial direction, 30μm in 10 second with 3N loads for a human maxillary central incisor.

Droschl et al. (1992) developed a new method to measure the tooth movement “in vivo”. In Droschl’s method, measured blocks with calibrated holes in each side of the blocks were attached to brackets; then an electronic sliding calliper was used to measure the movement between tooth and blocks of anchored segments in three dimensions. Although Droschl’s method was simpler, it was not suitable to track the movement with time. Later, newer techniques based on magnetic and optoelectronic techniques were developed to monitor the tooth movement for three-dimensional analysis.

Middleton et al. (1996) used laser techniques to detect the tooth movement in a clinical test. A LAS-5010 laser displacement sensor was chosen (Figure 2.15).

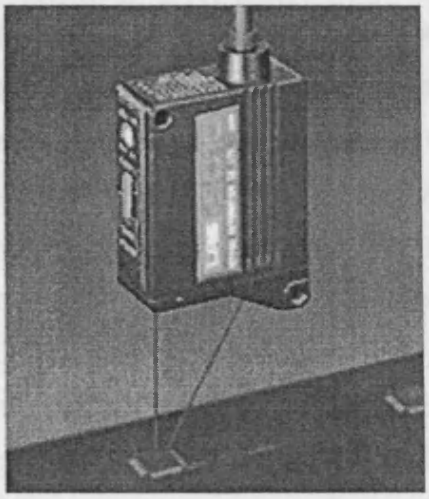

Figure 2.15 LAS-5010 laser displacement sensor (Plant Control & Automation).

The LAS-5010 sensor uses a 1mW visible laser diode light source; it has a resolution of 10μm, measuring range of ±5mm with a reference distance of 50mm away from the target. The size of light spot on the target was less than 1mm diameter. The sensor is based on laser triangulation method to measure the distance to targets by detecting a laser spot accurately. The laser triangulation method is so named because the sensor enclosure, the emitted laser beam and the reflected laser light form a triangle. The laser beam is emitted from the instrument and is reflected from a measured target surface to a collection lens. The collection lens is located adjacent to the laser emitter. The lens focuses an image of the laser spot on a linear array CCD. The position of the spot image on the CCD is then processed to determine the distance to the target by software. The LAS-5010V operates on any DC voltage between 12 & 24V regulated, and gives an output signal of 4-20mA which is linear and proportional to the measurement range. Laser measurement techniques were also used in measuring tooth movement by Yamamoto et al. 1989; Hayashi et al. 2002. The disadvantage of laser triangulation method is that the accuracy of measuring tooth movement is reduced by head movement of volunteers due to the absolute measurement method.

Yoshida et al. (2000) developed a magnetic sensor (Hall Effect) measurement system. The system consisted of eight magnetic sensors and two magnets to measure three-dimensional displacement. Eight Hall elements were aligned, one at each corner of a cube around the magnet and mounted on an aluminium channel in order to measure three-dimensional displacements of the tooth. Hall elements were covered with epoxy resin for the purpose of insulation and moisture-proofing. Two sensor units were placed at the front and at the back of a front tooth subjected to orthodontic forces. Magnets and sensors were respectively fixed to the subject tooth and posterior teeth. Sensors detected displacements of two magnets extended from the subject tooth separately in real time. The two magnets were placed in the centre of each sensor unit and then attached to the subject tooth by an aluminium rod. The force in the backward direction was applied to the left maxillary central incisor at different levels. The force was delivered by applying a lead weight to a titanium angle extended from the subject tooth. The magnetic measurement method was also used by Yamada et al. 1990; Miura 1998; Ioi et al. 2002 to study tooth movement. But to date, this method has not been used in clinical experiments due to safety reasons.

Sander et al. (2002) used digital macrophotogrammetry (DMP) techniques to obtain information on the three-dimensional movement of a tooth. Analysis of the DMP images provided the movement of a tooth during treatment. In the measurement system, the preconditions are that the markers attached on the brackets must be clearly visible by DMP; a scaling frame needs to be fixed on the teeth; four measuring points should be visible to each bracket; the control points on the frame must be positioned in three-dimensions, and their positions must be able to be determined with sufficient accuracy. The system can provide resolutions of 1μm for translation and 0.1° for rotation. However, the strict measuring conditions and location of a scaling frame set on teeth restricted application of the system in clinical studies.

From all the studies described above, no method can demonstrate tooth rotation in 3D space. To investigate tooth movements in 6DOF, Hayashi et al. (2002) used the finite helical axis method to calculate the orthodontic tooth movement according to the data obtained from surface-scanning system using a slit laser beam. The helical axis method has been used to analyse joint function by Spoor and Veldpaus (1980); Woltring et al. (1985); Gallo et al. (1997) and Gallo et al. (2000); DeLong et al. (2002). The finite helical axis is an instantaneous axis of rotation obtained from the calculation. The motion of an object from one position to another can be broken down into a rotation about and a translation along the instantaneous axis of rotation, except pure translation but no rotation. The helical axis method uses 6 parameters to describe the motion of an object. The 6 parameters are 1) 2 coordinates where the helical axis has an intersection point with a plane in the global reference system, 2) 2 cosine angles to describe the direction of the helical axis, 3) the length of translation of a motion object along the helical axis, and 4) the rotation angle of an object about the helical axis. The parameters (1) and (2) determine the location and direction of the helical axis; (3) and (4) express the translation of the object along the helical axis and the rotation angle about the helical axis. Apart from the helical axis method, a rectangular coordinate system method has also been used to calculate tooth translation and rotation in 3D space by Smith and Burstone (1984); Tanne et al. (1988); Pedersen et al. (1990); Iwasaki et al. (2000); Rhee et al., (2001). In the rectangular coordinate system method, a 3D coordinate system was established by taking the tooth centre of resistance as the origin to analyse tooth movement in a finite element model. This method was found not to be reliable for analysing molar rotation because the root of a molar is different to the root of an incisor or others, and tooth centre of resistance of molar is difficult to be determined.

2.5 Optical motion analysis techniques and applications

Optical motion analysis techniques are combined together with techniques of optics, electronics, image processing, computer and mechanics etc. In this study, the Qualisys motion capture system was used. This system includes the Qualisys track manager (QTM) software, PC and two ProReflex-MCU120 infrared cameras, which are called the motion camera units (MCUs). The MCUs are the infrared “cameras” and associated signal processing circuit required to convert visual image to digital image on the PC. The infrared cameras emit infrared radiation which is reflected back by the retroreflective markers, giving a high contrast between the markers and the background. Markers can be passive markers which are painted by infrared reflective powder or covered by infrared reflective tape, or active markers which are made by infrared emitting diode.

2D images of the markers, projected on CCD of the cameras, are digitised and processed in real time by the signal processing circuit in the MCUs, and sent to

PC in real time via a serial computer interface. 2D coordinates of the central point of each marker image are calculated by the camera system and displayed on the monitor in real time. The QTM software, including linearization, calibration, models etc, is used to view and convert the images from 2D to 3D. This software allows capturing of 2D camera data, showing marker positions and giving 2D coordinates in global coordinate system, which is defined by the system calibration. It then allows tracking of the 2D data into 3D images and coordinates, based on a number of parameters that can be determined in the QTM software tools. This is normally done after the data has been captured. All capturing and tracking of marker movements must be preceded by the system calibration, that is, the volume within which the measurements are taking place must be defined in terms of a 3D coordinate system, and the relative positions of the 2 MCUs are fixed. Calibration is required every time the cameras are repositioned. The QTM software also can export 2D or 3D coordinates of global coordinate system to a .tsv file that can be used by other software, such as Matlab, for data processing. The maximum sampling frequency of the MCUs is 120Hz.

In fact, the Qualisys motion capture system can employ a maximum of 16 optical infrared cameras. Here, we use two MCUs. For measuring a small field of view, the focal length of the camera lens is longer than normally used for gait analysis. Thus the cameras can be placed at a more convenient distance.

Optical motion capture system have been widely applied in biomechanical engineering in the past two decades, to measure gait, posture and joint movement, such as the toes, knee, hip, shoulder, elbow, wrist, spine etc in a large field of view (Hinterkausen et al. 1998; D'Apuzzo 2000; Holt et al. 2000; Hirokawa et al. 2001; Hunt et al. 2001; Jones et al. 2001a; Murray et al. 2003; Thelen and Anderson 2001; Angeli 2001; Higgins and Molloy 2003; Park et al. 2004; de Asla et al. 2006). Several companies can supply motion capture system including: Qualisys Company; Vicon Company; Ariel Dynamics Inc. and Motion Analysis Corporation etc.

In principle, the Qualisys ProReflex-MCU120 motion capture system is not only used to capture the movement in a large field of view, but also can be used as a precision instrument to measure very small scale displacement, such as tooth movement, strain and deformation in biomechanics and other areas of engineering, in a small field of view. In fact, the system characteristics in a small field of view have not been properly developed until now, and this development forms a basic step in the current study.

Chapter 3 Evaluation of the characteristics of the optical motion analysis system for small-scale measurements

3.1 Introduction

Motion capture systems have been widely used in biomechanics for measuring different movements (see section 2.5). Haggmann-Henrikson et al. (1998) used the Qualisys Mac Reflex three-dimensional motion capture systems to measure chewing movements under load. In principle, motion capture systems could be capable of very accurate measurements by providing appropriate optics and calibration techniques, and could provide a valuable tool in many engineering applications, such as the measurement of deformations of material testing or testing of implant constructs. However, apart from the manufacturer's technical data which claims that the system resolution is equal to 1/60,000 of the field of view, the system accuracy, repeatability and noise have not been previously reported in the literature.

This chapter will introduce the calibration methods used with motion capture system, evaluate how accurately and repeatably the ProReflex-MCU120 Qualisys motion capture system measures small displacements and characterise the noise in the system. Specifically, the following questions will be answered:

- What is the actual resolution of the Qualisys system in a small field of view (68 x 51mm)?
- How accurately does the system measure small displacements in three orthogonal directions?
- How repeatable are the displacement measurements?
- What is the optimal camera convergence angle for system accuracy and repeatability?
- What are the noise characteristics of the system?
- At the end of the chapter, the results will be presented and discussed.

3.2 Methods of motion capture system calibration

For 3D measurement, a motion capture system requires calibration of the cameras every time when the cameras are repositioned. Through the calibration, a usable measurement field and the global coordinate system of the camera system are determined. In the determined field of view, the motion capture system captures marker movements in 3D space (the markers are fixed on the measured object), reproduces the marker movements on the monitor, and gives 3D coordinate values of markers. For camera calibration, there are two common methods – wand calibration and frame calibration. These two methods will be described in the form in which they are implemented in the Qualisys system with the QTM software.

The wand calibration method is shown in Figure 3.1. The L frame with four spherical markers is used to establish a global coordinate system and the wand in T shape with two spherical markers is used to calibrate the field of view. Moving the wand in 3D space, this will determine a volume within which the measurements are taking place.

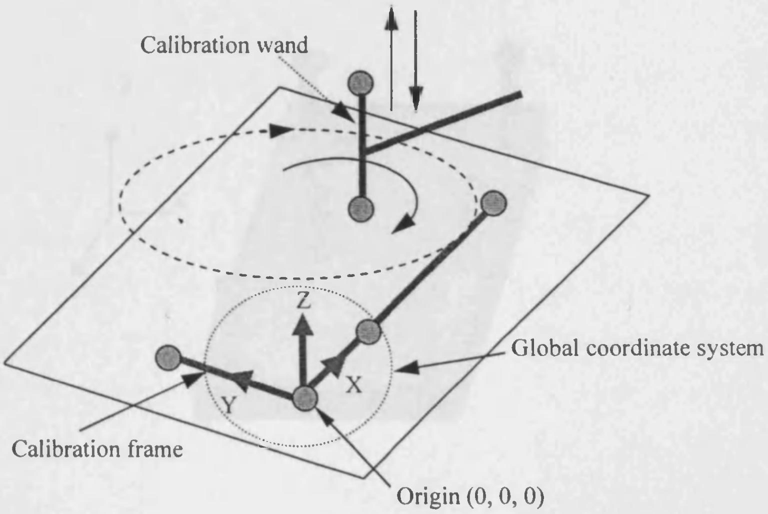

Figure 3.1 The structure of wand calibration and definition of coordinate system.

Before camera calibration, the distance between the markers fixed firmly to each end of the wand was measured accurately by standard equipment with accuracy of 0.5mm; the origin of global coordinate system on the L frame was determined and the distances between the origin and other markers were measured accurately as well; all these distances measured were input to the PC as a standard in the Qualisys QTM software to calibrate the cameras. The calibration time was taken 10s at sample frequency of 60 Hz.

The method of frame calibration is shown in Figure 3.2. The calibration frame must configure a 3D space with at least 6 markers, referenced from the Qualisys QTM manual. For the calibration frame, firstly one marker is chosen as the origin in 3D space, the positions of other markers relative to the origin marker are measured accurately by the Mitutoyo CMM with resolution of 0.1μm(made in Japan), and then the 3D marker positions were input to the PC as the standard in the Qualisys QTM software to calibrate the camera system. The user has the option to choose either frame calibration or wand calibration. It was decided to assess both methods for the purposes of small scale measurement and a large scale measurement.

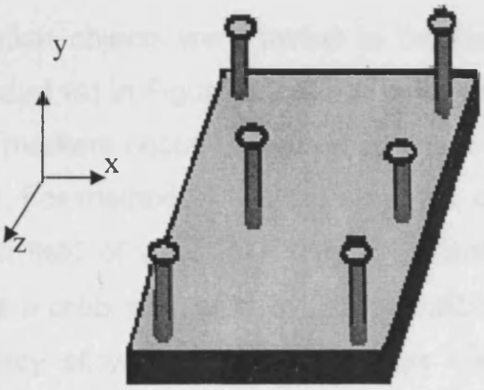

Figure 3.2 Calibration frame and global coordinate system determined by the calibration frame.

The resolution of the motion capture system depends on the size of the field of view. For the Qualisys motion capture system, the system resolution stated by the manufacture is 1/60,000 of diagonal field of view. To measure a small-scale movement, such as tooth movement, a small field of view is needed to obtain maximum resolution. Firstly, the camera parameters (focus and aperture) and positions were adjusted to be as close as possible to the markers and clearly see the markers on the monitor, and then the distance between the camera and the markers were measured (69±0.5cm). According to pin hole model of camera (Willson and Shafer 1994), a (68×51) ±0.5mm field of view was calculated and used in measuring tooth movement.

For the small field of view $(68 \times 51\,\text{mm})$ ±0.5mm, the calibration objects supplied by Qualisys, using the wand calibration method, could not be used because the markers (12mm in diameter) and L frame were too big to use in such small field of view. Therefore, a number of different calibration objects were developed to attempt to calibrate the Qualisys motion capture system, as shown in Figure 3.3 (a), (b), (c) and (d). In order to compare the measurement accuracy, two types of marker have been used – diamond markers and spherical markers (Liu et al. 2006c).

Four different calibration objects were tested in the system calibration. It was found that the method of (a) in Figure 3.3 is not suitable to calibrate the camera system because the markers occupy a large proportion of the field of view and are easily obstructed. For method of (b), the structure of the frame was still too big to use in a small field of view $(68 \times 51\,\text{mm})$ ±0.5mm. The most successful methods for the camera calibration were the frame calibration methods of (c) and (d) in Figure 3.3. They allow the closest distance between the markers and cameras. The instructions about how to using four different calibration objects are shown in Appendix E.

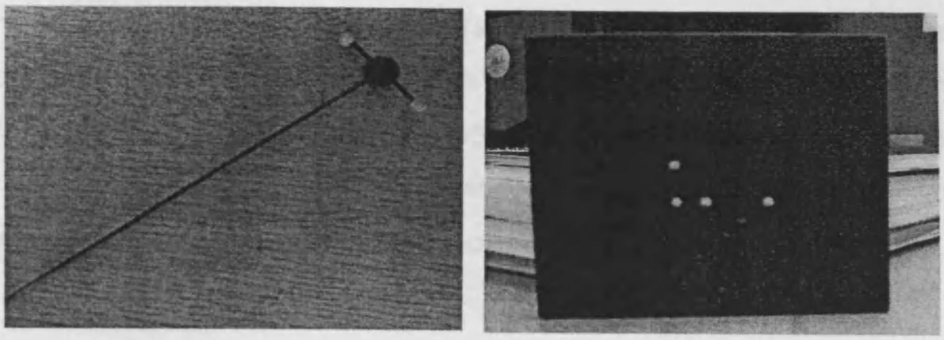

(a)

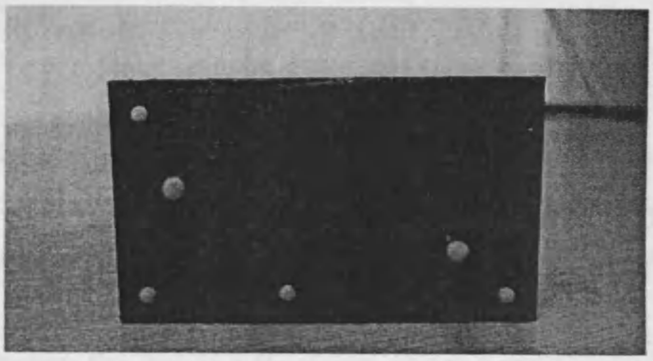

(b)

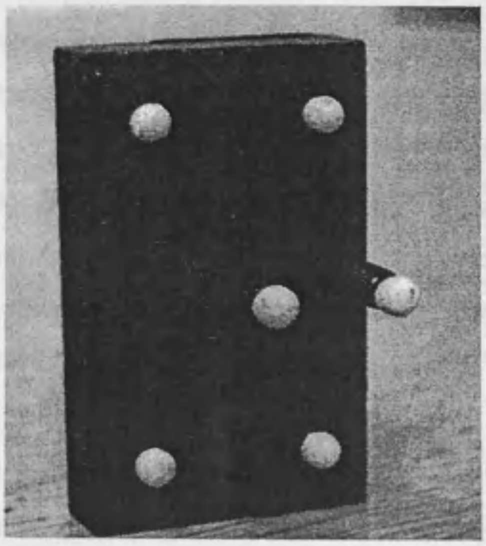

(c)

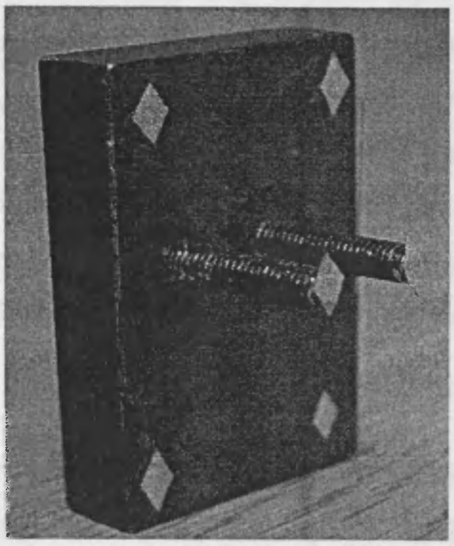

(d)

Figure 3.3 The calibration objects. (a) Wand calibration with the spherical markers of 2.5mm in diameter. (b) Frame calibration with the spherical markers of 2.5mm in diameter and frame 70 x 45 x 30 mm. (c) Frame calibration with the spherical markers of 2.5mm in diameter and frame size 20 x 35 x 20 mm. (d) Frame calibration method with the diamond markers of 2 x 4 mm.

3.3 Method of evaluation of system characteristics – resolution, accuracy, repeatability, camera convergence angle and noise

To evaluate the system characteristics, the two cameras were placed as close as possible to the markers to maximise the system resolution. The global coordinate system was established through the camera calibration, shown in Figure 3.4.

The distance between the camera locations and the markers was approximately 69.0cm. The camera angles of elevation were zero and horizontal convergence angle was 78° (referenced from section of 3.3.2, evaluation of optimal camera angles). A (68×51) ±0.5mm overlapped field of view was created by the two cameras. Two different types of markers were used in the experiments (spherical markers and elongated diamond markers). Spherical markers are conventionally by used in motion analysis systems, as their profile remains the same when viewed from different directions. However elongated diamond markers may potentially provide slightly better accuracy in the Qualisys system, as they take advantage of the different horizontal and vertical resolution of the CCD sensor (Liu et al. 2005).

The smallest spherical markers that could be used in this study were 2.5mm in diameter and were manufactured by using clear acrylic balls (supplied by The Precision Plastic Ball Company Limited, UK) and superglue cemented with infrared reflective powder. The diamond markers were 2×4 mm and were made from retroreflective tape supplied by 3M Company, UK (Figure 3.5). The camera system was calibrated by using the method of frame calibration, as introduced in section of 3.2, and the calibration frames are shown in Figure 3.3 (c) and (d).

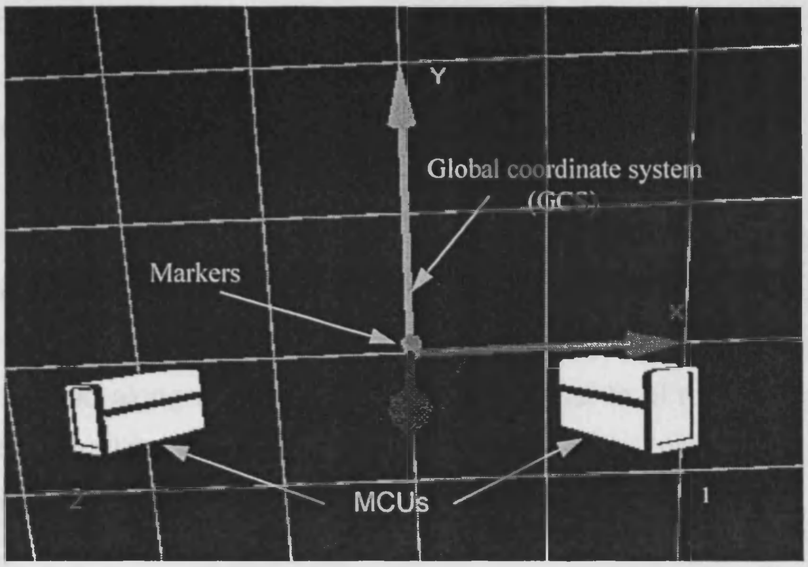

Figure 3.4 The global coordinate system established by the camera calibration.

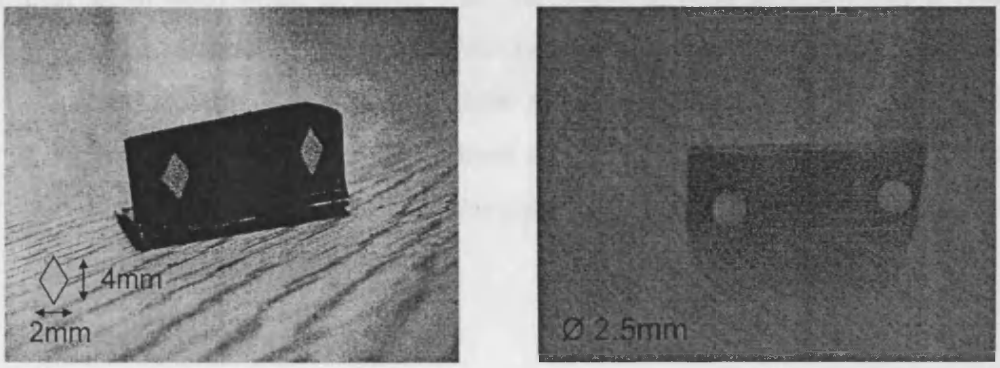

Figure 3.5 The diamond markers and the spherical markers employed for evaluation of the system.

3.3.1 Resolution, accuracy and repeatability

The resolution and accuracy of the system were evaluated using a National Physical Laboratory (NPL) wedge type comparator with a resolution of 0.25μm as a standard. The NPL wedge comparator consists of a large precision micrometer which moves an accurately machined wedge. The inclined surface of the wedge then moves the measurement head. Because the angle of the wedge is small, this achieves better resolution than a standard micrometer. Two markers, either diamond markers 2×4mm or spherical markers 2.5mm in diameter, were attached to the moveable head of the comparator, 12.0mm apart measured by the standard ruler with accuracy of 0.5mm , for measuring the displacement. Two markers were moved along one axis and the displacements of two markers were detected by the Qualisys cameras. The comparator was rotated to measure along different axes, as shown in Figure 3.6 (a), (b) and (c).

Two markers were moved in ten steps along each axis, and seven different step sizes were used (0.5μm, 1μm, 2μm, 3μm, 5μm, 10μm, and 20μm). The whole process was repeated five times on five days under different light intensity and temperature. The positions of the markers on the target were captured at every point, that is, at both ends of each step, for two seconds at a sampling rate of 60Hz, giving 120 frames of data for each point. The mean value of 120 frames was calculated as the value of one time measurement. This reduced random error in the measurements due to ambient vibration. The mean value, maximum error, minimum error, error band, hysteresis error and standard deviation were calculated using the following methods.

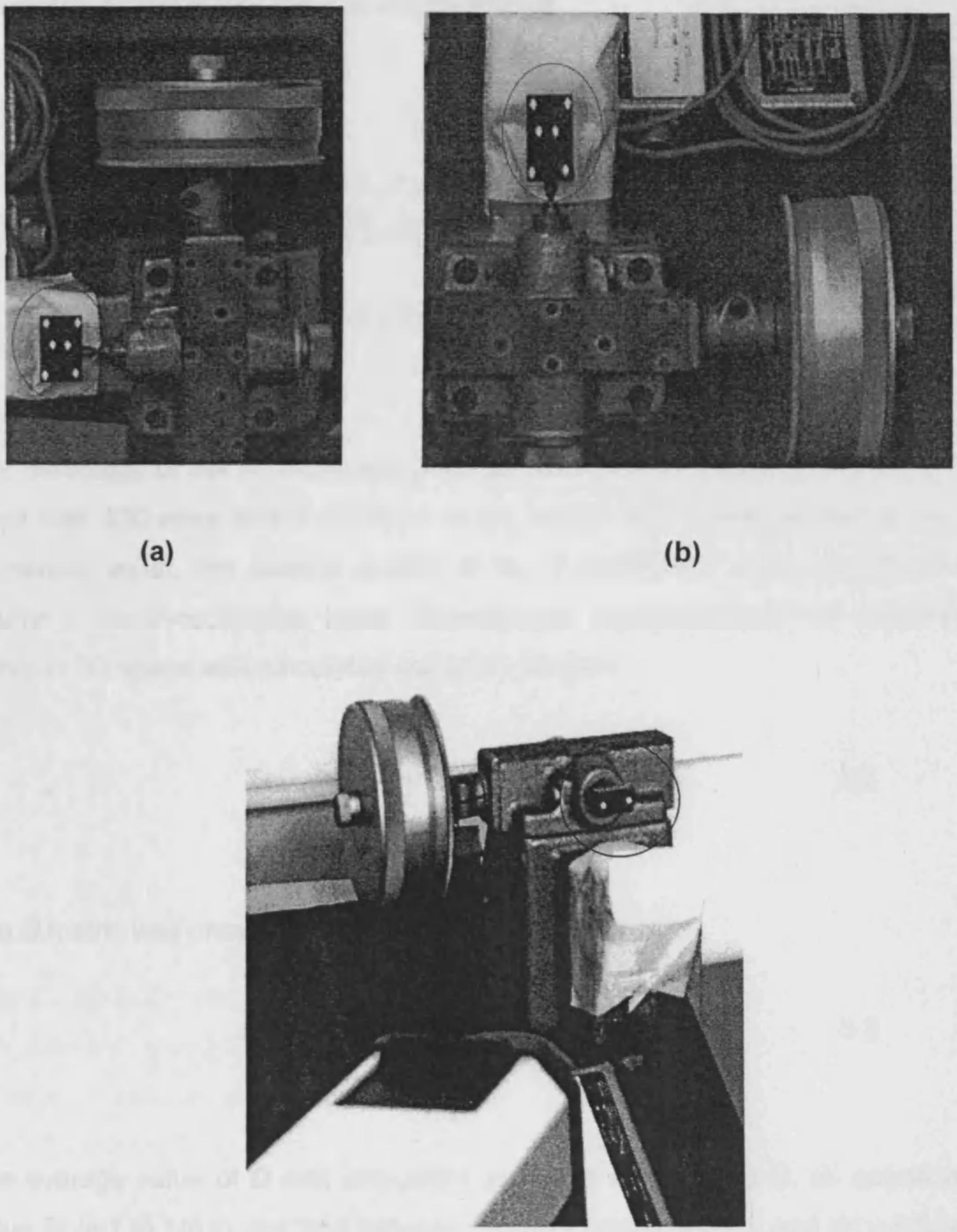

(a)

(b)

(c)

Figure 3.6 The markers moved with moveable head of the comparator. (a) Markers moved in x direction. (b) Markers moved in y direction. (c) Markers moved in z direction.

The matrix ***b**_i_* was established as shown follows:

$$\boldsymbol{b}_i = \begin{bmatrix} b_{11}, b_{12}, b_{13} \\ b_{21}, b_{22}, b_{23} \\ \cdots\cdots \\ b_{k1}, b_{k2}, b_{k3} \end{bmatrix}, \quad k = 120 \qquad 3.1$$

***b**_i_* is the matrix of the *ith*-measured point *(i=1 to 11)* in 11 measured points of 10 steps with 120 rows and 3 columns. In the matrix ***b**_i_*, the first column is the *x*-coordinate value, the second column is the *y*-coordinate value, and the third column is the *z*-coordinate value. The distance (step) between two measured points in 3D space was calculated using the function:

$$d = \sqrt{(x_2 - x_1)^2 + (y_2 - y_1)^2 + (z_2 - z_1)^2} \qquad 3.2$$

The ***D*** matrix was created with one column and 120 rows.

$$\boldsymbol{D} = [d_1;\ d_2;\ \ldots\ldots d_k] \qquad 3.3$$

The average value of ***D*** was calculated using the equation (3.4), as actual step value *Bj (j=1 to 10)* in one time between *(i+1)th* measured point and *ith* measured point.

$$B_j = \frac{\sum_{k=1}^{120} d_k}{120} \qquad 3.4$$

Every point in 11 measured points was repeatedly measured five times each in increasing (row: 1 - 5) and decreasing movement (row: 6 - 10), so two step matrices $\boldsymbol{C_1}$ and $\boldsymbol{C_2}$, which were calculated using the next measured point *(i+1)* value minus the last measured point *(i)* value, were created as:

:

$$C_1 = \begin{bmatrix} B_{11}, B_{12}, \ldots B_{1i}, \ldots B_{1n} \\ B_{21}, B_{22}, \ldots B_{2i}, \ldots B_{2n} \\ \ldots\ldots \\ B_{51}, B_{52}, \ldots B_{5i}, \ldots B_{5n} \end{bmatrix}, \quad \mathrm{n=10} \tag*{3.5}$$

$$C_2 = \begin{bmatrix} B_{61}, B_{62}, \ldots B_{6i}, \ldots B_{6n} \\ B_{71}, B_{72}, \ldots B_{7i}, \ldots B_{7n} \\ \ldots\ldots \\ B_{101}, B_{102}, \ldots B_{10i}, \ldots B_{10n} \end{bmatrix}, \quad \mathrm{n=10} \tag*{3.6}$$

The $\boldsymbol{C_1}$ and $\boldsymbol{C_2}$ are the step matrices of the comparator increasing and decreasing movement respectively, measured five times at eleven points. The average step values matrices $\boldsymbol{I_a}$ and $\boldsymbol{I_b}$ of $\boldsymbol{C_1}$ and $\boldsymbol{C_2}$ were calculated respectively. The "*a*" expresses increasing movement; "*b*" expresses decreasing movement.

$$I_a = [I_1,\ I_2 \ldots I_i,\ \ldots I_n] \tag*{3.7}$$

$$I_b = [\ I_1,\ I_2 \ldots I_i, \ldots I_n] \tag*{3.8}$$

From the actual step value minus the average step value, error matrices E_1 and E_2 were obtained. E_1 is the step error matrix for increasing movement measured five times; E_2 is the step error matrix for decreasing movement measured five times. From the matrices E_1 and E_2, Matlab (The MathWorks, Inc.) software calculated the maximum value error E_{max}, minimum value error E_{min} and average value error E_{mean} in matrices of E_1 and E_2 respectively. The error band was calculated as:

$$E_{band} = E_{max} - E_{min} \qquad 3.9$$

The hysteresis error E_{hys} and standard deviation S_{td} were calculated from the error matrices and actual step matrices. The hysteresis error was defined as the difference between the values of the step up measurements and the corresponding step down measurements when the marker was moved in steps in one direction and then in steps back to the starting point. Sensitivity was also calculated by using the actual measured step divided by the ideal step, expressed as a percentage.

$$Sensitivity = \frac{actual\ measured\ step}{ideal\ step} \times 100\% \qquad 3.10$$

The sensitivity was used to evaluate the actual resolution of the system. The resolution was defined as the minimum step size that the system could be detected. The resolution of the motion capture system was found to be 10μm in the determined field of view (see section 3.2).

The system accuracy was defined as the maximum absolute error in the measurement range divided by the measurement range, expressed as a percentage, shown as the following function:

$$Accuracy = \pm \frac{\max imum\ absolutely\ error}{measurement\ range} \times 100\% \qquad 3.11$$

To compare the measurement accuracy with the different markers, the diamond markers and the spherical markers were measured alternately in the same experimental conditions, repeated five times. The accuracy was calculated from measured data, in the *x, y,* and *z* directions respectively. The results are presented in Figure 3.9.

Repeatability was evaluated by repeating the measurements of step up and step down in each direction for five times on different days, under different temperatures and ambient light conditions. The standard deviation *(σ)* of the measurements was calculated as the system repeatability:

$$\sigma = \sqrt{\frac{\sum_{i=1}^{N}(x_i - X)^2}{N-1}} \qquad 3.12$$

N – number of measurements;

x_i - the ith measurement value;

X – average value of measurements.

The results of repeatability are shown in Figure 3.10.

3.3.2 Camera convergence angle

The system reproducibility was evaluated with changing camera convergence angle in a small field of view of (68×51) ±0.5mm. The system characteristics affected by camera convergence angle were evaluated by using the NPL wedge comparator, through adjusting the camera convergence angle. Previous researchers (Woods et al., 1993) demonstrated a geometric relationship model between image space coordinates and the camera convergence angle, and discussed reasons of image distortions in theory; Lawson and Wu (1997) discussed a geometric error model in relation to camera convergence angle applied to three-dimensional particle image velocimetry. They found that larger camera convergence angles could reduce the geometric error of an image in 3D space. Thornton et al. (1998) studied the effects of camera placement on accuracy for convergence angle from 15° to 45° at a distance of 4m between the cameras and the object. They found that the standard deviation was reduced with increasing camera convergence angle with a camera angle of elevation with zero. But in a small field of view and camera convergence angle changing from 15° - 90°, the effects of convergence angle on accuracy and repeatability have not been explored. Investigating the optimal camera convergence angle and an optimal range are very useful for clinical experiments ensuring reliable and accurate measurement results.

Firstly, a reference point in the field of view was determined according to the 2D camera view of the markers, shown in Figure 3.7.

On the top surface of each motion capture unit, central points were detected by slide callipers and marked separately as *a, b,* and *c, d*. Straight lines connecting the points '*a* to *b*' and '*c* to *d*' were used to define the motion capture unit optical axes. Camera convergence angle (α) was defined as the intersect angles between the axes of the two motion capture units, as shown in Figure 3.8.

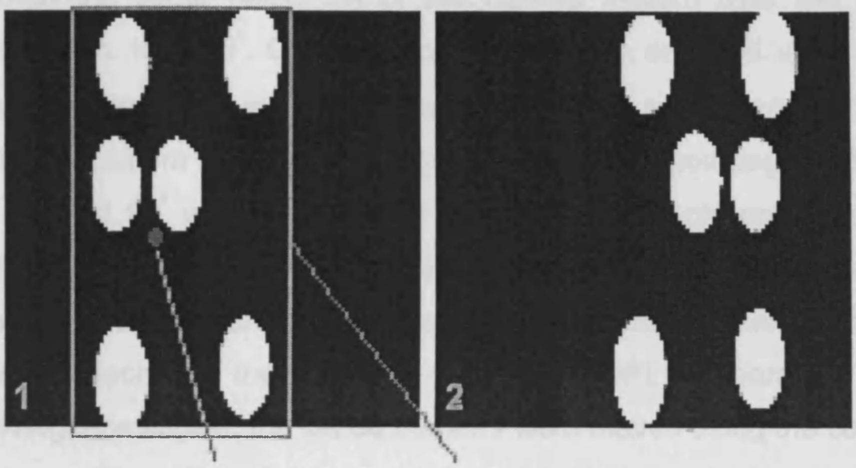

Figure 3.7 A reference point determined using 2D camera views of the markers.

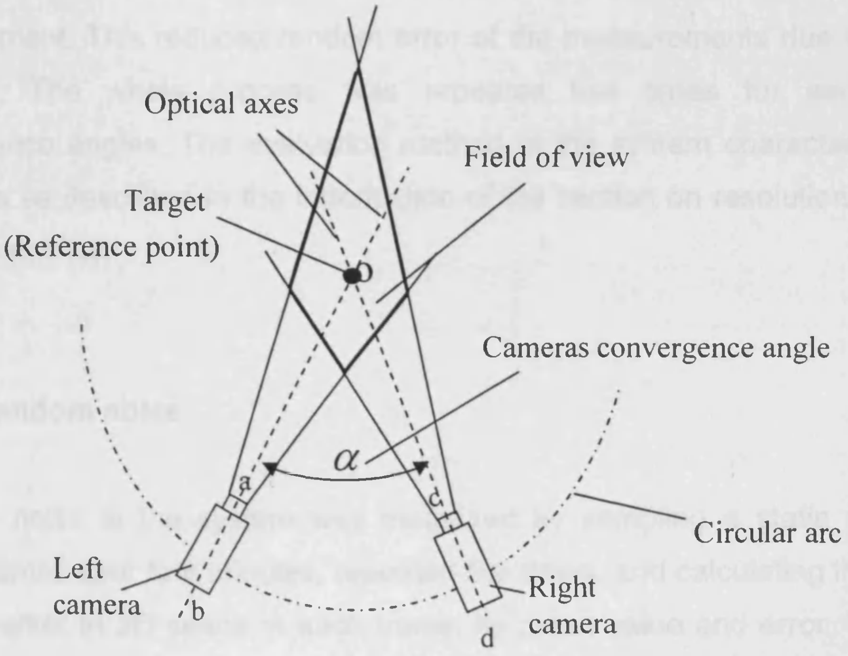

Figure 3.8 The cameras placement in evaluating camera convergence angle.

The cameras were moved to vary the convergence angles along a circular arc. This ensured the same resolution of the camera system over the range of experiments from 15° - 90°. Convergence angles were detected using a Diatec Universal Bevel Protractor with a graduation of 5′. The system was recalibrated for each of the camera positions. Six horizontal convergence angles of 15°, 30°, 45°, 60°, 75° and 90° were detected to evaluate the effects on accuracy and repeatability of the system. Two different types of markers were used in the experiments (spherical markers and elongated diamond markers). The tested markers were attached to the moveable head of the NPL comparator. For each of the convergence angles, the tested markers were moved using the comparator in four steps of 50μm. The Qualisys cameras detected the displacements of the tested markers. To compare the measurement accuracy with the different markers, the diamond markers and the spherical markers were detected alternately in the same experimental conditions. Every movement step was sampled for two seconds at a sampling frequency of 60Hz, giving 120 data frames. The mean value of 120 frames was calculated as the value of one time measurement. This reduced random error of the measurements due to ambient vibration. The whole process was repeated five times for each of the convergence angles. The evaluation method of the system characteristics was the same as described in the introduction of the section on resolution, accuracy and repeatability.

3.3.3 Random noise

Random noise in the system was measured by sampling a static marker for 28800 frames over four minutes, repeated five times, and calculating the position of the marker in 3D space in each frame, its mean value and error. The errors expressed the system random noise, which includes ambient vibration, temperature drift and time drift in the signal processing circuit of the MCUs. Noise level was defined as the root mean square (rms) amplitude (equal to one standard deviation (σ) of the signal about the mean value). Assuming a normal distribution, the noise signal would be expected to lie in this band 95% of the time (the 95% confidence interval is $\pm 1.96\sigma$). Thus the noise band was defined as 3.92σ.

3.4 Results

The system resolution was found to be 10 μm in the 68.18 x 51.14mm field of view. When the steps were 0.5, 1, 2, 3 and 5μm, the measured step as a percentage of the actual step divided by ideal step was less than 80% for each of the steps. For steps over 10μm, the system was found to be sensitive enough to repeatably measure the micro-displacement, as shown in Table 3.1. Note that this is the resolution of the whole system, not just the resolution of the cameras.

Table 3.1 Percentage of actual measuring step size divided by ideal step size for step sizes of 0.5, 1, 2, 3, 5, 10, 20μm in x, y, z direction, for the diamond marker and the spherical marker.

Step size	Diamond marker (%)			Spherical marker (%)		
(μm)	X	Y	Z	X	Y	Z
0.5	7.3	5.5	6.0	6.2	21.1	22.4
1	20.0	30.1	10.5	26.0	31.2	28.8
2	17.8	49.7	30.4	10.6	22.8	29.2
3	40.1	46.5	53.2	48.9	47.4	63.2
5	71.3	69.7	79.8	73.4	74.3	79.6
10	91.7	94.5	95.2	91.4	89.7	97.6
20	101.2	100.5	102.5	101.3	103.1	103.3

In the 20-200μm range, the maximum absolute displacement errors in *x*, *y*, and *z* directions were found to be ±2.1μm, ±3.0μm and ±2.35μm for the diamond markers, and ±3.25μm, ±4.25μm and ±2.5μm for the spherical marker. The system accuracy, in the 20-200μm range, was found to be ±1.17%, ±1.67% and ±1.31% for the diamond markers, and ±1.81%, ±2.37% and ±1.39% for the spherical markers in *x*, *y*, and *z* directions, respectively. The lowest accuracy was found in the *y* direction, for the spherical markers, as shown in Figure 3.9.

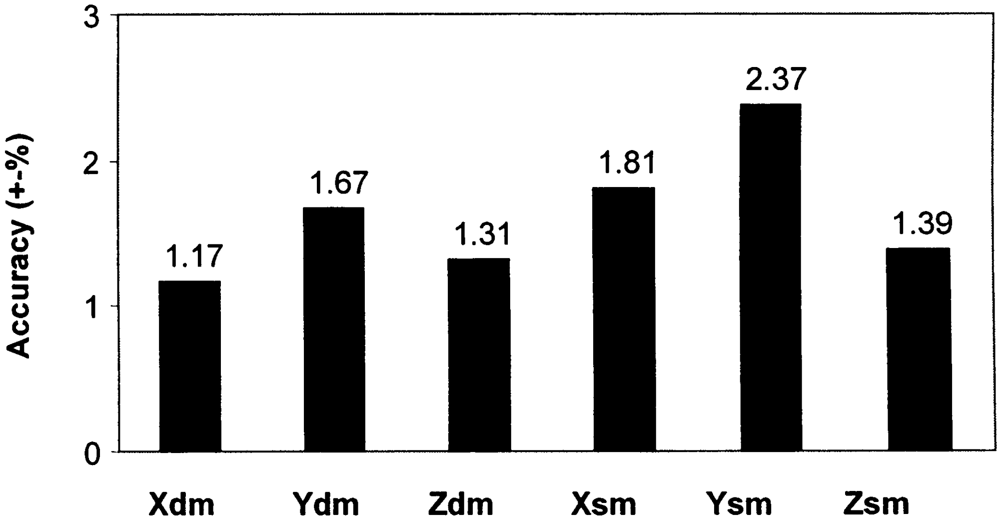

Figure 3.9 The system measurement accuracy (±%) in the 20-200μm ranges of *x*, *y*, *z* directions, for the diamond markers (dm) and the spherical markers (sm). The results were calculated as the percentage of maximum absolute error in the full range divided by the measurement range.

The repeatability defined as standard deviation, in the 20-200μm ranges, was found to be ±1.7μm, ±2.3μm and ±1.9μm for the diamond markers, and ±2.6μm, ±3.9μm and ±1.9μm for the spherical markers in the *x*, *y* and *z* directions respectively, as shown in Figure 3.10.

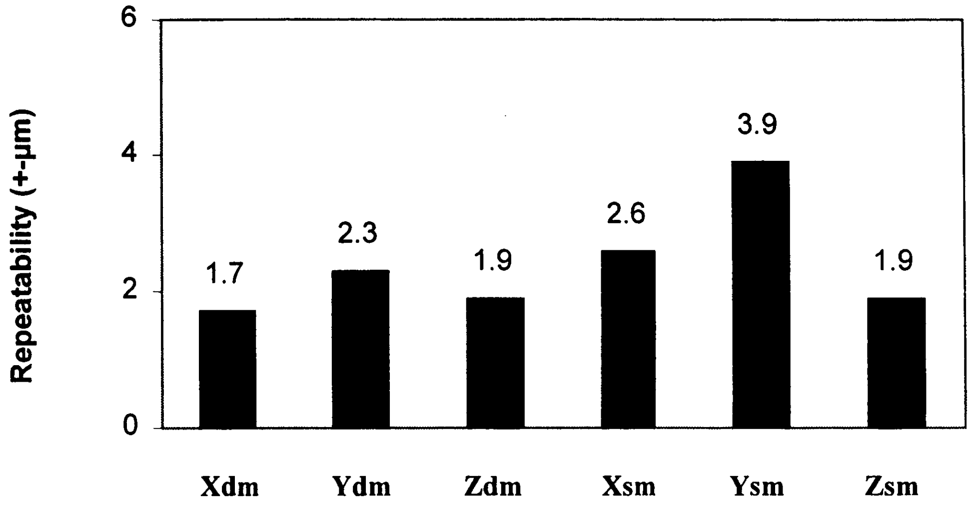

Figure 3.10 The system repeatability (± µm) in the 20-200µm ranges of the *x, y, z* directions, for the diamond markers (dm) and the spherical markers (sm). The results were calculated with the standard deviation.

The hysteresis error produced by the NPL wedge comparator was calculated from the measured data. The average hysteresis error in the measurement of *x, y* and *z*-directions was 18.6(µm) for the diamond markers and 18.4(µm) for the spherical markers in the 20-200µm range, as shown in Figure 3.11.

The system random noise level (defined as the standard deviation σ, which is equal to the RMS amplitude) was ±1.47µm. Random noise band was calculated using a 95% confidence interval that is equal to ±1.96σ (defined as 3.92σ), and was found to be 5.76 µm, as shown in Figure 3.12.

For clearly viewing the noise variation, one section of random noise was taken to be shown in Figure 3.13.

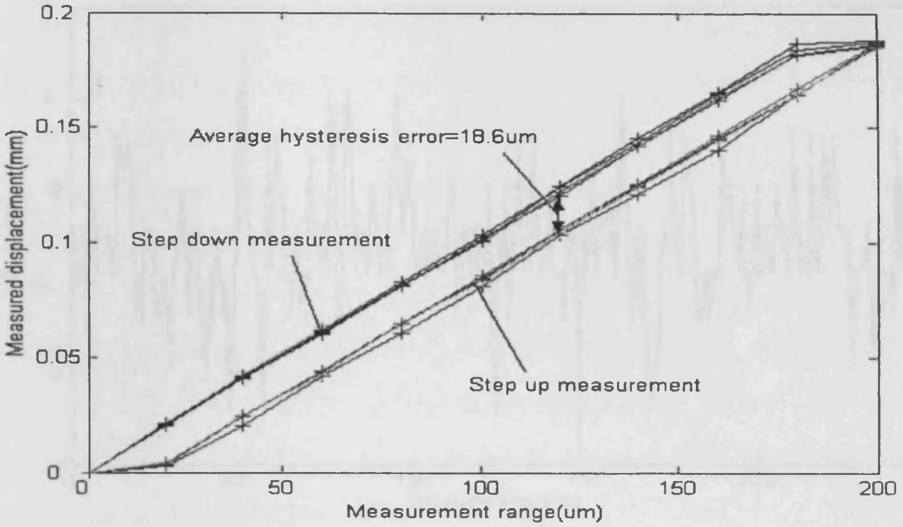

Figure 3.11 The repeatability and hysteresis errors. Hysteresis errors existed between the step up measurement and then step down measurement.

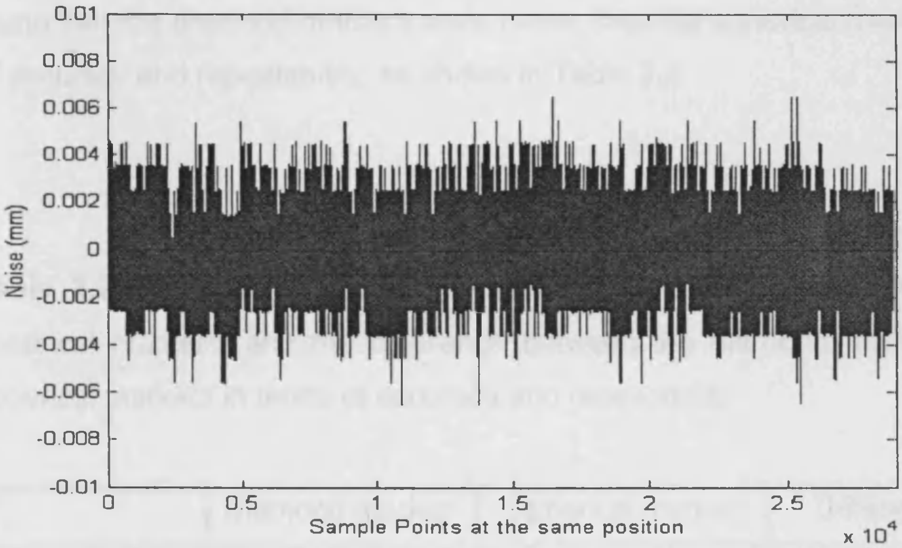

Figure 3.12 The system random noise. A total of 28800 data frames were sampled at a relative static state and calculated the position of every frame in 3D space, its mean value, errors and standard deviation σ. Random noise band, defined as 3.92σ, was 5.76μm.

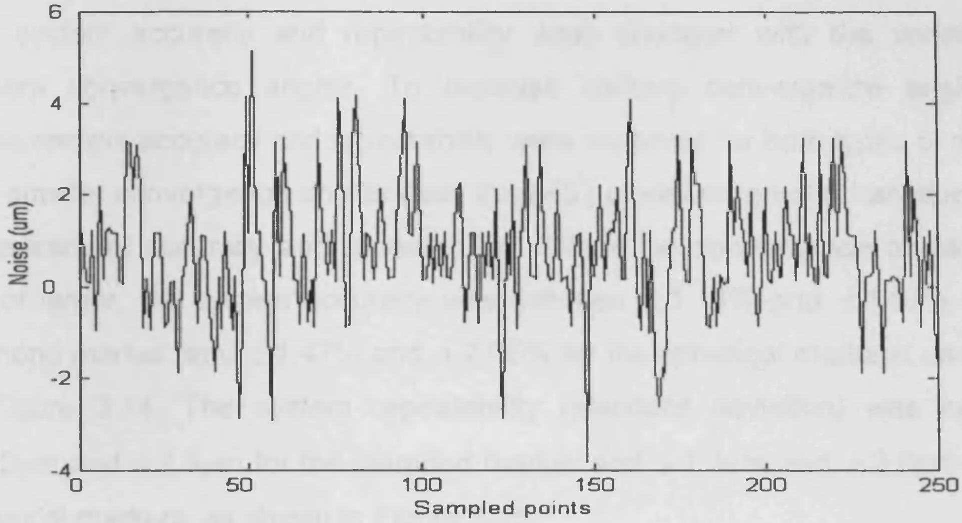

Figure 3.13 A typical section of random noise (250 data points).

In the system measurements, comparing the results in Figure 3.9 and 3.9, it was found that the diamond markers were better than the spherical markers in terms of accuracy and repeatability, as shown in Table 3.2.

Table 3.2 The accuracy and repeatability of the diamond markers and the spherical markers, and the difference between the diamond markers and the spherical markers in terms of accuracy and repeatability.

	Diamond marker			Spherical marker			Difference (Δ)		
Coordinates	*x*	*y*	*z*	*x*	*y*	*z*	*x*	*y*	*z*
Accuracy (±%)	1.17	1.67	1.31	1.81	2.37	1.39	0.64	0.7	0.08
Repeatability (μm)	1.7	2.3	1.9	2.6	3.9	1.9	0.9	1.6	0

The system accuracy and repeatability were changed with the variation of camera convergence angles. To increase camera convergence angle, the measurement accuracy and repeatability were improved for both types of marker. The smaller convergence angles (less than 45°) produced greater variation in the measurement accuracy and repeatability. When the convergence angles were 45° or larger, the system accuracy was between ±1.16% and ±1.67% for the diamond marker, and ±1.47% and ±2.05% for the spherical markers, as shown in Figure 3.14. The system repeatability (standard deviation) was between ±1.2μm and ±2.3μm for the diamond marker and ±1.3μm and ±2.6μm for the spherical markers, as shown in Figure 3.15.

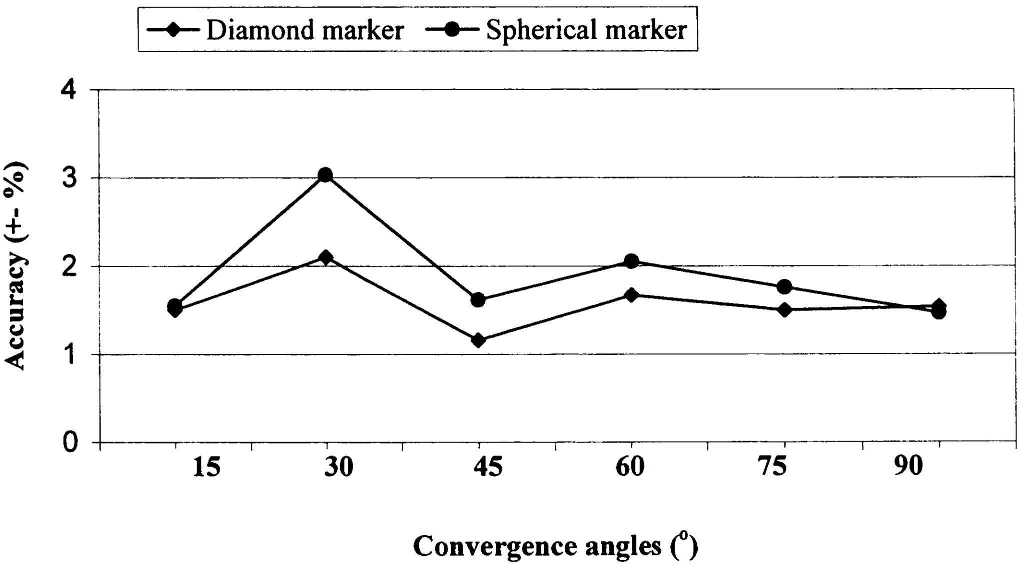

Figure 3.14 Accuracy of the optical motion analysis system as a function of the camera convergence angle for the diamond markers and the spherical markers.

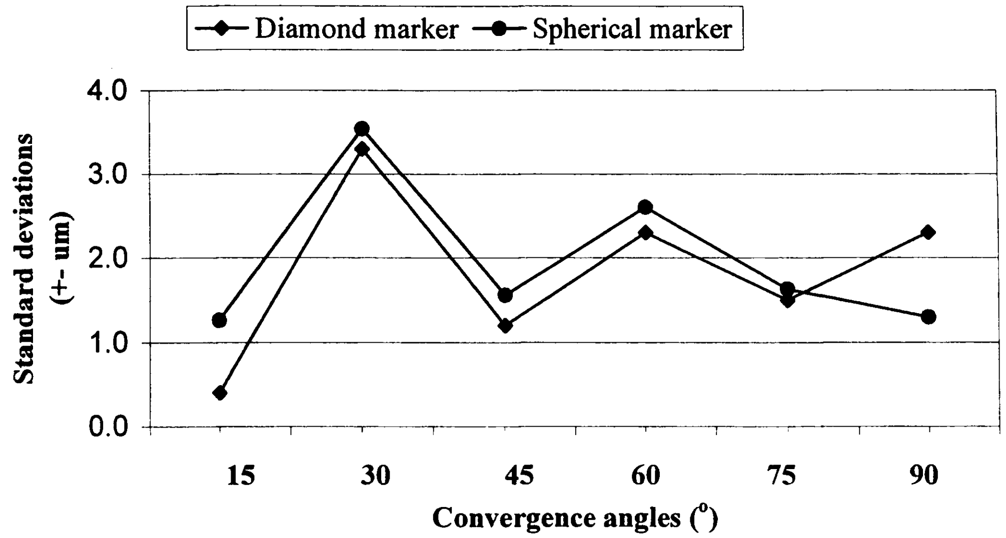

Figure 3.15 Repeatability of the optical motion analysis system as a function of the camera convergence angle for the diamond markers and the spherical markers.

The results of evaluating accuracy and repeatability with changing camera convergence angle provided suggestions for replacing the cameras in a clinical experiment.

3.5 Discussion

In a 68×51mm field of view, the system resolution found was 10μm, which is higher than the theoretical value of 1/60,000 of the field of view (1.14μm) given by the manufacture's technical literature. This is because the theoretical calculation given by the manufacturer may just consider the 16-bit resolution of the internal calculations in the camera, and ignores the system random noise. In fact, in the motion capture system, a charge-coupled device (CCD) is used to capture and transmit the signal of the images (markers). The CCD normally has high quantum efficiency, >90% across the visible and near infrared compared with photomultipliers 10–30% (http://www.chem.agilent.com/); a wide field of view may have background light levels and light originating at any depth can reach the CCD; a field of view with an adequately uniform illumination is difficult to supply; all of these factors could result in optical fluctuations, i.e., noise of the CCD system. In the CCD system, there are several sources of noise: camera dark current shot noise; photoelectron shot noise and camera readout noise (Che et al., 2001). In addition, the QTM software with the MCUs may add noise. Besides, vibration is another source of noise. There are two principal sources of vibration which can bring noise: ground vibration and acoustic noise. Ground or seismic vibration exists in all environments throughout the world. This noise has various sources, from waves crashing on coastal shorelines, wind blowing trees and buildings, man-made sources like machinery, heating, ventilating and air-conditioning systems, street traffic, and even people walking. Acoustic noise comes from many of the same sources, but is transmitted to the measured markers through air pressure waves. These generate forces directly on the measured markers. Even subsonic acoustic waves can produce differential pressure and disturb a load applied on the measured markers.

The system accuracy was evaluated separately in *x, y,* and *z* directions on a relative basis. The results suggested that the diamond marker had better accuracy than the spherical marker in all three directions (see table 3.2). The reason for accuracy difference may be that the diamond markers take advantage of the different horizontal and vertical resolutions of the CCD sensor; the perimeter of the elongated diamond markers is greater which provides more measurement points than for the circular markers; or the elliptic area surrounding the elongated diamond markers is bigger than the circular area surrounding the spherical marker and the elliptic area provides more measurement points than the circular area. The larger the area of marker, the higher the accuracy of calculating central point of the marker.

Repeatability was affected by the system random noise, reading error and hysteresis of the comparator. The repeatability and accuracy in the *x* and *z* directions were better than in the *y* direction (see table 3.2). This may be because the *y* direction assumed in the measurement was the same as the main direction of ambient vibration, which produced the principal part of the system random noise. Thus errors measured in the *y* direction were bigger than in the *x* and *z* directions.

Figures 3.14 and 3.15 demonstrated that the accuracy and repeatability were different between the elongated diamond markers and the spherical markers over the camera convergence angle range from 15° to 90°, but the graphs' trends for the two types of markers were similar along with the variation of camera convergence angle. The diamond markers showed better results than the spherical markers. The results of quantitive comparison between the diamond markers and spherical markers are shown in Table 3.3. When the camera convergence angle was from 45° to 90°, the camera system had good accuracy. The range of accuracy was from ±1.16% to ±1.67% for the diamond markers; and ±1.47% to ±2.05% for the spherical markers. From Figure 3.14, it is seen that there was more variation in accuracy, (up to ±3.03%), for the camera angles of 30°. The reason for unexpectedly high accuracy at 15° is unclear, but theory suggests that large error may be likely at such small angles (Lawson and Wu 1997).

The system error is another factor that can reduce measurement accuracy. It can be created from image aberrations due to the lens assemblies in the motion capture units although there is a correction for this in the QTM software, poor camera calibrations, temperature and time drift in the signal processing circuit and systematic calculation errors etc. The system error can be reduced through precision manufacture of the lens; cautious assemblies; precision production and measurement of the calibration frame; and a reasonable data processing etc.

Table 3.3 Accuracy and repeatability of the diamond markers and the spherical markers at different camera convergence angles, and the difference between the diamond markers and spherical markers in terms of accuracy and repeatability.

	Accuracy (±%)			Repeatability (μm)		
Degree	Diamond marker	Spherical marker	Difference (Δ)	Diamond marker	Spherical marker	Difference (Δ)
15°	1.5	1.55	-0.05	0.4	1.3	-0.9
30°	2.1	3.03	-0.93	3.3	3.54	-0.24
45°	1.16	1.62	-0.46	1.2	1.56	-0.36
60°	1.67	2.05	-0.38	2.3	2.6	-0.3
75°	1.5	1.76	-0.26	1.5	1.63	-0.13
90°	1.54	1.47	0.007	2.3	1.3	1

Overall, the evaluation results demonstrated that the ProReflex-MCU120 motion capture system has sufficient accuracy for measuring micro movement, such as tooth movement, and could potentially be useful in many material deformation measurements in biomechanics and elsewhere.

Chapter 4 Methods of data acquisition, processing and software evaluation

4.1 Introduction

Tooth movement has been measured using many different methods such as laser displacement sensor (Jones et al., 2001b), eddy current measuring system (Dorow et al., 2003c), magnetic sensors (Yoshida et al., 2000) etc. Tooth movements in 6DOF were calculated using the method of finite helical axis by Hayashi et al., (2002). This method has also been used to analyse joint function in the last two decades (see Chapter 2). Although there are many different methods to be used in measuring and processing tooth movements, the real biomechanical properties of the PDL have still to be investigated. This is because the methods of tooth measurement and data processing were unsatisfactory, and the results of experiments were with an excessive deflection. In this study, a novel system of measuring micro movement, such as tooth movement, was developed (see Chapter 3). For obtaining tooth movement in 6DOF, a new method of calculating tooth movement in 6DOF needed to be developed. This chapter will introduce a three coordinate system method, that is, three coordinate systems are a global coordinate system (GCS) (see Figure 3.4), a marker cluster coordinate system (MCS) and an anatomical coordinate system (ACS), to calculate tooth movement in 6DOF. The chapter starts with an introduction, and subsequently, the methods of data acquisition and calculation of tooth movement of 6DOF will be described in detail in sections 4.2, 4.3 and 4.4. Section 4.5 will present the methods used to evaluate the developed software. Finally, the results will be presented and discussed.

4.2 Method of data acquisition

Data acquisition begins with the system calibration. The frame calibration method was used (see Chapter 3). Then the following steps were carried out to complete the data acquisition.

4.2.1 Calibration of the pointer and determination of anatomical coordinate system

In the system of measuring tooth movement, the anatomical coordinate system (ACS) of the tooth, as shown in Figure 4.1, was used as a reference coordinate system to study tooth movement. This is because the anatomical coordinate system is more meaningful for calculating tooth movement than any randomly defined coordinate system. One axis (*z*) of the ACS is along the long axis of tooth; another axis (*y*) is the lingual axis, which was used in previous studies of tooth movement (see Chapter 2); the third axis is *x*- axis of the ACS. The exact definition of the anatomical coordinate system is explained in section 4.3.4.

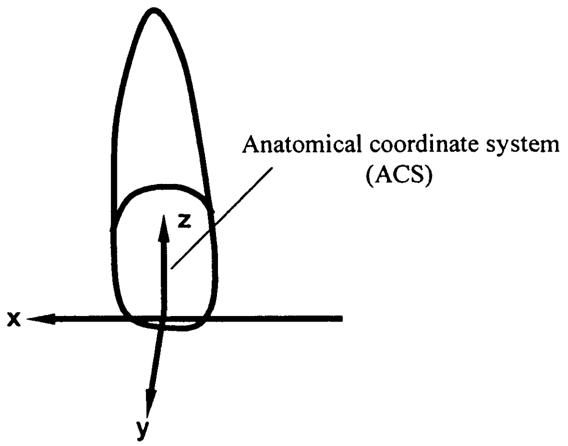

Figure 4.1 Anatomical coordinate system of the tooth

To determine the ACS of tooth, the pointer method was used based on the knee kinematics measurement developed by Holt et al. (2000). The pointer was used to identify three landmark positions on the measured tooth, as shown in Figure 4.2.

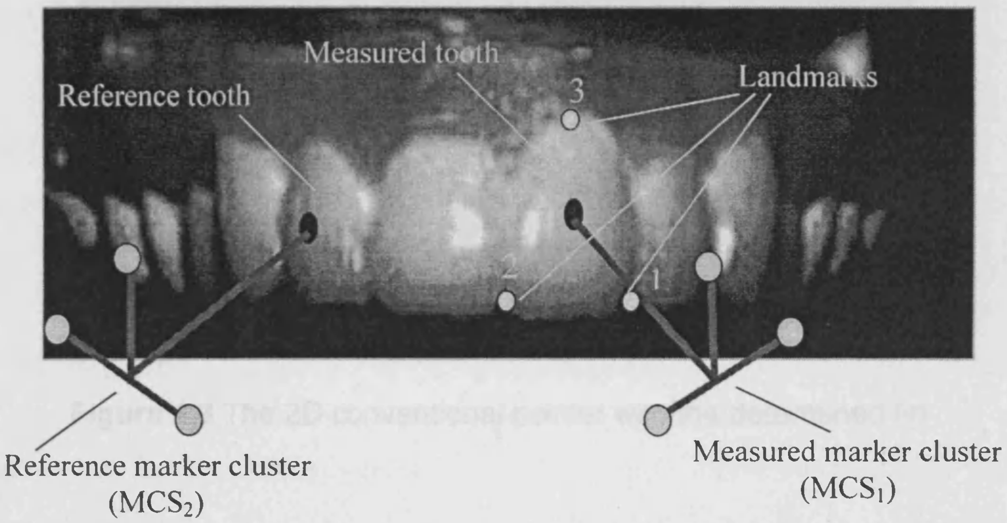

Figure 4.2 The marker clusters and identification of landmark positions

The tip of the pointer was placed at the positions of three landmarks respectively; the MCUs captured the states of the pointer at three landmarks. From the captured data, the ACS of the tooth was established by using landmark vectors through vector calculation. The detail, how to establish the ACS of tooth using designed Matlab software, is described in section 4.3.4, which describes the determination of the coordinate systems - global, marker cluster and anatomical.

Two types of pointer (2D and 3D) were designed and made successfully in this study, as shown in Figure 4.3and 4.4 Figure 4.3showed the 2D conventional pointer. The coordinate values of the tip position in the pointer coordinate system, which is established by four markers on the pointer, were measured accurately by the CMM and input to the developed Matlab software before the pointer was used.

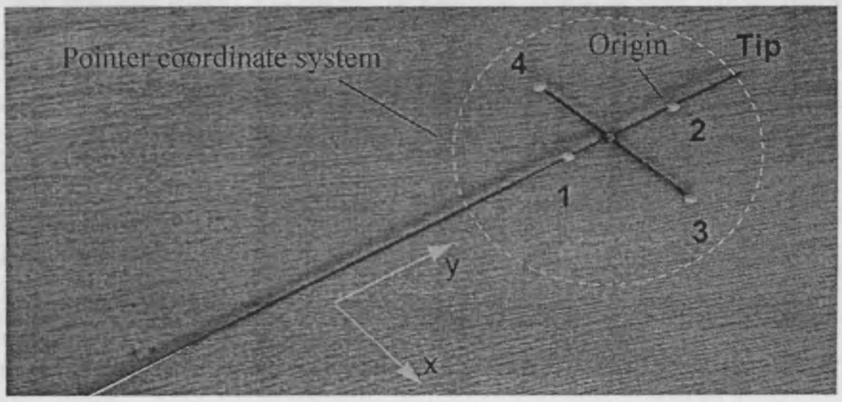

Figure 4.3 The 2D conventional pointer with the determined tip

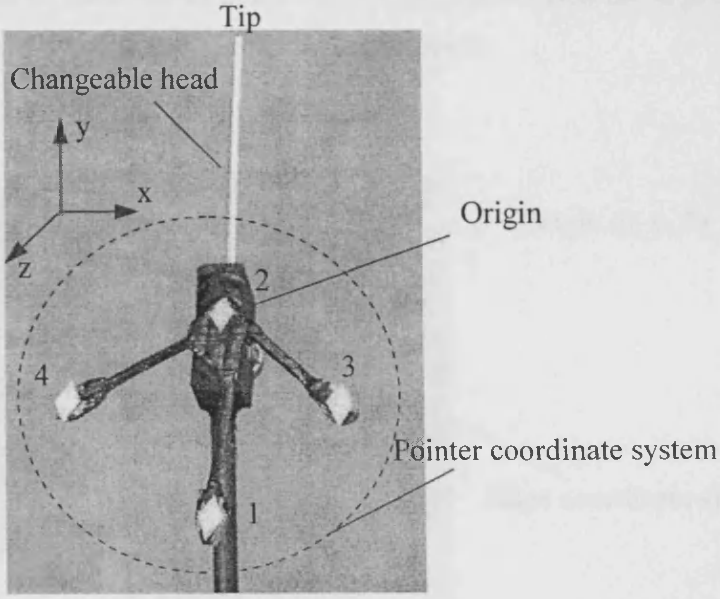

Figure 4.4 The 3D pointer with changeable tip

The advantages of the 2D conventional pointer are that it is easier to manufacture and to design the software than for the 3D pointer, because with the 2D pointer, it is not necessary to change the head, and the position of the tip is already measured by the CMM. That is, the position of tip does not need to be calculated by the software. However since the head of the 2D pointer could not be changed, this created a hygiene problem when more than one volunteer was tested during the experiments. Therefore a 3D pointer with a changeable head was designed (Figure 4.4. With the design of the 3D pointer, the software was programmed to automatically calculate the position of the tip of the pointer. The method of calculating the tip used an assistant plane, which has three markers and a fixed point *"q"*, was shown in Figure 4.5. The position of *"q"* was measured using a travelling microscope before the assistant plane was used. Then the marker positions in 3D space, including three markers on the assistant plane and four markers on the pointer, were captured, when the tip of the pointer was placed at *"q"*, by the Qualisys motion capture system. From the captured data of marker positions in 3D space, the tip position was calculated by the software. The detailed method of calculating of the tip position of the pointer is presented in section 4.3.3. The software is presented in Appendix B.

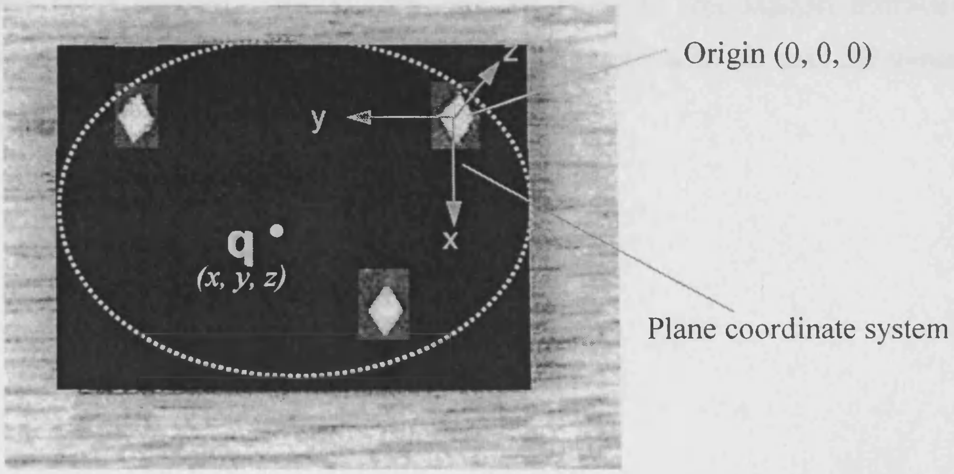

Figure 4.5 The assistant plane for calculating tip position of the pointer.

4.2.2 The measurement of the natural position of the tooth

In measuring tooth movement, a relative measurement method was used, that is, movement of the measured tooth with its attached marker cluster was measured relative to the position of the reference tooth with its attached reference marker cluster, as shown in Figure 4.6 Thus the initial (natural) positions of the measured tooth and the reference tooth need to be known by capturing the two marker clusters (measured marker cluster and reference marker cluster). The advantage of this method is that it avoids the deflection brought by head movement of volunteers while measuring tooth movement.

The marker clusters were made using black carbon fibre, and clear acrylic balls with diameter of 2.5mm, glued with the reflective powder, as shown in Figure 4.7

In the natural positions of teeth (without load), the MCUs captured the two marker clusters (reference and measured) at the same time. The captured data with 3D coordinate values in the GCS was stored in the PC with a file name of xx10 (xx was the name of the volunteer), and then the data were exported to a .tsv file using the QTM system. The .tsv file can be input to the Matlab software for analysis of the data. The two marker clusters captured with 2D and 3D views are shown in Figure 4.8(a) and (b).

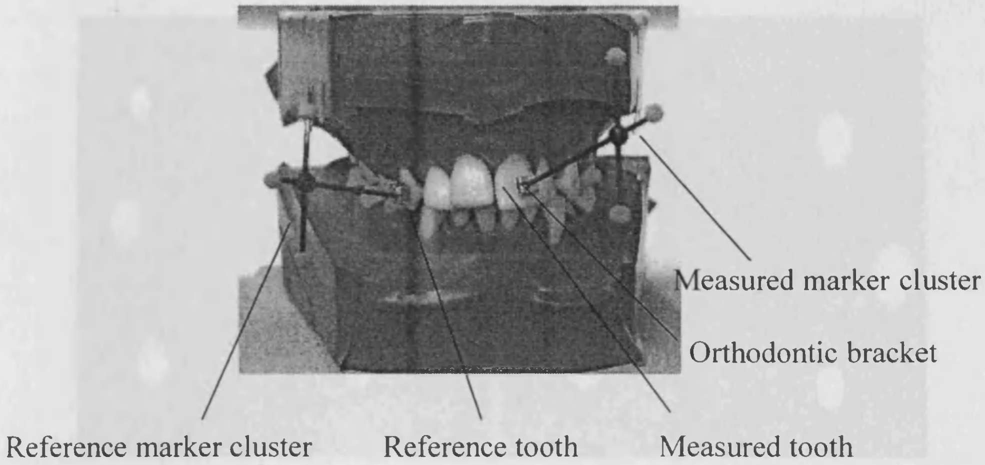

Figure 4.6 The marker clusters fixed on the measured tooth and the reference tooth.

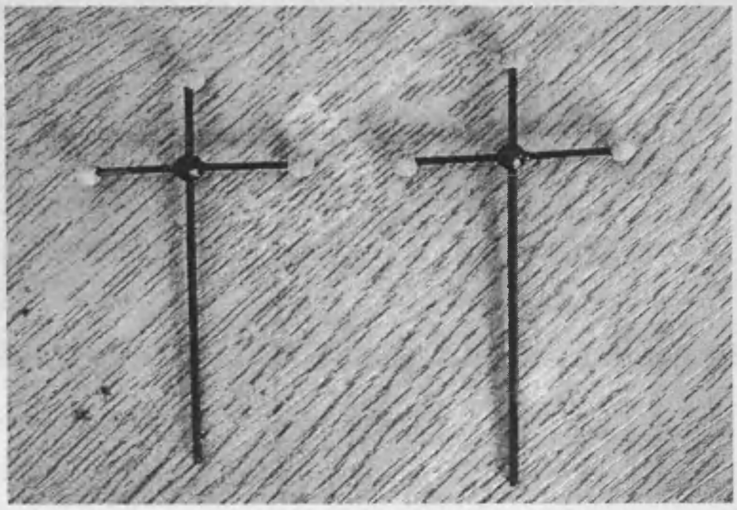

Figure 4.7 The marker clusters with holding bar

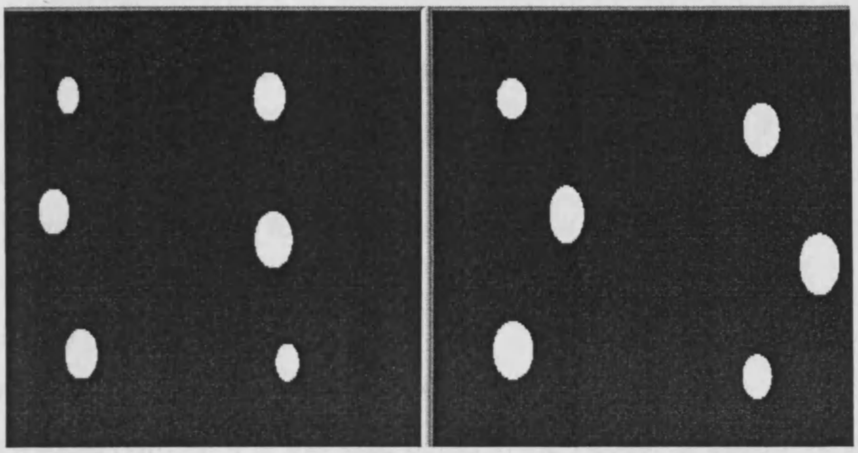

(a)

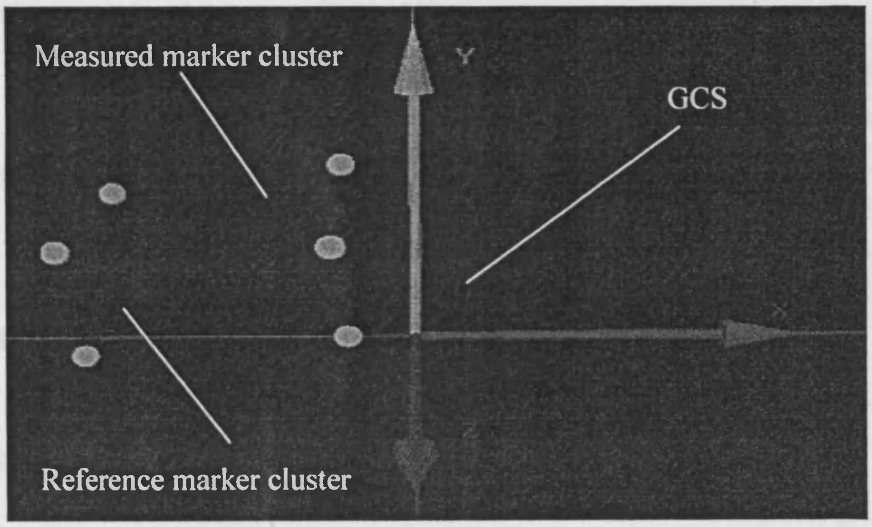

(b)

Figure 4.8 View of the reference marker cluster and measured marker cluster in unloaded state. (a) 2D camera views, (b) 3D camera views.

4.2.3 The measurement of tooth movement under load

When the load was applied to the measured tooth, the states of the two marker clusters were captured by the MCUs. The captured data with *x, y* and *z* value in the GCS were stored in the PC with created file name of xx111, xx112...etc. The file name is explained as the following:

- xx is the name of the volunteer;
- the first number 1 is the first time visit;
- the middle number 1 is the load acted in the buccal direction, (if the middle number is 2, it means the load acted in the lingual direction; if the middle number is 3, it means the load acted on the direction of vertical intrusion; if the middle number is 4, it means the load acted on the direction of vertical extrusion; if the middle number is 5, it means twisting loading);
- the last number is the number of the measurements.

Then the captured data were exported to .tsv files using the QTM system. The .tsv file can be input to the Matlab software for analysis of the data.

4.3 Method of data processing

4.3.1 Introduction of the method

Firstly a number of Cartesian coordinate systems were determined and established. They were: the global coordinate system (GCS); the tooth anatomic coordinate system (ACS); and the marker cluster coordinate systems (MCS) including the measured marker cluster coordinate system (MCS_1) and the reference marker cluster coordinate system (MCS_2). Then transformation matrices were calculated using the Soderkvist and Wedin (1993) method, including transformation matrices from the MCS_1 to the GCS (T_{MG1}); from the MCS_2 to the GCS (T_{MG2}), from the MCS_1 to the ACS (T_{MA1}) and from the MCS_2 to the ACS (T_{MA2}).

Movement of the ACS was found using T_{MG1}, T_{MG2}, T_{MA1} and T_{MA2} (some transformation matrices were inverted to obtain a required transformation direction.), through the product of the transformation matrices from the right to the left, as shown in equation 4.1:

$$T=T_{MA1} * T_{GM1} * inv(T_{GM2}) * inv(T_{MA2}); \qquad 4.1$$

The relationship of equation 4.1 can also be described in Figure 4.19

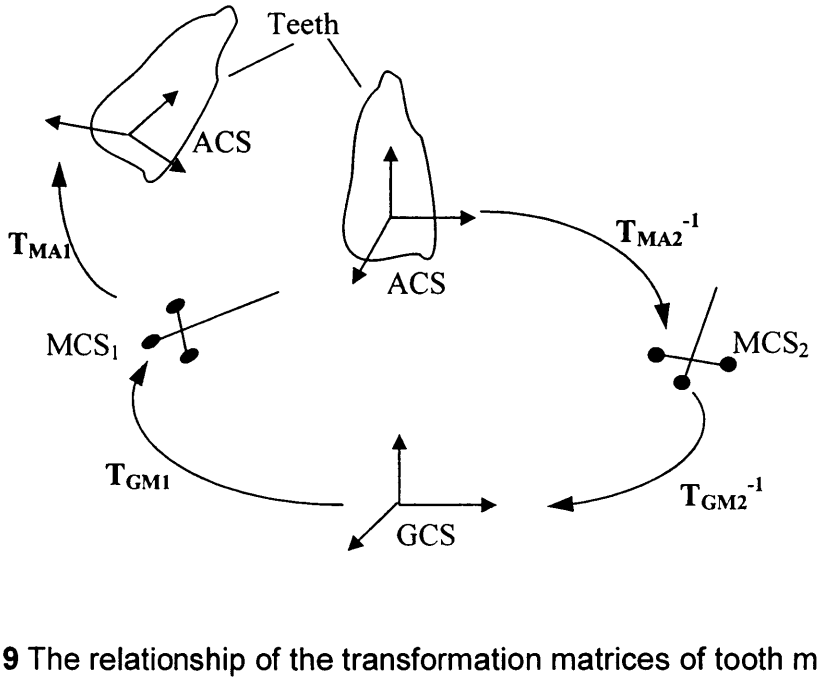

Figure 4.9 The relationship of the transformation matrices of tooth movement.

4.3.2 The software design block diagram

The data processing software in Matlab was designed based on the knee function program developed by Holt et al. (2000). The block diagram of the software is shown in Figure 4.10.

The main functions of the software designed for knee function and tooth data analysis were:

Knee function program:

- Using two segments with two marker clusters – tibial segment1 with marker cluster 1 and thigh segment2 with marker cluster 2;
- Landmarks 1, 2 were the same for segment1 and segment2, but landmark 3 was different for segment1 and segment2. For segment_1, landmark 3 was placed at the medial malleolus, and for segment_2, landmark 3 was placed at upper trochanter;
- Landmarks produced two ACS. Two ACS have the same origin (they sit on top of each other), but the opposite z direction (the z direction was down for segment_1 and up for segment_2);
- The transformation matrices of two marker clusters relative to the ACS were established (T_{MA1} and T_{MA2});
- The transformation matrices of the GCS relative to the marker clusters were established (T_{GM1} and T_{GM2});
- Using the ACS of segment_2 as the reference coordinate system, calculate the relative movement between segment1 and the segment2;
- The results of 6 DOF were given.

Tooth data analysis:

- Added the function of distinguishing the loading types in the beginning program by author;

- Added the filter for noise processing by author;
- Added the function of automatically calibrating the tip position of the pointer by author;
- Uses one segment to define the ACS – three landmarks were identified on the measured tooth changed by author;
- Two marker clusters were fixed on the measured tooth and the reference tooth;
- The transformation matrices of the measured marker cluster and reference marker cluster relative to the ACS were established (T_{MA1} and T_{MA2});
- The transformation matrices of the GCS relative to the measured marker cluster and reference marker cluster were established (T_{GM1} and T_{GM2});
- The results of 6 DOF were given.

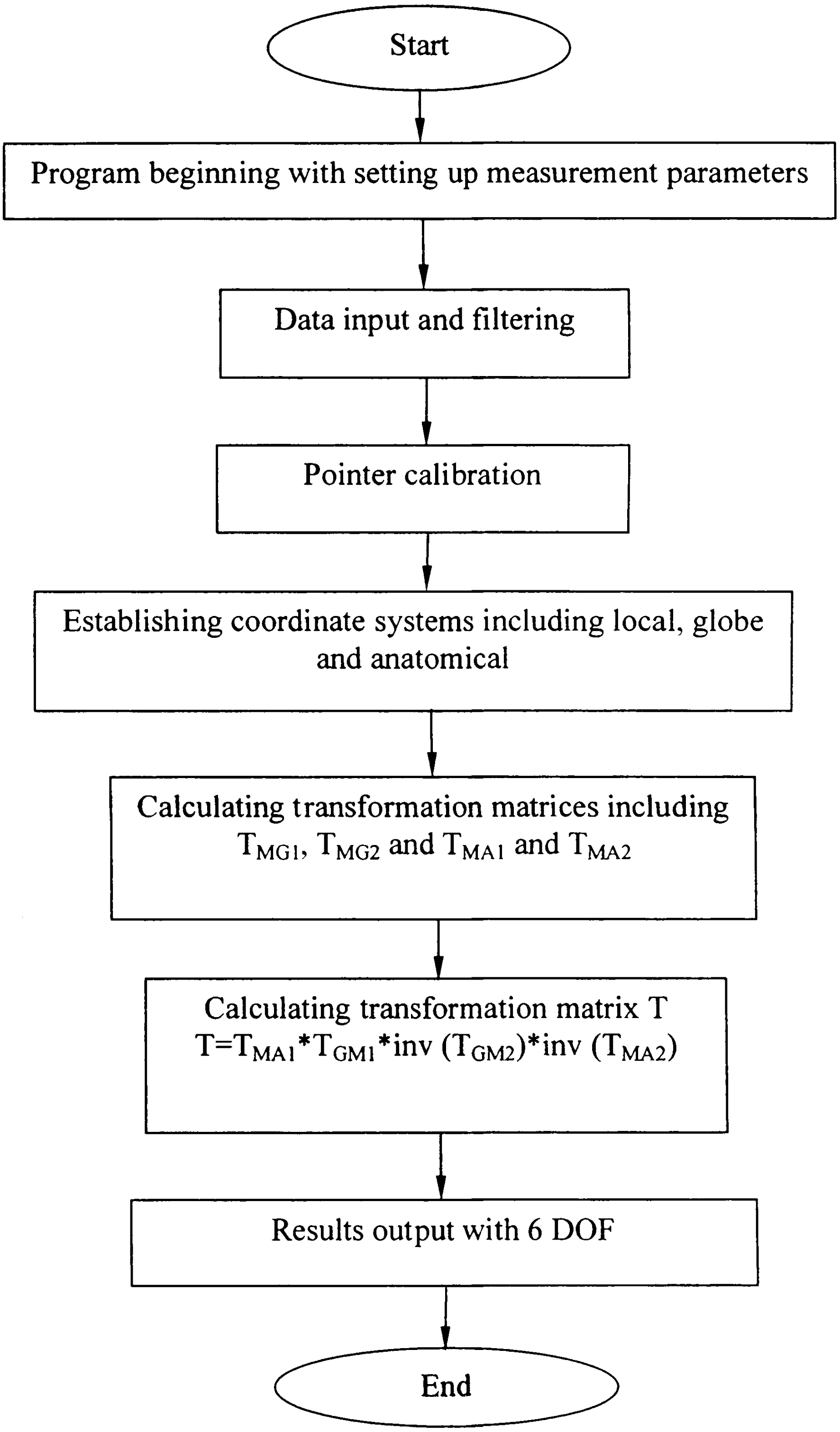

Figure 4.10 The software block diagram of the data processing

4.3.3 The method of calculating tip position

The 3D positions of the "*q*" point on the assistant plane were measured using the travelling microscope. The tip of the pointer was placed on the point "*q*". The MCUs captured the pointer's four markers and the assistant plane's three markers. Using the recorded data, the transformation matrices T_{SG} and T_{PG} were calculated. T_{SG} was a transformation matrix from the assistant plane coordinate system to the global coordinate system; T_{PG} is a transformation matrix from the pointer coordinate system to the global coordinate system. The position of the tip of the pointer in the pointer coordinate system was then calculated as shown in equation 4.2.

$$P = inv(T_{PG})*(T_{SG})*q \qquad 4.2$$

To identify the ACS of the tooth, the tip of the pointer was placed on each of the landmark positions in turn. The position of all markers, including the markers of the two marker clusters and the pointer, was captured by the MCUs, and the data was stored with file names xx1ac1, xx1ac2, and xx1ac3 (xx is the name of volunteer; 1, 2 and 3 are the landmark positions). Then the data were exported to a .tsv file to input to the Matlab software for analysis (Liu et al. 2006b). The tip of the pointer was placed on the landmark 3 and the MCUs 3D view is shown in Figures 4.11and 4.12

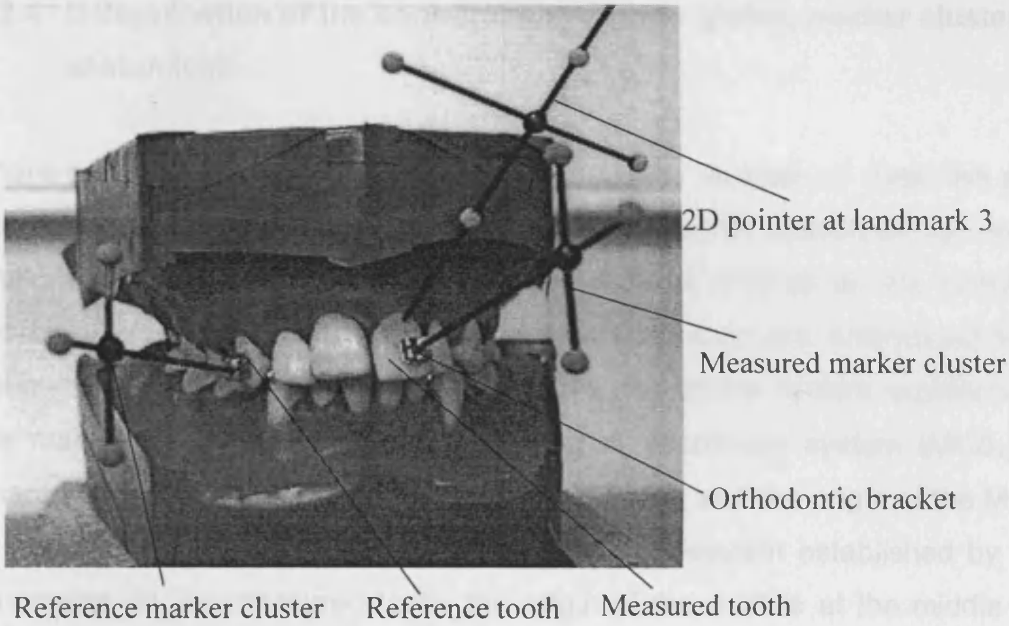

Figure 4.11 The pointer placed on landmark position 3.

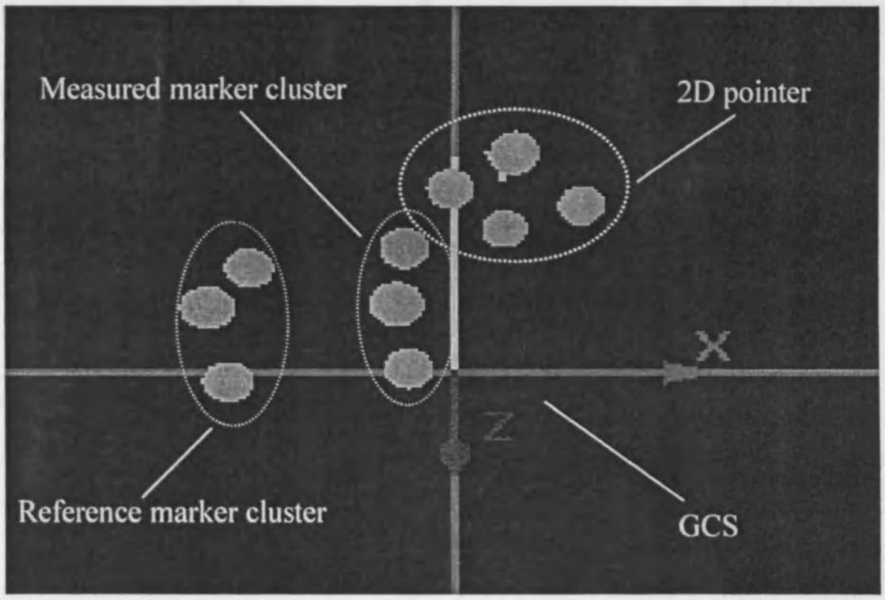

Figure 4.12 The 3D cameras view with recorded marker clusters and pointer.

4.3.4 Determination of the coordinate systems - global, marker cluster and anatomical

There are numbers of coordinate systems used in analysis of data: the global coordinate system (GCS); the marker cluster coordinate system (MCS) and the anatomical coordinate system (ACS). The GCS is defined as the coordinate system in laboratory space, and the directions of axes are determined by the calibration frame. The MCS is defined as the coordinate system established by the marker clusters: measured marker cluster coordinate system (MCS_1) and reference marker cluster coordinate system (MCS_2), and the origin of the MCS is at marker 2. The ACS is defined as a coordinate system established by three landmarks on the measured tooth, the origin of the ACS is at the middle point between the landmark 1 and the landmark 2. The coordinate systems are shown in Figure 4.13.

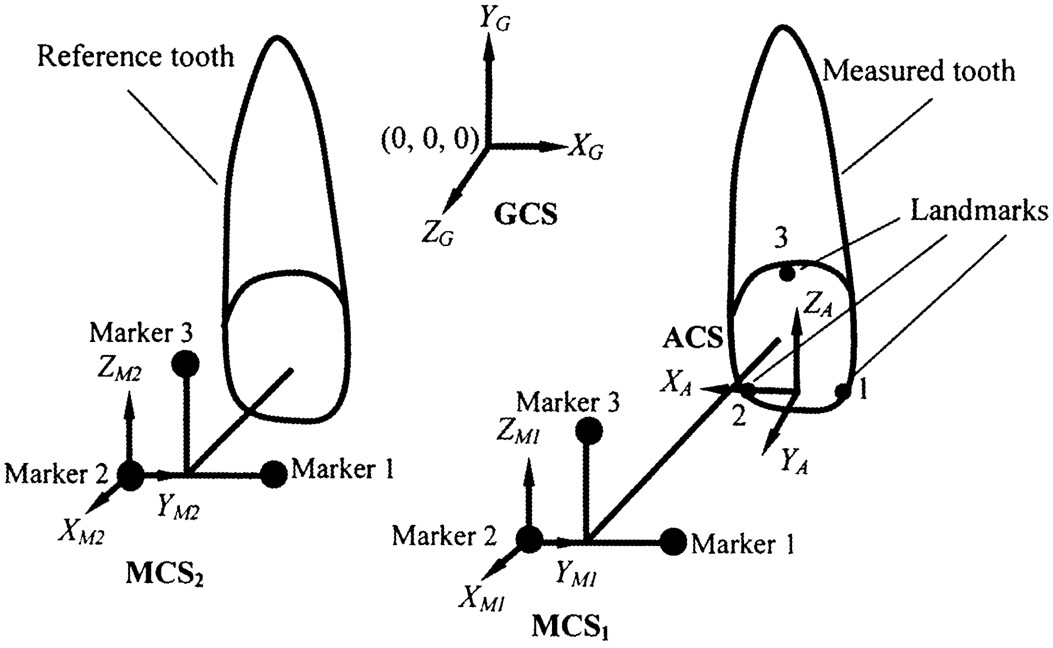

Figure 4.13 The determination of the coordinate systems – global, marker cluster and anatomical.

In the Figure 4.13 X_{M1}, Y_{M1} and Z_{M1} are the unit axis vectors of the MCS$_1$ which is established for the measured marker cluster through vector calculation; X_{M2}, Y_{M2} and Z_{M2} are the unit axis vectors of the MCS$_2$ which is established for the reference marker cluster through vector calculation. X_A, Y_A and Z_A are the unit axis vectors of the ACS which was established for the three landmarks through vector calculation (see below the detail program and Figure 4.14 which was described how to establish the ACS of tooth using designed Matlab software). X_G, Y_G and Z_G are the unit axis vectors of the GCS which is established using the camera calibration frame.

```
Origin=mean (MCSdata(1:2,1:3);  % calculating the origin from landmark 1 and 2.
                                  the origin was defined at the middle point
                                  between landmark 1 and 2. 1-2 are the order
                                  of landmark store in the QTM system, 1-3 are
                                  x, y and z coordinate values in the GCS;
```

```
U=(MCSdata(2,1:3)'-MCSdata(1,1:3)'); % defining vector U from landmark 2
                                  vector and landmark 1 vector; 1-3 are x, y and
                                  z coordinate values of landmark in the GCS;
```

```
X=U/sqrt((U(1)^2)+(U(2)^2)+(U(3)^2)); % the unit vector on the x- axis is
                                   U/ length (U) in the GCS;
```

```
W=(MCSdata(3,1:3)'-orgin(1,1:3)'); % defining a vector W from landmark 3
                                  vector and landmark 1 vector as the plane of
                                  the z-axis;
```

```
Ww=W/sqrt((W(1)^2)+(W(2)^2)+(W(3)^2)); % the unit vector on the Ww axis is
                                             W/ length (W) in the GCS;
```

```
Y=cross(Ww,X);  % defining the direction of the y-axis by the vector cross
                  product of Ww and X;

Z=cross(X,Y);  % defining the direction of the z-axis by the vector cross product
                 of X and Y.
```

(In the calculation program, a rotation matrix was used for the requirements of the mathematical calculation).

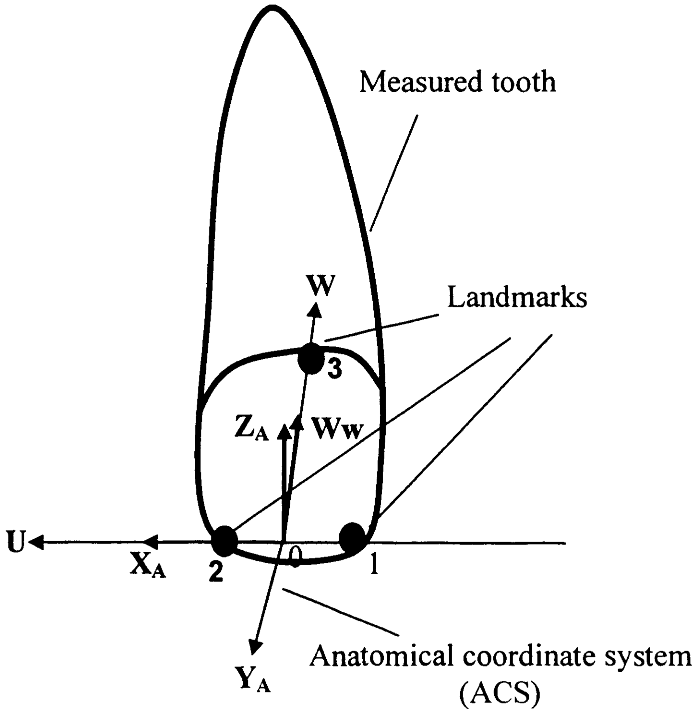

Figure 4.14 The anatomic coordinate system established by using the landmarks on the measured tooth

4.3.5 The transformation matrices

Assuming, in the first coordinate system (CS_1), the 3D coordinate values of three points on a rigid body are defined as $\{p_1, p_2, \ldots\ldots p_9\}$; in the second coordinate system (CS_2), the 3D coordinate values of the same three points are defined as $\{q_1, q_2, \ldots\ldots q_9\}$. Then the same three points in the CS_1 relative to CS_2 can be defined by the following equation (Kwon, 1998):

$$q = R \bullet p + d \qquad 4.3$$

Where ***R*** is a 3x3 rotation matrix, ***d*** is a 1x3 translation matrix. The equation 4.3 can also be written as:

$$\begin{bmatrix} q \\ 1 \end{bmatrix} = \left[\begin{array}{ccc:c} & R & & d \\ \hdashline 0 & 0 & 0 & 1 \end{array}\right] \times \begin{bmatrix} p \\ 1 \end{bmatrix} \qquad 4.4$$

$$T = \left[\begin{array}{ccc:c} & R & & d \\ \hdashline 0 & 0 & 0 & 1 \end{array}\right] \qquad 4.5$$

In the equation 4.5, both the rotation and translation are in a 4x4 transformation matrix ***T***. Thus the 3D coordinate values of the three points (***p*** *&* ***q***) in the CS_1 and the CS_2 can also be written in detail as the following forms:

$$\boldsymbol{p} = \begin{bmatrix} p_1 & p_2 & p_3 \\ p_4 & p_5 & p_6 \\ p_7 & p_8 & p_9 \\ 1 & 1 & 1 \end{bmatrix} \tag{4.6}$$

And

$$\boldsymbol{q} = \begin{bmatrix} q_1 & q_2 & q_3 \\ q_4 & q_5 & q_6 \\ q_7 & q_8 & q_9 \\ 1 & 1 & 1 \end{bmatrix} \tag{4.7}$$

The last row is filled with 1 in the equations 4.6 and 4.7 for the requirements of matrix calculation, because, in the equation 4.5, the transformation matrix $\boldsymbol{T}$ is a 4x4 transformation matrix.

In the designed software for data analysis, the transformation matrices T_{MG1}, T_{MG2}, T_{MA1} and T_{MA2} are all calculated using the above method with $\boldsymbol{p}$ and $\boldsymbol{q}$ defined as the following:

- When calculating the transformation matrix T_{MG1}, the coordinate values of the three positions on the measured marker cluster in the measured marker cluster coordinate system (MCS_1) are defined as $\boldsymbol{p}$; the coordinate values of the same three positions in the GCS were defined as $\boldsymbol{q}$; then $\boldsymbol{p}$ = {1 0 0 0 1 0 0 0 1}, and $\boldsymbol{q}$ = {$\text{origin}_{M1,G}$ + X' $\text{origin}_{M1,G}$ +Y' $\text{origin}_{M1,G}$ + Z'}. Where the $\text{origin}_{M1,G}$ is the coordinates of the MCS1 origin in the GCS, and X, Y and Z are the unit axes vectors. After $\boldsymbol{p}$ and $\boldsymbol{q}$ have been determined, method of Soderkvist and Wedin (1997) is used to calculate the transformation matrix T_{MG1}. Likewise, the method is used to calculate the T_{MG2}.

- When calculating the transformation matrix T_{MA1}, the coordinate values of the three positions on the measured marker cluster in the MCS_1 were defined as ***p***, the coordinate values of the same three positions in the ACS were defined by ***q***, then ***p*** = {1 0 0 0 1 0 0 0 1}, ***q*** = {$origin_{M,A}$ + X' $origin_{M,A}$ +Y' $origin_{M,A}$ + Z'}. Where $origin_{M,A}$ is the coordinates of the MCS_1origin in the ACS and *X, Y* and *Z* were the unit axis vectors. The method of calculations *X, Y* and *Z* are similarly introduced in the above section of the ACS establishing. Likewise, the method was used to calculate T_{MA2}.

The relative tooth movements are determined by the equation 4.1, which is $T=T_{MA1}*T_{GM1}*inv(T_{GM2})*inv(T_{MA2})$. The relationship of equation 4.1 can also be described in Figure 4.9.

Using the transformation matrix ***T***, the rotation angles about *x, y* and *z* directions and the translations in *x, y* and *z* directions are calculated according to the Grood and Suntay (1983) analysis method. The detail software, how to calculate the rotation angle and translation in the 6DOF from the ***T***, is described in Appendix C.

4.4 Method of evaluation of the data analysis software

The data analysis software calculates the results in 6DOF from the data captured by the infrared motion cameras. The accuracy, repeatability and noise of the Qualisys motion capture system have been evaluated in Chapter 3. However the accuracy of the data analysis software has not been evaluated before. In fact, the results of 6DOF in measuring tooth movement present the total accuracy of the Qaulisys motion capture system and the designed software. Thus, it is valuable to evaluate the overall system characteristics in measuring tooth movement.

A 3D metric translation stage with resolution of 10µm and a rotary stage with a graduation of 1.2′ were used as the standard of movement to generate the translation and rotation in *x*, *y*, and *z* axes respectively, as shown in Figure 4.15 Two marker clusters were separately fixed on the stages as the measured markers and a static object as the reference markers.

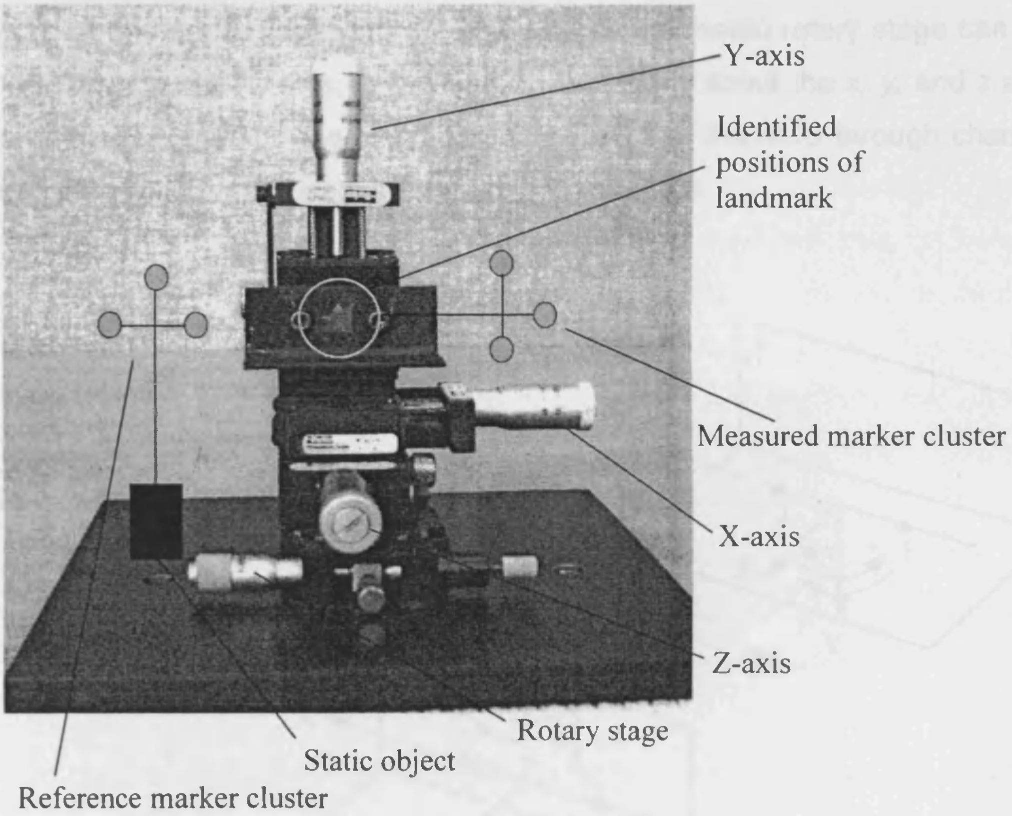

Figure 4.15 A 3D metric translation stages and a rotary stage to generate the translation and the rotation in *x*, *y*, and *z* axes.

For simulation of the translations in *x*, *y* and *z* axes, the 3D metric translation stage was moved continually using a step of 50 µm in the range of 0 - 300 µm to step up and step down. During the stage movement, the motion capture system captured the states of two marker clusters. In a period of measurement, all 13 points were captured with step up and step down. Every sampled point took 10s at the MCUs sampling frequency 60Hz and 600 frames were obtained for each measured point. The translation experiments were carried out in the *x*, *y*, and *z* axes, and were repeated 10 times under different light intensity and environmental temperature.

For simulation of the rotations about the *x*, *y* and *z* axes, the metric rotary stage was used to produce a varying angle. Because the metric rotary stage can only be rotated about the *y*-axis, to evaluate the rotations about the *x*, *y*, and *z* axes, the method of re-identifying directions of the axes of the ACS through changing landmark position were used, as shown in Figure 4.16

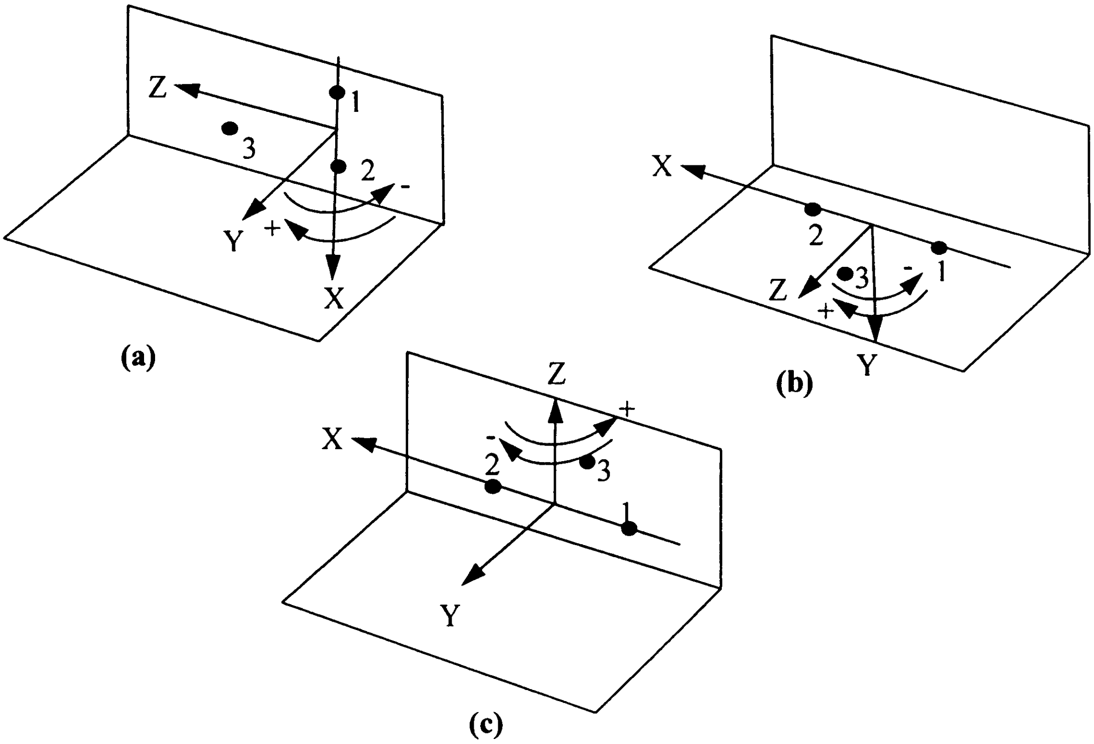

Figure 4.16 The 3D coordinate systems using pre-determined anatomical landmarks. (a) The landmark positions for the rotation about the *x*-axis, (b) The landmark positions for the rotation about the y-axis, (c) The landmark positions for the rotation about the z-axis.

The metric rotary stage was moved in steps of 0.5° in the range of 0° - 2.5° to increase the angle and then to decrease the angle. During movement of the rotary stage, the motion capture system captured the states of two marker clusters. In a period of measurement, all 9 points were captured as the angle was increased and decreased. Every sampled point took 10s at the system sampling frequency 60Hz and 600 frames were obtained for each measured point. The rotation experiments were carried out about the *x, y* and *z* axes, and were repeated 10 times under the different light intensity and environmental temperature.

An important thing in the evaluation was that the *x, y, z* directions of the ACS, which were determined by the landmarks in the designed software, and realized the *x, y, z* directions of the ACS by metric stages, must be in complete agreement. This is means the position of the landmarks can not be randomly identified. For evaluation of the translation in the *x, y, z* directions, the landmark positions were shown in Figure 4.16(b). For evaluation of the rotation about the *x, y z* directions, the landmark positions were shown in Figure 4.16(a), (b) and (c). To ensure the *x, y, z* direction of the ACS were completely parallel with the *x, y, z* directions of the metric stage, red marks were placed on the metric stages to determine the positions of the landmarks, shown in Figure 4.15 as circular areas.

The method of definitions and calculations of the overall system characteristics was the same as the method introduced in Chapter 3.

4.5 Results

The results given by the data analysis software are shown in Figure 4.17 (a), (b), (c), (d), (e) and (f). For the rotation measurements, the range of measurements was from 0 – 2.5°. For the translation measurements, the range of measurement was from 0 - 300μm.

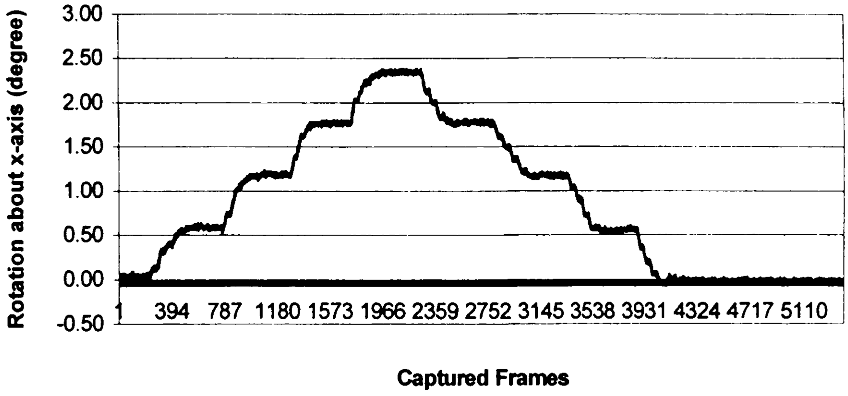
Rotation about x-axis (degree)
3.00
2.50
2.00
1.50
1.00
0.50
0.00
-0.50
1 394 787 1180 1573 1966 2359 2752 3145 3538 3931 4324 4717 5110
Captured Frames

(a)

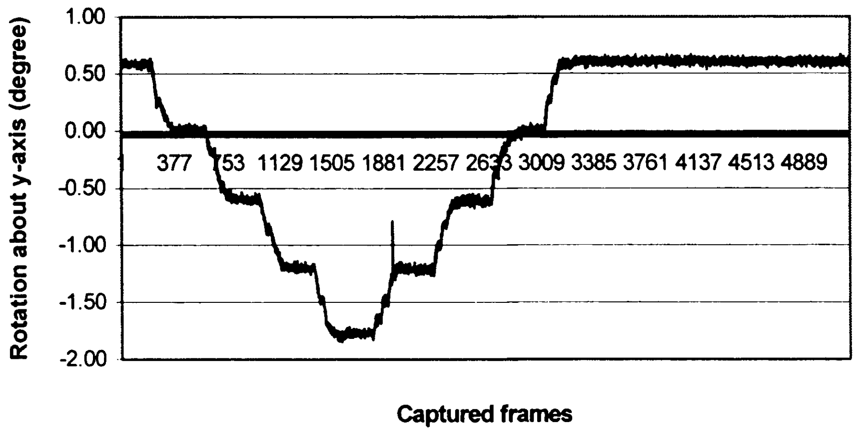
Rotation about y-axis (degree)
1.00
0.50
0.00
-0.50
-1.00
-1.50
-2.00
1 377 53 1129 1505 1881 2257 26 3 3009 3385 3761 4137 4513 4889
Captured frames

(b)

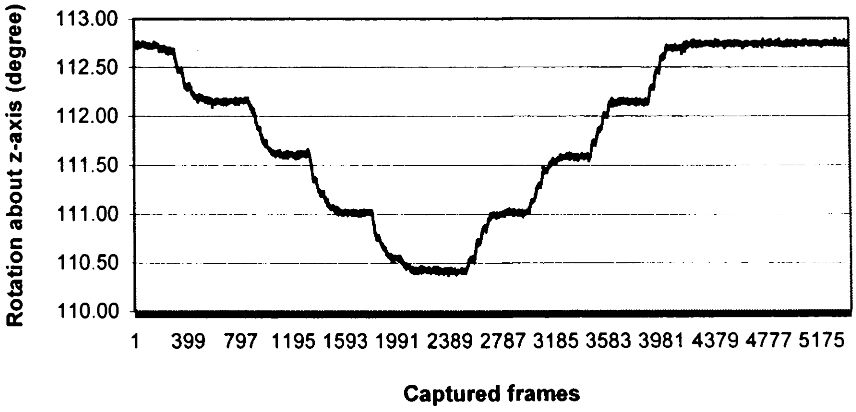
Rotation about z-axis (degree)
113.00
112.50
112.00
111.50
111.00
110.50
110.00
1 399 797 1195 1593 1991 2389 2787 3185 3583 3981 4379 4777 5175
Captured frames

(c)

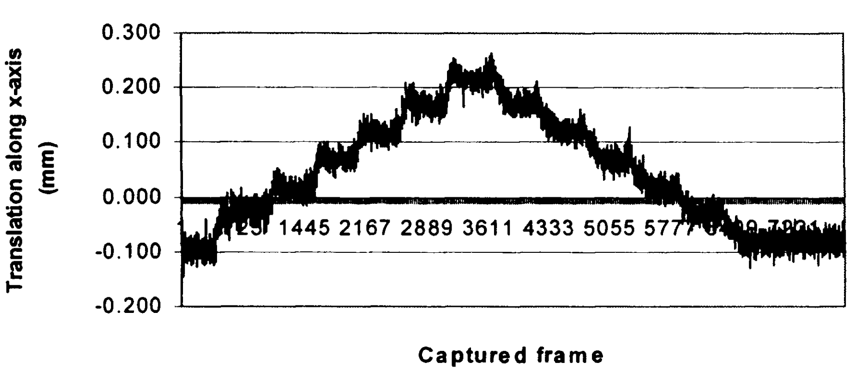

(d)

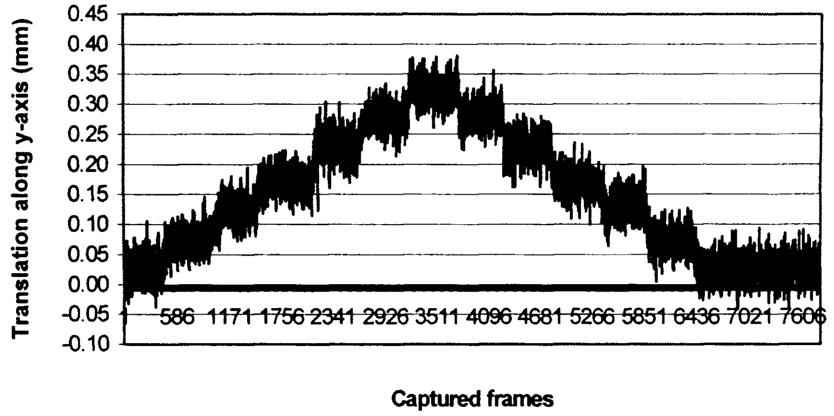

(e)

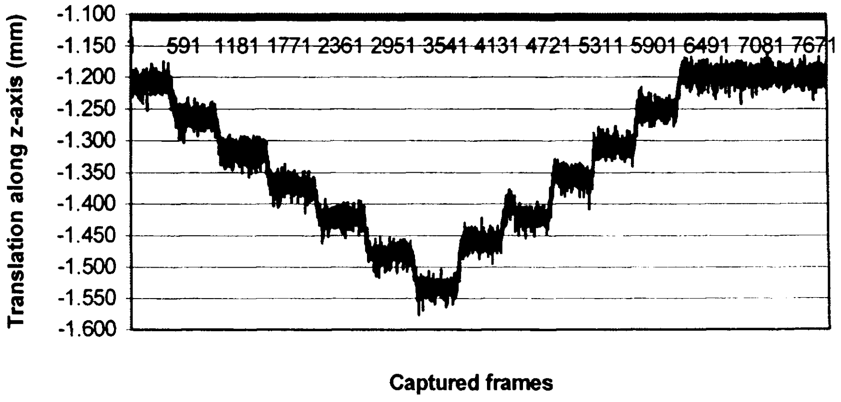

(f)

Figure 4.17 The results generated with the metric stage and software. (a), (b) (c) were the rotations about the *x*, *y*, *z* axes; (d), (e), (f) were the translations along the *x*, *y*, *z* axes.

Graphs showing the average of 10 repeated measurements are displayed in Figure 4.18 (a), (b), (c), (d), (e) and (f).

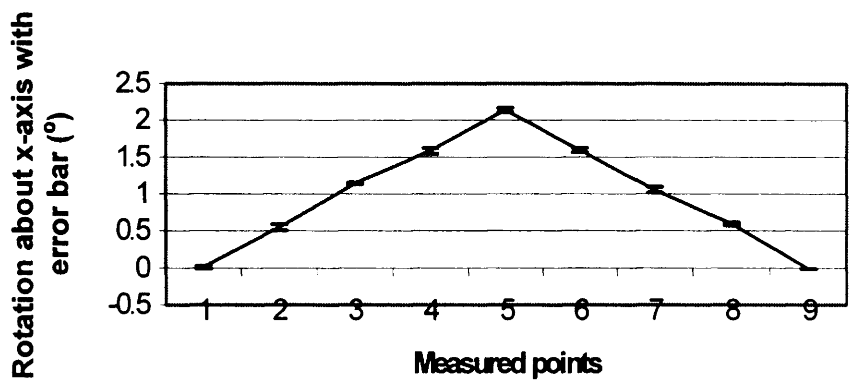

(a)

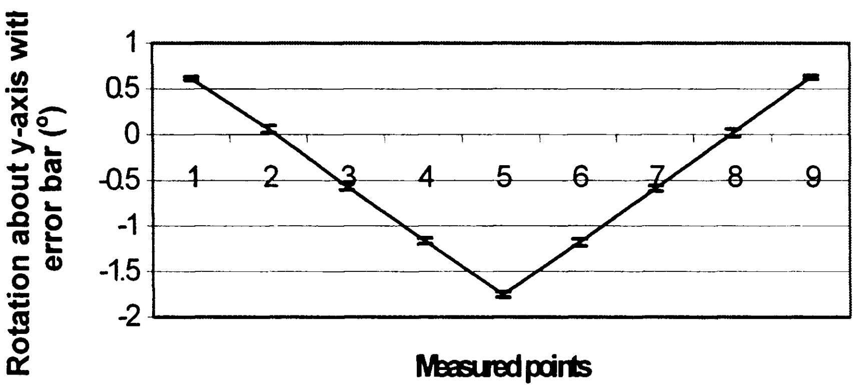

(b)

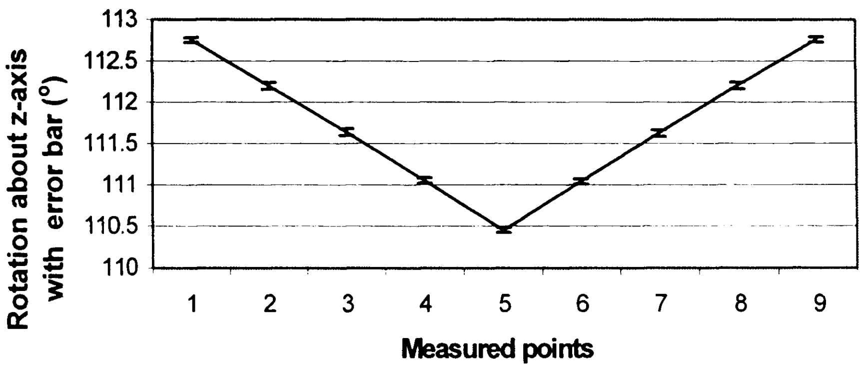

(c)

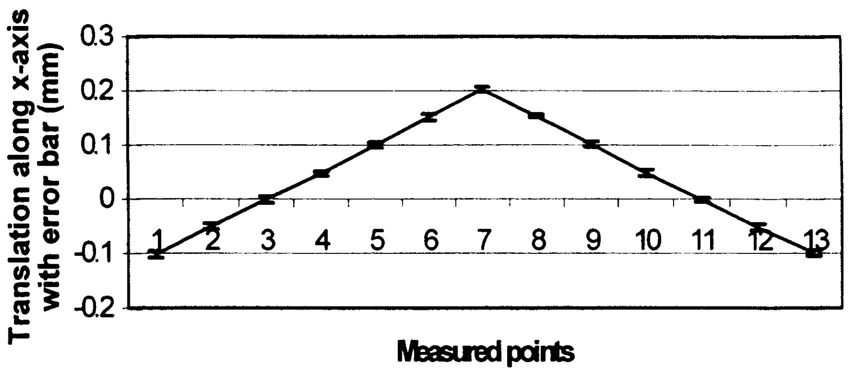

(d)

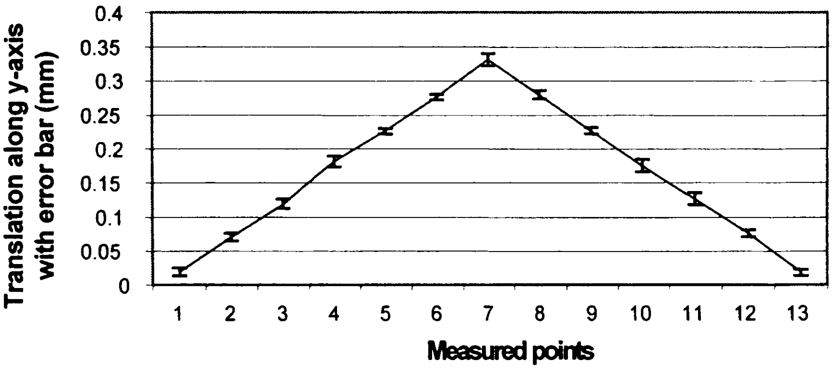

(e)

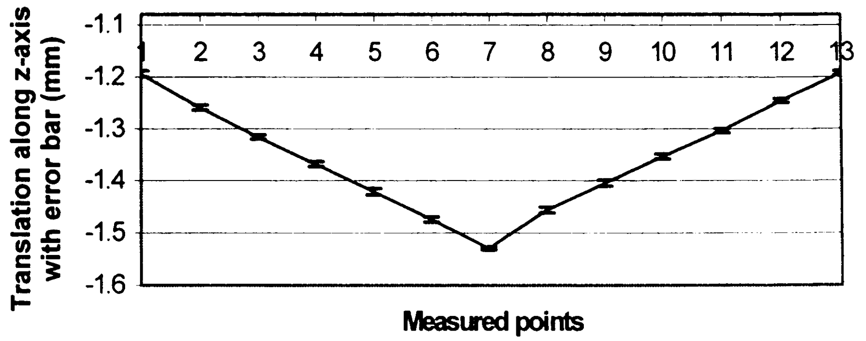

(f)

Figure 4.18 The results, showing the average of 10 repeated measurements, with error bars showing the standard deviation. (a), (b), (c) show the rotations about the *x*, *y*, *z* axes; (d), (e), (f) show the translations along the *x*, *y*, *z* axes.

Table 4.1 shows the maximum and minimum errors of rotation and translation in 10 repeated measurements with the rotation measurement range from 0 – 2.5°, and the translation measurement range from 0 - 300μm.

Table 4.1 The maximum and minimum errors of the rotation and the translation in 10 repeated measurements.

	X-axis rotation	Y-axis rotation	Z-axis rotation	X-axis translation	Y-axis translation	Z-axis translation
Error	(°)			(mm)		
Maximum error	0.08	0.06	0.06	0.016	0.023	0.012
Minimum error	-0.07	-0.07	-0.05	-0.012	-0.021	-0.014

From Table 4.1, the overall accuracy of the motion capture system in the rotation range from 0 – 2.5° and the translation range from 0 - 300μm was calculated and is shown in Figure 4.29. The accuracy is defined as the maximum absolute error divided by the measurement range.

The repeatability of the system in 10 repeated measurements is shown in Table 4.2 for the range of rotation from 0 – 2.5° and translation from 0 - 300μm. The maximum standard deviation in 10 repeated measurements was defined as the system repeatability, as shown in Figure 4.20.

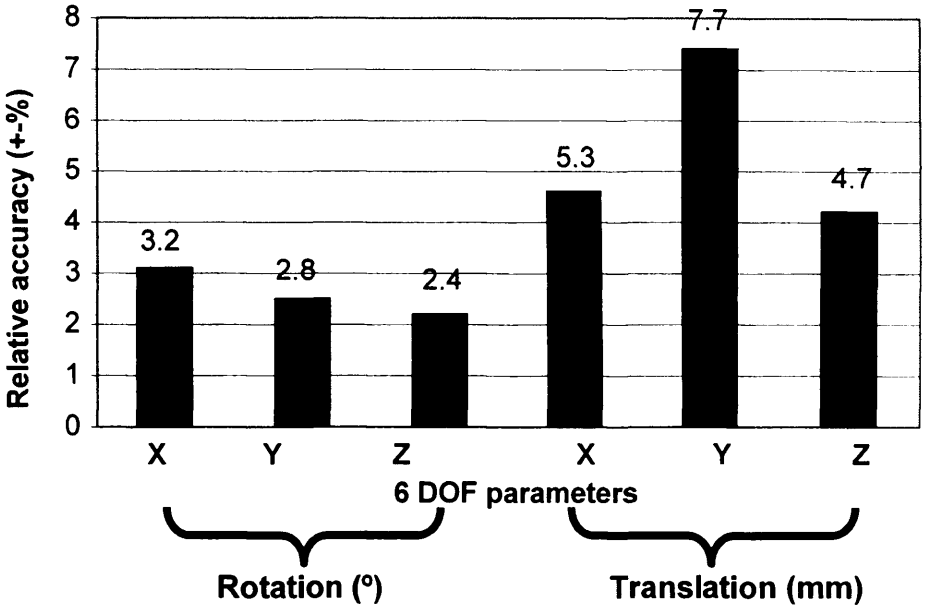

Figure 4.19 The accuracy of the system in the rotation range from 0 - 2.5° and the translation range from 0 - 300μm.

Table 4.2 The repeatability of the system, using measurements repeated 10 times with the range of rotation from 0 - 2.5° and translation from 0 - 300μm.

6DOF	X-axis rotation	Y-axis rotation	Z-axis rotation	X-axis translation	Y-axis translation	Z-axis translation
Measurement	(°)			(mm)		
1	0.04	0.03	0.03	0.008	0.014	0.007
2	0.04	0.04	0.03	0.006	0.014	0.004
3	0.03	0.03	0.02	0.009	0.012	0.006
4	0.04	0.04	0.03	0.006	0.008	0.004
5	0.03	0.02	0.02	0.008	0.007	0.004
6	0.05	0.02	0.02	0.009	0.006	0.003
7	0.02	0.03	0.02	0.008	0.010	0.005
8	0.03	0.03	0.02	0.007	0.008	0.004
9	0.03	0.02	0.02	0.006	0.008	0.004
10	0.03	0.02	0.03	0.006	0.007	0.007

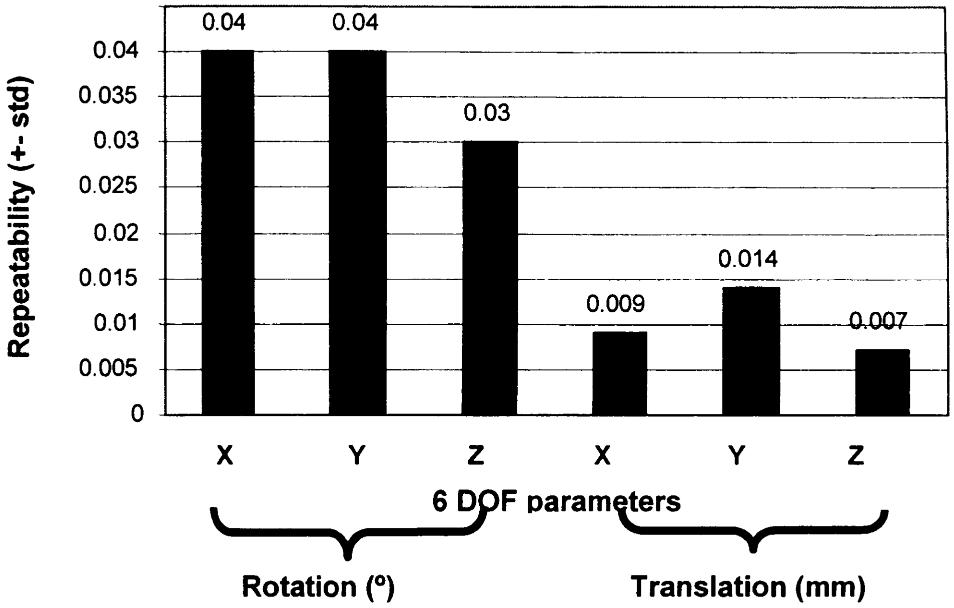

Figure 4.20 The repeatability of the system in the rotation range from 0 - 2.5° and the translation range from 0 - 300μm.

4.6 Discussion

From the measurement results, it is seen that the starting point in each of the measurements was not exactly the same; some graphs describe the movements from the increasing to the decreasing; and some graphs describe the opposite. The results raise a number of questions:

- Why were the step accuracy used to evaluate the system characteristics?
- Why was the starting point not at zero for some graphs in the results?
- Why did the directions of some movement not follow the variation from increasing to decreasing?

All the questions are discussed in this section.

In the evaluation of the system characteristics, the step accuracy and repeatability were calculated. This is because the starting point in each of the measurements, given by the metric stage, was not exactly the same; so errors can be created due to the mechanical system (metric stage) unrepeatability. Therefore, accuracy of the measured point can not express the system characteristics. But the step in each of the measurements given by the metric stage should be the same, except for unavoidable manual adjusting error of the metric stage. Thus accuracy and repeatability of the measured step can correctly demonstrate accuracy and repeatability of the overall system.

Although the measured marker cluster and reference marker cluster have the same coordinate origin in the ACS before the measurements, the two marker clusters were not coincident at the starting state. There was a starting angle and translation existing between the measured marker cluster and reference marker cluster. Therefore, the starting points in Figure 4.18 were not zero.

In the system evaluation, there are two coordinate systems. One was the metric stage coordinate system; another was the anatomical coordinate system. In the measurement of translation, if the directions of movement of the metric stage were the same as the ACS directions identified by the data analysis software, the movement graphs in the evaluation displayed an increase from the start point, and then a decrease. If the direction of movement of the metric stage was opposite to the ACS direction identified by the data analysis software, the movement graphs in the evaluation displayed a decrease from the start point, and then an increase. In the rotation measurement, the rotation direction is defined as if the thumb of the right hand is pointed in the direction of vector, the positive direction of rotation is given by the curl of the fingers (Cartesian coordinate system, Baker, 1998).

Teeth are a complex and irregular shape, it is difficult to define landmarks that correspond to the axes of the tooth, and are difficult to locate accurately and repeatably. If the width of a tooth is 5mm, and the location defined for landmarks 1 or 2 in Figure 4.2 has a location error of ±0.5mm (Figure 4.21). Then the error will produce a rotation of α = 11° between the ideal ACS and the actual ACS. The results are produced relative to the actual ACS, and are used for analysing the properties of the PDL. The rotation of the ACS may affect the analysis of the properties of the PDL, and thus affect the reliability of the FE model of the PDL. Thus the accuracy of landmark location is important problem. Further study is needed.

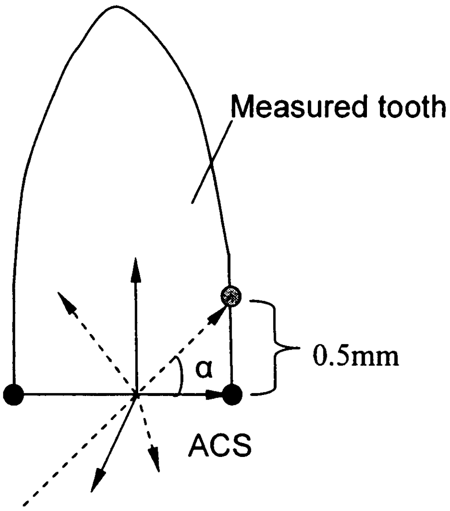

Figure 4.21 The ACS rotation produced by the location error of a landmark

However, the evaluation results of the overall system demonstrated that the motion capture system and the data analysis software are sufficient for measuring micro-scale movement, such as tooth movement. This is because the previous results of tooth measurement showed that when 0.5 N force was loaded to the tooth in the lingual direction, the range of tooth movement was from 12μm -132μm (Hickman, 1997).

Chapter 5 Design of mechanical loading devices

5.1 Introduction

With teeth masticating, the chewing force produces teeth movements of intrusion, extrusion, tipping and rotation. In fact, teeth movements relate to the PDL. Under load, by both forces and moments, teeth movements are governed by the material properties of the PDL. In a system of measuring tooth movements, a loading device is needed to produce load on the measured tooth. In previous studies, many loading methods were designed and used, such as air pressure loading on the human tooth (Jones et al., 2001b), spring loading with aluminium thread plate (Dorow et al., 2002c), magnetic loading on a cast of the teeth (Yoshida et al., 2000), spring loading with a sliding bar on the teeth of a dog (Von Böhl et al., 2004), and elastic archwire (orthodontic bracket) with sensor and rigid frame on the human tooth (Friedrich et al., 1999). Those methods have been introduced in Chapter 2. In this chapter, suggestions for new loading methods are presented. The design requirements in this study were:

- The loading device should produce five loading types: lingual and buccal load, intrusive and extrusive load, twisting load.
- The loading device should produce the maximum load of 1N with accuracy of 1%.
- The loading device does not allow producing an overload.
- The device must be electric safety in a clinical experiment.
- The loading head should be changeable for the hygienic reason.

According to the design requirements, these designed loading methods by author could produce five loading types, and load range from 0 - 5N according to the selected force sensor. These methods are compared each other and evaluated in twelve areas. The loading heads were designed as well. Material selection, analysis and size calculation of the structure are also presented in this chapter.

5.2 Concept designs

5.2.1 Method of overhang loading

The overhang-loading device consists of a support stand, loading beams and pulleys. The profile size designed is approximately 400 x 300 x 600mm, as shown in Figure 5.1. This system can produce load in the lingual and buccal directions, intrusion and extrusion, and twisting. The force is created in two ways: (1) using dead weights acting on the system, (2) using a solenoid or DC motor with an electrical control system. Figure 5.1 presents using dead weights to create force. When the weight is applied to the end of pulley 4 or 5, the loading beam on the right hand side will produce a force in the lingual or buccal directions. When weight is applied to the ends of pulley 6, the loading beam on the right hand side will produce load of intrusion and extrusion. When weight was applied to the end of pulley 3 and 4 at the same time, both loading beams on the left hand side and the right hand side work at the same time, and produce a twisting load. For Figure 5.1, the sensor is used for the actuator which is solenoid or DC motor. The loading spring in Figure 5.1 had two functions: (1) to ensure the loading beam is acting on the tooth in the unload state, (2) to produce a spring force on the tooth.

The system of overhang loading has the following features:

- Structure: flexible, capable of producing multi-loads;
- Complexity: simple for using weight, complex for using solenoid because the support stands are required to fix the solenoids;
- Reliability: middle, depends on the reliability of the hanging wire;
- Operation: easier for using weights than for using a solenoid;
- Cost: when using weight about £550, when using solenoids about £3000.

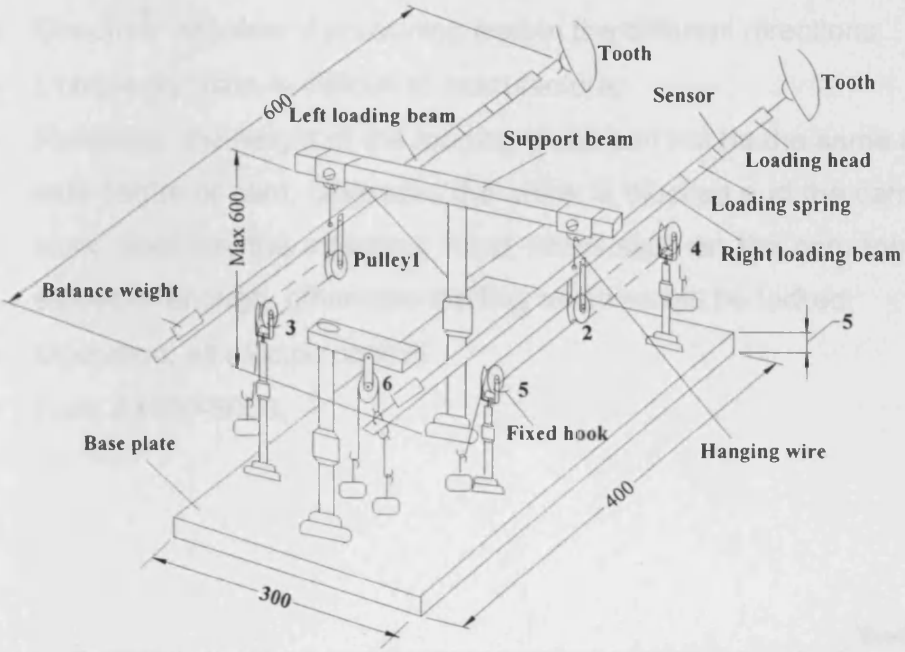

Figure 5.1 Overhang Loading Method.

5.2.2 Method of cam loading

A cam loading method is shown in Figure 5.2. The system consists of the cam, support stand, guide, loading beams, sensor and actuator (solenoid). The profile size was approximately 600 x 80 x 650mm. The system can produce load in the lingual and buccal directions, and intrusion and extrusion. The load is produced by the solenoids. The pull and push of the solenoids creates the movement of the loading crank, as a step towards to bring the cam rotation. Because one end of the loading beam is acted on the incline of the cam through the reset spring, so the cam rotation will bring the loading beam to move along the incline of the cam, and produce load in the lingual and buccal directions, and intrusion and extrusion.

The cam loading system has the following features:

- Structure: capable of producing load in the different directions;
- Complexity: cam is difficult to manufacture;
- Reliability: the height of the loading crank can not be the same level as the axle centre of cam, otherwise the crank is blocked and the cam would not work. Besides, the attaching head which slips on the cam tooth must be smoothly enough, otherwise loading beam would be locked;
- Operation: all electric control.
- Cost: £4500-5000.

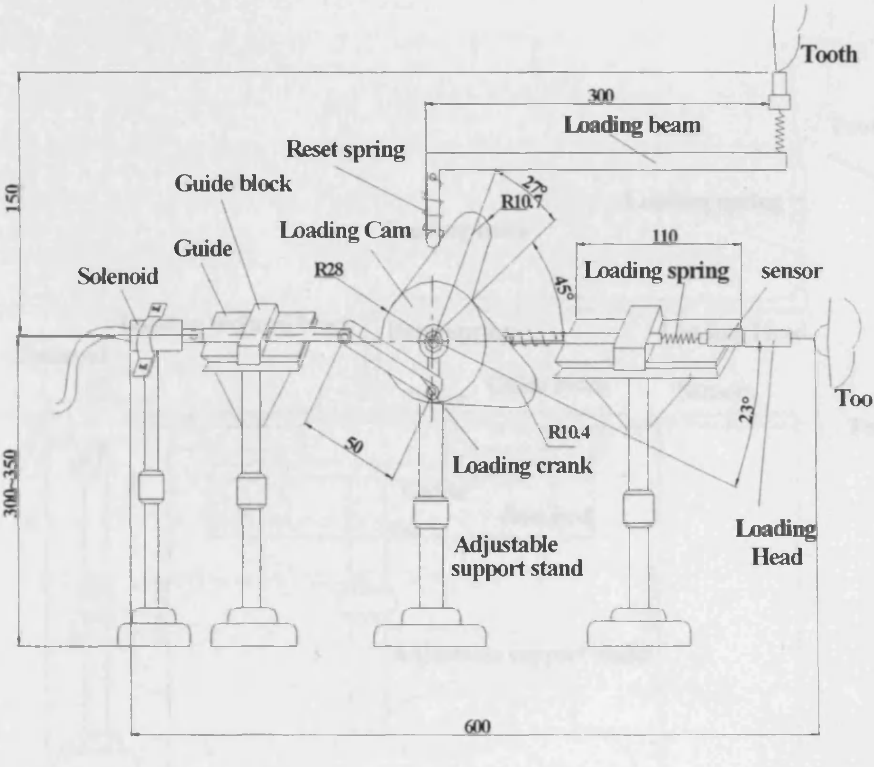

Figure 5.2 The Cam loading method

5.2.3 Method of Inclined block loading

Inclined block loading is shown in Figure 5.3. The system consists of the inclined block, support stand, guide, loading beams, sensor and solenoid. The profile size was approximately 650 x 75 x 550mm. This system could produce load in the lingual and buccal directions, and intrusion and extrusion. The load was produced by solenoids. When the solenoid worked in the functions of pull and push, it brought the movement of the guide block and the inclined block, as a step towards to produce load in the lingual and buccal directions and intrusion and extrusion.

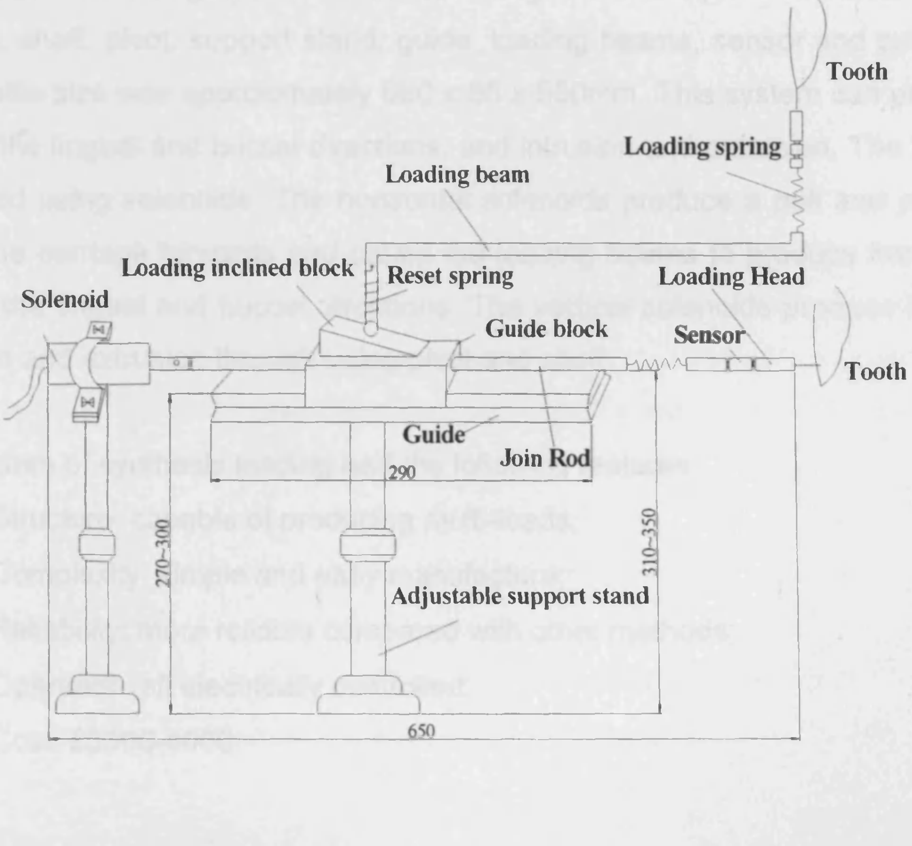

Figure 5.3 The inclined block loading system.

The system of Inclined block loading has the following features:

- Structure: capable of producing multi-loads.
- Complexity: reset spring and the frame are needed to ensure the loading beam can be stable and movable on the incline block;
- Reliability: stability of the loading beam, which produced load of intrusion and extrusion, was difficult to ensure if the structure was simple;
- Operation: all electrically controlled;
- Cost: £3000-3500.

5.2.4 Method of synthesis loading

The synthesis loading system is shown in Fig.5.4. The system consists of the bearing, shaft, pivot, support stand, guide, loading beams, sensor and solenoid. The profile size was approximately 680 x 65 x 550mm. This system can produce load in the lingual and buccal directions, and intrusion and extrusion. The load is produced using solenoids. The horizontal solenoids produce a pull and push to move the carriage forwards and cause the loading beams to produce horizontal load in the lingual and buccal directions. The vertical solenoids produce load of intrusion and extrusion through using pivot and shaft.

The system of synthesis loading had the following features:

- Structure: capable of producing multi-loads;
- Complexity: simple and easy manufacture;
- Reliability: more reliable compared with other methods;
- Operation: all electrically controlled;
- Cost: £3500-4000.

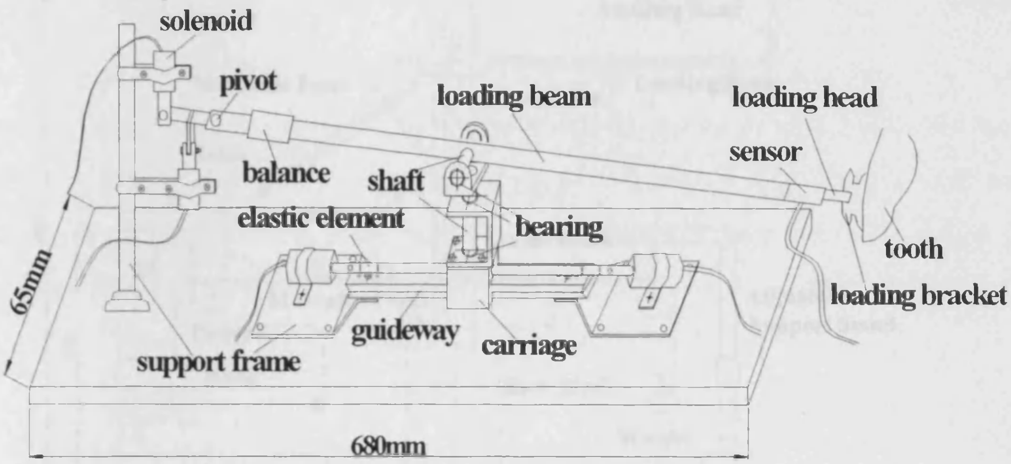

Figure 5.4 The synthesis loading method

5.2.5 Method of pitman loading

The pitman loading system is shown in Figure 5.5 (a) and (b). The system consists of two parts. Each of parts consisted of a pitman, loading beam, guide, weight and support stand. The profile size was approximately 600 x 70 x 450mm. The first part produces loads of intrusion and extrusion, whilst the 2nd part of the system produces loads in the lingual and buccal directions. The load is created by weights.

The system of pitman loading had the following features:

- Structure: capable of creating multi-loads;
- Complexity: require smooth both of sideway and movable point;
- Reliability: the loading beam should be strong enough in the vertical direction;
- Operation: weight loading;
- Cost: £1000-1500.

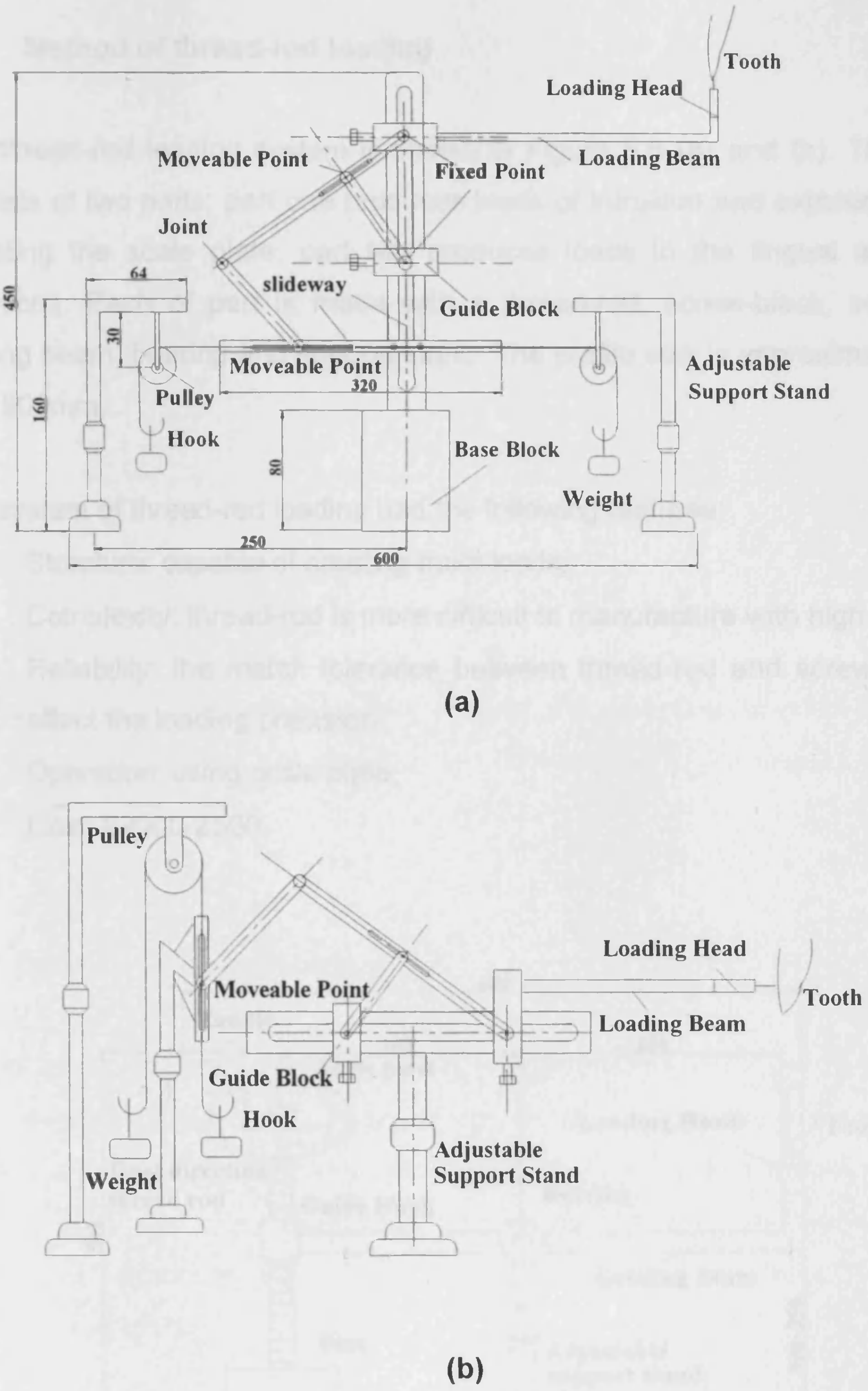

Figure 5.5 The pitman loading system. (a) part one to create loads in intrusion and extrusion, (b) part two to create loads in the lingual and buccal directions.

5.2.6 Method of thread-rod loading

The thread-rod loading system is shown in Figure 5.6 (a) and (b). The system consists of two parts: part one produces loads of intrusion and extrusion through adjusting the scale plate; part two produces loads in the lingual and buccal directions. Each of part is made with a thread-rod, screw-block, scale plate, loading beam, bearing and support stand. The profile size is approximately 600 x 70 x 500mm.

The system of thread-rod loading had the following features:

- Structure: capable of creating multi-loads;
- Complexity: thread-rod is more difficult to manufacture with high precision;
- Reliability: the match tolerance between thread-rod and screw-block will affect the loading precision;
- Operation: using scale plate;
- Cost: £2000-2500.

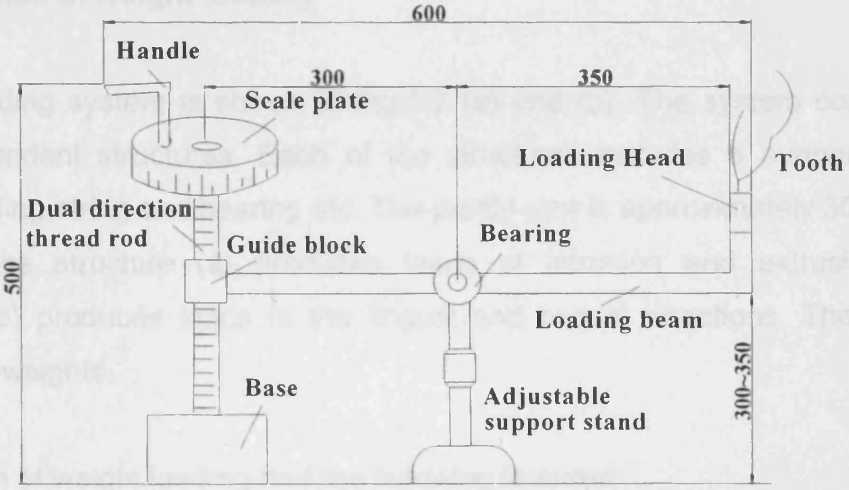

(a)

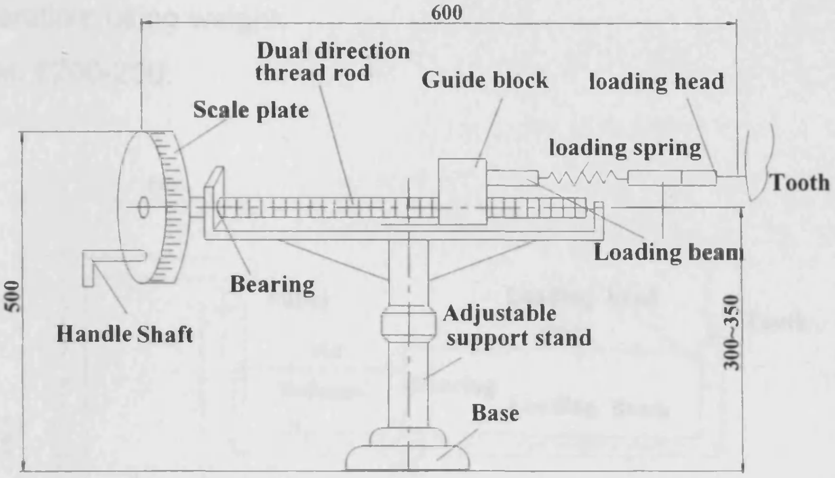

(b)

Figure 5.6 The thread-rod loading system. (a) part one to produce load of intrusion and extrusion, (b) part two to produce load in the lingual and buccal directions.

5.2.7 Method of weight loading

Weight loading system is shown in Fig.5.7 (a) and (b). The system consists of two independent structures. Each of the structures includes a support stand, pulley, loading string and bearing etc. The profile size is approximately 309 x 55 x 190mm. The structure (a) produces loads of intrusion and extrusion. The structure (b) produces loads in the lingual and buccal directions. The load is created by weights.

The system of weight loading had the following features:

- Structure: capable of creating load of intrusion, extrusion and lingual load;
- Complexity: simple;

- Reliability: reliable;
- Operation: using weight;
- Cost: £200-250.

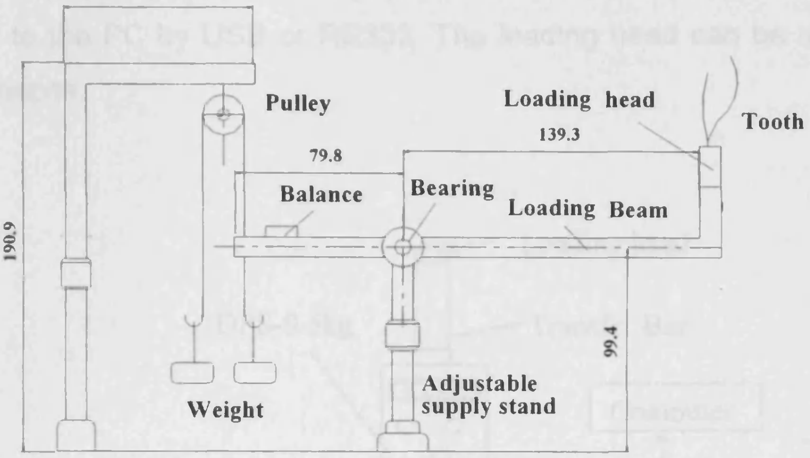

(a)

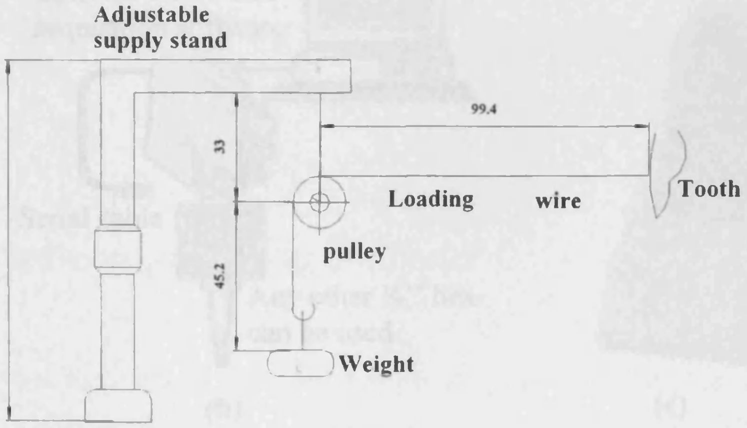

(b)

Figure 5.7 The weight loading. (a) part one to produce load of intrusion and extrusion, (b) part two to produce load in the lingual direction.

5.2.8 Method of Instrument loading

The torque screwdriver DSD-4kg and Push/pull force gauge DPS-0.5kg or FB-1kg was chosen as the loading tool. The pictures of loading tools are shown in Figure 5.8 (a), (b) and (c). The equipment has a digital output which can be connected to the PC by USB or RS232. The loading head can be made to any required shapes.

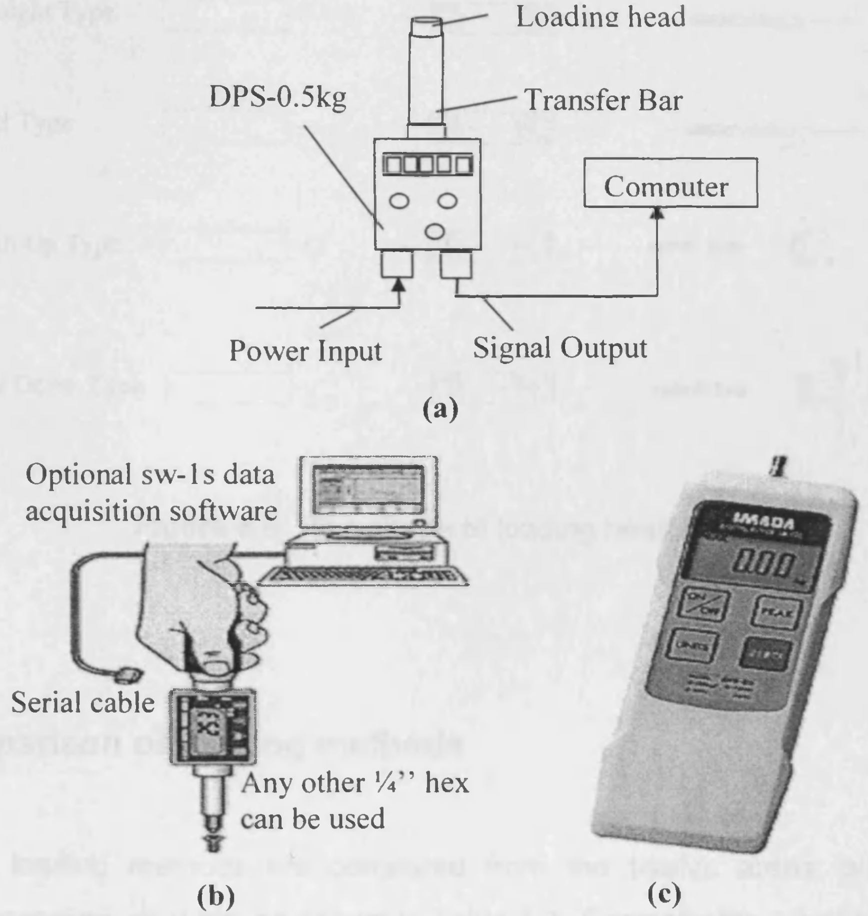

Figure 5.8 The Instrument loading. (a) block diagram, (b) torque screwdriver DSD-4kg, (c) force gauge DPS-0.5kg (supply by Electromatic Equipment Co., Inc.).

5.3 Design of the loading heads

The designs of the loading head shapes are shown in Figure 5.9. The straight type was used for producing load in the buccal direction. The pull type was used for producing load in the lingual direction. The push up type was used for producing load of intrusion and twisting. The pull down type was used for producing load of extrusion.

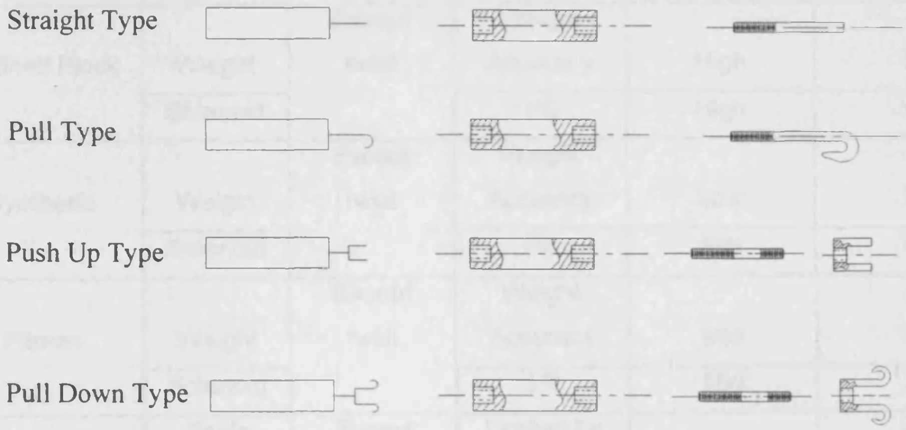

Figure 5.9 The shape of loading heads

5.4 Comparison of loading methods

The eight loading methods are compared from the twelve areas: structure, features, operation, cost etc, as shown in Table 5.1. Currently the weight loading method has been used in this study as it was easy to use and inexpensive. For future studies, the synthesis method is proposed to be used as the manufacturing process, because the control elements are most appropriate and relatively easy to realise.

Table 5.1 Comparison of loading methods

		1	2	3	4	5
	Methods	Loading Type	Loading Direction	Loading Accuracy	Mechanical Complexity	Computer Controllability
1	Overhang	Weight	All	Weight Accuracy	Low	No
		Solenoid		1%	Mid	Yes
2	Cam	Solenoid	Except twist	1%	High	Yes
3	Inclined Block	Weight	Except twist	Weight Accuracy	High	No
		Solenoid		1%	High	Yes
4	Synthesis	Weight	Except twist	Weight Accuracy	Low	No
		Solenoid		1%	Mid	Yes
5	Pitman	Weight	Except twist	Weight Accuracy	Mid	No
		Solenoid		1%	Mid	Yes
6	Thread Rod	Scale Plate	Except twist	Limited by thread	High	No
7	Weight	Weight	All	Weight Accuracy	Low	No
		Solenoid		1%	Mid	Yes
8	Instrumentation	Meter	All	Meter Accuracy	Low	No

To continue Table 5.1 Comparison of loading methods

	6	**7**	**8**	**9**	**10**	**11**	**12**
	Calibration Needed	Reliability	Easy Operating	Easy Clean End	Material	Size (mm)	Cost
1	Yes	Mid	Yes	Yes	Aluminium	400x300x600	£550~600
	Yes	Mid	No				£3000~3200
2	Yes	Low	No	Yes	Aluminium	600x80x650	£4500~5000
3	Yes	Low	Yes	Yes	Aluminium	650x75x550	£600~800
	Yes	Low	No				£3000~3500
4	Yes	Mid	Yes	Yes	Aluminium	680x65x550	£900~1300
	Yes	Mid	No				£3500~4000
5	Yes	Mid	Yes	Yes	Aluminium	600x70x450	£1000~1500
	Yes	Mid	No				£3200~3500
6	Yes	Mid	Yes	Yes	Steel	600x70x500	£2000~2500
7	Yes	High	Yes	Yes	Aluminium	307x55x190	£200~250
	Yes	High	No				£3000~3200
8	No	High	Yes	Yes	Steel		£850

5.5 Size calculation of loading beam

The ability of the loading beam to resist bending deformation is dependent on its size and material properties. The structure of the loading beam in the tooth loading system is represented in Figure 5.10.

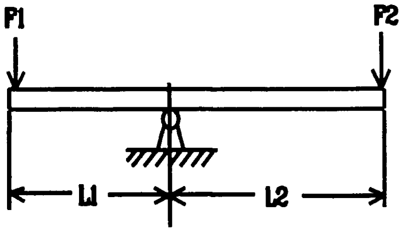

Figure 5.10 The tooth loading beam

F1 is produced by the loading weight and the balance, and F2 by the sensor and the loading head. According to law of equilibrium for a loaded beam, F1 is found from the following function:

$$F_1 \times L_1 = F_2 \times L_2 \qquad 5.1$$

$$F_1 = \frac{L_2}{L_1} \times F_2 \qquad 5.2$$

Therefore, value of the balance can be calculated from F_1 taking out value of weight. To analyse the beam deflection caused by F_2, the right hand side of the fulcrum of the loading beam (Figure 5.10) can be simply drawn, as shown in Figure 5.11.

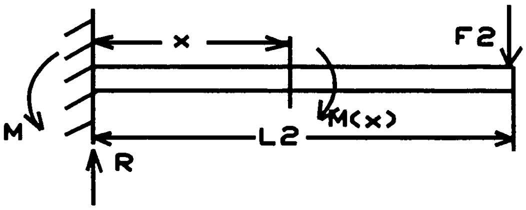

Figure 5.11 The right hand side of the fulcrum of the loading beam, produced from Figure 5.10

From Fig.5.11, the following functions can be formed according to the equilibrium condition of forces and moments:

$$R - F_2 = 0, \qquad M - F_2 \times L_2 = 0 \qquad 5.3$$

That is

$$R = F_2, \qquad M = F_2 \times L_2 \tag{5.4}$$

At any point x on the beam, the bending moment is

$$M(x) = Rx - M \tag{5.5}$$

$$M(x) = F_2 \times x - F_2 \times L_2 = F_2(x - L_2) \qquad 0 < x \le L_2 \tag{5.6}$$

Substituting equation 5.6 into the equation of a small deflection $\frac{d^2y}{dx^2} = \frac{M}{EI}$ (Burr 1981), (where *M* is the bending moment of the beam, and *EI* is the flexural stiffness of the beam), the bending equation of a small deflection can be rewritten as:

$$\frac{d^2y}{dx^2} = \frac{F_2(x - L_2)}{EI} \tag{5.7}$$

And

$$\begin{aligned}\frac{dy}{dx} &= \int \frac{F_2(x - L_2)}{EI} dx \\ &= \frac{F_2}{2EI}(x - L_2)^2 + C_1\end{aligned} \tag{5.8}$$

Then

$$\begin{aligned}y &= \int \left[\frac{F_2}{2EI}(x - L_2)^2 + C_1 \right] dx \\ &= \frac{F_2}{6EI}(x - L_2)^3 + C_1 x + C_2\end{aligned} \tag{5.9}$$

Where y is the bending distance from the neutral axis, and C_1 and C_2 are two constants of integrating. According to the boundary condition, $x = 0,\ y = 0,\ \frac{dy}{dx} = 0,\ C_1 = -\frac{F_2 \times L_2^2}{2EI}$, and $C_2 = \frac{F_2 \times L_2^3}{6EI}$. At the end of beam, $x = L_2$, the bending distance y of the beam is at its maximum value, that is

$$y_{\max} = -\frac{F_2 \times L_2^3}{3EI} \qquad 5.10$$

In equation 5.10, the sign indicates the direction of the bending moment $M(x)$ which is opposite with the marked direction. For a solid beam, $I = \frac{\pi D^4}{64}$, (Polak, 1991). Substituting $I = \frac{\pi D^4}{64}$ into equation 5.10, the relationship between the beam diameters and the bending distance is:

$$D^4 = \frac{64 F_2 L_2^3}{3\pi E \times y_{\max}} \qquad 5.11$$

In the tooth loading system, $L_2 = 325mm$, $F_2 = 1.1N$, and $y_{\max} = 0.25mm$, then the beam diameter will be:

For the solid beam:

(1). Aluminium beam, $E = 70 \times 10^9\ {}^{N}\!/_{m^2}$

$$D^4 = \frac{64 \times 1.1 \times 0.325^3}{3 \times 3.14 \times 70 \times 10^9 \times 2.5 \times 10^{-4}} = 1.467 \times 10^{-8} m^4$$

$$D_{aluminium} = 11mm$$

(2). Stainless steel beam, $E = 200 \times 10^9 \, {}^{N}\!/_{m^2}$,

$$D^4 = \frac{64 \times 1.1 \times 0.325^3}{3 \times 3.14 \times 200 \times 10^9 \times 2.5 \times 10^{-4}} = 0.514 \times 10^{-8} m^4$$

$$D_{Stainlesssteel} = 8.5mm$$

For the tube beam, $I = \frac{\pi(D^4 - d^4)}{64}$, according to the equation 5.10, the relationship between the dimension and the bending distance of the beam will be

$$D^4 - d^4 = \frac{64 F_2 L_2^3}{3\pi E y_{\max}} \qquad 5.12$$

Assuming

$$\alpha = \frac{d}{D} \qquad 5.13$$

Then

$$D^4 = \frac{64 F_2 L_2^3}{3\pi E y_{\max}(1 - \alpha^4)} \qquad 5.14$$

Here the size of the tube beam was discussed with two kinds of materials for three different α values. Here, $L_2 = 325mm$, $F_2 = 1.1N$, $y_{\max} = 0.25mm$, using the equations 5.13 and 5.14, the size of tube beam was calculated with two different materials and three different α values (that is ratio of tube diameters of inside and outside), and is shown in Table 5.2.

Table 5.2 Size of tube beam with two different materials and three different α values.

Ratio of diameters of inside and outside	Material and size of tube beam			
	Aluminium $E = 70 \times 10^9 N/m^2$		Stainless steel $E = 200 \times 10^9 N/m^2$	
	Outside diameter (D) mm	Inside diameter (d) mm	Outside diameter (D) mm	Inside diameter (d) mm
$\alpha = 0.5$	11.1	5.55	8.6	4.3
$\alpha = 0.6$	11.4	6.84	8.7	5.2
$\alpha = 0.7$	11.8	8.26	9.02	6.32

5.6 Shaft

5.6.1 Shaft shape, material and structure design

Shape The shaft is an important part of the loading device. It performs the actions of rotation and swaying movement of the beam. There are different types of shaft, e.g., straight shaft, crankshaft etc. The straight shaft is divided into a spindle (a short shaft) and a transmission shaft. Generally the spindle bears a bending moment, but does not transmit torsion. The inner stress in the spindle shaft is a static bending stress. The transmission shaft bears torsion, but it does not take a bending moment. The inner stress in the transmission shaft is divided into a static shear stress and varying shear stress. In the tooth loading system, the spindle shaft was used to sway the loading beam.

Material The shaft material needs to satisfy the requirements of strength, rigidity and easy of manufacture. Normally the shafts are made from carbon steel and alloy steel. Here stainless steel was chosen as the shaft material. Table5.3 (Ashby, 1993) shows the mechanical properties of some metals.

Table 5.3 Mechanical properties of metal materials

Material	Properties			
	Yield Strength N/mm^2(MPa)	Tensile Strength N/mm^2(MPa)	Elongation % in 2 mm	Hardness BHN
Aluminum and Alloys	35	91	1.4	23
Steel, Low Alloy	351	527	1.1	170
Steel, High Carbon	632	984	0.8	201
Steel, Low Carbon	253	422	1.4	310
Steel,	527	829	0.9	200
Steel, Medium Carbon	365	612	0.9	170
Steel, Stainless	562	703	1.0	250

Structure design In the tooth loading system, the shaft (for synthesis loading system) was designed, as shown in Figure 5.12.

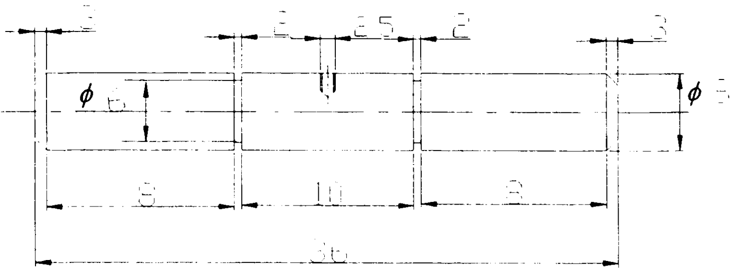

Figure 5.12 Shaft structure for the tooth loading device

In Figure 5.12, there are two securing grooves. The C-clips are fitted into the grooves to resist the relative movement between the loading beam and the shaft. On the top of the shaft, a threaded hole resists the relative rotation between the loading beam and the shaft.

5.6.2 Shaft size calculation

In the tooth loading system, the shaft carries mostly bending moment. Thus, torsion was ignored in the size calculation of the shaft, because it was very small. The shaft with load *F* is shown in Figure 5.13. *F* is the weight of total load on the loading beam.

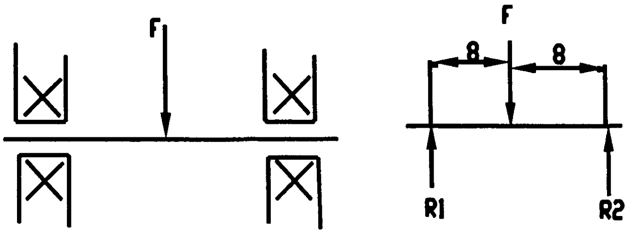

Figure 5.13 The tooth loading shaft with loads

The reaction forces *R1* and *R2* can be calculated using $\sum M = 0$. Taking moments about point R1 gives: $8F - 16R_2 = 0$, which implies that $R2 = \frac{F}{2}$. Taking moments about R2 gives $8F - 16R_1 = 0$, which implies that $R1 = \frac{F}{2}$. Substituting C_1 and C_2 into equation 5.9, the shaft deformation is given as:

$$y(x) = \frac{F}{6EI}(x - l)^3 - \frac{F l^2}{2EI}x + \frac{F l^3}{6EI} \qquad 5.15$$

Where F is the weight of total loading beam, and l = 8*mm*, x is the distance from arbitrary point to the end of fixed point. The maximum deformation of the shaft occurs at the point at which $y(x)'' = 0$.

$$y' = \frac{F}{2EI}(x-8)^2 - \frac{64F}{2EI} \qquad 5.16$$

$$y'' = \frac{F}{EI}(x-8) \qquad 5.17$$

From equation 5.17, it can be seen that the y_{max} occurs at the point of x = 8*mm* on the shaft. The maximum deformation of the shaft from equation 5.15 is given:

$$y_{\max} = -\frac{(8\times10^{-3})^3 F}{3EI} \qquad 5.18$$

Where the F is total weight, including balance weight W1, loading beam weight W2, loading head and sensor weight W3. The distribution of F is shown in Figure 5.14.

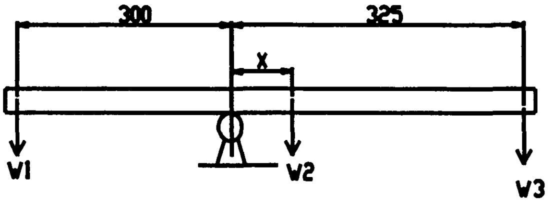

Figure 5.14 Load distributions on the loading beam

Here the aluminium beam has D = 10mm, $x = \frac{300+325}{2} - 300 = 12.5mm$, and $W_3 = 110g$,

$$W_2 = V\rho = \frac{\pi D^2 l}{4}\rho$$
$$= \frac{3.14 \times (10\times10^{-3})^2 \times 625\times10^{-3}}{4} \times 7860$$
$$= 386g$$

In a static situation,

$$W_1 = \frac{12.5W_2 + 325W_3}{300} = \frac{12.5\times386 + 325\times110}{300} = 130g$$

Therefore, $F = W_1 + W_2 + W_3 = (0.13+0.386+0.11)\times9.8 = 6.14N$. Steel's elastic modulus is $E = 200\times10^9 N/m^2$, if the diameter of the shaft is 4mm, then $I = \frac{\pi D^4}{64} = \frac{3.14\times(4\times10^{-3})^4}{64} = 0.126\times10^{-10}m^4$. Substituting F, E and I into the equation 5.16, the largest deflection of the shaft is:

$$y_{\max} = \frac{(8\times10^{-3})^3 \times 6.14}{3\times200\times10^9\times0.126\times10^{-10}} = 0.4\mu m$$

5.6.3 Strength proof

Equation 5.19 can be used to investigate whether the shaft bending strength is within the limits of the material tensile strength.

$$[\sigma] \ge \sigma_{\max} = \frac{32k_m M}{\pi D^3} \qquad 5.19$$

Equation 5.20 can be used to test whether the shaft shear strength is within the limits of the material shear strength.

$$[\tau] \geq \tau_{\max} = \frac{16k_sT}{\pi D^3} \qquad 5.20$$

In the tooth loading system, the shaft is considered to be a stationary shaft, and K_m and K_s are equal to 1 (Faires, 1965).

If the shaft diameter is 4mm, from equation 5.19 the maximum tensile strength of the shaft produced by the load *F* will be

$$\sigma_{\max} = \frac{32M}{\pi D^3} = \frac{32 \times 8 \times 6.14}{3.14 \times 4^3} = 7.82MPa \qquad 5.11$$

From Table 5.2, the limited tensile strength of medium carbon steel is 612$N/mm^2(MPa)$. Comparing the above $\sigma_{\max}$ with 612$N/mm^2(MPa)$, the value of $\sigma_{\max}$ is much less than the limited material tensile strength. Because the both ends of shaft were jointed with the ball bearings, so there was no torsion applied to the shaft. Therefore the 4mm diameter shaft is safety for the tooth loading system.

5.7 Mechanical parts selection

Bearing A miniature shielded bearing (MR104ZZ, SMB) was selected for the bearing in the loading system. The bearing has an outside diameter of 10mm and a width of 4mm. The maximum dynamic and static loads are 600N and 190N respectively.

Rail guide The rail guide in the loading system (MN7-205-G1-V1, Schneeberger) has length of 205mm, width of 7mm, 925N dynamic loading capacities and 1560N static loading capacities, and weights of 216.3 g/m.

Actuator Two kinds of actuators can be used to produce a force: solenoid and a DC linear motor. The structure, specification, work principle and selection of actuators will be presented in the next chapter.

In this chapter, the loading methods and loading heads have been designed. By comparing and analysing all loading methods, the synthesis loading method is chosen as the tooth loading method for future experiments. In the calculations of loading beam and shaft, the synthesis loading was used as a reference. The stress, strain, deformation of the loading beam and shaft were analysed. Materials and sizes of the loading beam and shaft were chosen and calculated. Mechanical parts in the loading system are selected. Using the synthesis method combined with the weight loading method, twisting loading can be realized.

Chapter 6 Control system circuit design

6.1 Introduction

The control system is used to control the loading device which applies a load to the measured tooth. This chapter presents the design methods of the control system, the sensor calibration, circuit system design, circuit experiments and the analysis in the area of electric techniques. Negative feedback was used in the control system to ensure accurate loading control.

6.2 Control system design

6.2.1 Control system block diagram

The control system block diagram is shown in Figure 6.1. The system consisted of control command, differential amplifier, proportional-integral-derivative (PID) control, pulse width modulator (PWM), power driver circuit, actuator, force sensor (loading cell) and sensor amplifier.

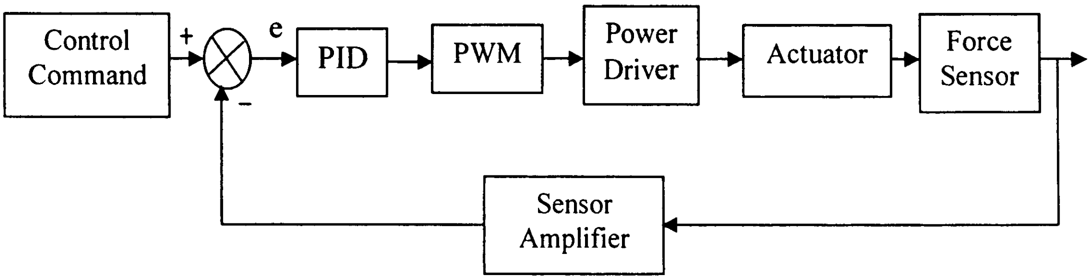

Figure 6.1 The block diagram of the control system

In Figure 6.1, the force sensor detects the load applied to the measured tooth, and produces an output signal to the sensor amplifier to be used as the feedback control signal. The control command given from the signal generator is compared with the output signal of the sensor amplifier at the comparator inputs. The error signal is produced by the comparator, and input to the PID control circuit. The PID circuit adjusts the error signal. If the error signal is positive, then the PID control circuit creates a relevant positive signal output. If the error signal is zero, then the PID circuit outputs zero. If the error signal is negative, then the PID circuit creates a negative signal output. The advantage of the PID control circuit is that it leaves no steady state error because an integral circuit is used. The output of the PID circuit is the input of the PWM circuit. The PWM circuit gives a control signal of the power switch drive circuit of the actuator. The output pulse width of the PWM circuit is adjusted according to the amplitude of the PID output signal, and controls the load (applied to the measured tooth) to be increased or decreased. The PWM output is the input of the power switch drive circuit of the actuator. A Metal Oxide Semiconductor Field Effect Transistor (MOSFET) is used to realize the power switch drive circuit of the actuator.

6.2.2 Components selection

Force sensor In the system for measuring tooth movement, the loading error is required to be $\pm 1\%$ of the loading range of 0.5N, i.e. the maximum error to be ±0.005N. Consequently a high accurate force sensor was selected. There are many companies to supply the force sensor, such as G S Sensors Ltd; Honeywell Control Systems Ltd; The Strain Gauging Co. Ltd.; Interface force measurements Ltd; Entran Company and FGPSensors & Instrumentation etc. Comparing the sensor's structure, size and characteristics of different companies, the SMT1-5N force sensor (SMT series, Interface) was chosen, because of its satisfying features:

- maximum range 5N;
- nonlinearity ±0.05% full scale (FS) (the maximum nonlinearity error is ±0.0025N);
- hysteresis ±0.03% FS (the maximum hysteresis error is ±0.0015N);
- nonrepeatability ±0.02% Rated Output (RO) (the maximum nonrepeatability is ±0.001N);
- creep in 20 minutes ±0.025% (the maximum creep in 20 minutes is ±0.00125N).

The rated output is also known as terminal output which is the mV/V output at the rated capacity. The SMT1-5N force sensor is shown in Figure 6.2.

Figure 6.2 The SMT1-5N load cells

Sensor amplifier From the manufacture's calibration for the force sensor, it is known that the output sensitivity of the force sensor is 1.83896(mv/V)/500g. Thus the output sensitivity with mass is 0.0368mv/g in supply voltage of 10V (Interface Company Technical Notes). The aim of the sensor amplifier is to amplify a smaller signal to a bigger to satisfy the requirements of the signal level of control system. Recently, National Semiconductor recommended a new instrumentation amplifier AD8230. AD8230 is a rail-to-rail, zero-drift, precision instrumentation amplifier. One of the applications of AD8230 is as a sensor amplifier, such as for thermocouples and load cells etc, because of its good characteristics: the minimum value of common mode rejection ratio (CMRR) is 110db at 60Hz; the gain of the amplifier is from 10 to 1000; the maximum offset voltage is 10μV at supply power ± 5V; the maximum temperature offset drift is $50nV/^0C$ and the maximum gain nonlinearity is 20ppm (parts per million). The CMRR is usually defined as the ability of a balanced input to reject the part of the incoming signal which has the same amplitude and phase on both input terminals, referenced to ground. The unit of CMRR is specified in dB.

Comparator The comparator is used to compare the control command with the output signal of the sensor amplifier, and outputs an error signal as an input signal of the PID control. The low-noise, precision operational amplifier OP27 was selected. OP27 is a low noise, precision operational amplifier whose characteristics can be compared with those of the AD8230, but cheaper than AD8230, and OP27 Package is the Dual In-line Package (DIP) that is easier use in breadboard than the Small Outline Integrated Circuit package (SOIC) of the AD8230. The OP27 has an excellent CMRR of 126db, an offset voltage of 10μV and an offset drift of $0.2\mu V/^0C$.

PID The OP27 was used in the PID control circuit because of its good characteristics.

PWM The PWM circuit provides a switch control signal, with an adjustable pulse width, to the switch drive circuit. The pulse width is varied according to the amplitude of the PID output signal. The PWM circuit consists of a triangle wave generator and a comparator. The output signal of the triangle wave generator is compared with the PID output signal at the input terminals of the comparator. Then the comparator outputs a pulse signal with a certain duty cycle that is dependent on the output amplitude of the PID. In the PWM circuit, the linearity feature of the triangle wave signal is important for accuracy of control loading. The precision waveform generator ICL8038 was selected. The ICL8038 features are: low frequency drift with temperature is 250ppm/°C; linearity of triangle wave output is 0.1%; frequency range is from 0.001Hz to 300 kHz; variable duty cycle is from 2% to 98% and high level outputs TTL to 28V.

Power driver The power driver is used to amplify the energy of the control signal as the actuator normally needs a larger current to drive. There are many elements can be chosen, for example, TIP 110 Darlington transistor, ZHB6718 SM-8 bipolar transistor H-bridge, ZXMHC6A07T8 complementary 60V enhancement mode MOSFET H-bridge, IRFZ34N power MOSFET, STP60NF06 power MOSFET etc. In the experiments, a TIP 110 was used to drive the solenoid, and a ZHB6718 was used to drive the linear motor.

Actuator The actuator is used to produce the load, controlled by the system control signal. There are two kinds of parts that can be used as an actuator: a solenoid and a DC linear motor, for example, SDT2039L tubular solenoid; and NCC05-11-011-1X DC linear motor etc. The main difference between the solenoid and the DC linear motor is that the solenoid has a stationary coil and a movable iron plunger, and a coil with current generates a magnetic field which attracts an iron plunger. For the NCC05-11-011-1X linear motor or LA-10-12-027A voice coil actuator, a stationary iron component and a permanent magnet replaces the iron plunger and a coil is movable, so the movable coil with current can be pushed or pulled depending on the current direction. Also these two linear motors, which generate approximately a force of 5N and stroke of 10mm with a coil, are different with typical linear motors which have multiple coils and a much larger range of force and a long stroke. However, in theory, the DC linear motor and the solenoid have a similar working principle. From Faraday's law of electromagnetic induction, if a conductor with current is placed in a permanent magnet field, the conductor will experience a Lorentz force and produce movement. The Lorentz force is proportional to the current applied to the coil (F=kBLIN).

Due to different structures between the DC motor and the solenoid, they have different advantages in application. For the solenoid, the advantage is that the control circuit is simpler, but it cannot produce bi-directional forces (pull and push) at the same plunger end. The advantage of the DC linear motor is that bi-directional movements can be produced by changing the direction of the current applied in the coil. But the control circuit is more complex to realize the bi-directional movements. To control the DC motor, a PWM system and H-bridge driver are commonly used (Chow et al., 2003; Dixon and Leal, 2002; Yedamale, 2004). In this study, the LA-10-12-027a voice coil actuator was chosen as the actuator. The features of LA-10-12-027a are: continuous force 4.8N; stroke ± 4.57mm; force sensitivity 5.56 N/AMP; DC resistance 11Ω.

6.2.3 Circuit design

Sensor amplifier circuit The functions of the output lines of the sensor are defined by the manufacturer and shown in Figure 6.3. The sensor power was supplied by the programmable precision voltage reference AD584, shown in Figure 6.4. The sensor amplifier circuit was designed by author as shown in Figure 6.5.

The amplifier gain was calculated according to the following equation:

$$Gain = 2(1+\frac{R_7}{R_8}) \qquad 6.1$$

The AD8230 accepts a maximum R_7 = 100kΩ, and R_8 = 200Ω. So the ideal gain that we designed is 1002 (G = 1002).

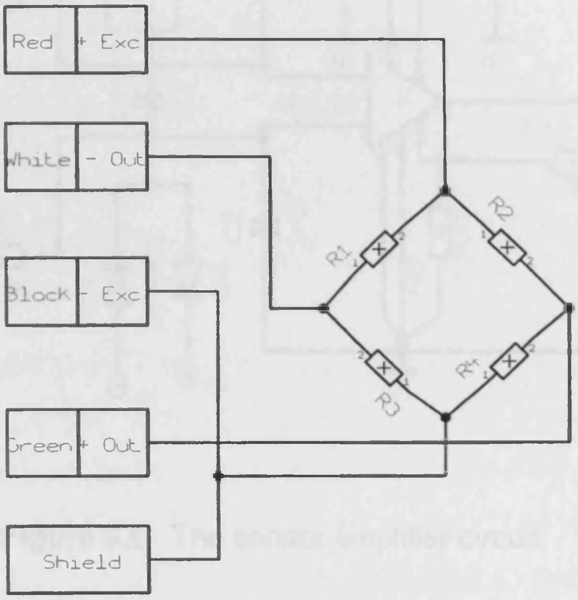

Figure 6.3 The definition of sensor external connecting lines.

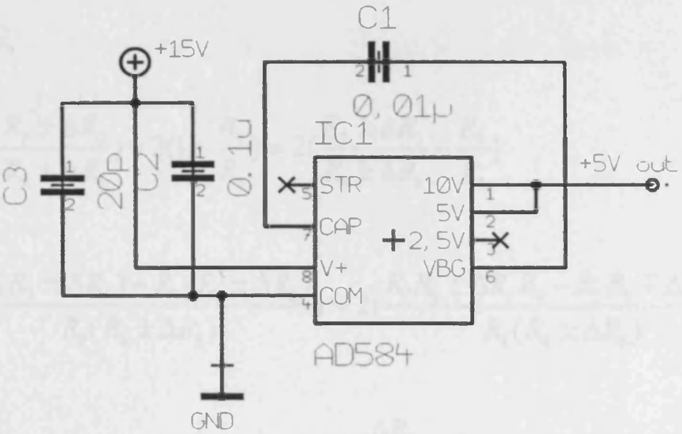

Figure 6.4 The programmable precision voltage reference AD584.

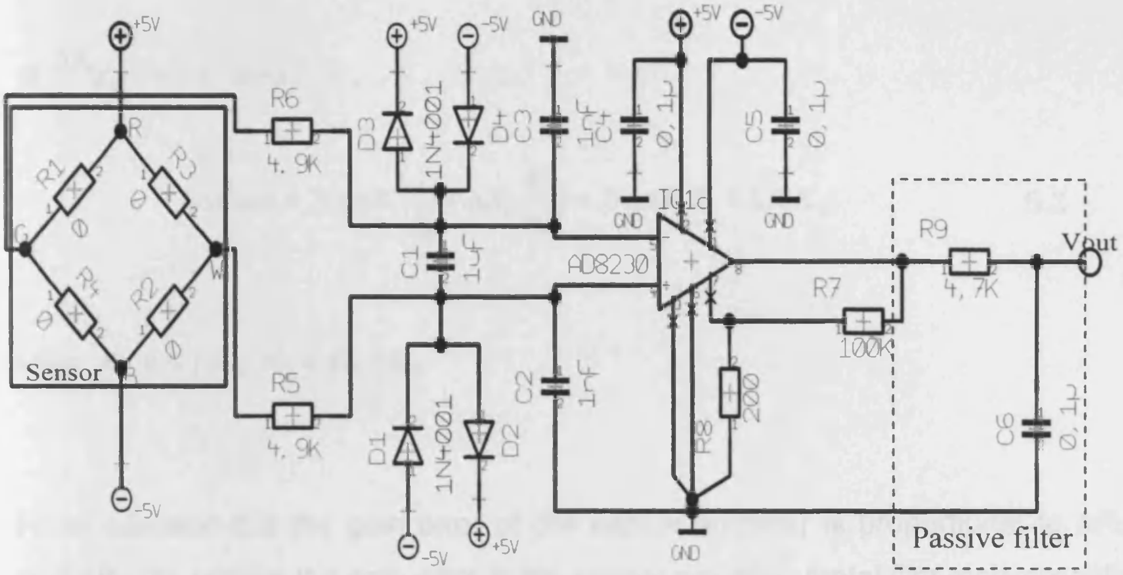

Figure 6.5 The sensor amplifier circuit.

In fact, because of the error in the resistance R_7 and R_8, the error results in a gain error of the sensor amplifier. The gain error of the sensor amplifier is calculated below:

$$\Delta Gain = G_1 - G_0 \qquad 6.2$$

$$= 2\left(1+\frac{R_7 \pm \Delta R_7}{R_8 \pm \Delta R_8}\right) - 2\left(1+\frac{R_7}{R_8}\right) = 2\left(\frac{R_7 \pm \Delta R_7}{R_8 \pm \Delta R_8} - \frac{R_7}{R_8}\right)$$

$$= 2\left(\frac{R_8(R_7 \pm \Delta R_7) - R_7(R_8 \pm \Delta R_8)}{R_8(R_8 \pm \Delta R_8)}\right) = 2\left(\frac{R_7R_8 \pm \Delta R_7 R_8 - R_7 R_8 \mp \Delta R_8 R_7}{R_8(R_8 \pm \Delta R_8)}\right)$$

$$= 2\left(\frac{\pm \Delta R_7 R_8 \mp \Delta R_8 R_7}{R_8^2\left(1 \pm \frac{\Delta R_8}{R_8}\right)}\right) = 2\left(\frac{\pm \Delta R_7 \mp R_7 \frac{\Delta R_8}{R_8}}{R_8\left(1 \pm \frac{\Delta R_8}{R_8}\right)}\right)$$

If ${}^{\Delta R_8}\!/_{R_8} << 1$, then

$$\Delta Gain \approx 2(\pm\Delta R_7 \frac{1}{R_8} \mp \Delta R_8 \frac{R_7}{R_8^2}) = 2(\pm\Delta R_7 K_1 \mp \Delta R_8 K_2) \qquad 6.3$$

Here, $K_1 = 1 / R_8$, $K_2 = R_7 / R_8$.

From equation 6.3 the gain error of the sensor amplifier is proportional to ΔR_7 and ΔR_8. To reduce the gain error in the sensor amplifier, metal film resistors with 0.1% accuracy were used for R_7 and R_8, because the wire-wound resistor usually has higher parasitic inductance than the metal resistor. The parasitic inductance could affect an amplifier's high-frequency performance (Cawthorne et al., 1997). Experience has shown that wire-wound resistors in the gain feedback loop may degrade the offset voltage performance (application notes from the Analog Devices).

The nulling circuit of the sensor amplifier designed by author is shown in Figure 6.6. In the nulling circuit, OP07 was used because it has ultrastable time property: maximum 1.5 µV/Month (Data sheet of Analog Device).

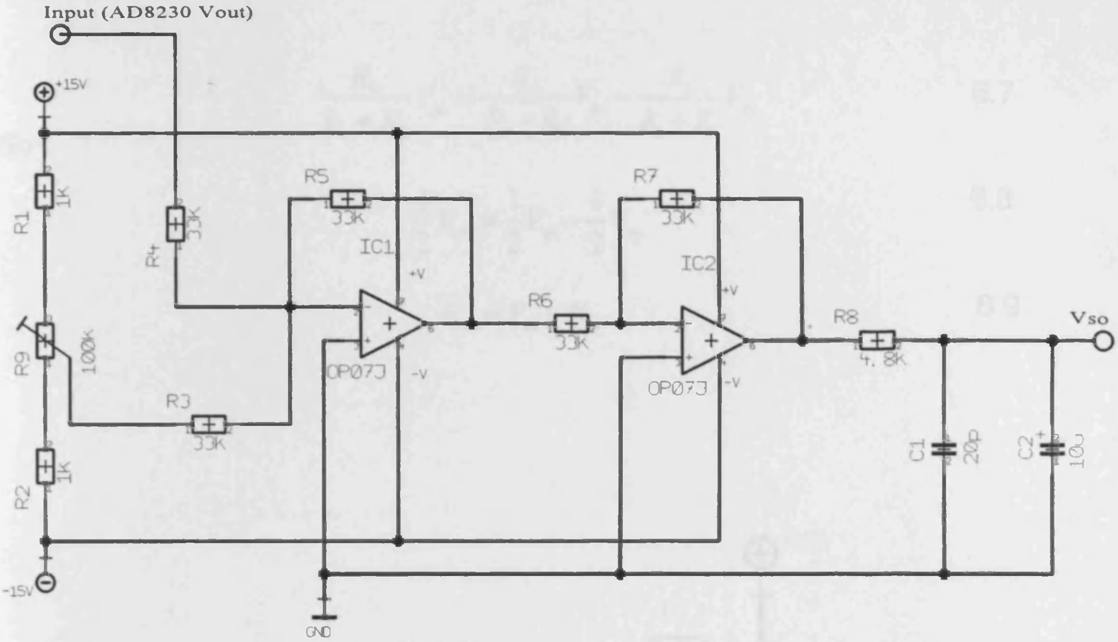

Figure 6.6 The nulling circuit of the sensor amplifier

Comparator The comparator is designed by author, as shown in Figure 6.7. The relationship between the inputs V_{ss} and V_{so} and the output V_{eo} is expressed by the following equation:

$$V_{eo} = \frac{R_3}{R_1}(V_{ss} - V_{so}) \qquad 6.4$$

Since:

$$V_{so}^{'} = \frac{R_4}{R_2 + R_4} V_{so} \qquad 6.5$$

$$V_{ss}^{'} = \frac{R_3}{R_1 + R_3} V_{ss} - \frac{R_1}{R_1 + R_3} V_{eo} \qquad 6.6$$

And $V_{so}^{'} = V_{ss}^{'}$, $R_1 = R_2 = R_3 = R_4$, then

$$\frac{R_4}{R_2 + R_4} V_{so} = \frac{R_3}{R_1 + R_3} V_{ss} - \frac{R_1}{R_1 + R_3} V_{eo} \qquad 6.7$$

So

$$\frac{1}{2} V_{eo} = \frac{1}{2} V_{ss} - \frac{1}{2} V_{so} \qquad 6.8$$

$$V_{eo} = V_{ss} - V_{so} \qquad 6.9$$

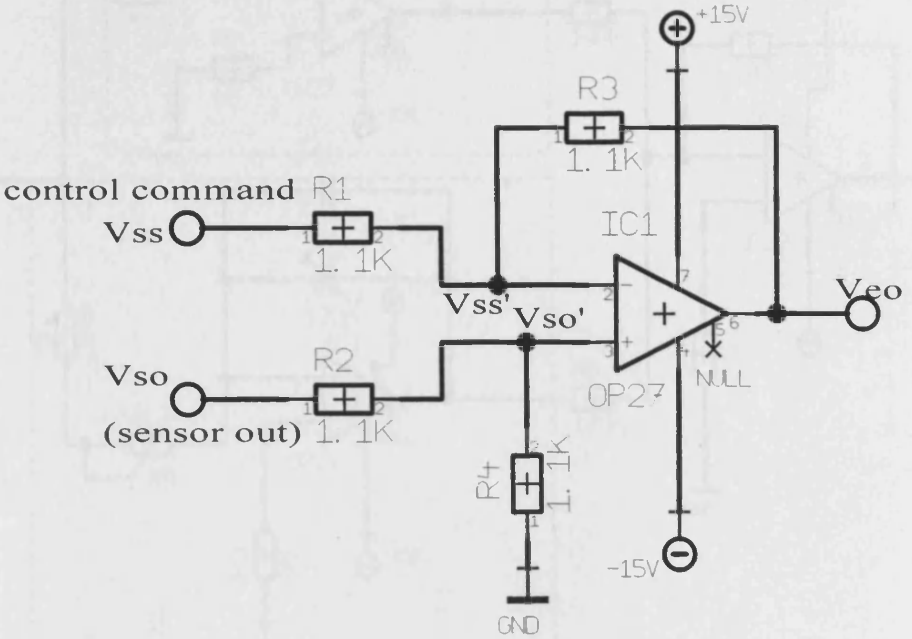

Figure 6.7 Negative feedback differential amplifier circuits

PID control circuit In the loading control system, PI control was used. Because PI control response uses the control loop to reduce the offset to zero, the output is close to the set-point, and control response does not produce “overshoot”. D control is easy to produce “overshoot”. Although PID control response can return to set-point quickly, the control response exhibits “overshoot”. This is not expected in the tooth loading control system. Thus the PI control circuit was designed by author, as shown in Figure 6.8.

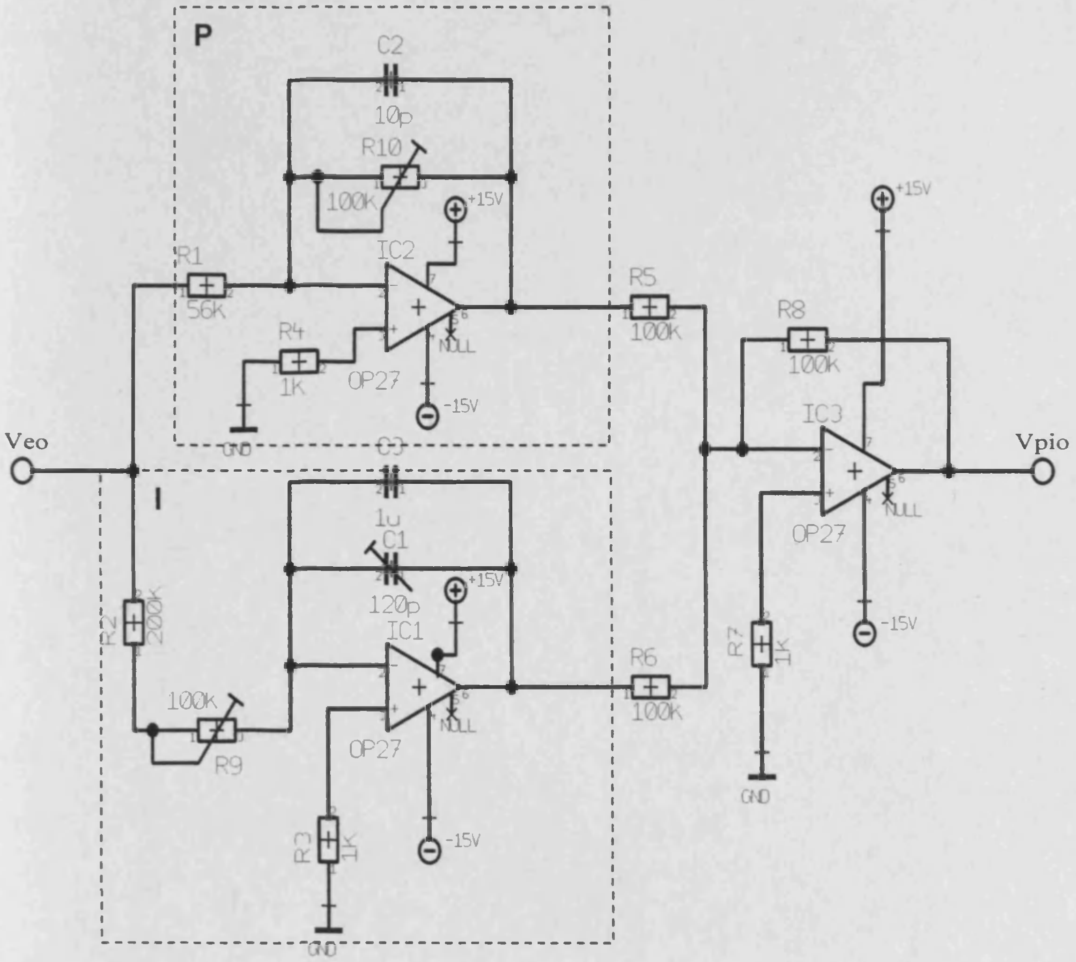

Figure 6.8 The PI control circuit.

The proportional circuit is made up using R_1, R_{10} and $IC2$. The proportional parameter is decided by R_{10}/R_1. C_2 is the filter capacitance. The integral circuit is made up with R_2, R_9, C_1, C_3 and $IC1$. The integral time parameter is adjusted by

R_9 and C_1. Here R_2 and C_3 are used to increase the integral time constant and adapt the requirements of the control system since the tuning capacitance C_1 (trimmer) has a limited adjustable range of values. *IC3* and R_5, R_6, R_8 perform an adding voltage circuit to add the P and I signals and give an output signal of the PI control circuit.

The PI circuit output voltage V_{pio} is expressed by the following equation:

$$V_{pio} = V_p + V_i \qquad 6.10$$

Here V_p , V_i are expressed as:

$$V_p = -\frac{R_{10}}{R_1} V_{eo} \qquad 6.11$$

$$V_i = -\frac{\dfrac{1}{(C_1 + C_3)s}}{R_2 + R_9} V_{eo} \qquad 6.12$$

Where 's' is the Laplace operator, $s = \frac{d}{dt}$

$$CsV_i = -\frac{1}{R} V_{eo} \qquad 6.13$$

That is

$$\dot{V}_i(t) = -\frac{1}{RC} V_{eo}(t) \qquad 6.14$$

So

$$V_i(t) = -\frac{1}{RC} \int V_{eo} dt \qquad 6.15$$

Here $C = C_1 + C_3$, $R = R_2 + R_9$. V_{ipo} is given by:

$$V_{pio} = -(\frac{R_{10}}{R_1} V_{eo} + \frac{1}{RC} \int V_{eo} dt) \qquad 6.16$$

The maximum integral time, which makes the output value of the integral circuit reach to its maximum output value of 0.632, is given by $T = RC$ = 300kΩ x 1μF =0.3 s. The integral time can be adjusted by changing the value of the integral resistors R_2, R_9 and the integral capacitance C_1.

PWM circuit The PWM circuit is designed by author for controlling a DC linear motor. The PWM circuit was combined with a H - bridge power driver and a logical control circuit to realize automatic control of the bi-directional movement of the DC linear motor.

The working principle of the PWM circuit is that it produces a square wave with a variable on-to-off ratio. The average on time can be varied from 0 to 100 percent according to the PWM input control signal. The variable amount of power in the PWM circuit is transferred to the load. The advantage of the PWM circuit over the resistive power controller is its high efficiency. For example, at 50% level of power, the PWM uses 50% of full power to the load; but a resistive controller consumes about 71% of the full power to load. In fact, 50% of the full power goes to the load and other 21% is wasted heating the series resistor (Cook, 1999). Another advantage of the PWM is that the pulse amplitude of the PWM output can reach the voltage of the power supply. A motor needs more power (high voltage) to overcome the internal motor resistances more easily at the early work stage. The PWM circuit is designed by author, as shown in Figure 6.9.

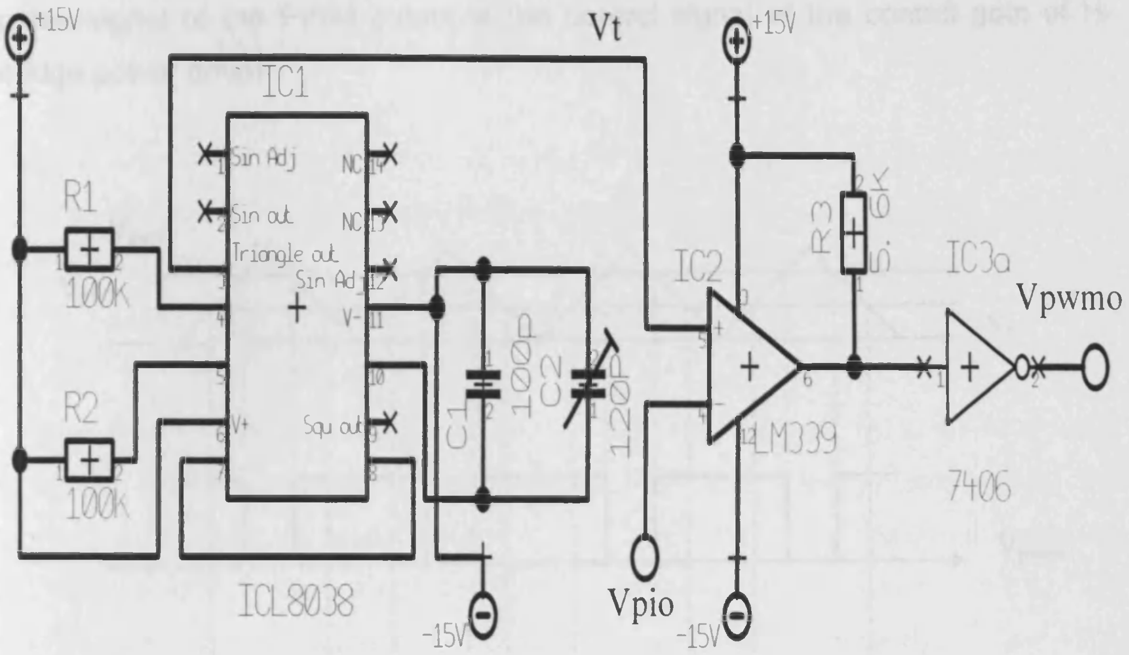

Figure 6.9 The PWM circuit.

In Figure 6.9, ICL8038 is a waveform generator to generate sine, square and triangle waveforms. Here the function of the triangle waveform V_t of ICL8038 was used. The comparator LM339 compares the triangle waveform signal V_t with the output signal V_{pio} of the PI control circuit and produces an output signal of a square wave. The working principle is that when the triangle waveform signal V_t rises over the PI control circuit output voltage V_{pio}, the comparator outputs high level, whereas the comparator outputs low level. The inverter IC3 7406 changed the 180 degrees phase of the comparator output signal (Figure 6.10) to produce a pulse signal output which was coincident with the PI control signal. When the PID signal was higher, the pulse width (positive) of the PWM output was increased, that is the load applied on the measured tooth was increased. Whereas if the PID signal was lower, the pulse width of the PWM output was decreased, that is the force applied on the measured tooth was reduced. The pulse signal of the PWM output is the control signal of the control gate of H-bridge power driver.

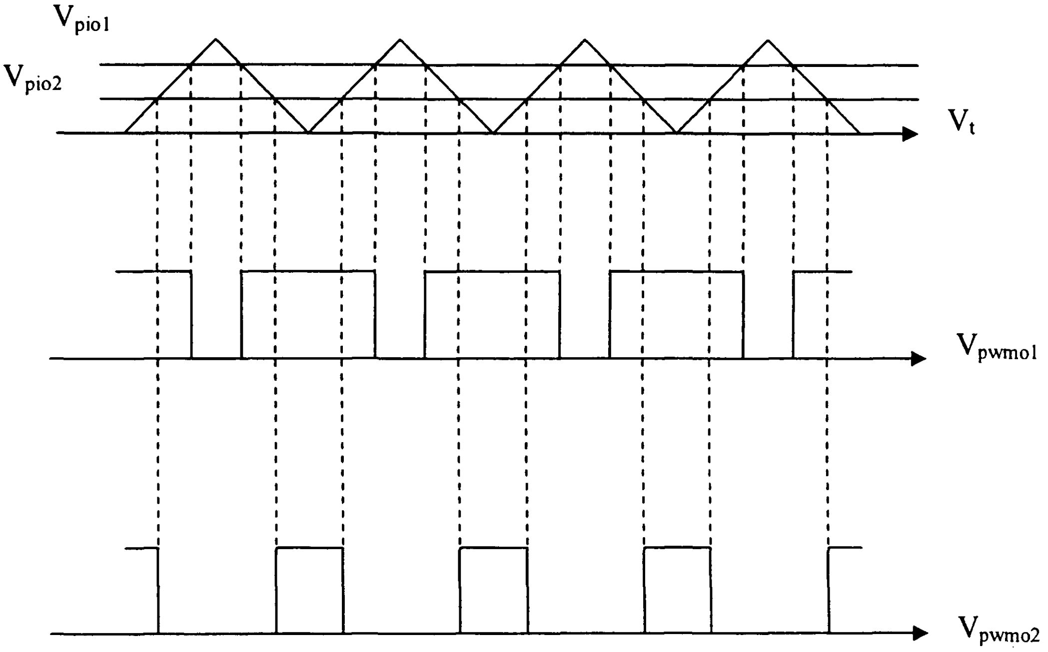

Figure 6.10 The ideal pulse waveform of the PWM output through the inverter.

The frequency range of the triangle waveform signal is normally set from 1 kHz to 200 kHz (Barr 2001). If the frequency of the triangle waveform signal is too high, the waveform will get worse due to the effect of high frequency noise and harmonic distortion. If the frequency is too low, the motor will not run smoothly due to the effect of the motor inertia.

In this design, the period T of triangle waveform is $T = t_1 + t_2$, $t_1 = R_1C/0.66$, $t_2 = R_1R_2C/0.66(2R_1\text{-}R_2)$, $f = 1/T$, and $R = R_1 = R_2 = 100k\Omega$, $C = 160pF$, so $t_1 = t_2$, $T = 2RC/0.66 = 48\mu s$. Thus the frequency of triangle waveform is f = 0.33/RC = 20.6

kHz. Therefore, in this design, the frequency was designed to be about 20 kHz. The experiments result showed that the DC motor ran smoothly under this frequency.

Power amplifier circuit The purpose of a power amplifier is to replicate a signal and make it larger. Here the power amplifier was used to drive the actuator. In this study, the two kinds of power amplifier were designed which could be used for the solenoid and the linear motor.

Figure 6.11 shows a common-emitter power amplifier to be used to drive a solenoid. The output voltage was taken from the collector terminal of the transistor. The supply voltage was +15V. The variation of the input signal V_i, acting at the transistor base, results in a change of the base current I_b. The variation of the base current I_b results in the variation of the collector current I_c which is through the solenoid (load). In Figure 6.11, R_3 is the load resistor (solenoid); D_1 is a protective diode to protect the transistor; R_2 is a biasing resistor for obtaining quiescent conditions; R_4 is a protective resistor of the load because the solenoid allowes the maximum voltage under 100% duty cycle is 12V .

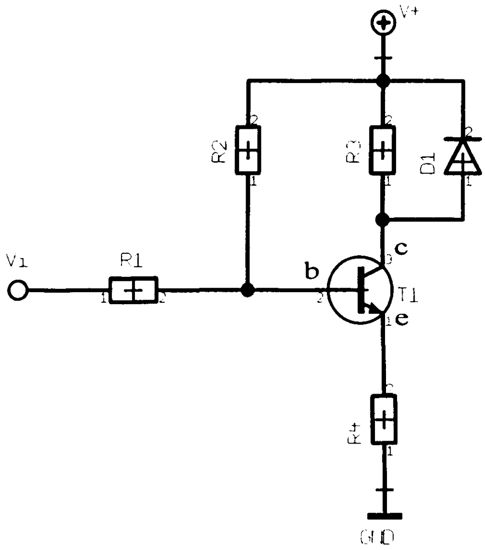

Figure 6.11 The common-emitter transistor power amplifier

A quiescent condition needs to be set up to ensure that the power amplifier works in its operating region when a variable input signal is added at the transistor base and the output signal is without signal distortion. The quiescent condition is set up through determination of the parameters of the circuit system.

In Figure 6.11, a TIP110 silicon darlington transistor is selected because the solenoid maximum current is 0.58A, (known from the manufactory specifications, *$I = V/R_3 = 12/20.7 = 0.58A$* under condition of 100% duty). The values of the biasing resistor R_2 and the protective resistor R_4 were calculated 86kΩ and 5.2Ω, respectively. Assuming that the TIP110 gain is 1000, the threshold voltage V_b is 2.1V, (known from TIP110 characteristics graph), and I_b is selected as 150 μA, then R_2 can be calculated by the following function:

$$V_+ = I_b R_2 + V_b \qquad 6.17$$

$$\begin{aligned} R_2 &= \frac{V_+ - V_b}{I_b} \\ &= \frac{15-2.1}{150\times10^{-6}} = 86k\Omega \end{aligned} \qquad 6.18$$

R_4 is a protective resistor. When TIP110 is in saturation (V_{ce}=0.2V), 3V must be reduced on R_4 to ensure that the voltage V_l of the solenoid is not greater than the maximum voltage 12V, when the current I_c, is 0.58A. Thus, R_4 can be calculated by the following function:

$$V_+ = I_c R_4 + V_l \qquad 6.19$$

$$\begin{aligned} R_4 &= \frac{V_+ - V_l}{I_c} \\ &= \frac{15-12}{0.58} = 5.2\Omega \end{aligned} \qquad 6.20$$

This power amplifier circuit has been tested, as shown in Figure 6.12. The solenoid plunger movement was measured by the Qualisys motion capture system. Note the plunger of the solenoid can only produce uni-direction movement. This is determined by the structure of the solenoid. Here the plunger of the solenoid is pushing against a spring.

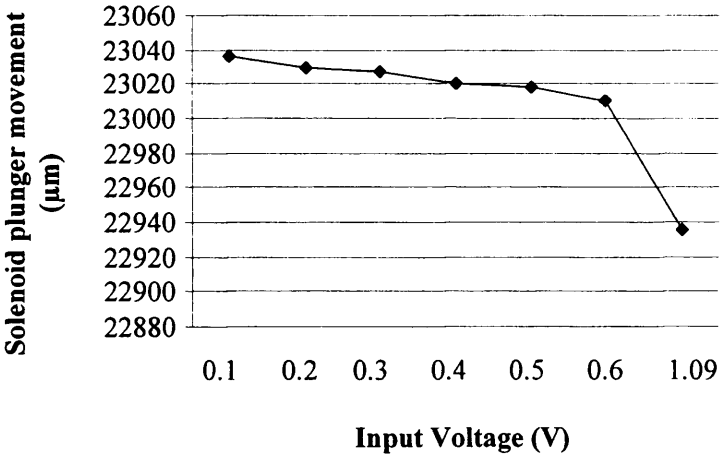

Figure 6.12 The power amplifier test with the solenoid

Figure 6.13 designed by author shows the power amplifier circuit to drive the DC linear motor. For clearly explaining the procedure of the drive circuit working, a complete drive circuit is presented in Figure 6.13 (a) and (b). Figure 6.13 (a) was used to drive the motor in order to produce a horizontal force; Figure 6.13 (b) was used to drive the motor in order to produce a vertical force. The two motors are combined together in order to produce a twisting force.

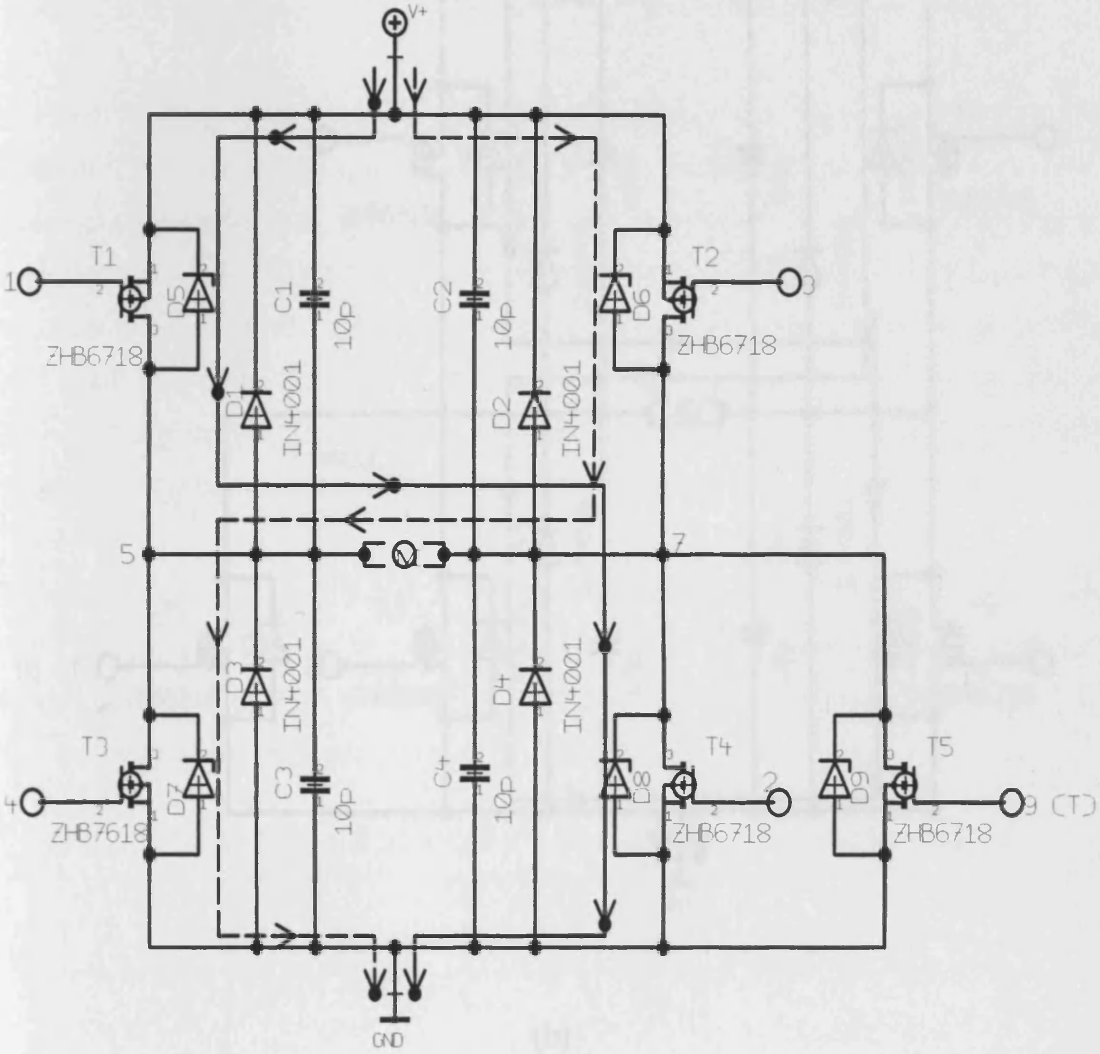
V+
T1
1
ZHB6718
D5
C1
10p
C2
10p
D6
T2
3
ZHB6718
D1
IN4001
D2
IN4001
5
M
7
D3
IN4001
D4
IN4001
T3
4
ZHB7618
D7
C3
10p
C4
10p
D8
T4
2
ZHB6718
D9
T5
9 (T)
ZHB6718
GND

(a)

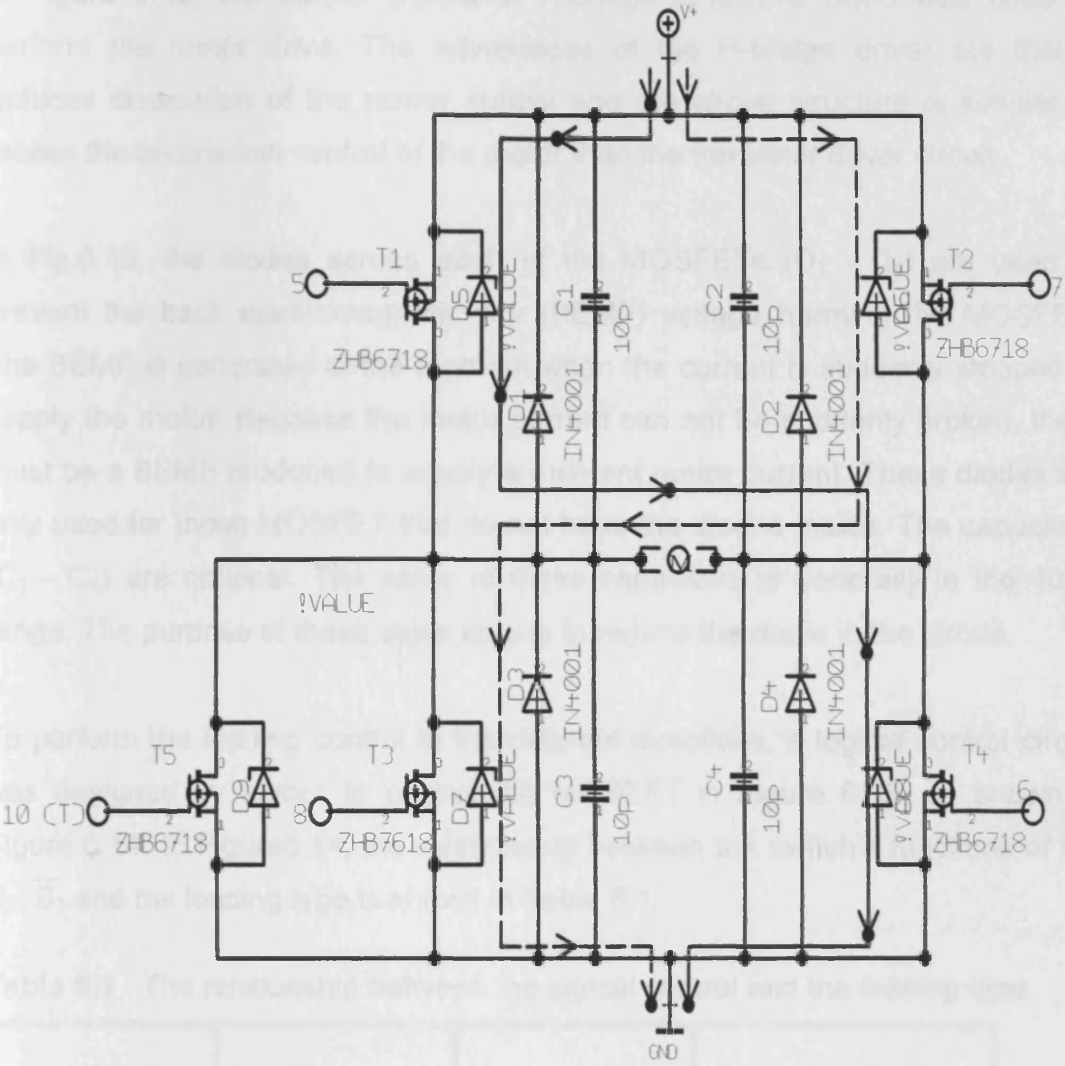

(b)

Figure 6.13 The DC linear motor power drive circuit, (a) used to drive the motor in order to produce a horizontal force; (b) used to drive the motor in order to produce a vertical force; and (a) & (b) combined together to drive the motor in order to produce a twisting force.

In Figure 6.13, the bipolar transistor H-bridge ZHB6718 SM-8 was used to perform the motor drive. The advantages of the H-bridge driver are that it reduces dissipation of the power supply and the circuit structure is simpler to realise the bi-direction control of the motor than the transistor driver circuit.

In Fig.6.13, the diodes across each of the MOSFETs (D_1 - D_4) are used to prevent the back electromagnetic flux (BEMF) voltage harming the MOSFET. The BEMF is generated at the moment when the current is suddenly stopped to supply the motor. Because the motor current can not be suddenly broken, there must be a BEMF produced to supply a moment motor current. These diodes are only used for those MOSFET that do not have the diodes inside. The capacitors (C_1 - C_4) are optional. The value of these capacitors is generally in the 10pF range. The purpose of these capacitors is to reduce the ripple in the circuit.

To perform the loading control in the different directions, a logical control circuit was designed by author to control the MOSEFT in Figure 6.13, as shown in Figure 6.14. In Figure6.14, the relationship between the switch's functions of S_1, S_2, S_3 and the loading type is shown in Table 6.1.

Table 6.1 The relationship between the logical control and the loading type

S_1	S_2	S_3	Loading Type
OFF	OFF	ON	Horizontal Push
OFF	ON	ON	Horizontal Pull
ON	OFF	ON	Vertical Push
ON	ON	ON	Vertical Pull
X	X	OFF	Twisting

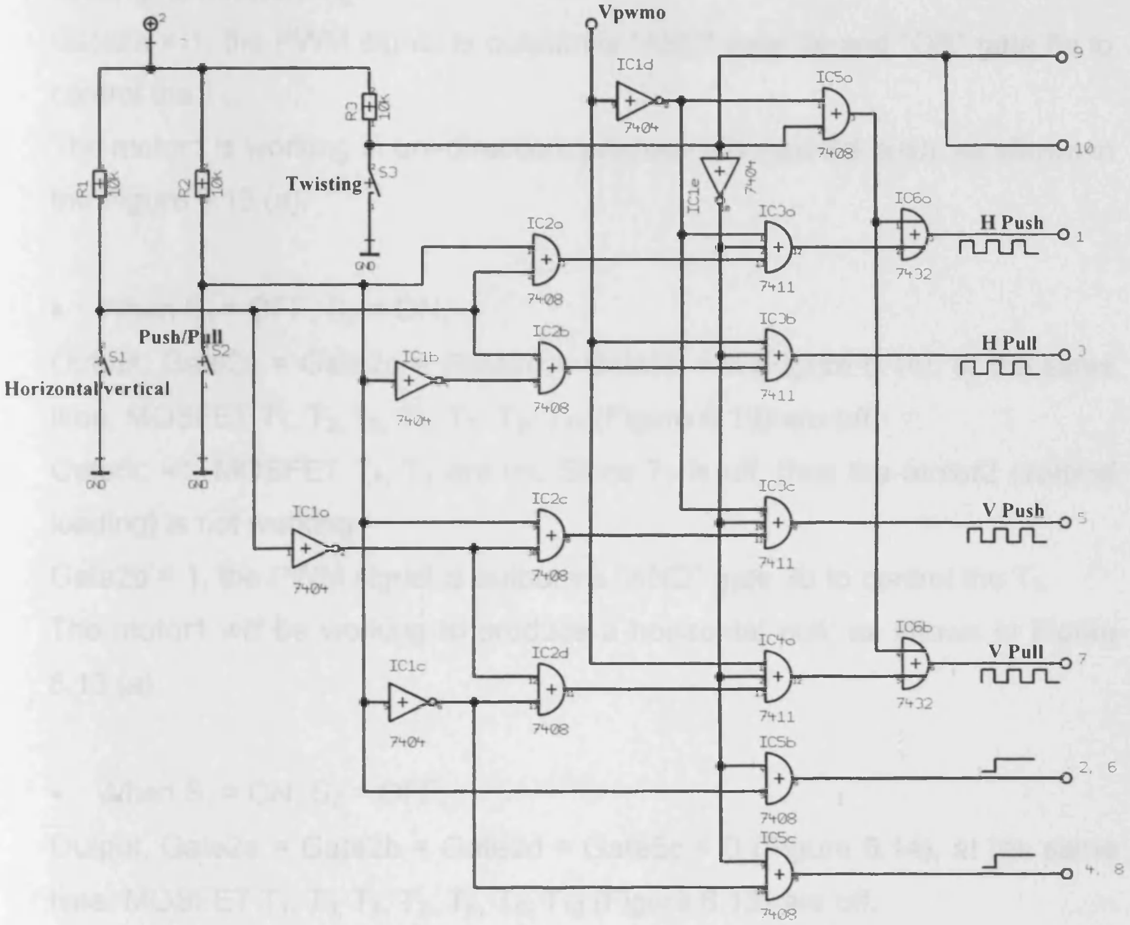

Figure 6.14 The logical control circuit of the MOSEFT power drive

The detail processing of the logical control is described below:

(1) S_3 = ON

- When S_1 = OFF, S_2 = OFF,

Output, Gate2b = Gate2c = Gate2d = Gate5c = 0 (Fig.6.14), at the same time, MOSFET T_3, T_4, T_5, T_7, T_8, T_9, T_{10} (Fig.6.12 (a) and (b)) are off, Gate5b =1, MOSFET T_2, T_6 are on. Since T_5 is off, thus the motor2 (vertical loading) is not working.

Gate2a = 1, the PWM signal is output via "AND" gate 3a and "OR" gate 6a to control the T_1.

The motor1 is working in uni-direction, produce a horizontal push, as shown in the Figure 6.13 (a).

- When S_1 = OFF, S_2 = ON,

Output, Gate2a = Gate2c = Gate2d = Gate5b = 0 (Figure 6.14), at the same time, MOSFET T_1, T_2, T_5, T_6, T_7, T_9, T_{10} (Figure 6.13) are off,

Gate5c =1, MOSFET T_4, T_8 are on. Since T_7 is off, thus the motor2 (vertical loading) is not working.

Gate2b = 1, the PWM signal is output via "AND" gate 3b to control the T_3.

The motor1 will be working to produce a horizontal pull, as shown in Figure 6.13 (a).

- When S_1 = ON, S_2 = OFF,

Output, Gate2a = Gate2b = Gate2d = Gate5c = 0 (Figure 6.14), at the same time, MOSFET T_1, T_3, T_4, T_7, T_8, T_9, T_{10} (Figure 6.13) are off,

Gate5b =1, MOSFET T_2, T_6 are on. Since T_1 is off, thus the motor1 (horizontal loading) is not working.

Gate2c = 1, the PWM signal is output via "AND" gate 3c to control the T_5.

The motor2 will be working to produce a vertical pull, as shown in Figure 6.13 (b).

- When S_1 = ON, S_2 = ON,

Output, Gate2a = Gate2b = Gate2c = Gate5b = 0 (Figure 6.14), at the same time, MOSFET T_1, T_2, T_3, T_5, T_6, T_9, T_{10} (Fig.6.15) are off,

Gate5c =1, MOSFET T_4, T_8 are on. Since T_3 is off, thus the motor1 (horizontal loading) is not working.

Gate2d = 1, the PWM signal is output via "AND" gate 4a and "OR" gate 6b to control the T_7.

The motor2 will be working to produce a vertical push, as shown in Figure 6.13 (b).

(2) S_3 = OFF,

S_1 and S_2 are at arbitrary level (high or low),

Output, Gate3a = Gate3b = Gate3c = Gate4a = Gate5b = Gate5c = 0 (Figure 6.14), at the same time, MOSFET T_2, T_3, T_4, T_5, T_6, T_8 (Figure 6.13) are off.

T_9 and T_{10} states are directly set ON by S_3.

The PWM signal is output via "OR" gate 6a, 6b to control the T_1 and T_7.

The motor1 and motor2 will be working at the same time, but their work directions are opposite to produce a twisting loading, as shown in Figure 6.13.

6.2.4 Sensor output characteristic detection

The output characteristic of the load cell SMT1-5N with the sensor amplifier was measured using dead weights and an M830B multi meter. The dead weights were put on the sensor in the following order: 10gf, 20gf, 30gf, 40gf and 50gf. The sensor's output through the sensor amplifier was measured by M830B equipment. The measurement results are presented in Table 6.2 and Figure 6.15. The sensor has a very good linearity, as shown in Fig.6.15.

Table 6.2 The output characteristics of the sensor with sensor amplifier

Load (N)	Output voltage from the sensor amplifier (V)						
	1	2	3	4	5	Mean	Std
0.0997	0.30	0.31	0.31	0.30	0.31	0.31	0.005
0.1966	0.63	0.62	0.63	0.62	0.63	0.63	0.005
0.3095	1.01	1.01	1.00	1.01	1.02	1.01	0.007
0.4092	1.34	1.34	1.34	1.35	1.33	1.34	0.007
0.4900	1.65	1.65	1.65	1.65	1.64	1.65	0.005

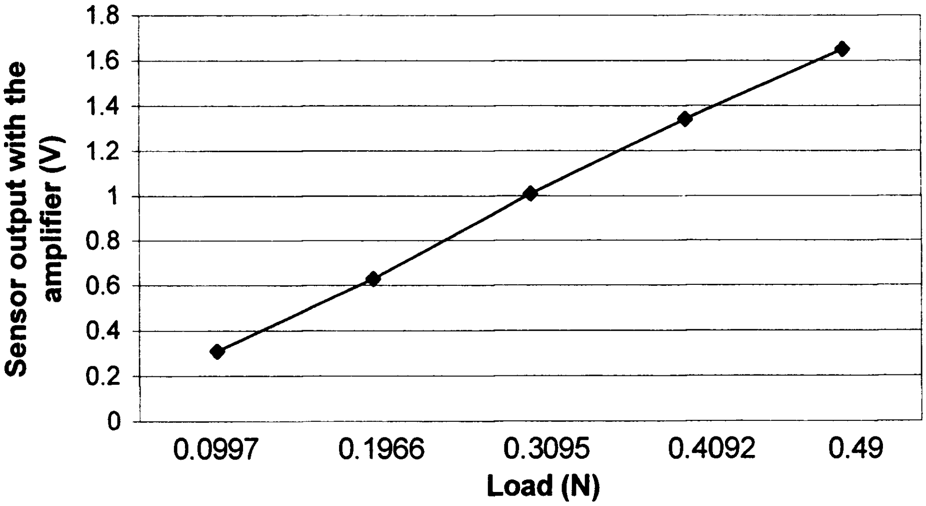

Figure 6.15 The mean output characteristic of the SMT1-5N sensor with the amplifier.

6.3 Control system test

The control system circuit was built by author on a breadboard as shown in Fig.6.16. The circuit system was tested part by part before being used to control the loading device. The solenoid and a 3W DC motor were used as the actuator respectively. The 3W DC motor replaces the linear motor during the test due to a delay in the delivery of the linear motor. The circuit output waveforms were detected by using the FLUKE 123 Industrial Scopemeter (20MHz).

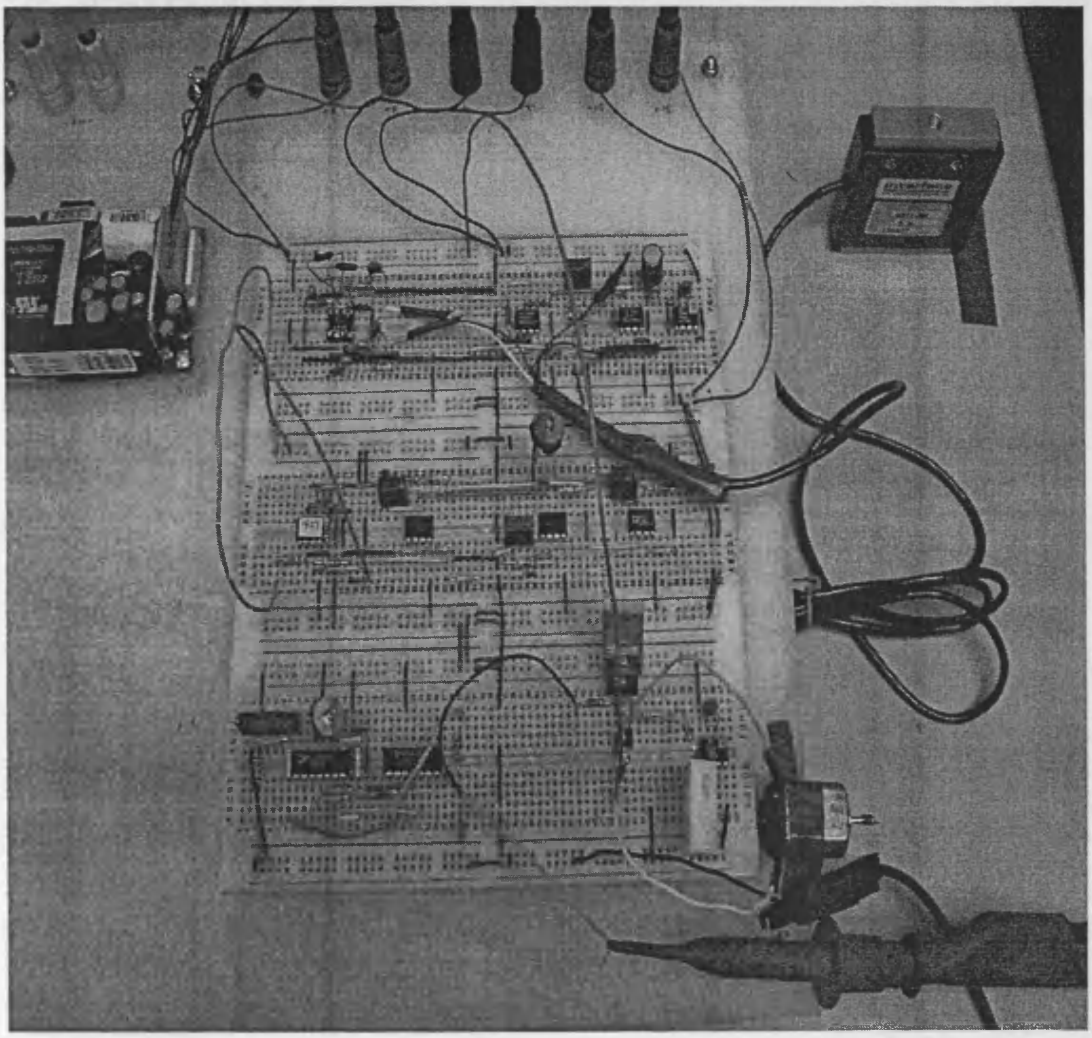

Figure 6.16 The loading control system connected on a breadboard.

For the integral circuit, according to equation 6.15, the output voltage of the integral circuit is $Vi = (V_{eo}/ RC)\ t$. When $V_{eo} = 2.46V$ (measured by M830B equipment), the integral time constant $RC = 0.3s$ (known from design, $R=300K\Omega$, $C=1\mu F$), and the integral time t is $t= 1s$, thus, in the ideal case, the integral circuit output is $Vi = 8.2V$. The practical output waveforms of the integral circuit measured by FLUKE 123 Industrial Scopemeter (20MHz) are shown in Figure 6.17. In Figure 6.17 (a), the integral capacitance is C = 1μF (T=RC=0.3s, when t=1s, Vi=8.2V), (b) the integral capacitance is C = 1.1 μF (T=RC=0.33s, when t=1s, Vi=7.4V), (c) the integral capacitance is C= 1.2 μF (T=RC=0.36s, when t=1s, Vi=6.8V). The practical measured results were the same as the theoretical design.

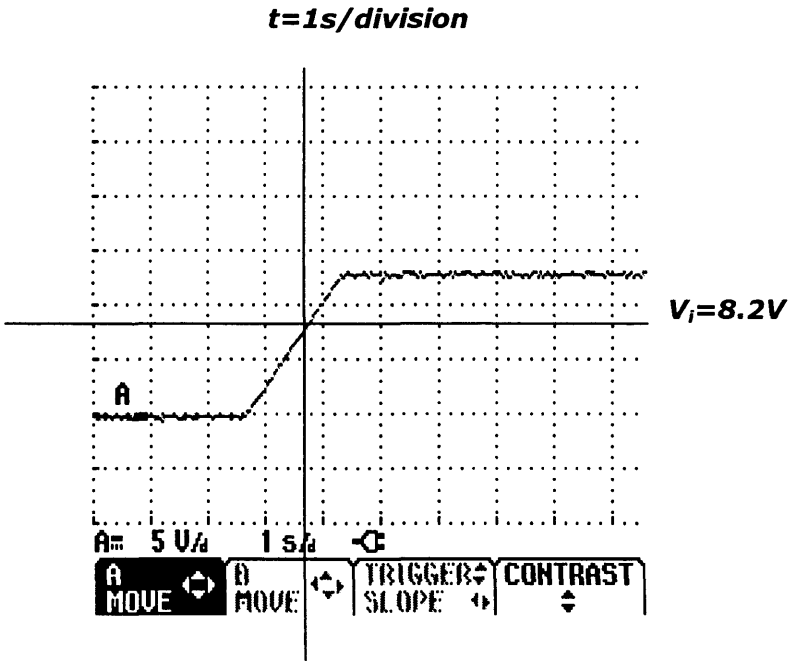

(a)

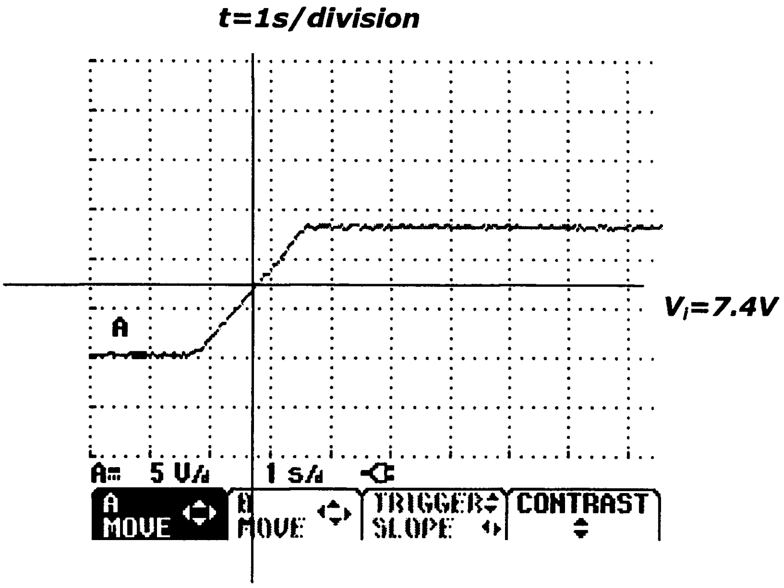

(b)

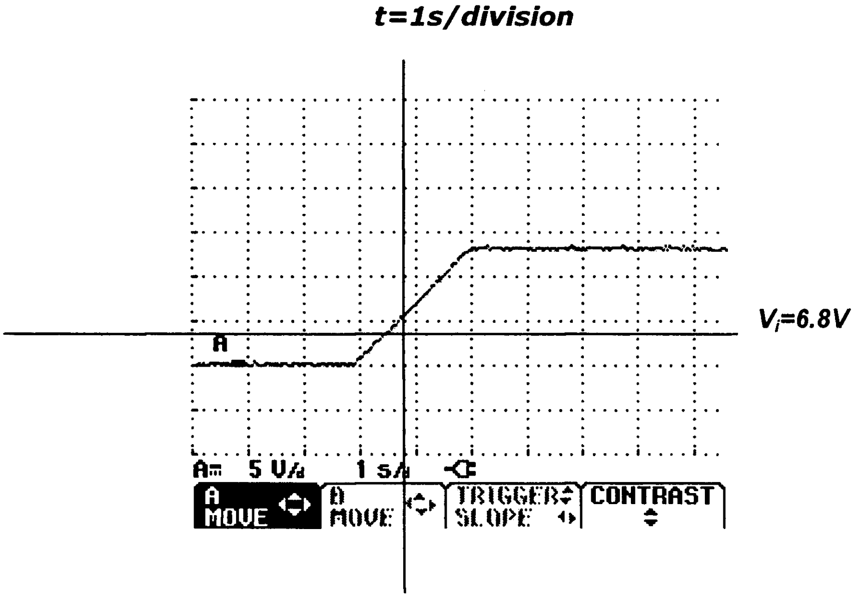

(c)

Figure 6.17 The actual integral circuit output, (a) integral capacitance C = 1μF (T=0.3s), (b) integral capacitance C = 1.1μF (T=0.33s), (c) integral capacitance = 1.2μF (T=0.36s).

For the PWM circuit, the frequency of the triangle waveform in the ideal case is 20.6 kHz (known from design) and the pulse width of the PWM output varies along with the input signal (or PID circuit output). The actual output of the triangle waveform was measured using the FLUKE 123 Industrial Scopemeter, as shown in Figure 6.18. From Figure 6.18, the actual measured period of the triangle waveform is approximately 2.4 x 20µs. The actual measured frequency of the triangle waveform is *f=1/t=20.8 kHz*.

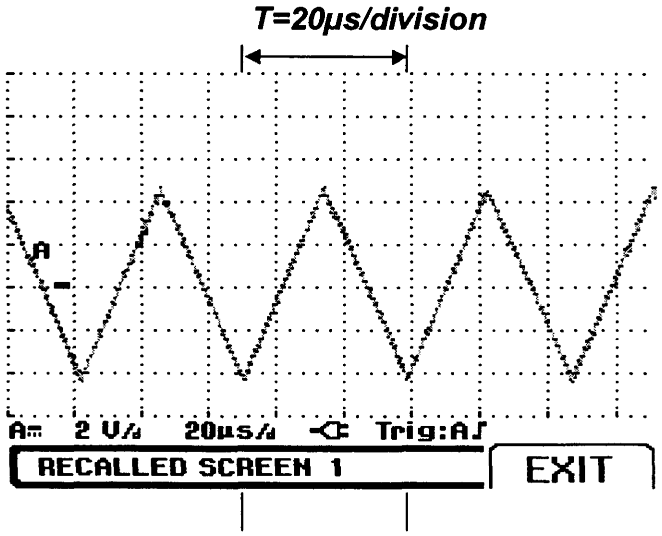

Figure 6.18 The actual triangle waveform in PWM circuit

The practical pulse output of the PWM circuit was measured using the FLUKE 123 Industrial Scopemeter, as shown in Figure 6.19. Figure 6.19 (a) shows a duty cycle of about 25%, corresponding with an input of about 2.1V (measured by a multimeter). Figure 6.19b shows a duty cycle of about 33%, corresponding with an input of about 2.8V. Figure 6.19c shows a duty cycle of 50%, corresponding with input of 4.2V. Figure 6.19 demonstrates that the pulse width is changed with the input signal of the PWM circuit.

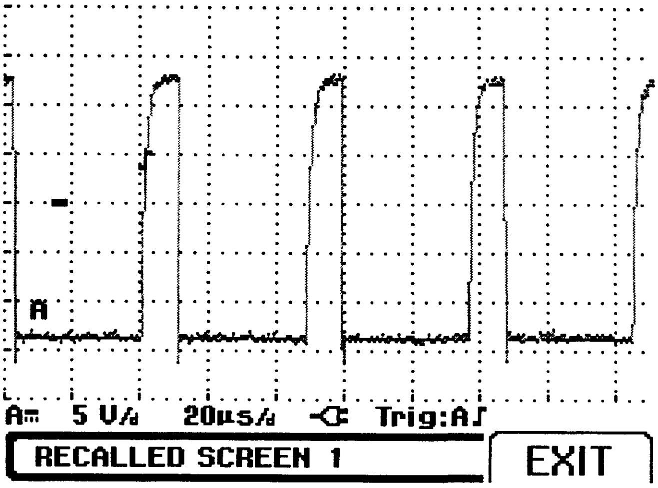
A
A⎓ 5 V/d 20µs/d Trig:A∫
RECALLED SCREEN 1
EXIT

(a)

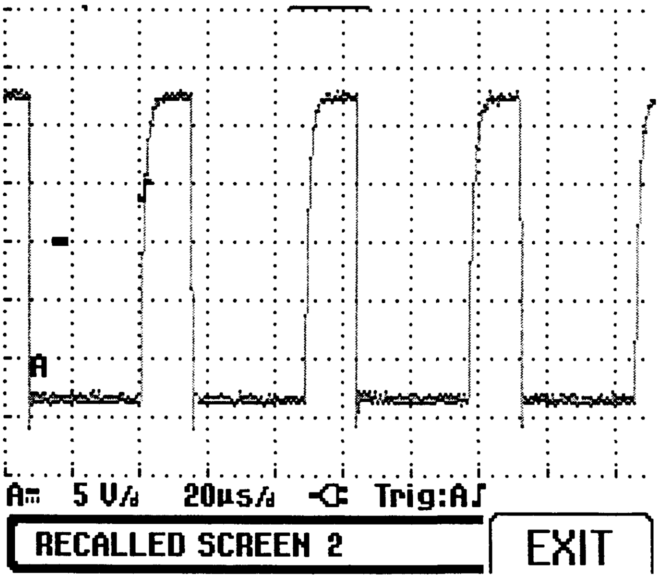
A
A⎓ 5 V/d 20µs/d Trig:A∫
RECALLED SCREEN 2
EXIT

(b)

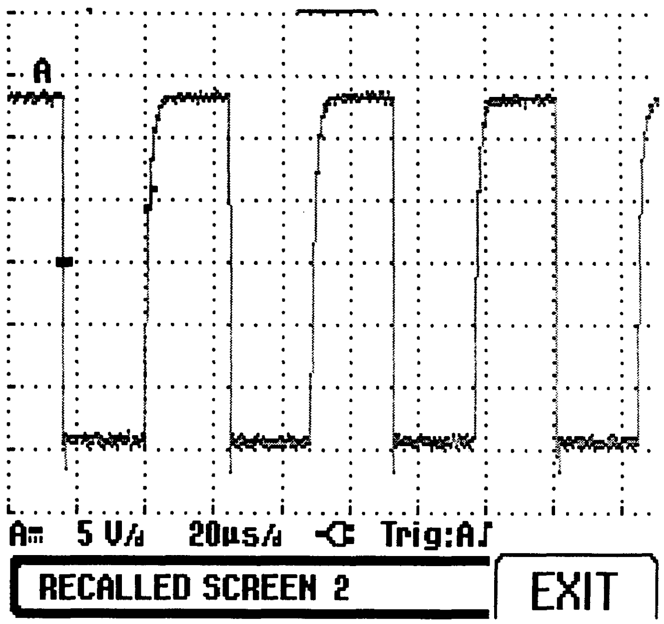

(c)

Figure 6.19 The actual PWM circuit pulse output, (a) the duty cycle of about 25%, (b) the duty cycle of about 33%, (c) the duty cycle of about 50%

6.4 Control system noise analysis

Electrical noise can usually be defined as an unwanted signal which is always present in a circuit system. Its presence tends to impede the reception of the wanted signal and is usually the limiting factor in wanted signal detection. There are many sources which produce noise. They may be broadly classified as natural or artificial. Artifical or man-made noise is mainly from electrical equipment. This produces noise which often has regular properties.

Noise generally covers a very wide range of frequencies, and it is not possible to avoid it by choosing any particular frequency band. Hence, the evaluation of the noise power in a system is based on its total value within some defined bandwidth which often is the bandwidth of the receiver used or the bandwidth of the transmission system under study.

There are two most important types of noise associated with electronic components: thermal noise and shot noise. Both of them give rise to noise power in the system. Thermal noise always exists in the electronic system. Shot noise exists in semiconductor devices.

Thermal noise is caused by random thermally excited vibrations of charge carriers in a conductor, such as resistors. A resistor contains a number of free electrons. Due to thermal agitation, these free electrons are moving about continuously in the conductor causing collisions with the atoms and a continuous exchange of energy takes place. This accounts for the resistance property of the conductor and, though there is no current in the conductor on open-circuit, the random motion of electrons in the conductor produces voltage fluctuation across the conductor which accounts for a mean-square noise voltage $\overline{\upsilon_i^2}$ at its terminals. The thermal noise effect was investigated experimentally by Johnson (Johnson 1928) and theoretically by Nyquist (Nyquist 1928). Experimental results showed that the thermal noise voltage depends upon temperature, its mean-square value $\overline{\upsilon_i^2}$ is given by

$$\overline{\upsilon_i^2} = 4kTR\Delta f \qquad 6.21$$

Where k is Boltzmann's constant (1.383 x 10^{-23} J/K), T is the absolute temperature (^{0}K), R is the resistance of the conductor and Δf is the bandwidth of the system. If R = 100kΩ, Δf = 20kHz, and T = 290K then with k = 1.383 x 10^{-23} J/K, the mean-square value of noise obtains $\overline{\upsilon_i^2}$ = 32 x 10^{-12} or $\upsilon_{rms} = [\overline{\upsilon_i^2}]^{1/2}$ = 5.7 μV.

Shot noise is present when carrier transportation occurs across two media, as a semiconductor junction. The current flow in a semiconductor junction is due to the emission of electrons from the cathode which then travel to the anode. Each electron carries a discrete amount of charge to the anode and produces a small current pulse. The summation of all the current pulse produces the average anode current I_a in the semiconductor junction. However, the emission of electrons is a random process depending on the surface condition of the cathode, shape of the electrodes, and the potential between them. This gives rise to random fluctuation in the number of emitted electrons and so the junction-current contains a time-varying component. Since each electron arriving at the anode is like a 'shot', the fluctuating component gives rise to a mean-square shot noise current $\overline{i_s^2}$. If the semiconductor junction-current is i(t), it can be written as

$$i(t) = I_a + i_s(t) \qquad 6.22$$

Where I_a is the average anode current and $i_s(t)$ is the shot noise component. This is demonstrated in Figure 6.20 (Buckingham 1983). Shot noise can be written as

$$\overline{i_s^2} = 2eI_a\Delta f \qquad 6.23$$

Where e is elementary charge (1.60217646 × 10^{-19} coulombs) and Δf is the effective bandwidth of the system.

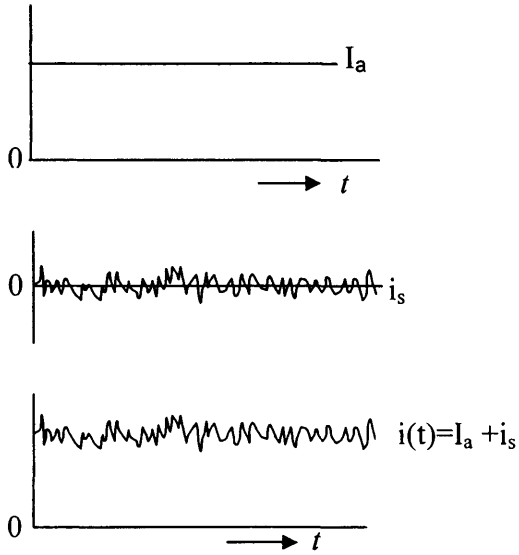

Figure 6.20 The semiconductor junction-current with shot noise.

Another type of noise is the 1/*f* noise. 1/*f* noise is present in all conduction phenomena. The 1/*f* noise effect depends on the circuit bandwidth. It may or may not be an important contribution.

In the loading control system, the noise level at the each section was measured by using the FLUKE 123 Industrial Scopemeter. The results are shown as below:

Sensor amplifier: terminal output = 13 (*mV p-p*)
Differential amplifier: terminal output = 27 (*mV p-p*)
Proportional circuit: terminal input = 27 (*mV p-p*), terminal output = 56 (*mV p-p*)
Integral circuit: terminal input = 27 (*mV p-p*)

Noise in the control system may come from two paths: one is from system thermal noise of the components due to many resistors used in the system; another path is ground noise. The ground noise is created from the so-called ground loops. When the system ground and the instrument ground are connected at different points, a close loop is formed, as shown in Figure 6.21. In this loop, the potential difference, between system ground and the instrument ground, produces a current I, then the current I produces an unwanted voltage V_G. The voltage V_G is called the ground noise.

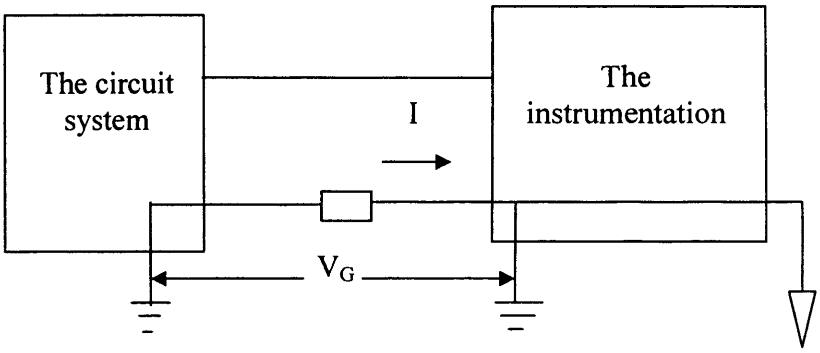

Figure 6.21 The ground noise in the circuit measurement

Noise has to be concerned for precision electronic measurement equipment with an analogue circuit system. The method of reducing noise could be to use passive or active filters, or connect the ground point at a common point.

In the loading control system, the passive filters were used to reduce the effect of noise, and the motor driver used the MOSEFT power switch which was controlled by the digital signal of the TTL gate circuit. This greatly increased the ability of the control system to prevent disturbance or noise.

Chapter 7 Clinical experiments and result analysis

7.1 Introduction

This chapter integrates all of the techniques and methods introduced in previous chapters to study tooth movement in the clinical setting. The chapter presents the experimental method in the clinical setting with human volunteers. Then the results of the experiment under different loading situations are presented. Finally, noise, noise processing, and experimental results will be discussed.

7.2 Methods

Volunteers, with heathy teeth and a regular array, especially where the measured tooth was not crowded with the adjacent teeth, were chosen. This is because crowded teeth produce an acting and reacting force between each other, this will affect the individual measurement and will not give an accurate response of tooth movement when a load is applied to the measured tooth. In the experimental preliminary stage, the volunteer's mouth was opened and fixed with a cheek retractor to protect the marker clusters from being moved or damaged, as shown in Figure 7.1. Two marker clusters, each with three spherical markers, were fixed on the tooth to be measured and the reference tooth by a clinical orthodontic specialist, using the specific brackets and the cement, as shown in Figure 7.2. The ultraviolet light applied in dentistry was used to cure the cement quickly.

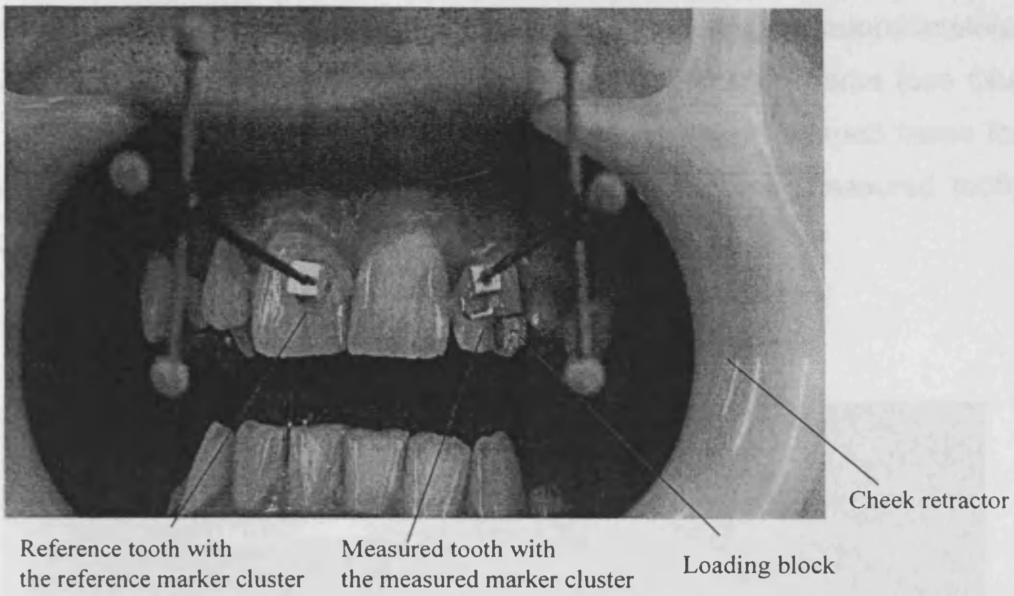

Figure 7.1 The mouth opened using a cheek retractor and teeth with the marker clusters and the loading block.

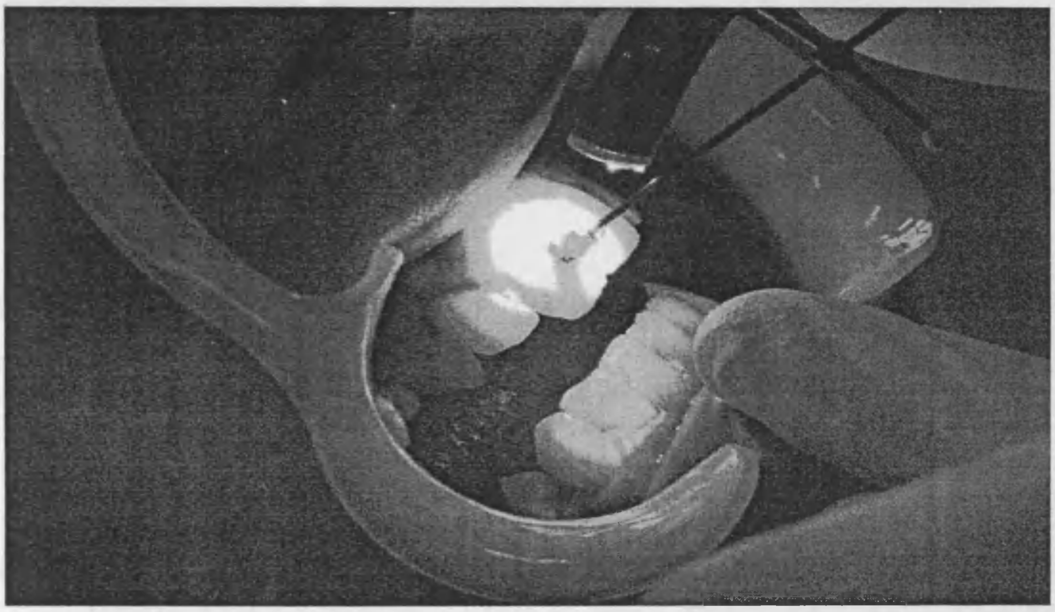

Figure 7.2 A clinical orthodontic specialist is fixing the marker clusters on the measured tooth and the reference tooth using the specific brackets, cement and the ultraviolet light.

Two Qualisys MCUs were placed with a convergence angle of approximately 75°. The motion capture system was calibrated by a calibration frame (see Chapter 3). The volunteer's head was relaxed to rest on a bridge shaped frame for the stable measurements while the load was applied to the measured tooth, as shown in Figure 7.3.

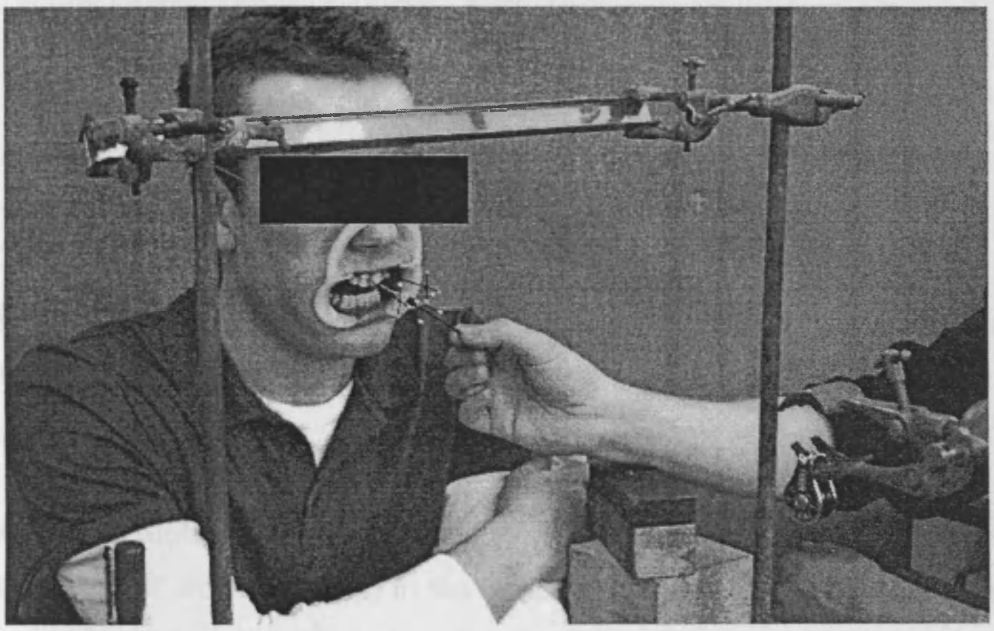

Figure 7.3 The volunteer's head was relaxed to rest on a bridge shaped frame and the pointer used to identify the three landmarks.

Three landmarks were identified using the marked pointer (see Chapter 4) on the measured tooth, in Figure 7.3. The positions of the three landmarks and the ACS are shown in Figure 7.4. The ACS was determined by the developed data analysis software (detail see Chapter 4).

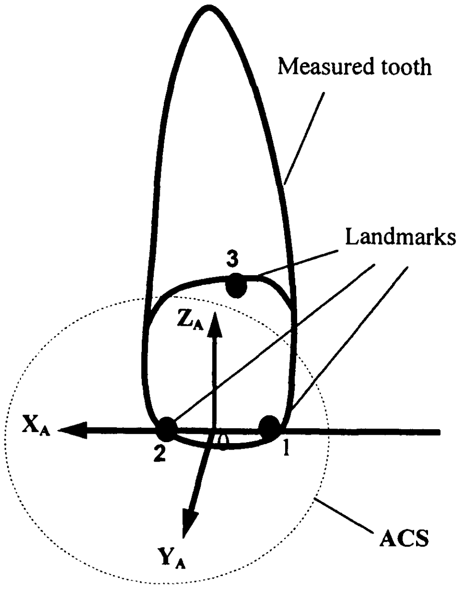

Figure 7.4 The positions of the three landmarks identified in the experiments, and the ACS.

Loads of 0.196N, 0.294N and 0.49N were applied to the measured tooth using the method of weight loading, in the buccal direction and the intrusive direction. The loading beam was made by a black carbon fibre with the length of 400mm and diameter of 2mm.

For loading in the buccal direction, before the loading beam was rested on the pulley, its middle point was determined, and a fine wire was fixed at the middle point and held the weight. Then the loading beam, with the weight held by an experimental person, was rested on the pulley. The middle point of the loading beam left a distance with the pulley, and the loading head touched to the loading block on the measured tooth. Then the weight was released resulting in the load in the buccal direction being produced on the measured tooth (see Figures 5.7 and 7.5).

For loading in the intrusive direction, in preliminary stage, the middle point of the loading beam was rested on the pulley; the loading head touched to the bottom edge of the tooth on the measured tooth; the weight was fixed at the other end of the loading beam and held by an experimental person. Then the weight was released resulting in the load being produced on the measured tooth in the intrusive direction. Figure 7.5 shows how the load was applied to the measured tooth in the buccal direction.

Figure 7.5 The load was applied to the measured tooth in the buccal direction.

The loading duration was 10s and 30s. For 10s loading duration, two time phases were used: the first phase took approximately 5s, in which the load was applied to the measured tooth; and then the load was removed from the measured tooth to let the measured tooth restore in the 2nd phase approximately 5s. For 30s loading duration, three time phases were used: the first phase took approximately 5s as the preliminary stage (unloaded); second phase took approximately 10s to act the load to the measured tooth; and then the load was removed from the measured tooth to let it restore in the 3rd phase for approximately 15s. The reasons for choosing the different loads and setting the different loading time phases were: (1) to investigate the amount of tooth movement under the different loads; (2) to investigate the real-time response of tooth movement under the different loads and the different loading time phases. The tooth movements were captured by the Qualisys motion capture system.

The tooth movements in 6DOF were calculated from the captured data using the developed data analysis software (see Chapter 4). Because the original data captured by the motion capture system mixed with noisy signal, noise processing was necessary. In the noise processing, a mean window filter and a digital lowpass Butterworth filter were used to reduce the effect of noise. The results filtered by the different filters are compared.

For the mean window filter, firstly it is necessary to determine a window width, then the mean value of data in the window width is calculated as the measured value; then the window shifts with a step of one sampled frame, the mean value of data in the window width is calculated again as the next measured value; and so on. The mean window filter is a very efficient way to reduce noise and produces a smoothed graph or image. But with a mean window filter, data will be lost at the ends of the sampled data. The number of lost data is equal to a window width. This effect in tooth measurement is discussed in the section 7.4.3. A digital lowpass Butterworth filter needs to designs an order n with cutoff frequency W_n. The digital lowpass Butterworth filter is a frequency filter which is based on the Fourier Transform. The Butterworth filter is realized by a computer with Matlab software in this study. The order and the cutoff frequency of the Butterworth filter were tested with the sampled data. A digital lowpass Butterworth filter in an order 5 with cutoff frequency W_n of 0.1 were designed.

7.3 Results

7.3.1 0.196N and 0.294N loaded in the buccal direction for 10s

When the load of 0.196N and 0.294N were separately applied to the measured tooth in the buccal direction for 10s, the expected tooth translation should be produced in the *y* direction and might be a little displacement in the *x* direction of the ACS, because the loading block was not fixed exactly at the long axis of tooth and the design of the PDL soft tissue displays a structure of inclined fibre to the long axis of tooth; tooth rotation was possibly caused about the *z* and *x* axes of the ACS. From the results of 6DOF, tooth movements were not demonstrated clearly with the load of 0.196N and 0.294N applied to the measured tooth in the buccal direction for 10s, because tooth movements were very small and the measured signals were mixed with various random noises. The experimental results tested with two volunteers in the different ages and the different genders are shown in appendix D (1) and (2) and appendix F (1) and (2).

7.3.2 0.294N loaded in the buccal direction for 30s

When the load of 0.294N was applied to the measured tooth in the buccal direction for 30s, the expected tooth translation should be mainly produced in the *y* direction; tooth rotation was possibly created about the *x* and *z* axes of the ACS. The experimental results show that the tooth translation in the *y* direction and rotation in the *z* direction of the ACS were approximately 32μm and 0.07°. Tooth rotation about the *x* axis was approximately 0.09°. Tooth movements in the other directions could not be clearly identified because the load was too low. The detail tooth movements in 6DOF are shown in appendix D (3).

7.3.3 0.49N loaded in the buccal direction for 30s

When the load of 0.49N was applied to the measured tooth in the buccal direction for 30s, the expected tooth translation should be mainly produced in the *y* direction; tooth rotation was possibly created about the *x* and *z* axes of the ACS. In fact, the experimental results showed that tooth translation in the y direction of the ACS was 41μm and rotations about the *x* and *z* directions of the ACS were 0.1° and 0.06°. Tooth movement in the other directions could not be clearly identified because tooth movement was too small under load of 0.49N. The detail results of tooth movement in 6DOF under load of 0.49N are shown in appendix D (4). Figure 7.6 shows tooth translation in the *y* direction of the ACS under load of 0.49N with the original signal and the signal filtered by a mean window filter.

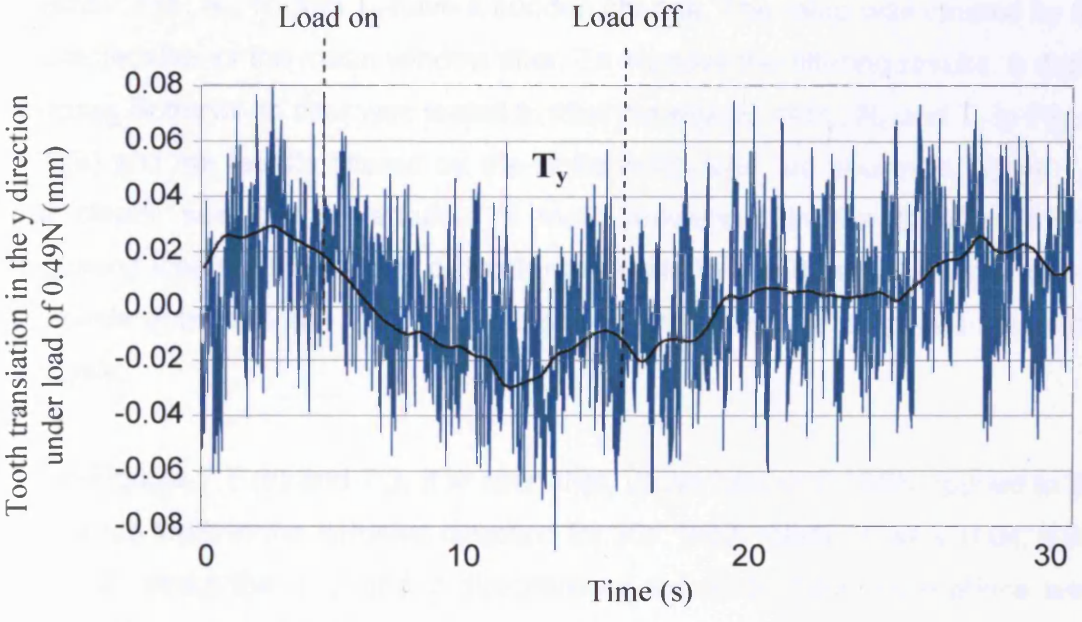

Figure 7.6 Tooth translations in the *y* direction of the ACS under load of 0.49N, the original signal and the signal filtered by a mean window filter

7.3.4 0.196N loaded in the intrusive direction for 30s

When the load of 0.196N was applied to the measured tooth in the intrusive direction for 30s, in an ideal situation, intrusive movement of the tooth should be produced in the *z* direction of the ACS, and no tipping movement would be created. In practice, because the loading block was not fixed exactly at the long axis of the tooth and the design of the PDL soft tissue displays a inclined structure to the long axis of tooth, thus tooth movement may not be produced only in the z direction of the ACS (intrusion), but also tipping movement in the other directions of the ACS. Tooth movements in 6DOF with the original signals and the signals smoothed by a mean window filter are shown in Figure 7.7.

From Figure 7.7 (b), it is seen that the signals filtered by a mean window filter exist a ramp, such as Figure 7.7 (b) R_y, R_z and T_x, when the original signals in Figure 7.7 (a) R_y, R_z and T_x have a sudden change. The ramp was caused by the characteristics of the mean window filter. To improve the filtering results, a digital lowpass Butterworth filter was tested to filter the signals of R_y, R_z and T_x in Figure 7.7 (a) and the results filtered by the Butterworth filter are shown in Figure 7.8. For clearly seeing the variation of tooth movement in the duration of the beginning loading, the graphs of tooth movement in this duration are marked by the circle dots in Figure 7.8. The sections of circle dots are amplified for further analysis.

From Figures 7.7 (b) and 7.8, it is seen that, under load of 0.196N applied to the measured tooth in the intrusive direction for 30s, tooth rotations were 0.04, 0.07° and 0.2° about the *x*, *y* and z directions of the ACS; tooth translations were 37µm, 15µm and 54µm in the *x*, *y* and *z* directions of the ACS. The results tested with another volunteer are shown in appendix F (3) for further study.

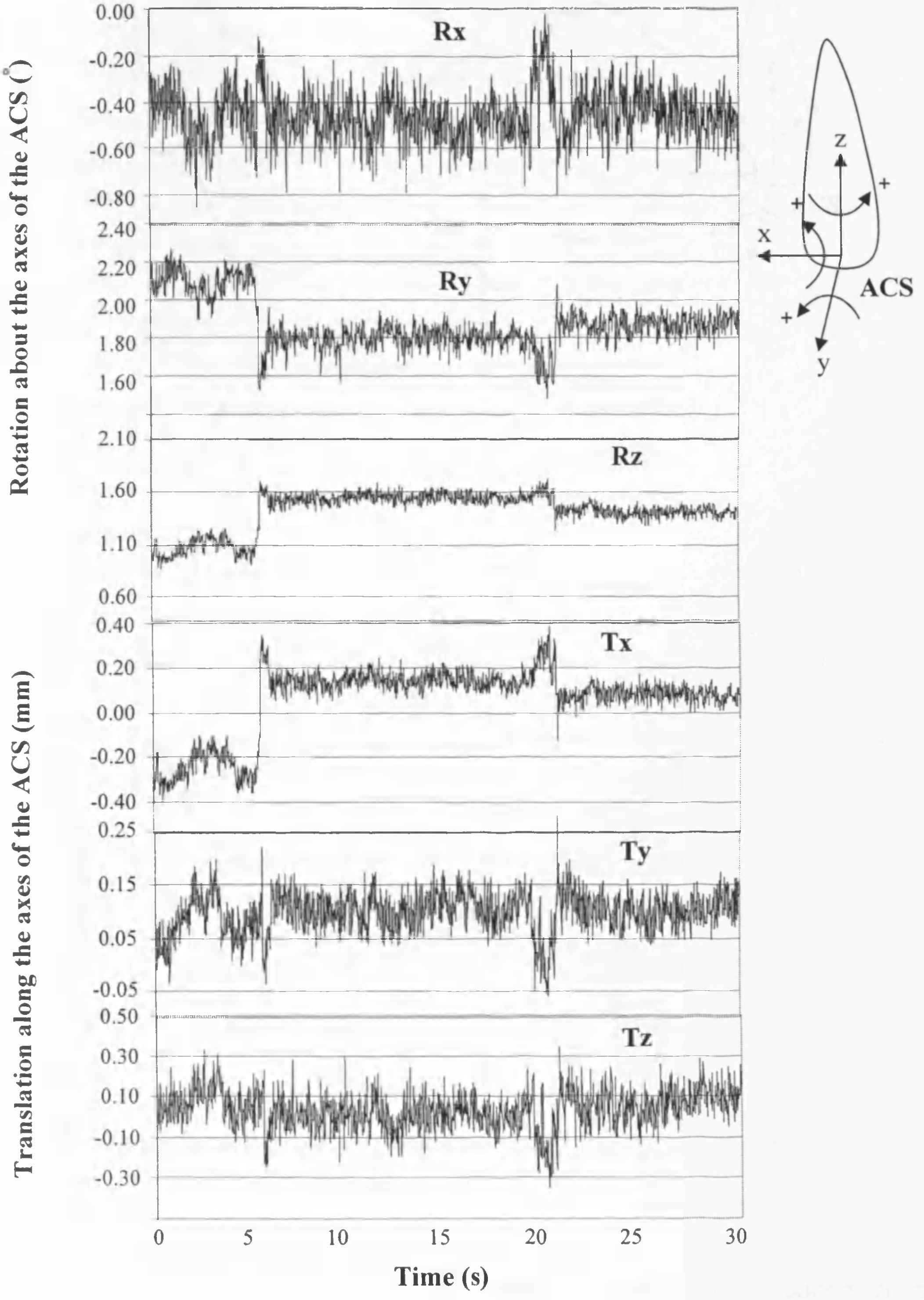

(a) Original signal with load of 0.196N for 30s loaded in the direction of intrusion.

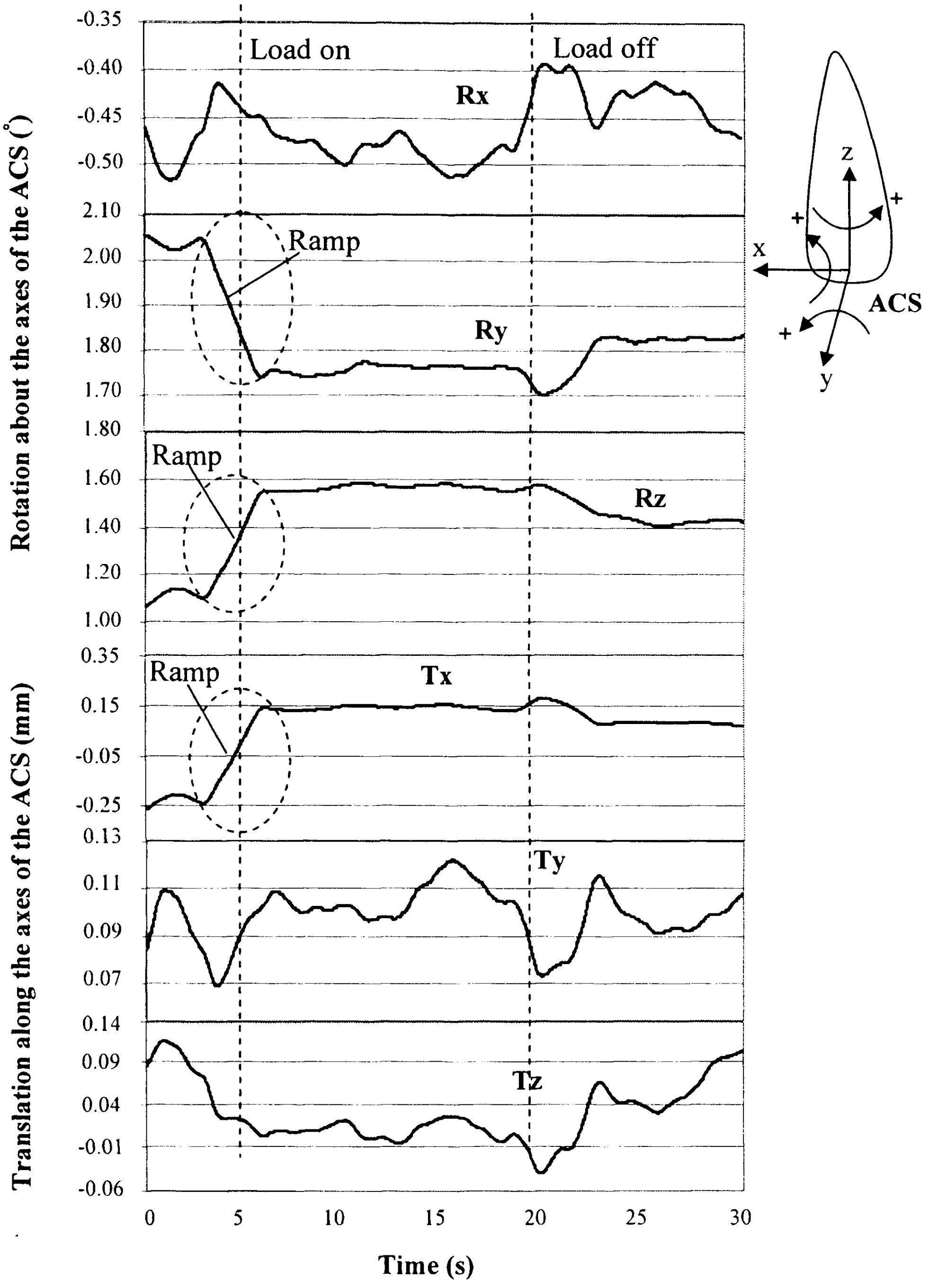

(b) Smoothed signal with load of 0.196N for 30s loaded in the direction of intrusion.

Figure 7.7 Tooth movements in 6DOF under load of 0.196N, loaded in the direction of intrusion for 30s.

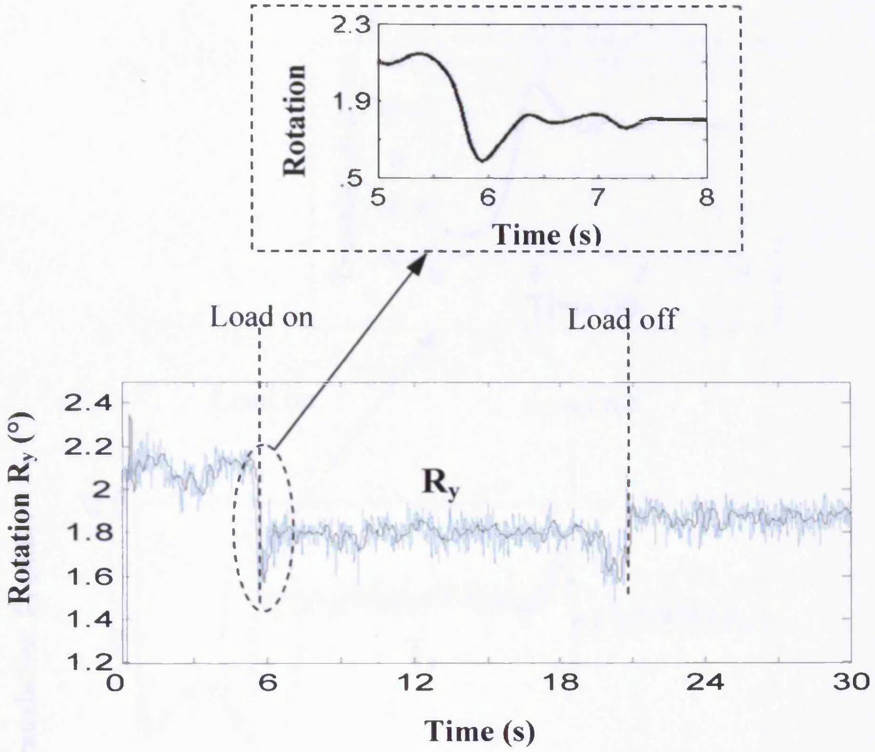
2.3
1.9
.5
Rotation
5
6
7
8
Time (s)
Load on
Load off
2.4
2.2
2
1.8
1.6
1.4
1.2
Rotation R$_y$ (°)
R$_y$
0
6
12
18
24
30
Time (s)

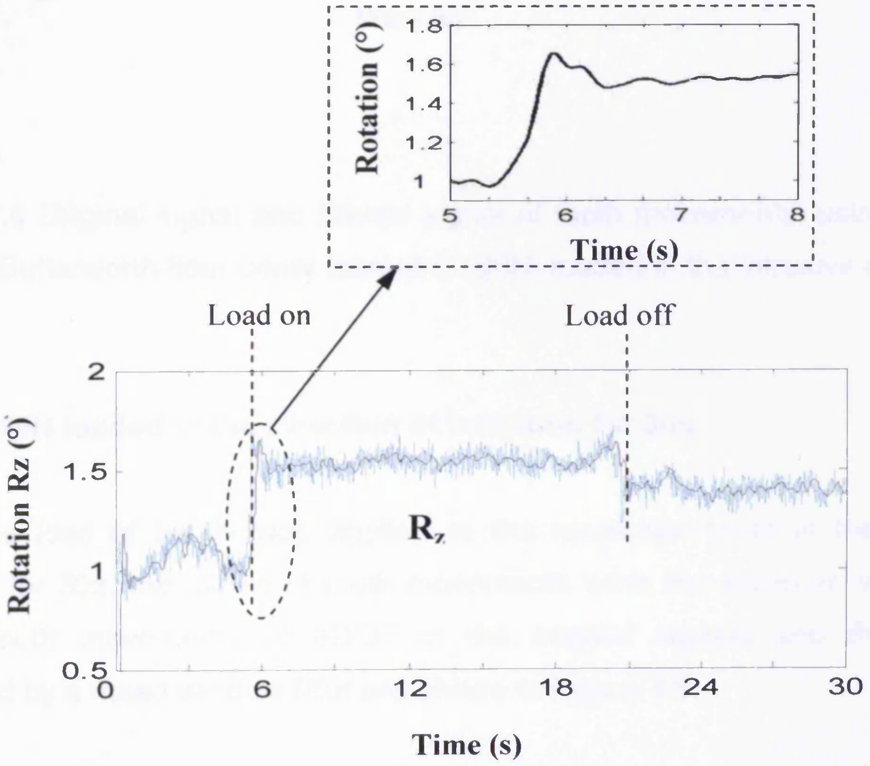
1.8
1.6
1.4
1.2
1
Rotation (°)
5
6
7
8
Time (s)
Load on
Load off
2
1.5
1
0.5
Rotation Rz (°)
R$_z$
0
6
12
18
24
30
Time (s)

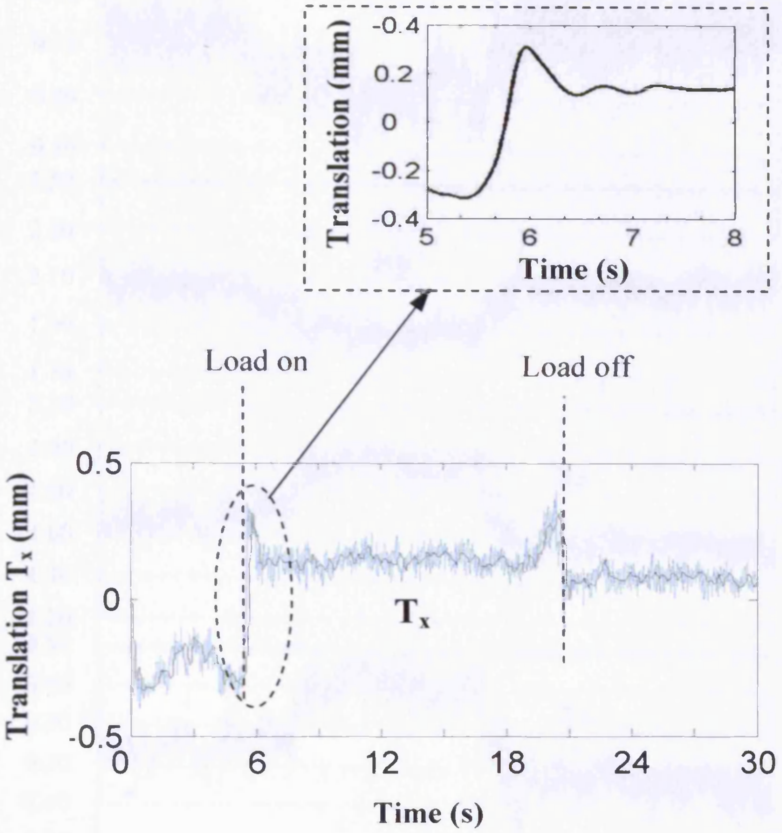

Figure 7.8 Original signal and filtered signal of tooth movements, using a digital lowpass Butterworth filter under load of 0.196N, loaded in the intrusive direction

7.3.5 0.49N loaded in the direction of intrusion for 30s

When the load of 0.49N was applied to the measured tooth in the intrusive direction for 30s, the states of tooth movements were the same as the section 7.3.4. Tooth movements of 6DOF in the original signals and the signals smoothed by a mean window filter are shown in Figure 7.9.

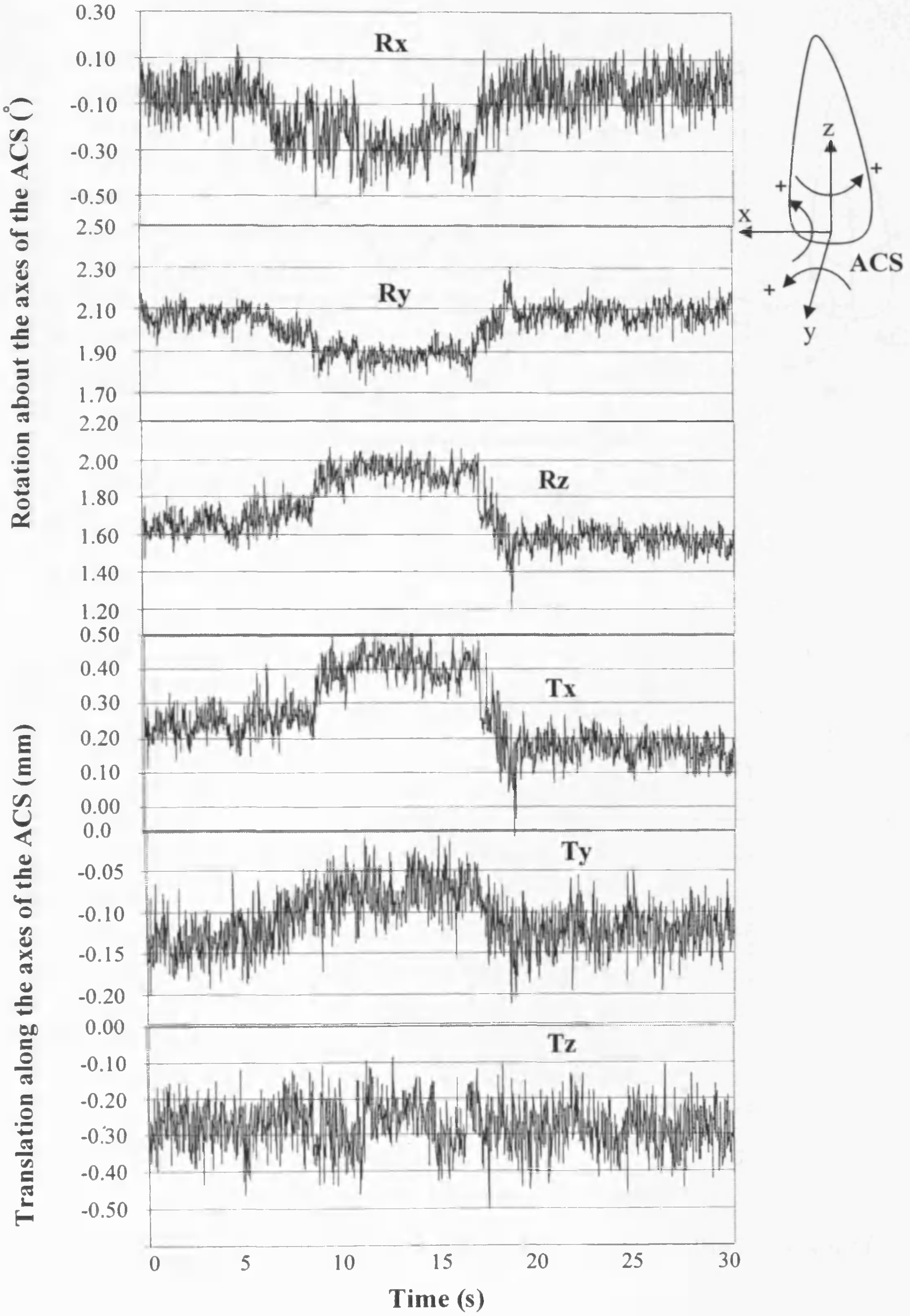

(a) Original signal with load of 0.49N for 30s loaded in the direction of intrusion.

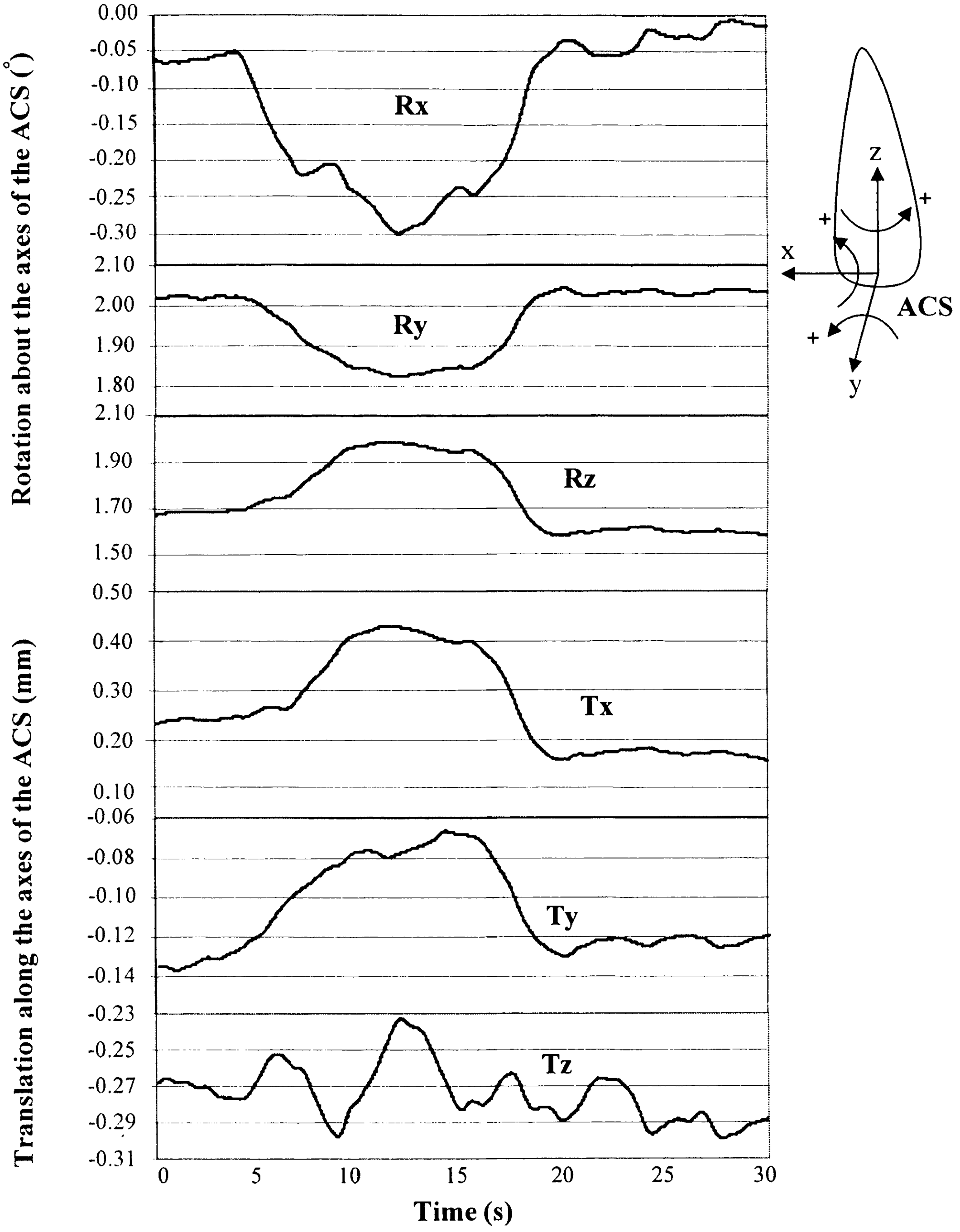

(b) Smoothed signal with load of 0.49N for 30s loaded in the direction of intrusion.

Figure 7.9 Tooth movements in 6DOF under load of 0.49N, loaded in the direction of intrusion for 30s.

From Figure 7.9 (b), it is seen that, under load of 0.49N applied to the measured tooth in the intrusive direction for 30s, tooth translations were 140μm, 51μm and 25μm in the *x*, *y* and *z* directions of the ACS; tooth rotations were 0.26°, 0.19° and 0.35° about the *x*, *y* and *z* directions of the ACS.

7.4 Discussion

7.4.1 Noise

Noise is a random signal mixed within detected signals or images. Its existence would decrease the possibility of a real signal or image being accurately detected. In the measurements of tooth movement, noise is very important, because it could affect a real signal of tooth movement being accurately detected and identified.

In the system of measuring tooth movements, noise may come from many different paths, such as marker clusters instability caused by volunteer's breathing and heartbeat, and air flow, temperature change etc; MCUs vibration caused by environmental or building vibration (ground noise); quantization errors causing corrupted pixels in the camera signal processing; image noise or image instability caused by the marker's surface reflectance textures; and the bar holding the three markers on the cluster may be too long causing vibration etc. All these noises were mixed in the original signals of tooth measurement in the section 7.3.

Generally, in the system of measuring tooth movement, noise could be divided into three types: system noise, man-made noise and environmental noise. The system noise includes quantization errors and image noise. Man-made noise includes breathing, heartbeat and bar vibration etc. Environmental noise includes all instable factors except the system noise and man-made noise. In the measurements of tooth movement, some noises, such as man-made noise and environmental noise, may possibly be reduced. This needs to be proved in the future work.

7.4.2 Noise processing

The aim of noise processing is to obtain a clear, real and smooth image or signal. The method of noise processing often uses a filter to process a noise signal. Filter can be divided into two types: time domain filters and frequency domain filters. Time domain filters, such as window filter, process a signal or an image directly in the time domain. Frequency domain filters process an image or a signal in the frequency domain, such as the Butterworth filter.

A mean window filter was used to reduce the noise in the signal. At the same time, a Butterworth filter was designed for comparing the results with the different filters. The mean window filter uses a shift window through calculating the mean value in the window as a measured value, and then shifts the window with one step, that is one sampled frame, and calculates the next measured value to realise the filtered signal. The advantages of the mean window filter are that it is simple, and reproduces a clear and smooth signal, and a real signal can be restored by using a suitable window width. The disadvantage is losing data at the end of sampled signal. The number of data lost is equal to a window width. In applications, if the window width is too narrow, noise could not be removed sufficiently; if the window width is too wide, the real signal could be distorted, and a number of data is lost at the end of the data. The results filtered by the mean window filter may exist a ramp change in the section which the original signal has a sudden change in. This is because the mean window filter calculates the mean value of the filtered signal in a window width. The Butterworth filter improves this lack of the mean window filter (see Figure 7.8), because the realization of the Butterworth filter is based on the principle of the RC filter. The higher the order of the Butterworth filter, the quicker the drop of the frequency response at the cutoff frequency ω. But the high order of the Butterworth filter will reduce the amplitude of the filtered signal. In this study, the Butterworth filter was designed in an order 5 with the cutoff frequency W_n of 0.1. The relationship between the W_n and the cutoff frequency ω of the frequency response of the Butterworth filter is $W_n = \omega$ /(sampled frequency/2) (The MathWorks, Inc.). That is the cutoff frequency ω of the frequency response of the Butterworth filter is ω=3Hz at the sampled frequency of 60Hz.

In the measurements of tooth movement, an appropriate window width was determined by a number of experiments. This has been proved by the smoothed signals in section 7.3. In noise processing, 5% of the sampled data (the data were captured at the sample frequency 60Hz for 30s) were lost at the end of data. For a graph of tooth movement in section 7.3, this is equal to 1.5s at the end of graph, in which tooth recovering state was missed. This missing could be made up by increasing the experimental time if it is necessary. In fact, for the study of tooth movement, a little missing does not affect the analysis of the relationship between the load and the tooth movement in the loading duration. In the study of tooth movement, the most important thing is tooth movement under load, because it could help orthodontists to make a correct, efficient treatment plan.

7.4.3 Experimental results

From section 7.3.3, it is known that when the load was applied to the measured tooth in the buccal direction, tooth movement was created, not only translation in the expected axis of the ACS, but also rotation about other axes. This may be because the load was not applied at the centre of resistance of tooth; also it was not on the long axis of tooth (the loading model and tooth movement are shown in Figure 7.10). Thus the load produced tooth movements of translation and rotation about the different axes.

With load increasing from 0.294N to 0.49N, tooth translation increased from 32μm to 41μm, increasing 9μm in the *y* axis of the ACS; tooth rotation increased from 0.09° to 0.1°, increasing 0.01° about the *x* axis of the ACS; tooth rotation about the *z* axis remained at the same level. This may be because the break time between two experiments was too short, and residual stress or deformation still remained in the PDL. This resulted in a different fluid pressure distribution in the water and blood surrounding the root of the tooth. Thus the fluid pressure in the water and blood surrounding the root of the tooth resisted tooth movement in the *z* direction. Similar effects may have taken place when the load is applied in the direction of intrusion.

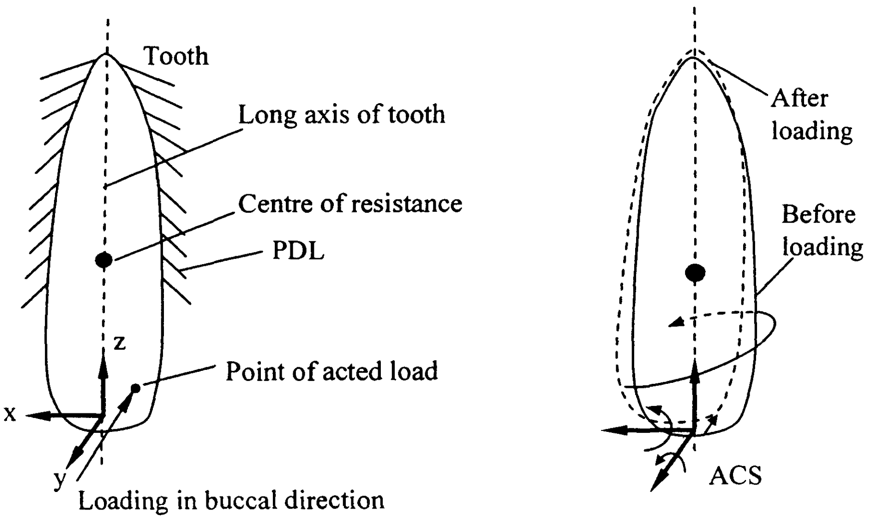

(a) **(b)**

Figure 7.10 (a) loading model of tooth; (b) tooth movements under load.

From section 7.3.4, it is known that when the load was applied to the measured tooth in the intrusive direction, tooth movement was created with translation and rotation in 6DOF. With the load increasing from 0.196N to 0.49N, tooth translations increased from 37μm and 15μm to 140μm and 51μm, increasing 103μm and 36μm, in the *x* and *y* directions of the ACS respectively, and tooth rotations were increased 0.22°, 0.125° and 0.15° about the *x*, *y* and *z* axes respectively. Tooth translation in the *z* direction was less (29μm) than for the load of 0.196N. The reasons may be that the break time between two experiments was too short; residual stress and deformation in the PDL meant that the PDL at the apical root of the tooth was narrower than the natural state when the load of 0.49N was applied to the measured tooth. Thus fluid pressure surrounding the apical root of the tooth may have resisted tooth translation in the *z* direction of the ACS. The tooth was easily moved in the other directions with less resistance under the action of intrusion force. This explanation could be described in Figure 7.11. From Figure 7.11, it is seen that the design of the PDL makes it easier for the tooth to translate along the *x* and *y* axes, and rotate about the *y* and *z* axes than to translate along the *z* axis.

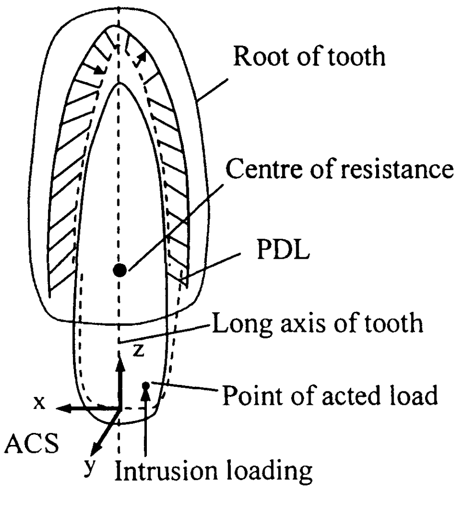

Figure 7.11 The PDL deformation under load in the direction of intrusion.

From section 7.3.4, it is also known that tooth translation in the *z* direction was unstable (or fluctuating). This may be because the *z* direction of the ACS was the same as noise directions produced by environmental vibration, heart beat and breathing etc. Thus the effect of noise in the *z* direction was more evident than in the other directions.

When a fixed load was applied to the measured tooth, tooth movement increased gradually to the maximum value. This shows that the PDL is not completely elastic, but may be viscoelastic. The previous results, of Picton (1962), Wills et al. (1978), Moxham and Berkovitz (1979), also showed that the PDL has viscoelastic properties.

Overall, a novel system of measuring and calculating tooth movement has been sufficiently developed. The system can be potentially useful in applications of many other small-scale measurements.

Chapter 8 Discussion

8.1 Introduction

A novel system of measuring and calculating tooth movement has been developed. Initial experiments with volunteer have been carried out using the system. The particular questions and problems that emerged during the development of the system and the experiments have been discussed in the corresponding chapters. This chapter is a general discussion, and the following aspects will be considered: - the system characteristic parameters and their effects; comparison of the experimental results with previous work in the literature; possible future applications of the system; and the scientific achievements of this study.

8.2 System characteristic parameters and their effects

During the system development, four characteristic parameters of the system were evaluated and discussed in detail in Chapter 3 and 4, namely the resolution, accuracy, repeatability and noise. Of the various possible parameters, accuracy is often used as a representative parameter to describe the system characteristics. In a measurement system, various unstable factors, error and noise directly and indirectly affect the system measurement accuracy. So the overall accuracy presents a complete measurement of the effects of the various unstable factors.

In this project, in fact, two systems were developed: one is the existing QTM system, applied on a small scale; another is called the biomechanical measurement system, which combines the QTM system, data analysis software, and marker cluster and pointer etc to enable measurements of tooth movement under load in 6DOF.

For the QTM system, the system characteristics were evaluated with two different shapes of markers (diamond markers and spherical markers) to compare the difference in the system accuracy. The evaluations showed that the diamond marker had better accuracy than the spherical marker. This may be because the perimeter of the elongated diamond markers is greater which provides more measurement points than for the circular markers. In the development of the QTM system, it was found that many unstable factors affected the system accuracy, such as CCD noise; quantization errors; camera lens distortion; variation of temperature and light intensity; and environmental or ground vibration etc. Of all these factors, ground vibration may be a stronger orientation than others and its effect was found to be more important. This can be seen from Figure 3.9. In Figure 3.9, accuracy in the *y* direction was worse than in the other directions. This may be because the y direction calibrated in the QTM system was the same as the direction of ground vibration. The effects of various unstable factors in the system accuracy were evaluated in terms of noise. Noise presents a random error in the measurement results. It is an important factor that affects the system accuracy.

Resolution and repeatability are two different parameters which are related to accuracy. In a measurement system, accuracy describes an error between the ideal value and the actual value; resolution describes a minimum value which the system can measure or detect. High resolution in a measurement system is a preliminary condition to create high accuracy; high resolution does not guarantee high accuracy. Repeatability and accuracy are two relative characteristic parameters. Generally, they have the following relationships: that is, high accuracy certainly leads to high repeatability, but high repeatability does not always imply high accuracy. This relationship can be seen in the developed system, in Figures 3.9 and 3.10, 3.14 and 3.15.

8.3 Comparison of the experimental results with previous work

In the experimental results in Chapter 7, it was seen that when the load was applied to the measured tooth in the buccal direction, the tooth translations were 32μm for a load of 0.294N and 41μm for a load of 0.49N in the *y* direction of the ACS, tooth rotations were 0.09° and 0.07° for load of 0.294N and 0.1° and 0.06° for load of 0.49N in the *x* and *z* directions; when the load was applied in the intrusive direction, tooth movements were 37μm, 15μm and 54μm for load of 0.196N and 140μm, 51μm and 25μm for load of 0.49N in the *x, y* and *z* directions of the ACS, tooth rotations were 0.04°, 0.07° and 0.2° for load of 0.196N and 0.26°, 0.195° and 0.35° for load of 0.49N about the *x, y* and *z* directions. These results demonstrated that (1) tooth translation occurred in the buccal direction when load was applied in this direction; (2) when load was applied in the intrusive direction, the tooth movements that were created were not only translations, but also rotations in 6DOF; (3) the results corroborate the previous finding (Picton 1962, Wills et al. 1978, Moxham and Berkovitz 1979) that the PDL may have a viscoelastic property. These results give a practical description and quantity of tooth movement under load, and could be useful as reference for orthodontists in treatment of patients being more efficiently and economically in time and cost.

Comparing the results with previous work, Hickman (1997) found that a load of 0.5N, which was applied to human upper central incisors in the lingual direction, produced tooth displacements of approximately 12–132μm. She measured tooth movement in one dimension using a LAS5010 laser displacement sensor. Muhlemann (1951) employed a dial indicator attached intra-orally to record the displacement of the central incisor of a monkey and found that a load of 1N produced a tooth displacement of approximately 150μm. Parfitt (1960) reported that tractional forces of approximately 0.15N and 0.3N in the extrusive direction caused tooth displacement of a human maxillary central incisor of approximately 6μm and 8μm, and 1N caused tooth displacement of about 20μm. Picton (1962, 1963) used similar apparatus (strain gauge and movement transducers) to study tooth movement in the human maxillary incisor, and obtained similar results to those of Parfitt (1960). However, Picton emphasized that since the adjacent reference teeth were also probably displaced by the load, the values obtained for tooth displacement were not to be regarded as absolute.

Obviously, the different measurement methods, objects and loads created different results in terms of tooth movement. However, there is one result which was coincident in all these experiments: i.e., tooth movement was easily produced in the buccal direction when load was applied in this direction. This can be seen from comparing all experimental results in the similar loads, but giving different quantity of tooth movements: (1) when the load was approximately 0.5N and loaded in the lingual or buccal direction, tooth movements produced in the same direction were: Hickman, 12-132μm on human tooth; my result, 41μm on human tooth; (2) when the load was applied in the intrusive or extrusive direction, tooth movements produced in the same direction were: Parfitt, 20μm under load of 1N on human tooth; my result, 25μm under load of 0.49N on human tooth.

To analyse the different results given by the different measurement methods, we found that: (1) the laser displacement sensor was used to measure the movement of the light spot, and then to determine tooth movements according to a triangulation method. Thus when it was used to measure tooth movement, instability of head or breathing of the volunteer would directly affect the correctness of measurement results; (2) the dial indicator has a similar problem to the laser measurement method, because the dial indicator uses a probe to touch on the measured tooth to measure the displacements of tooth under load. Instability of head or apparatus could lead to incorrect results; (3) for strain gauge and movement transducers, drift of time and temperature in the signal processing circuit and circuit noise would bring errors in the measurement results and Picton has mentioned that since the adjacent reference teeth were also probably displaced by the load, the results of tooth movement were not to be regarded as absolute.

Regarding the different measurement methods, it is seen that previous methods of measuring tooth movement only produced results in one dimension. To date, the system developed in this study is unique, as it can measure tooth movement in living human teeth and produce precision results in 6DOF. This is important to measure tooth movement in 6DOF because the experimental results demonstrated that the teeth may move more about different axes than in the loading direction.

8.4 Applications

The QTM motion capture system can be used in micro-scale measurements, to detect displacements and deformations of structures and materials under load in 3D space. It could be useful, as a novel optical precision measurement system, for applications in a wider engineering field. The system can use the diamond markers and spherical markers.

The biomechanical measurement system could be useful in areas such as biomechanical studies; dental implant research; tooth and jaw movement etc, in which it is necessary to detect or measure the movements with 6DOF in 3D space. In such applications, the system requires two marker clusters and a pointer, and the marker clusters need to be fixed on the measured objects.

This system may be useful in applications of language study, such as speech; or spatial state research, such as determining the relative state of two spatial objects in 6DOF.

8.5 Scientific achievements

1. Motion analysis techniques can be applied not only in large field of view to measure gait or posture etc, but also in a small field of view to measure micro scale movements, such as tooth movements;

2. Tooth movement can be measured in living human teeth with 6DOF in 3D using motion analysis techniques. This has advanced techniques for tooth which could only be measured in one dimension before;

3. The experimental results demonstrated that tooth movements under load can be produced more about different axes, including translations and rotations, than in the loading direction;

4. The experimental results showed that the large tooth movement occurs in the buccal direction under load applied in this direction;

5. Based on current work, five papers have been published: one was published by the Journal of Biomechanics (Liu et al. 2005); four have been presented in different conferences. They were: The Fourth IASTED International Conference on Biomedical Engineering (Liu et al. 2006a); 7th International Symposium on Computer Method in Biomechanics and Biomedical Engineering (Liu et al. 2006b); ISB 9th International Symposium on the 3D Analysis of Human Movement (Liu et al. 2006c); 5th World Congress of Biomechanics (Liu et al. 2006d).

Chapter 9 Conclusions and further work

9.1 Conclusions

1. The Qualisys ProReflex-MCU120 motion capture system has been used for small scale measurements and the system characteristics were evaluated. The results demonstrated that the Qualisys ProReflex-MCU120 motion capture system can be applied not only in a large field of view to study posture, knee function, gait etc, but also in a small field of view to accurately measure small scale movements, such as tooth movements.

2. The evaluation of the effects of camera convergence angle provides valuable information for future clinical experiments.

3. Data analysis software has been developed to process tooth movements in 6DOF using captured data. The developed software can be used in applications of dental implant or jaw movement research.

4. The 3D pointer can be automatically calibrated with the developed software.

5. Noise has been processed to obtain smooth graphs.

6. Characteristics of a complete system, combining the QTM system, data analysis software, marker clusters, pointer etc, have been evaluated. The results demonstrated that the system can measure tooth movement accurately and could be useful in applications of dental implant research or chewing movement study etc.

7. Tooth loading devices were designed and evaluated. The components using in the loading devices were selected. The different designs offer various possibilities for future development and could be useful for other researchers in this field.

8. The loading control system was designed and tested in breadboard form. Detailed information was provided, such as circuit parameters, element selections, sensor application and actuator etc. The control method can be used not only in tooth measurement, but also in some other applications, such as position control etc.

9. The literature on tooth movement and properties of the PDL has been systematically reviewed, together with that on relevant measurement techniques and data processing methods.

10. A novel system of measuring and calculating tooth movement has been developed. The system combines multi-disciplinary knowledge and techniques. This development will open up many possibilities in dental research and provides a valuable tool to study the properties of the PDL.

9.2 Further work

1. To establish a robust and accurate relationship between load and tooth movements in 6DOF through a number of experiments in young adult volunteers, male and female with healthy teeth and regular array.

2. To establish a substantial finite element model of the PDL to allow quantitative determination of the material parameters of the PDL, using an inverse FE approach to identify parameters in an appropriate material model.

3. To connect with clinical treatments, validate the FE model of the PDL and make it has a practical value in the field of orthodontics.

Reference

Analog Devices, Data sheets, *Analog devices, Inc.* 2004.

Angeli, T. 2001. Simulation and measurement results of knee extention activated physiologically and by means of function electrical stimulation. *Computer Methods in Biomechanics and Biomedical Engineering, Rome, Italy.*

Anneroth, G., and Ericsson, S.G., 1967. An experimental histological study of monkey teeth without antagonist. *Odontologisk Revy.* 18, pp345.

Ashby, F. Michael, 1993. Materials Selection in Mechanical Design. *Oxford: Pergamon.*

Baker, M. J., 1998. Maths - Cartesian coordinate systems – Rotations. [www]. <URL: http://www.euclideanspace.com/maths/geometry/coordinatesystems/rotation/index.htm. (15 March 2005).

Berkovitz, B.K.B., Moxham, B.J. and Newman, H.N. 1995. The periodontal ligament in health and disease. *Second Edition. London : Mosby-Wolfe.*

Bourauel, C., Vollmer, D., Jäger, A. 2000. Application of Bone Remodeling Theories in the Simulation of Orthodontic Tooth Movements. *Journal of Orofacial Orthopedics.* 61 (4), pp266 – 279.

Bradlaw, R., 1939. The innervation of teeth. *Proceedings of the Royal Society of Medicine.* 32, pp1040-1053.

Brashear, A.D., 1936. The innervation of the teeth. An analysis of nerve fibre components of the pulp and peridental tissues and their probable significance. *The Journal of Comparative Neurology.* 64, pp169-185.

British Orthodontic Society, 2001. [www]. <URL: http://news.bbc.co.uk/1/hi/health/1370783.stm, (06 May 2004)

Buckingham, M.J., 1983. Noise in electronic devices and systems, *Chichester [West Sussex, England] : E. Horwood ; New York : Halsted Press.*

Burr, H.A., 1981. Mechanical Analysis and Design. *New York : Elsevier.*

Burstone, C.J., Pryputniewicz, R.J. and Bowley, W.W., 1978. Holographic measurement of tooth mobility in three dimensions. *Journal of Periodontal Research.* 13, pp283-294.

Cappello, A., Cappozzo, A., Della-Croce, U. and Leardini, A., 1997. Bone position and orientation reconstruction using external markers. In: P. Allard, A. Cappozzo, A. Lundberg and C. Vaughan, Editors, *Three Dimensional Analysis of Human Locomotion, London, John Wiley & Sons Ltd*, pp147–172.

Cappozzo, A., Catani, F., Leardini, A., Benedetti, M.G. and Della-Croce, U., 1996. Position and orientation in space of bones during movement: experimental artifacts, *Clinical Biomechanics*. 10, pp90–100.

Cawthorne, A.B. Whan, C.B. Lobb, C.J., 1997. Influence and evaluation of parasitic inductance in shuntedJosephson junctions. *IEEE Transactions on Applied Superconductivity*. Volume: 7 (2), Part 3, pp 2355-2358.

Che, D., Bao, Y., Muller, U.R., 2001. Novel surface and multicolor charge coupled device-based fluorescent imaging system for DNA microarrays. *Journal of Biomedical Optics*. Vol. 6 (4), pp. 450-456.

Chow M.Y. and Tipsuwan, Y., 2003. Gain adaptation of networked DC motor controllers based on QOS variations. *IEEE Transactions on industrial electronics*. Vol. 50(5), pp936-943.

Coehlo, A. and Moxham, B.J., 1989. Intrusive mobility of the incisor tooth of the guinea pig. *Archives of Oral Biology*. 34, pp383-386.

Cook, G.F., 1999. Pulse width modulator for 12 and 24 volt applications. [www]. <URL: www.solorb.com/elect/solarcirc/pwml. (15 March 2005).

Coolidge, E.D., 1937. The thickness of the human periodontal membrane. *Journal of the American Dental Association*. 24, pp1260.

D'apuzzo, N., 2000. Motion capture by least squares matching tracking algorithm. *Proceeding of Avatars2000, 30 November – 1 December, Lausanne, Switzerland.* pp124-132.

De Asla, R.J., Wan, L., Rubash, H.E., Li, G., 2006. Six DOF in vivo kinematics of the ankle joint complex: Application of a combined dual-orthogonal fluoroscopic and magnetic resonance imaging technique. *Journal of Orthopaedic Research*. 24(5), pp1019-1027.

DeLong, R; Ko, C-C; Olson, I; Hodges, J S; Douglas, W H, 2002. Helical axis errors affect computer-generated occlusal contacts. *Journal of Dental Research*. 81 (5), pp338-343.

Dental education, 1997. [www]. <URL: *http://www.tooth.net/info/Toothdevelpprimary.htm* (07 February 2004).

Diamant, J., Keller, A., Baer, E., Litt, M. and Arridge, R.G.C., 1972. Collagen ultrastructure and its relation to mechanical properties as a function of ageing. *Proceedings. Biological sciences / The Royal Society.* 180, pp293-315.

Dixon, J. and Leal, I.A., 2002. Current control strategy for brushless DC motors based on a common DC signal. *IEEE Transactions on Power Electronics.* Vol.17(2), pp232-240.

Dorow C, Krstin N, Sander FG. 2002a. Experiments to determine the material properties of the periodontal ligament. *Journal of Orofacial Orthopedics.* 63(2), pp94-104.

Dorow C, Krstin N, Sander FG. 2003a. Determination of the mechanical properties of the periodontal ligament in a uniaxial tensional experiment. *Journal of Orofacial Orthopedics.* 64(2), pp100-107.

Dorow, C., Krstin, N. Sander, F.G., 2003b. Determination of the mechanical properties of the periodontal ligament in a uniaxial tensional experiment. *Journal of orofacial orthopedics.* pp1434-5293.

Dorow, C., Krstin, N., Sander, F.G., 2002b. Examination of the viscoelastic material properties of the periodontal ligament "in vivo". *The 5th international symposium on computer method in biomechanics and biomedical engineering-4.*

Dorow, C., Krstin, N., Sander, F.G., 2002c. Experimental model of tooth mobility in the human "in vivo". *Biomedical Technology.* 47(1-2), pp20-25.

Dorow, C., Schneider J. and Sander, F. G., 2003c. Finite element simulation of in vivo tooth mobility in comparison with experimental results. *Journal of Mechanics in Medicine and Biology.* 3 (1), pp79-94.

Droschl H, Bantleon HP, Muchitsch AP, Weiland F., 1992. A new method for the quantitative and qualitative measurement of tooth movements. *Fortschr Kieferorthop.* 53(1), pp11-15.
Faires, Virgil Moring 1965. "Design of Machine Elements. *New York, Macmillan.*

Friedrich, D., Rosarius, N., Ran, G., Diedrich, P., 1999. Measurement system for in vivo recording of force system in orthodontic treatment-concept and analysis of accuracy. *Journal of Biomechanics.* 32, pp81-85.

Fullmer, H.M., 1959. Observations on the development of oxytalan fibres in the periodontium of man. *Journal of Dental Research.* 38, pp510-516.

Gallo, L. M.; Fushima, K.; Palla, S. 2000. Mandibular helical axis pathways during mastication. *Journal of Dental Research*. 79 (8), pp1566-1572.

Gallo, L. M; Airoldi, G. B; Airoldi, R. L; Palla, S. 1997. Description of mandibular finite helical axis pathways in asymptomatic subjects. *Journal of Dental Research*. 76 (2), pp704-713.

Green, T.P., Allvey, C. J. and Adams, A.M., 1994. Spondylolysis. Bending of the inferior articular processes of lumber vertebrae during simulated spinal movements. *Spine*. 19(23), pp 2683-2691.

Grood, E.S. and Suntay, W. J., 1983. A joint coordinate system for the clinical description of three – dimensional motions: application to the knee. *Journal of Biomechanical Engineering.* 105, pp136-144.

Grubb D., 1999. Structure and properties of teeth - natural composite materials. [WWW]. <URL: *http://dentistry.umkc.edu/microscopy/ESEMPICT/dent-jimst.JPG* (06 February 2004)

Haggman-Henrikson, B., Eriksson, P. O., Nordh, E. and Zafar, H., 1998. Evaluation of skin- versus teeth-attached markers in wireless optoelectronic recordings of chewing movements in man. *Journal of Oral Rehabilitation*. 25(7), pp527-534.

Hayashi, K., Araki, Y., Uechi, J., Ohno H. and Mizoguchi, I., 2002. A novel method for the three-dimensional (3-D) analysis of orthodontic tooth movement – calculation of rotation about and translation along the finite helical axis. *Journal of Biomechanics*. 35, pp45-51.

Heners, M., 1974. Syndesmotic limiting movement of the periodontal ligament. *International dental journal*. 24, pp319-327.

Hickman, J., 1997. A Validated finite element method study of maxillary incisor tooth movement. *MSc Thesis in Cardiff University.*

Higgins, J. and Molloy, D. 2003. "Model Based Approach to Non-Intrusive Human Motion Capture", *Irish Signal and Systems Conference 2003, Limerick, 30 June - 2 July.*

Hinterkausen M., Bourauel C., Siebers G., Haase A., Drescher D. and Nellen B., 1998. In vitro analysis of the initial tooth mobility in a novel optomechanical set-up. *Medical Engineering & Physics*. 20, pp40-49.

Hirokawa, S., Yamamoto, K., Ishikawa S. and Tsuruno R., 2001. Measurement of strain distribution on the ACL using a modified motion capturing method. *5th. International Symposium on Computer Method in Biomechanics & Biomedical Engineering-3, Rome, October.*

Holt, C.A., Hayes, N. J., van Deursen, R. W .M. and O'Callaghan, P. O., 2000. Three-dimensional analysis of the tibiofemoral joint using external marker clusters and the JCS approach – Comparison of normal and osteoarthritic knee function. *5th. International Symposium on Computer Methods in Biomechanics and Biomedical Engineering 3, Rome, October.* pp. 289-294.

Hunt, C. M., Evans, S. L., Holt, C. A., Jones, L., Ahuja, S., Dillon, D., Davies P. and Howes, J., 2001. The use of 3D motion analysis techniques to measure the effect of pedicle screw system with cross-links on spine stability. *Computer Method in Biomechanics & Biomedical Engineering-3.*

Inoue, Y., 1989. Biomechanical study on orthodontic tooth movement: change in biomechanical property of the periodontal tissue in terms of tooth mobility. *Osaka Daigaku Shigaku Zasshi.* 34(2), pp291-305.

Interface, 2004. Sensor data sheet, *Interface Ltd.*

Intersil, 2001. Data sheets, *Intersil Ltd.*

Ioi H, Morishita T, Nakata S, Nakasima A, Nanda RS., 2002. Evaluation of physiological tooth movements within clinically normal periodontal tissues by means of periodontal pulsation measurements. *Journal of periodontal research.* Apr; 37(2):110-7.

Iwasaki, L. R., Haack, J. E., Nickel, J. C. and Morton, J., 2000. Human tooth movement in response to continuous stress of low magnitude. *American Journal of Orthodontics and Dentofacial Orthopedics.* 117 (2), pp175-183.

Johnson, J.B., 1928. Thermal agitation of electricity in conductors, *Physical Review.* 32, pp97-109.

Jones L., Holt C. A. and Morgan-Jones R. 2001a. A motion analysis application to estimate dynamic frontal plane knee moments for clinical management of tibial osteotomy patient outcomes. *Fifth International Symposium on Computer Methods in Biomechanics and Biomedical Engineering, Rome, October.*

Jones, M. L., Middleton, J., Volp, C., Hickman J. and Danias, C., 2001b. Biomechanical modelling in orthodontics – following a theme? The development of a validation system for modelling orthodontic tooth movement. *5th. International Symposium on Computer Method in Biomechanics &*

Biomedical Engineering – 3. pp 663-672.

Jones, M.L., Middleton, J., Hichman, J., Volp, C., Knox, J., 1998. The development of a validated model of orthodontic movement of the maxillary central incisor in the human subject. *Russian Journal of Biomechanics.* 2, pp36-44.

Kawarizadeh, A., Bourauel, C., Zhang, D., Götz, W., Jäger, A., 2004. Correlation of stress and strain profiles and the distribution of osteoclastic cells induced by orthodontic loading in rat. *European Journal of Oral Sciences.* 112, pp140-147.

Knets, I., Laizans J., Dobelis M., Middleton J., Bigestans A., Vitins V., 2001. Stress analysis in the human mandible during simulated tooth clenching. *In: Computer Methods in Biomechanics & Biomedical Engineering-3, J. Middleton, M.L. Jone, N.G. Shrive, G.N. Pande (eds), The Netherlands, Gordon and Breach Science Publishers.* pp. 661-666.

Knox, J., Jones, M. L., DlpL-lng, P. H., Middleton J., and DlpL-lng, B. K., 2000. An evaluation of the stresses generated in a bonded orthodontic attachment by three different load cases using the finite element method of stress analysis. *Journal of orthodontics.* 27, pp 39-46.

Kronfeld, R., 1931. Histologic study of the influence of function on the human periodontal membrane. *Journal of the American Dental Association.* 18, pp1242.

Krstin, N., Dorow, C., Franke, R.P., Sander, F.G., 2002a. Experiments to determine the time dependent material properties of the periodontal ligament. *Biomedical Technology.* 47(7-8), pp202-208.

Krstin, N., Dorow, Ch., Franke, R.P. and Sander, F.G., 2002b. Experiment investigation of the viscoelastic material behavior of the periodontal ligament on specimens in vitro. *American Journal of Orthodontics and Dentofacial Orthopedics.* 121, pp257-65.

Kwon, Y. H., 1998. Axis transformation. [WWW]. <URL: *http://kwon3d.com/theory/transform.html* (26 February 2006).

Lashley, K.S., 1916. Reflex secretion of the human parotid gland. *Journal of Experimental Psychology.* 1, pp461-493.

Lewinsky, W. and Stewart, D., 1936. The innervation of the periodontal membrane. *Journal of Anatomy*. 71, pp98-102.

Lawson, N.J., Wu, J., 1997. Three-dimensional particle image velocimetry: error analysis of stereoscopic techniques. *Measurement Science and Technology*. 8, pp894-900.

Liu H., Holt C. Evans S. 2005. Accuracy and Repeatability of an Optical Motion Analysis System for Measuring Small Deformations of Biological Tissues. *Journal of Biomechanics*, on processing.

Liu H. Evans, S., Holt, C., Zhurov A. and Middleton. J. 2006a. Development of an optical motion analysis system to measure small movement in three-dimensional space. Proceedings of the fourth IASTED international conference on biomedical engineering. Innsbruck, Austria.

Liu, H., Holt, C., Evans, S., Zhurov A. and Middleton, J. 2006b. Three Coordinate Systems Method to Calculate Tooth Movement of Six Degrees of Freedom Using Motion Capture Data. The CMBBE, 7th international conference of computer methods on the biomechanics and biomedical engineering. Nice, France.

Liu, H., Holt, C., Evans, S.L. 2006c. Measuring tooth movement in 3D. The ISB, Ninth International Symposium on the 3D Analysis of Human Movement. Valenciennes, France.

Liu, H., Evans, S. L., Holt, C. Zhurov, A., Middleton J. and Knox, J. 2006d. Development of novel techniques in vivo measurement of mechanical properties of periodontal ligament. The 5th World Congress of Biomechanics. Munich, Germany.

Marsden, J.E. and Hughes, T.J.R., 1982. Mathematical foundations of elasticity. *Englewood cliffs: Prentice-hall* [2].

McGuiness, N. J. P., Wilson, A., Jones, M. L. and Middleton, J., 1991. A stress analysis of the periodontal ligament under various orthodontic loadings, *European Journal of Orthodontics*. 13, pp231–242.

McGuinness, N., Wilson, A.N., Jones, M., Middleton, J., Robertson, N.R., 1992. Stresses induced by edgewise appliances in the periodontal ligament – a finite element study. *The Angle Orthodontist*. 62(1), pp15-22.

Middleton J, Jones, M.L. and Wilson, A. N., 1990. Three-dimensional analysis of orthodontic tooth movement. *Journal of Biomedical Engineering*. 12 (4), pp319-327.

Middleton J, Jones, M.L. and Wilson, A. N., 1996. The role of the periodontal ligament in bone remodelling - the initial development of a time dependent model. *American Journal of Orthodontics & Dentofacial Orthopaedics*. 109 (2), pp155-162.

Middleton, J., Jones M. L. and Wilson, A. N. 1990. Three-dimensional analysis of orthodontic tooth movement. *Journal of Biomedical Engineering*. 12 (4), pp319-27.

Miura H, Hasegawa S, Okada D, Ishihara H. 1998. The measurement of physiological tooth displacement in function. *Journal of medical and dental sciences*. June; 45(2):103-15.

Moxham, B.J. and Berkovitz, B.K.B., 1979. The effect of axially directed intrusive loads and movements of the mandibular incisor of the rabbit. *Archives of Oral Biology*. 24, pp759-763.

Mühlemann, H.R., 1951. Periodontometry: a method for measuring tooth mobility. *Oral Surgery, Oral Medicine, Oral Pathology*. 4, pp1220-1233.

Murray, N., Goulermas, Y. and Fernando, T., 2003. Visual Tracking for a Virtual Environment. *9th International Conference on Human-Computer Interaction*. 1, pp1198-1202.

Natali A, Pavan P, Carniel E, Dorow C., 2004. Viscoelastic response of the periodontal ligament: an experimental-numerical analysis. *Connect Tissue Research*. 45(4-5), pp222-30.

Natali, A., Pavan, P., Pini, M., and Ronch, R., 2000. Numerical analysis of short time response of periodontal ligament. *12th conference of the European society of biomechanics, Dublin*. p29

NSF controls Limited Keighley, 2003. Data sheets.

Nyquist, H., 1928. Thermal agitation of electric charge in conductors. *Physical Review*. 32, pp110-113.

Orthodontics, 1999. [WWW]. <URL: http://www.unc.edu/depts/appl_sci/ortho/toothmovement/. (18 February 2004).

Pfaffmann, C., 1939. Afferent impulses from the teeth due to pressure and noxious stimulation. *Journal of Physiology*. 97, pp207-219.

Palmer, R., 1999. Teeth and implants. *British Dental Journal*. 187 (4), pp183-188.

Parfitt, G.J., 1960. Measurement of the physiological mobility of individual teeth in an axial direction. *Journal of Dental Research.* 39, pp608-618.

Park, W., Chaffin, D.B., Martin, B.J., Faraway, J.J. 2004. A computer algorithm for representing spatial–temporal structure of human motion and a motion generalization method. *Journal of Biomechanics.* 38(11), pp2321-2329.

Pedersen, E; Andersen, K; Gjessing, P E., 1990. Electronic determination of centres of rotation produced by orthodontic force systems. *European Journal of Orthodontics.* 12 (3), pp272-280.

Picton, D.C.A., 1962. Tilting movement of teeth during biting. *Archives of Oral Biology.* 7, pp151-159.

Picton, D.C.A., 1963. Vertical movement of cheek teeth during biting. *Archives of Oral Biology.* 8, pp109-118.

Picton, D.C.A., 1964. The effect of repeated thrusts on normal axial tooth mobility. *Archives of Oral Biology.* 9, pp55-63.

Picton, D.C.A., 1989. The periodontal enigma: eruption versus tooth support. *European Journal of Orthodontics.* 11, pp430-439.

Pini, M., Botsis,J., Zysset, Ph., Scherrer, S., and Contro, R., 2000. Tensile and compressive mechanical properties of the bovine periodontal ligament. *12th conference of the European society of biomechanics, Dublin.* p28.

Plant Control & Automation, 2000. [WWW]. <URL: http://www.pca-aus.com.au/products/manufacturer/nippon_5010.html (16 March 2004).

Polak, Peter 1991. Engineering Design Elements. McGraw-Hill.

Pryputniewicz, R. J., Burstone, C. J. and Bowley, W. W., 1978. Determination of arbitrary tooth displacements. *Journal of Dental Research.* 57, pp663-674.

Qian, H., Chen, J., and Katona, T.R., 1999. A finite element analysis of the influence of PDL fibres on orthodontic tooth movement. *International society of biomechanics meeting, Calgary.*

Qualisys Track Manager (QTM) User Manual, 2004. *Qualisys Company, Sweden.*

Ren, Y., Maltha, J.C., Van 't Hof, M.A. and Kuijpers-Jagtman, A.M., 2003. Age Effect on Orthodontic Tooth Movement in Rats. *Journal of Dental Research.* 82(1), pp 38-42.

Rhee, J. N., Chun, Y. S., and Row, J., 2001. A comparison between friction and frictionless mechanics with a new typodont simulation system. *American Journal of Orthodontics and Dentofacial Orthopedics.* 119 (3), pp292-299.

Rice G. K. 2006. The technical information on bone remodelling. [WWW]. <URL: http://www.archwired.com/how_braces_work.htm (25 August 2004).

Roberts-Harry, D. and Sandy, J. 2004. Anchorage control and distal movement. *British Dental Journal.* 196, pp255-263.

Ross, G.G., Lear, C.S. and Decou, R., 1976. Modeling the lateral movement of tooth. *Journal of Biomechanics.* 9, pp723-734.

Sander C. Geiger M, Sander F.G., 2002. Contactless measurement of canine retraction by digital macrophotogrammetry during hybrid retractor application. *Journal of Orofacial Orthopedics.* 63(6), pp472-82.

Sloan, P., 1978. Scanning electron microscopy of the collagen fibre architectur of the rabbit incisor periodontium. *Archives of oral biology.* 23, pp567-572.

Smith, R J; Burstone, C J, 1984. Mechanics of tooth movement. *American Journal of Orthodontics.* 85 (4), pp294-307.

Soderkvist I. and Wedin, PA., 1997. Determining the movements of the skeleton using well-configured markers. *Journal of Biomechanics.* 26(12), pp1473-1477.

Soncini, M. and Pietrabissa, R., 1999. Computational simulation of the tooth movement during the orthodontic treatment. *Computer methods in biomechanics and biomedical engineering.*

Spoor, C. W. and Veldpaus, F. E. 1980. Rigid body motion calculated from spatial co-ordinates of markers. *Journal of Biomechanics.* 13 (4), pp 391-393.

Stewart, D., 1927. Some aspects of the innervation of teeth. *Proceedings of the Royal Society of Medicine.* 20, 1675-1686.

Tanne, K., Koenig MSME, H. A. and Burstone, C. J., 1988. Moment to force ratios and the center of rotation. *American Journal of Orthodontics and Dentofacial Orthopedics.* 94 (5), pp426-431.

The MathWorks, Inc., 1994. Matlab Signal Processing Toolbox. [WWW]. <URL: http://www-ccs.ucsd.edu/matlab/toolbox/signal/butter.html (20 May 2006).

Thelen, D.G. and Anderson, F.C., 2001. An operational space tracking algorithm for generating dynamic simulations of movement, *Computer Methods in Biomechanics and Biomedical Engineering-3, Rome, Italy.*

Thornton, M.J., Morrissey, M.C., Coutts, F.J., 1998. Some effectes of camera placement on the accuracy of the Kinemetrix three-dimensional motion analysis system. *Clinical Biomechanics.* 13, pp452-454.

Trauner, F., 1912. The causes of progressive movement of the teeth towards the front. *American Journal of Orthodontics.* 3, pp144 -158.

Van der Sprenkel, H. B., 1936. Microscopical investigation of the innervation of the tooth and its surroundings. *Journal of Anatomy.* 70, pp233-241.

Volp, C. R., Weston, B. J., Knox, J., Williams, K., Jones, M. L., 1999. A method of evaluating dynamic tooth movement. *Proceeding of Computer Methods in Biomechanics & Biomedical Engineering.* pp461-470.

Von Böhl, M., Maltha, J., Von den Hoff, H. and Kuijpers-Jagtman, A.M., 2004. Changes in the periodontal ligament after experimental tooth movement using high and low continuous forces in beagle dogs. *The Angle Orthodontist.* 74 (1), pp16–25.

Wallace, J.S., 1904. General outline of the causes of irregularities of the teeth. *Dental Manufacturing, London.*

Webb, P.P., Benjamin, M., Moxham, B.J. and Ralphs, J.R., 1994. Age related changes in intermediate filament expression in the periodontium of the rat. *Joumal of Anatomy.* 184, pp198.

Wills D.J., Picton, D.C.A. and Davies, W.I.R. 1978. The intrusion of the tooth for different loading rates. *Journal of Biomechanics.*11, pp429-434.

Willson, G.R. and Shafer, A.S., 1994. What is the centre of the image? *Joumal of Optical Society of America.* 11, pp2946-2955

Wilson, A. N., Middleton, J., Jones, M. L. and McGuinness, N. J., 1994. The finite element analysis of stress in the periodontal liagment when subject to vertical orthodontic forces, *British Joumal of Orthodontics.* 21(2), pp161–167.

Woltring, H. J., Huiskes , R., de Lange, A. and Veldpaus, F. E. 1985. Finite centroid and helical axis estimation from noisy landmark measurements in the study of human joint kinematics. *Journal of Biomechanics.* 18 (5), pp379-389.

Woods, A., Docherty, T., Koch, R., 1993. Image distortions in streoscopic video system. *Proceedings of the SPIE.* 1915, pp36-48.

Yamada Y, Yoshida N, Kobayashi K, Yamauchi K. 1990. An application of magnet and magnetic sensor: measurement system for tooth movement. *IEEE transactions on bio-medical engineering.* Oct; 37(10):919-24.

Yamamoto K, Toshimitsu A, Mikami T, Hayashi S, Harada R, Nakamura S., 1989. Optical measurement of dental cast profile and application to analysis of three-dimensional tooth movement in orthodontics. *Medical & Biological Engineering.* 1(2), pp119-30.

Yedamale, P., 2004. Three ways to control a single-phase induction motor. [WWW]. <URL: www.designnews.com/article/CA486922.html. (15 March 2005).

Yoshida, N., Koga, Y., Kobayashi, K., Yamada, Y. and Yoneda, T., 2000. A new method for qualitative and quantitative evaluation of tooth displacement under the application of orthodontic forces using magnetic sensors. *Medical Engineering & Physics.* 22, pp293–300.

Ziegler, A., Keilig, L., Kawarizadeh, A., Jäger A. and Bourauel C., 2005. Numerical simulation of the biomechanical behaviour of multi-rooted teeth. *The European Journal of Orthodontics.* 27(4), pp333-339.

Abbreviations

2D or 3D	Two or three dimensions
6DOF	6 degrees of freedom
ACS	Anatomical coordinate system
ACS1	Moving tooth anatomic coordinate system
ACS2	Fixed tooth anatomic coordinate system
AFM	Atomic force microscopes
AL	Alveolar layer
BEMF	Back electromagnetic flux
CCD	Charge-coupled device
CL	Cemental layer
CMM	Coordinate measurement machines
CMRR	Common mode rejection ratio
CR	Centre of resistance
DC	Direct current
DFT	Discrete fourier transform
DIP	Dual in-line package
DMP	Digital macrophotogrammetry
DPS	Digital push/pull sensor
DSD	Digital screwdriver
FB	Force balance
FEM	Finite element method
FFT	Fast Fourier transform
FS	Full scale
GCS	Global coordinate system
LAS	Laser Analogue Displacement Sensors
LDS	Laser displacement sensors
LVDT	Linear variable differential transformer
MCS	Marker cluster coordinate systems

MCS1	Moving marker cluster coordinate system
MCS2	Fixed marker cluster coordinate system
MCU	Motion camera unit
ML	Middle layer
MOSFET	Metal oxide semiconductor field effect transistor
NPL	National physical laboratory
OD	Outside diameter
PDL	Periodontal ligament
PID	Proportional-integral-derivative
PWM	Pulse width modulator
QTM	Qualisys track manager
RMS	Root mean square
RO	Rated output
SF	Sharpey fibres
SOICP	Small outline integrated circuit package
USB	Universal Serial Bus

Appendix A

Glossary

Alveolar bone	The jaw bone that anchors the roots of teeth
Amplifier	A circuit that increases the voltage, current, or power of a signal.
Apex	The very bottom of the root of tooth
Arch Wire	A metal wire which is attached to brackets to move teeth.
Bicuspid	Pre-molar: transitional teeth behind the cuspids
Bracket	A metal or ceramic part that is glued onto a tooth and serves as a means of fastening the arch wire.
Buccal	The tooth surface which is next to cheeks. Usually only posterior teeth touch cheeks, so people usually use the term "buccal" only when talking about back teeth.
Calibration	To adjust the correct value of a reading by comparison to a standard.
Canine	Another name for the cuspids
Capacitance	The ability of a capacitor to store an electrical charge. The basic unit of capacitance is the Farad.
Capacitor	An electronic component having capacitive reactance.
Cavity	A small hole in one of teeth caused by tooth decay.
Cementum	A bony substance covering the root of a tooth.
Central	The two upper and two lower teeth in the very center of mouth
Common emitter amplifier	A BJT (bipolar junction transistor) circuit in which the emitter connection is common to both input and output.
Common-mode signals	Signals that appear simultaneously at two inputs of an operational amplifier (op-amp). Common mode signals are

	always equal in amplitude and phase.
Crown	The portion of a tooth above the gum line;
Cuspid	The pointy teeth just behind the laterals. These teeth have one cuspal (or point). Cuspids are also called canines.
Dentin	Inner layer of tooth structure, immediately under the surface enamel
Differential amplifier	An amplifier in which the output is in proportion to the differences between voltages applied to its two inputs.
Drift	A problem that can develop in tuned amplifiers when the frequency of the tuned circuit changes due to temperature or component aging.
Eddy currents	Currents induced into a conducting core due to the changing magnetic field. Eddy currents produce heat which is a loss of power and lowers the efficiency of an inductor.
Enamel	Hard tissue covering the portion of tooth above the gum line
Feedback	A portion of the output signal of an amplifier which is connected back to the input of the same amplifier.
Feedback amplifier	An amplifier with an external signal path from its output back to its input.
First Bicuspid	The teeth just behind the cuspids. These teeth have two cuspals
First Molar	The teeth just behind the second bicuspids. These teeth have a level surface with four cuspals
Gain	Increase in voltage, current and/or power. Gain is expressed as a ratio of amplifier output value to the corresponding amplifier input value.
Gingiva	Gum tissue
Gums	The pink areas around teeth
Incisor	Another name for the centrals and laterals
Incisors	Four upper and four lower front teeth, excluding the cuspids (canine teeth)

Infrared light	Light with wavelengths from 0.7 micron to about 0.1 millimeter is called infrared light. Infrared light is one type of light that is invisible to us.
Inverting amplifier	An amplifier that has a 180° phase shift from input to output.
Inverting input	In an operational amplifier (op amp) the input that is marked with a minus sign. A signal applied at the inverting input will be given 180° phase shift between input and output.
Lateral	The teeth just adjacent to the centrals
Lingual	The tooth surface next to tongue or things mounted on the tooth surfaces next to tongue.
Mandible	Lower jaw
Maxilla	Upper jaw
Molars	Three back teeth in each dental quadrant used for grinding food
Orthodontics	Dental specialty that treats misalignment of teeth
Osteoblasts	Cells which aid the growth and development of teeth and bones.
Osteoclasts	Cells which help create the sockets in bones. For example osteoclasps create the openings in jaw bone to hold teeth.
Peak to peak	Difference between the maximum positive and maximum negative values of an AC waveform.
Periodontal	Pertaining to gums. For example periodontal desiese is gum disease.
periodontal ligament	A soft tissue which connects between the root of tooth and alveolar bone
Power amplifier	An amplifier designed to deliver maximum power output to a load.
Pulp	The soft inner structure of a tooth, consisting of nerve and blood vessels.
RC time constant	Product of resistance and capacitance in seconds.

Root	Tooth structure that connects the tooth to the jaw
Rotation	A movement in which the tooth turned along the long axis of the tooth.
Scale	Set of markings used for measurement.
Second Bicuspid	The teeth just behind the first bicuspids. These teeth also have two cuspals
Second Molar	The teeth just behind the first. These teeth also have a level surface with four cuspals.
Third Molar	The teeth just behind the second molars. These teeth also have a level surface with four cuspals.
Tipping	A tooth movement in which the root of the tooth is tipped labially (lip) or lingually (tongue) to correct the angle of the crown of the tooth.
Torque	The rotation of a tooth on the long axis moving the root of the tooth in a buccal or labial direction.
Translation	A tooth movement in which the entire tooth moves forward or backward without tipping or rotating.

Appendix B

The calibration of the tip of the pointer

```
hole=[6.89;10.70;0.07;1];
GCSdata=DPSCSdata;
[SmG,SmL]=CalcLCS1(GCSdata);
data=[SmL;SmG];
[Tsg,res]=soder(data);

GCSdata=SPCSdata;
[PG,PL]=CalcLCS(GCSdata);
data=[PL;PG];
[Tpg,res]=soder(data);
point=inv(Tpg)*Tsg*hole;
```

Appendix C

6 DOF calculation

```
[m,n]=size(T);

if m~=4 | n~=4,

   disp(blanks(2));

   disp('To check the filetype that should be without headers')
else

   R(2)=(pi/2)-acos(T(3,1));

   R(1)=atan2(T(3,2),T(3,3));

   R(3)=-(atan2(T(2,1),T(1,1)));

   Tr(1)=-(T(1,4)+(T(3,4)*sin(R(2))));

   Tr(2)=-T(2,4);

   Tr(3)=T(3,4)+(T(1,4)*sin(R(2)));

end;

RandT=[(R*180/pi) Tr];
```

Appendix D

(1) Load of 0.196N for 10s loaded in the buccal direction

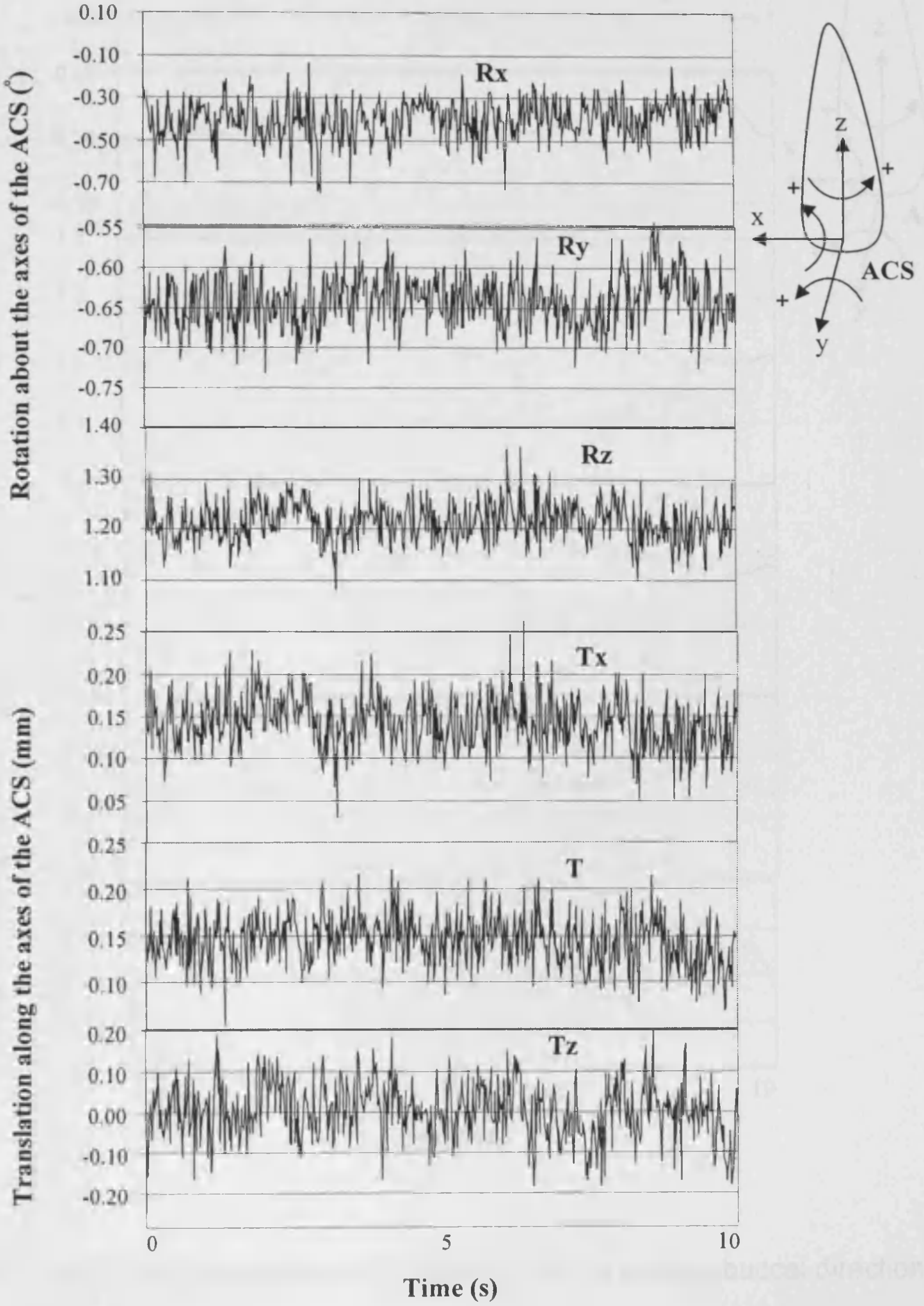

(a) Original signal with load of 0.196N for 10s in loading buccal direction.

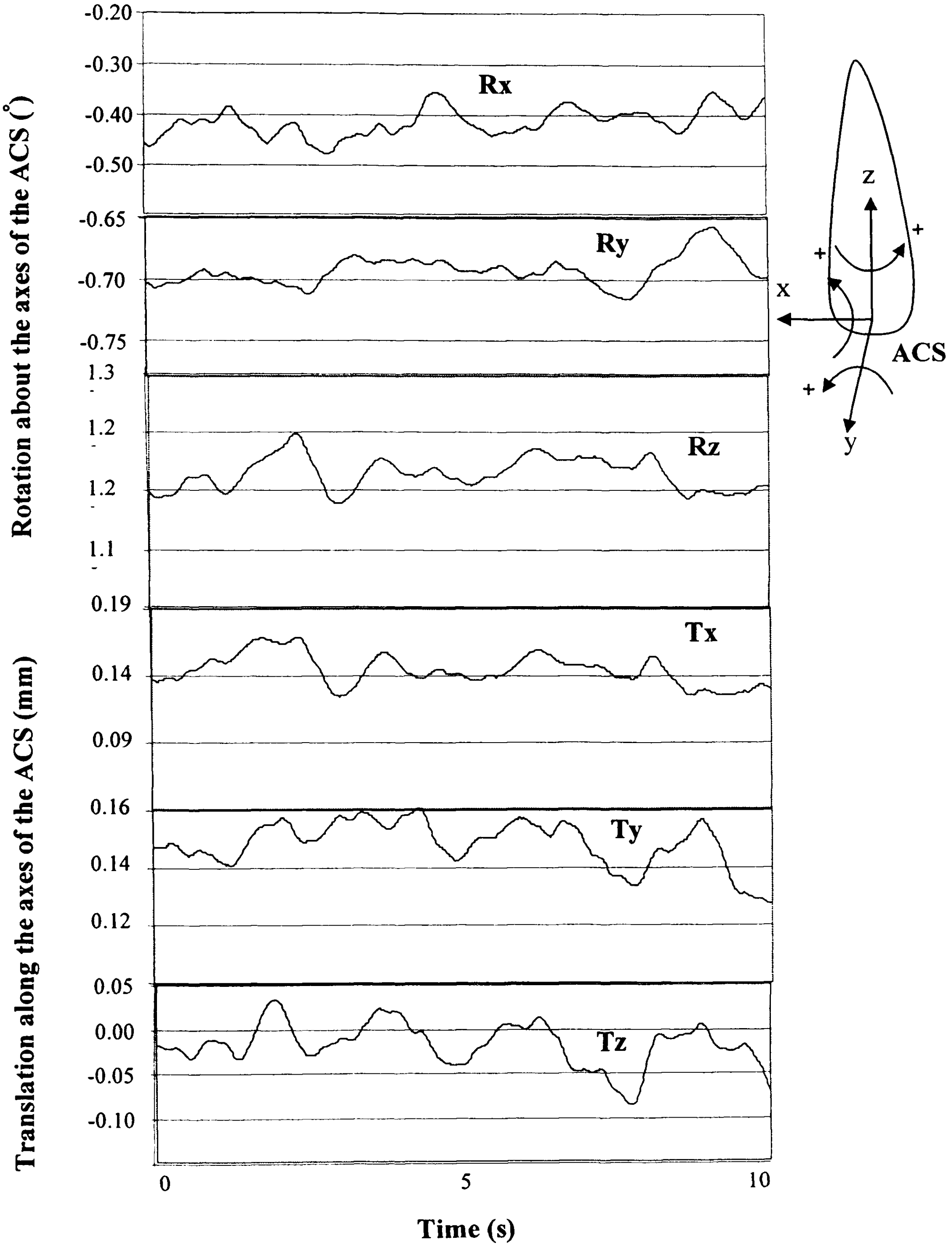

(b) Smoothed signal with load of 0.196N for 10s in loading buccal direction.

(2) Load of 0.294N for 10s loaded in the buccal direction

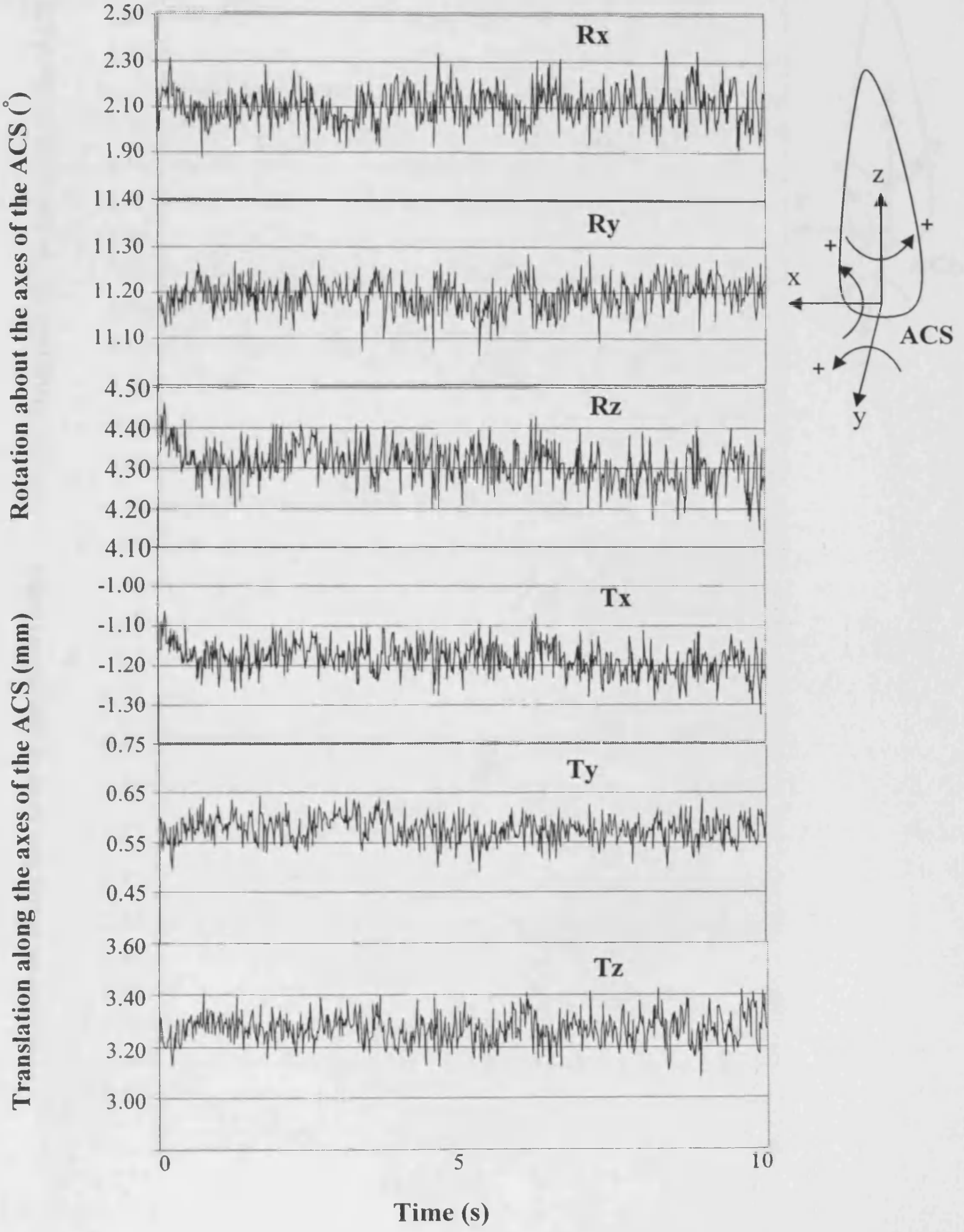

(a) Original signal with load of 0.294N for 10s loaded in the buccal direction.

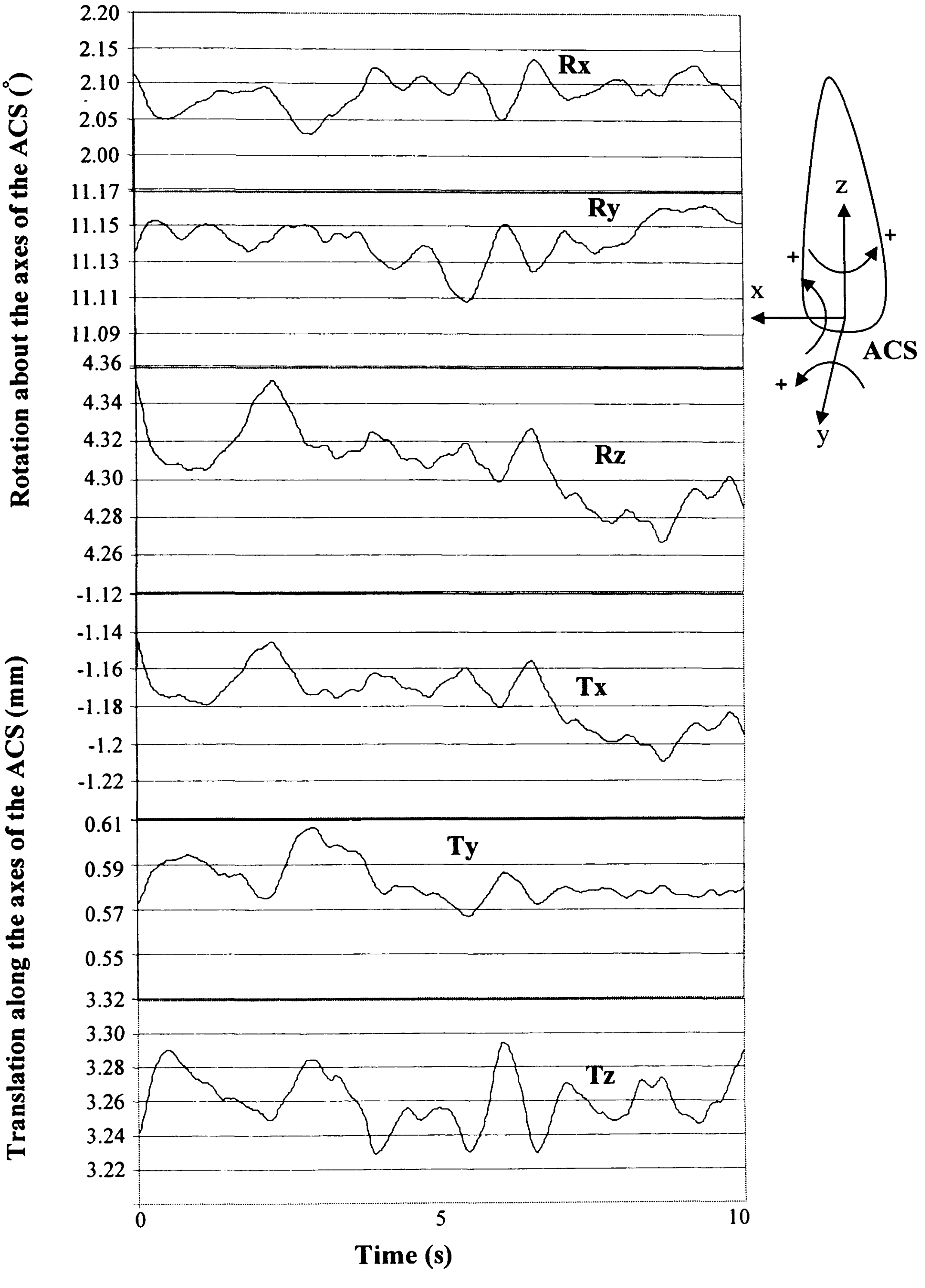

(b) Smoothed signal with load of 0.294N for 10s loaded in the buccal direction.

(3) Load of 0.294N for 30s loaded in the buccal direction

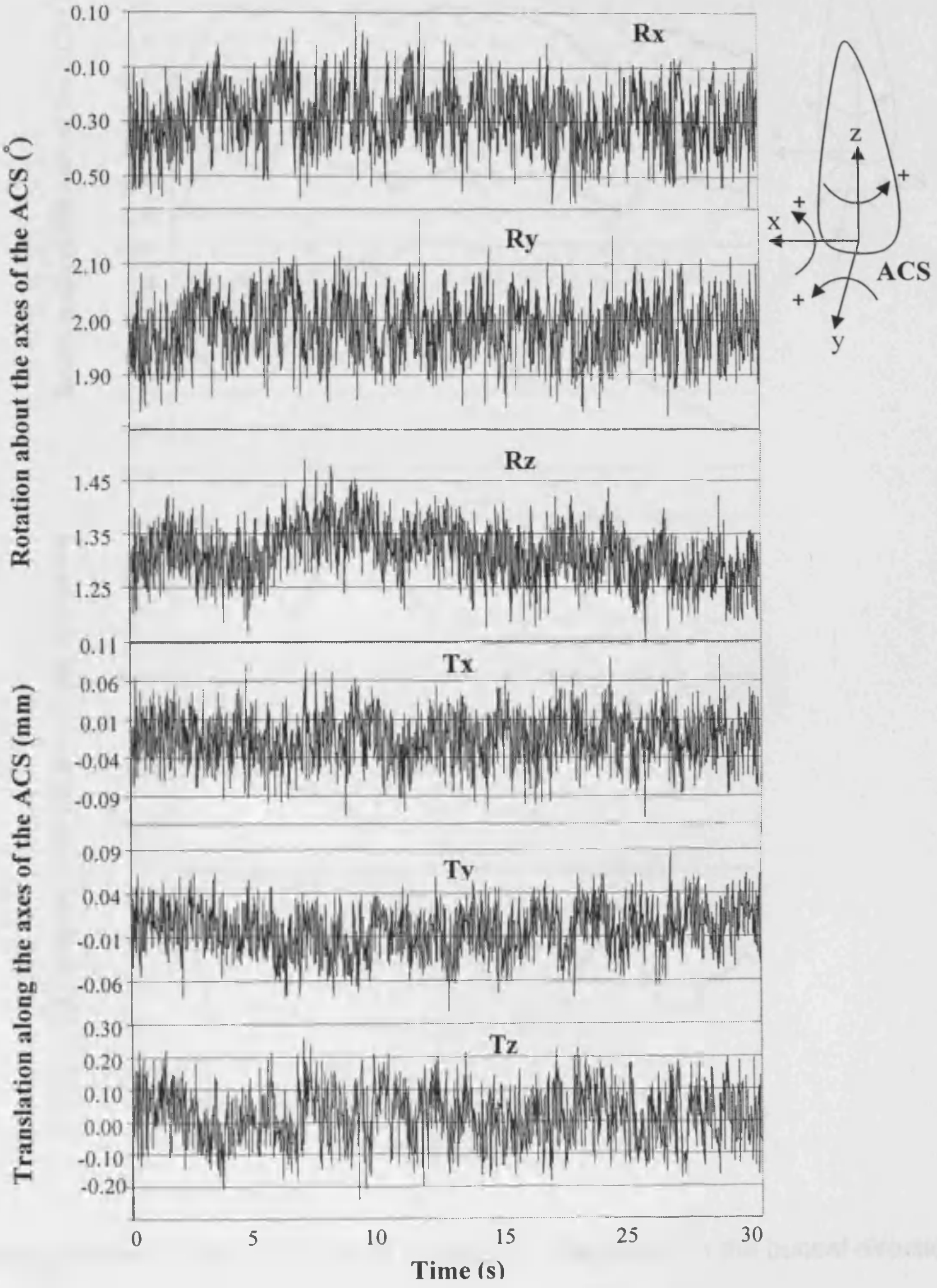

(a) Original signal with load of 0.294N for 30s loaded in the buccal direction.

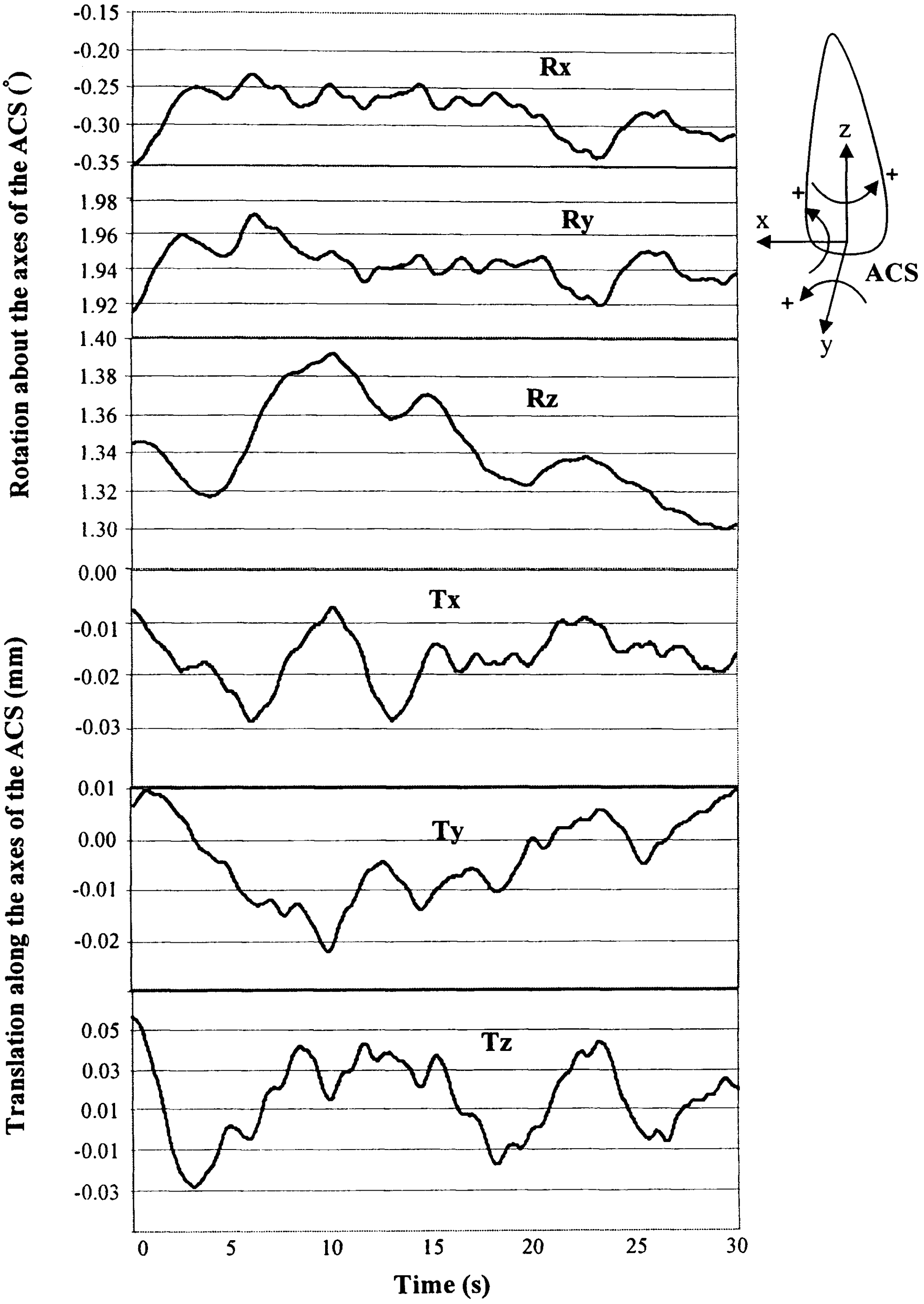

(b) Smoothed signal with load of 0.294N for 30s loaded in the buccal direction.

(4) Load of 0.49N for 30s loaded in the buccal direction

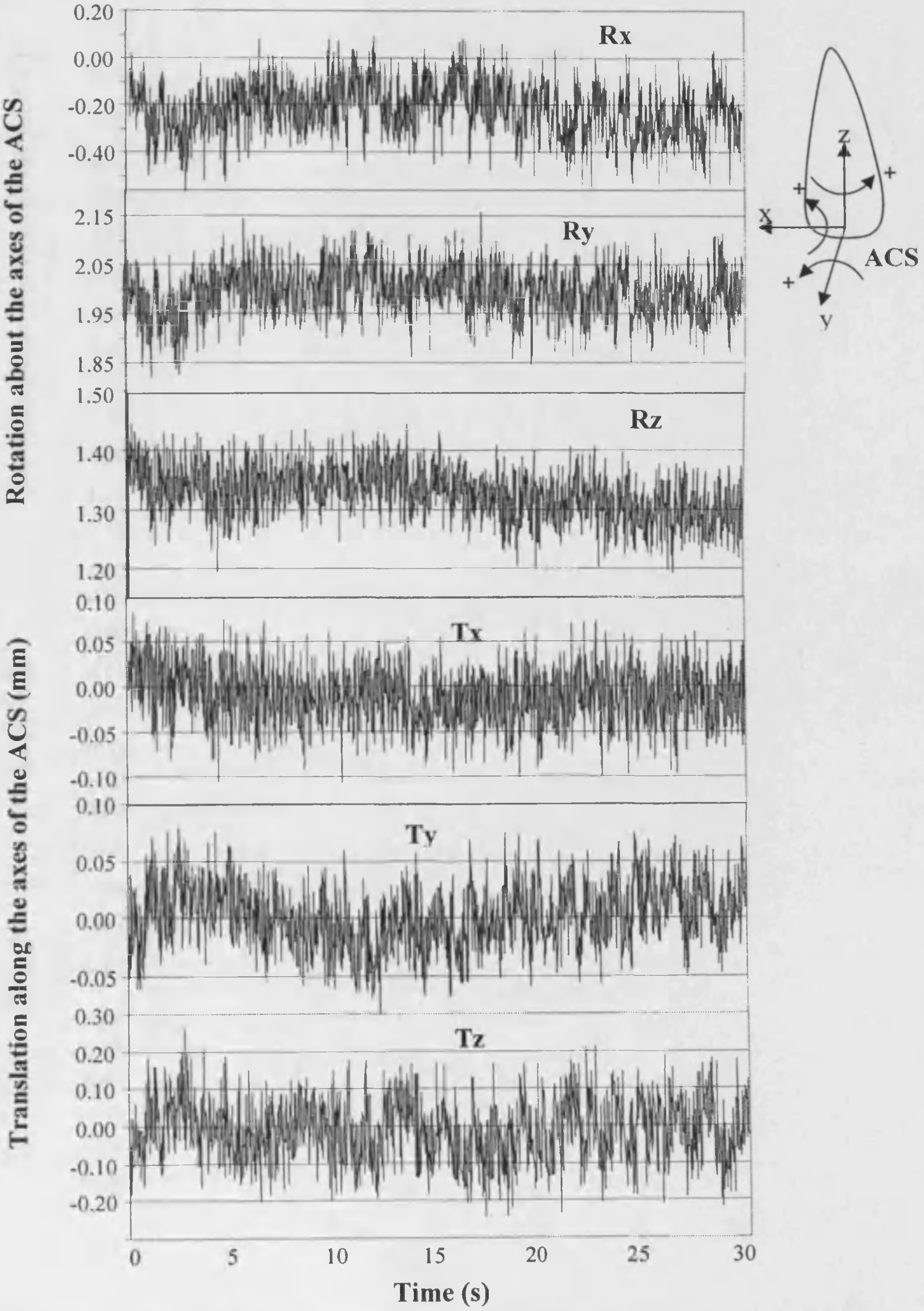

(a) Original signal with load of 0.49N for 30s loaded in the buccal direction.

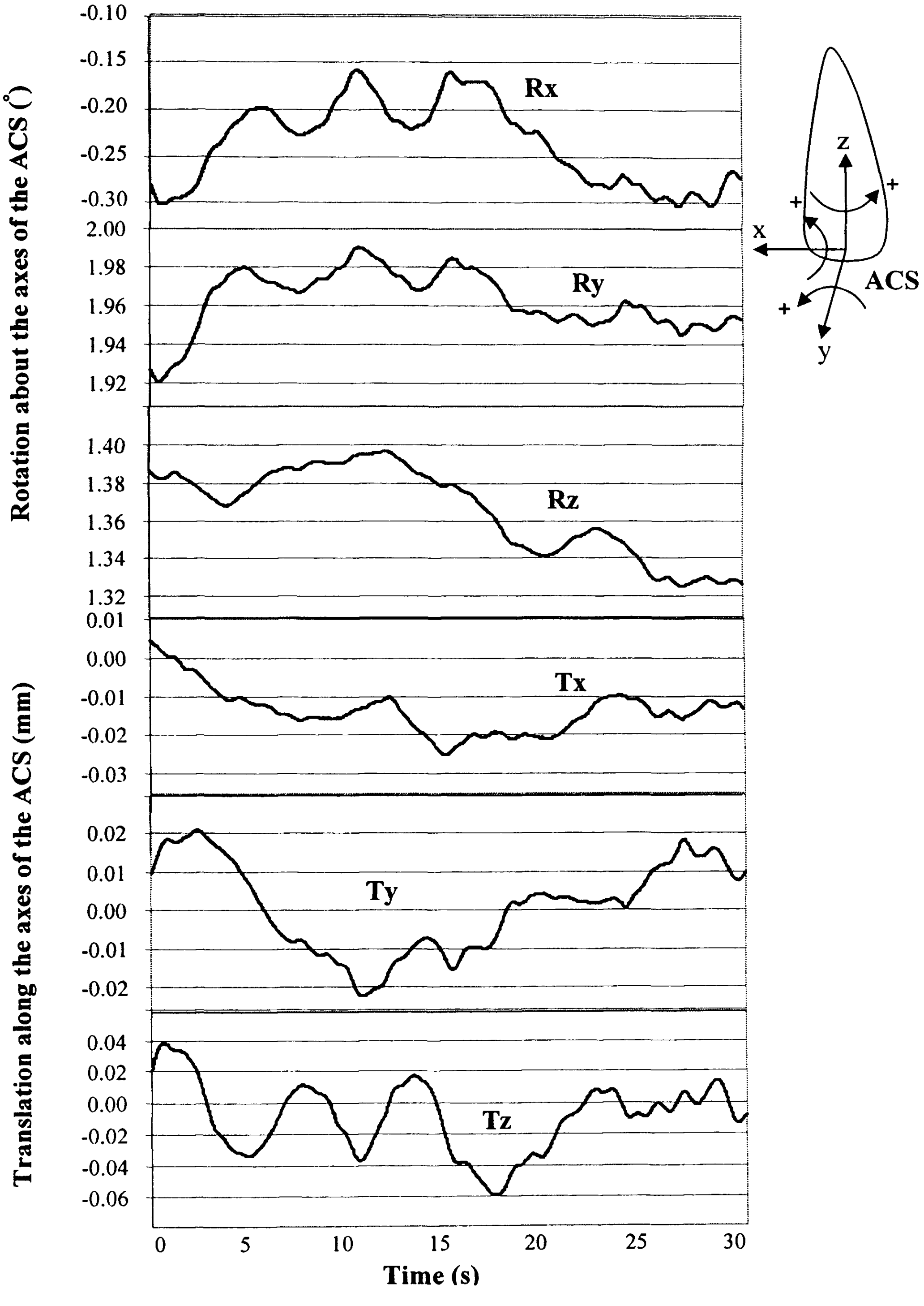

(b) Smoothed signal with load of 0.49N for 30s loaded in the buccal direction.

Appendix E

The data of calibration frames and wand calibration.

1. Frame calibration data:

a. Diamond markers coordinates

	X	Y	Z
1	0	0	0
2	0	27.704	-0.009
3	15.198	28.296	-0.034
4	14.787	1.358	0.016
5	2.633	17.407	11.668
6	10.087	17.42	11.62

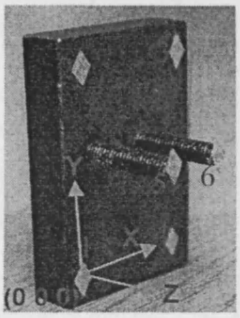

b. Spherical markers coordinates

	X	Y	Z
1	0	0	0
2	0	24.674	-0.078
3	12.13	24.554	0.038
4	12.064	-0.279	-0.06
5	2.034	14.733	14.35
6	10.12	14.589	14.066

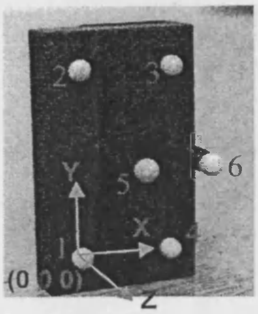

c. Big frame spherical markers coordinates

	X	Y	Z
1	0	0	0
2	0	33.208	0.019
3	25.151	0.712	-0.093
4	63.765	0.284	0.102
5	13.293	25.451	34.677
6	49.609	17.092	34.718

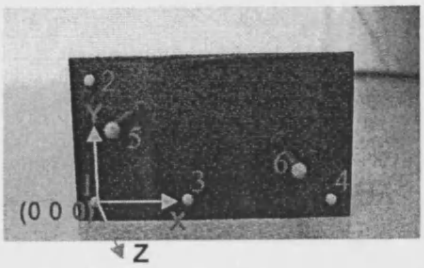

2. Wand calibration data

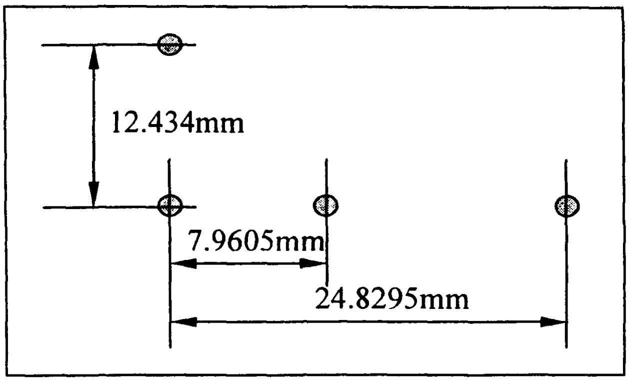

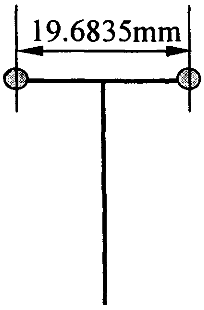

Appendix F

(1) Load of 0.196N for 30s loaded in the buccal direction

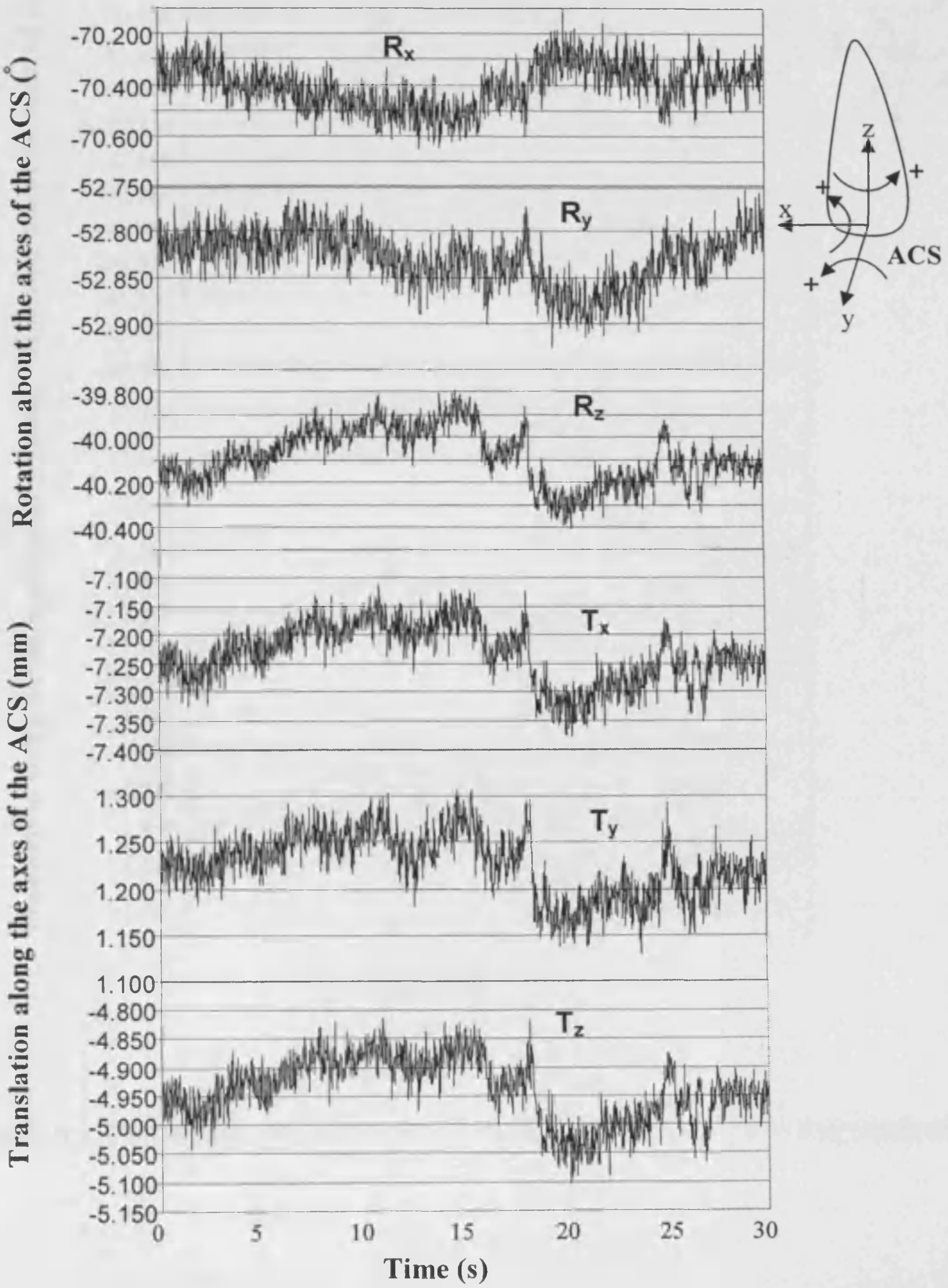

(a) Original signal with load of 0.196N for 30s loaded in the buccal direction.

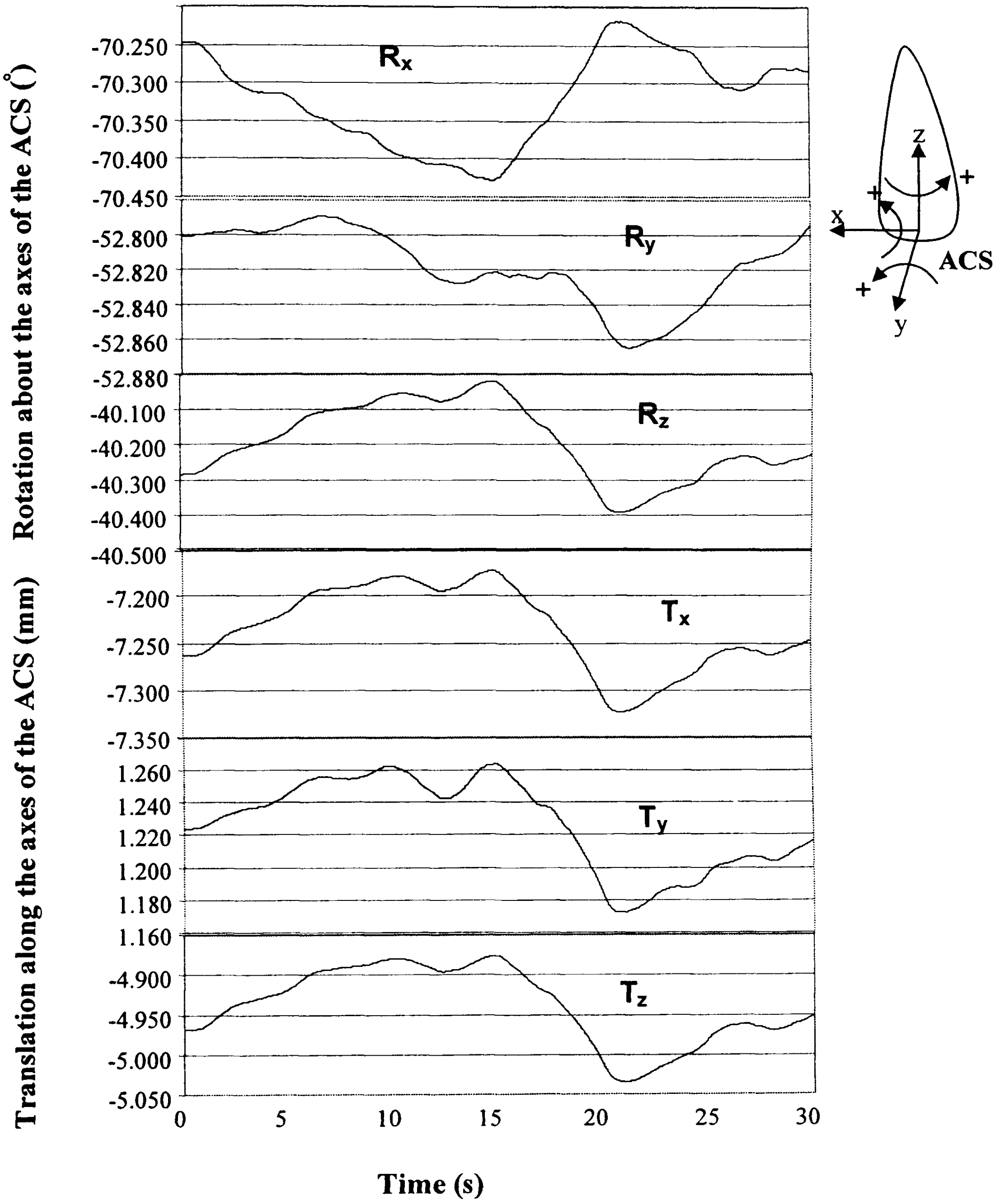

(b) Smoothed signal with load of 0.196N for 30s loaded in the buccal direction

(2) Load of 0.294N for 30s loaded in the buccal direction

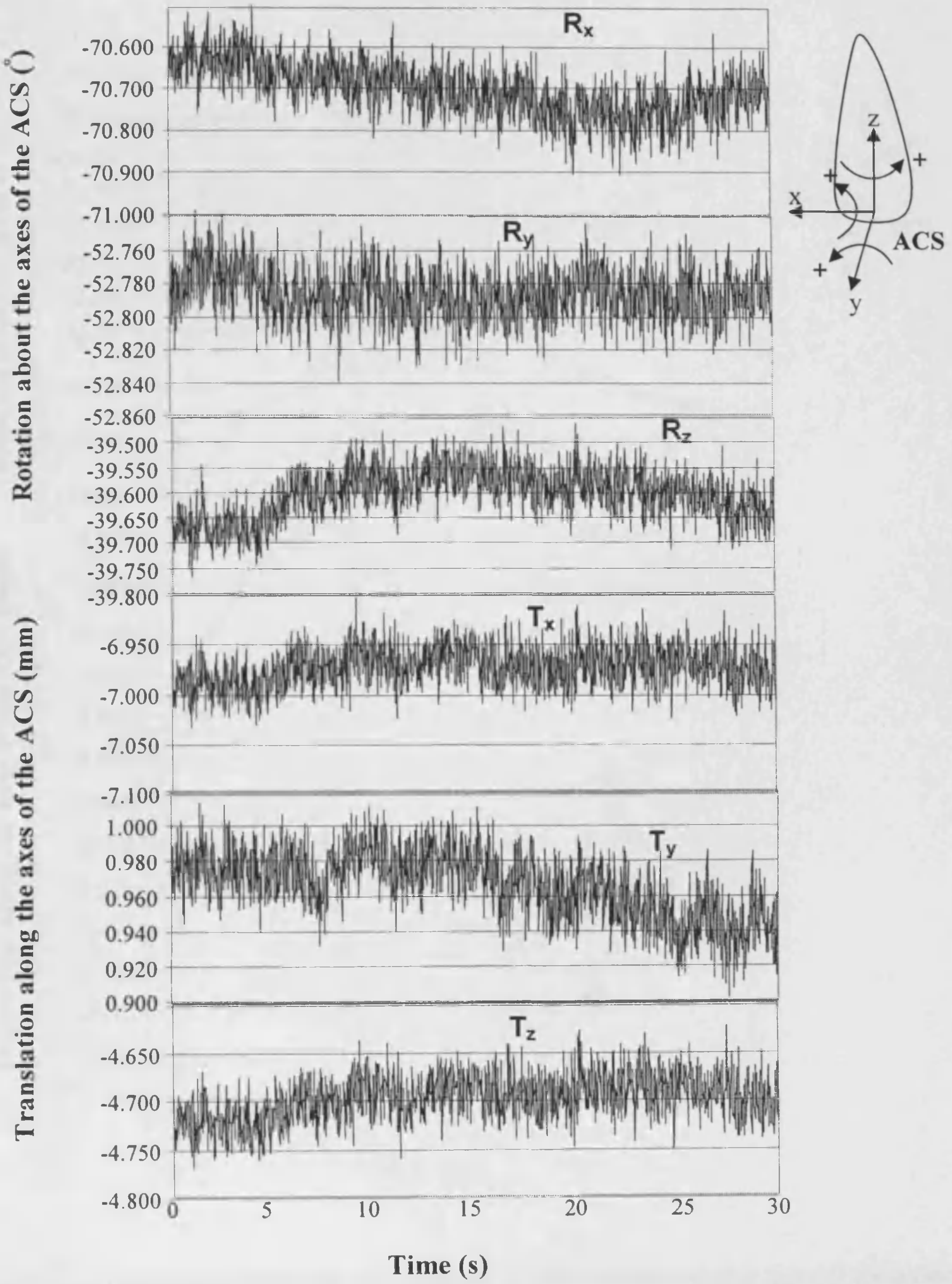

(a) Original signal with load of 0.294N for 30s loaded in the buccal direction.

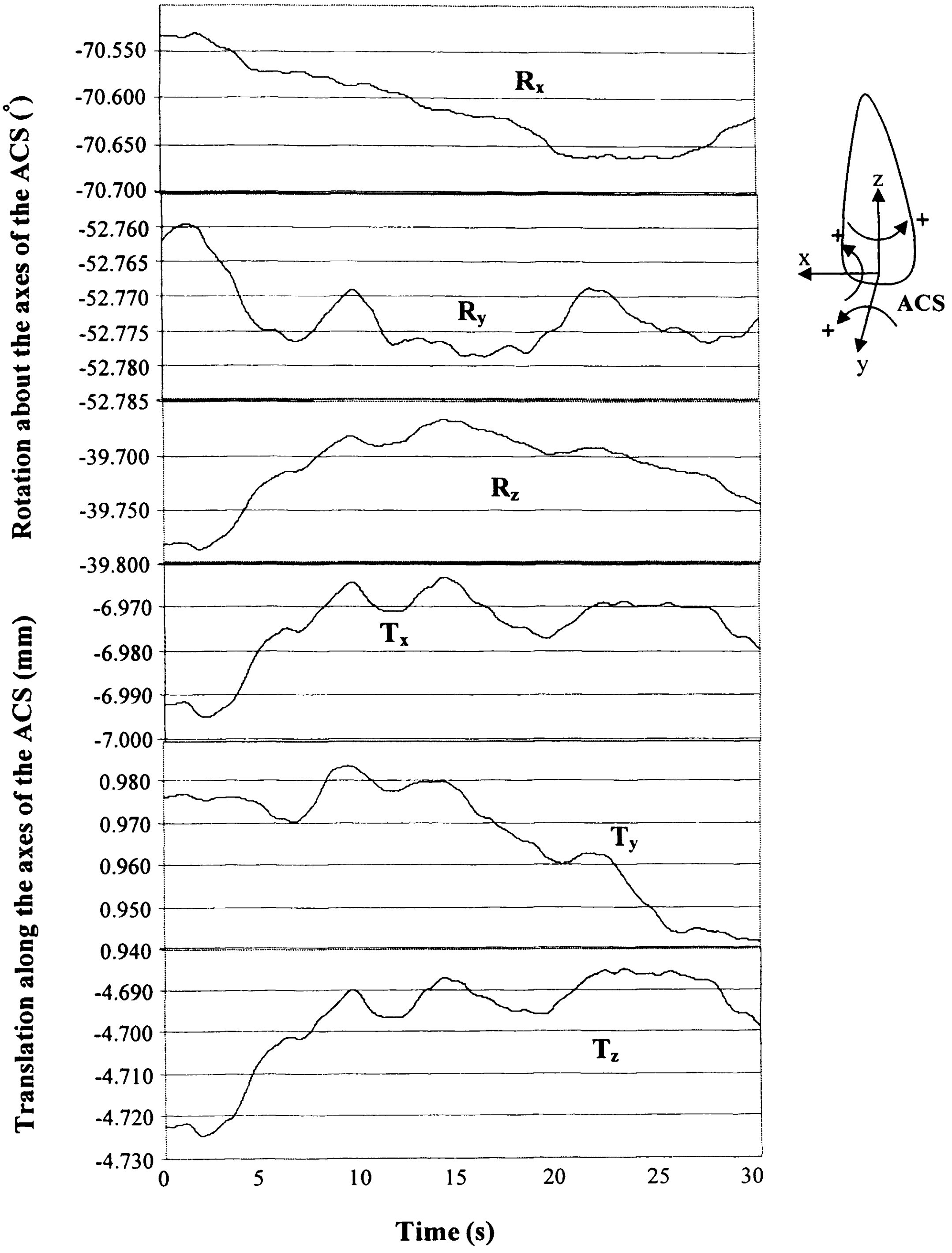

(b) Smoothed signal with load of 0.294N for 30s loaded in the buccal direction

(3) Load of 0.196N for 30s loaded in the intrusive direction

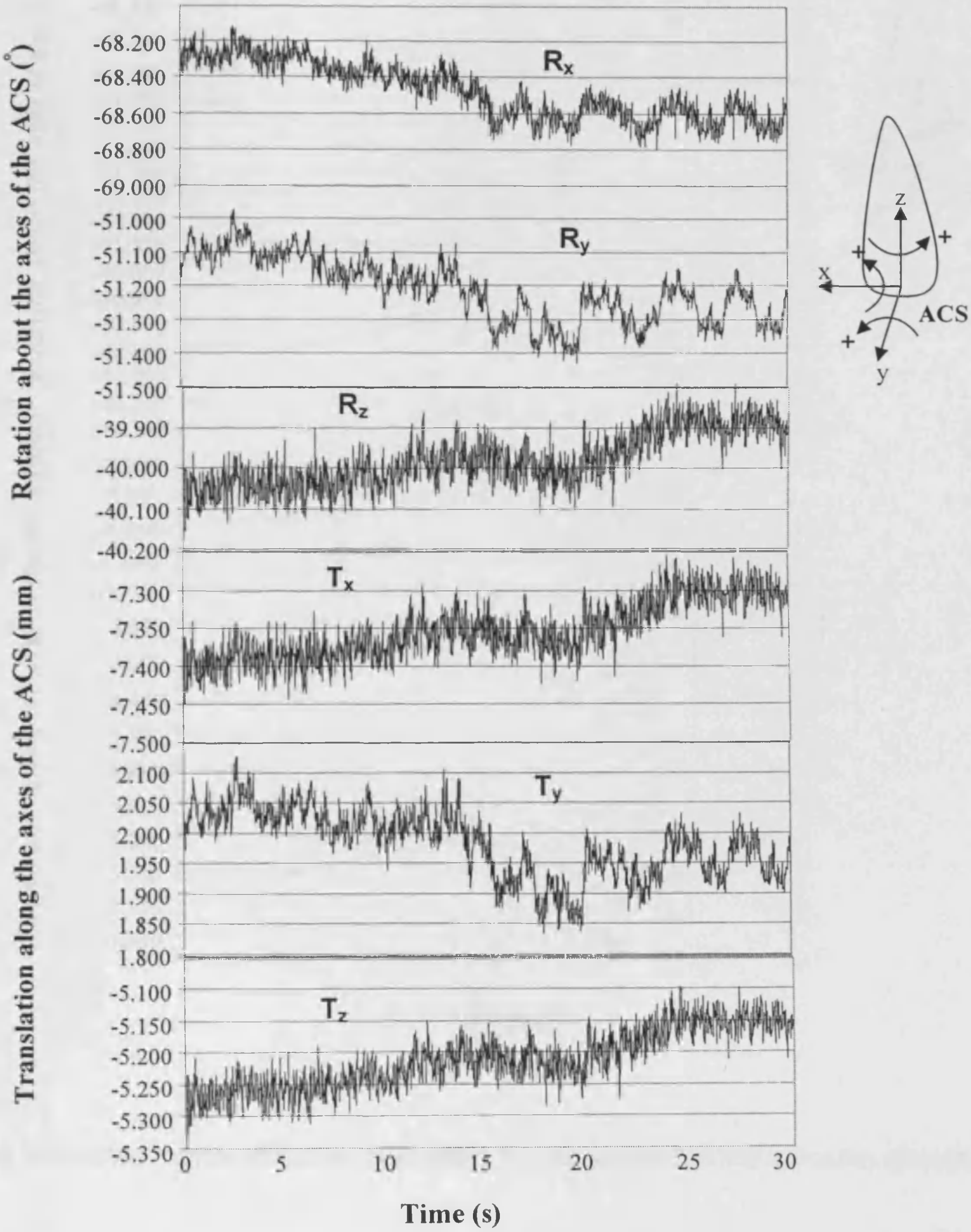

(a) Original signal with load of 0.196N for 30s loaded in the intrusive direction.

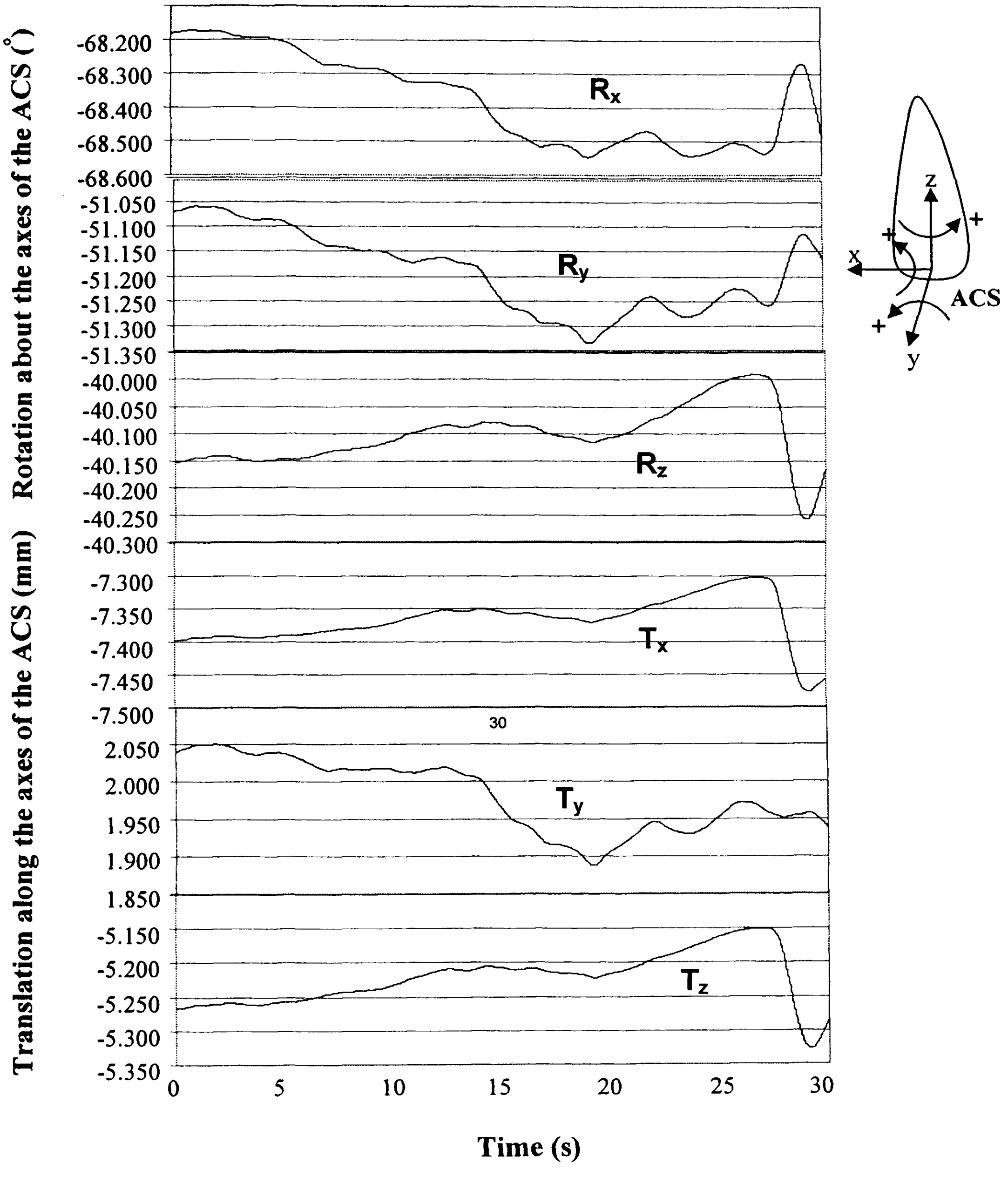

(b) Smoothed signal with load of 0.196N for 30s loaded in the intrusive direction